

**DEVELOPMENT OF IN VIVO NANOPARTICLE DISCOVERY
TECHNOLOGIES TO ENABLE EXTRA-HEPATIC GENE
THERAPIES**

A Dissertation
Presented to
The Academic Faculty

by

Cory Dane Sago

In Partial Fulfillment
of the Requirements for the Degree
Doctor of Philosophy in Biomedical Engineering in the
Wallace H. Coulter Department of Biomedical Engineering

Georgia Institute of Technology
Emory University
August 2019

COPYRIGHT © 2019 BY CORY SAGO

DEVELOPMENT OF IN VIVO NANOPARTICLE DISCOVERY TECHNOLOGIES TO ENABLE EXTRA-HEPATIC GENE THERAPIES

Approved by:

Dr. James Dahlman, Advisor
Department of Biomedical Engineering
Georgia Institute of Technology

Dr. Gabriel Kwong
Department of Biomedical Engineering
Georgia Institute of Technology

Dr. Philip Santangelo, Co-Advisor
Department of Biomedical Engineering
Georgia Institute of Technology

Dr. Wilbur Lam
Department of Biomedical Engineering
Georgia Institute of Technology

Dr. Krishnendu Roy
Department of Biomedical Engineering
Georgia Institute of Technology

Dr. MG Finn
Department of Chemistry
Georgia Institute of Technology

Date Approved: [May 13th, 2019]

ACKNOWLEDGEMENTS

My Ph.D. would not have been possible without the support and guidance of many individuals. First, and foremost, I would like to thank my family for the constant and unwavering support that they have always provided me.

I owe a great deal to James Dahlman; who has been always been amazing mentor and who I am now lucky enough to consider a great friend. I have always admired the patience and humility that you approach all things, and I am lucky that you took a chance on me when you offered me a spot in your lab after my first week rotating through.

I was lucky enough to work with many members in the Dahlman lab who are undoubtedly the quirkiest, most dedicated group of individuals that I know. I would like to thank Melissa Lokugamage for all of her help developing the science and also her friendship over the last two years of my Ph.D.

I would also like to thank all of my scientific mentors for giving me the opportunity to learn from them and for facilitating my growth as a scientist, especially, Gabe Kwong, Phil Santangelo, and MG Finn. Specifically, I would like to thank Lena Gamboa and Daryll Vanover for their support and friendship through the process.

TABLE OF CONTENTS

ACKNOWLEDGEMENTS	iii
LIST OF FIGURES	v
SUMMARY	viii
CHAPTER 1: A Direct Comparison of <i>in vitro</i> to <i>in vivo</i> nanoparticle delivery	1
1.1 Background	1
1.2 Results	4
1.3 Discussion	10
1.4 Methods & Materials	40
1.5 References	47
CHAPTER 2: Quantitative unbiased analysis of nanoparticle trafficking	51
2.1 Background	51
2.2 Results	52
2.3 Discussion	62
2.4 Methods & Materials	84
2.5 References	89
CHAPTER 3: Fast Identification of Nanoparticle Discovery	95
3.1 Background	95
3.2 Results	97
3.3 Discussion	105
3.4 Methods & Materials	135
3.5 References	141
CHAPTER 4: Directed evolution of LNPs for delivery to bone marrow	145
4.1 Background	145
4.2 Results	147
4.3 Discussion	157
4.4 Methods & Materials	179
4.5 References	184
CHAPTER 5: Identification of LNPs with Tropism to T-Cells	191
5.1 Background & Results	191
5.2 Methods & Materials	219
5.3 References	220
CHAPTER 6: Development of <i>in vivo</i> oligonucleotide anti-CRISPRs	222
6.1 Background & Results	222
6.2 Methods & Materials	242
6.3 References	246

LIST OF FIGURES

Figure 1.1	13
Figure 1.2	14
Figure 1.3	17
Figure 1.4	19
Figure 1.5	20
Figure 1.6	21
Figure 1.7	30
Figure 1.8	31
Figure 1.9	34
Figure 1.10	37
Figure 1.11	38
Figure 1.12	39
Figure 2.1	65
Figure 2.2	67
Figure 2.3	68
Figure 2.4	71
Figure 2.5	72
Figure 2.6	73
Figure 2.7	74
Figure 2.8	75
Figure 2.9	80
Figure 2.10	81
Figure 2.11	82

Figure 2.12	83
Figure 3.1	109
Figure 3.2	111
Figure 3.3	116
Figure 3.4	117
Figure 3.5	123
Figure 3.6	124
Figure 3.7	128
Figure 3.8	129
Figure 3.9	130
Figure 3.10	132
Figure 3.11	133
Figure 3.12	134
Figure 4.1	160
Figure 4.2	161
Figure 4.3	166
Figure 4.4	167
Figure 4.5	168
Figure 4.6	172
Figure 4.7	173
Figure 4.8	175
Figure 4.9	178
Figure 5.1	202
Figure 5.2	203
Figure 5.3	206
Figure 5.4	207

Figure 5.5	208
Figure 5.6	209
Figure 5.7	210
Figure 5.8	211
Figure 5.9	212
Figure 5.10	214
Figure 5.11	215
Figure 5.12	216
Figure 5.13	218
Figure 6.1	231
Figure 6.2	233
Figure 6.3	234
Figure 6.4	235
Figure 6.5	236
Figure 6.6	238
Figure 6.7	241

SUMMARY

In this body of work, we will broadly pursue the development of technologies that enable the development of non-viral gene therapies, primarily through the engineering of lipid nanoparticles (LNPs) and the genetic therapy payload itself. In each case, the developed technology is validated to be scientifically real and practically robust. We then utilize each tool to learn more about the biology underlying host-LNP interactions or displaying pre-clinical utility.

In Chapter 1, we utilize the first-generation barcoding system (“Jordan”) to probe the *in vitro-in vivo* relationship of LNP accumulation to endothelial cells and macrophages. This work is important as the field has traditionally relied on *in vitro* assays in the development of LNPs for hepatic and extra-hepatic delivery, we demonstrate no relationship between *in vitro* and *in vivo* results. These data highlight the utility of LNP discovery systems that function entirely *in vivo* and emphasize the importance of the further development of these next-generation assays.

In Chapter 2, we develop a novel and improved DNA barcoding system (“QUANT”). QUANT utilizes a rationally-designed DNA barcode containing a ddPCR-probe binding site to allow for the determination of absolute LNP biodistribution with >100,000,000X more sensitivity than ubiquitously used fluorescent methods, while still allowing for the multiplexing of >100 LNPs simultaneously. We apply QUANT to determine the impact of Caveolin 1 on the biodistribution of >200LNPs and found that caveolin 1 was critical for LNP accumulation in endothelial cells, as well as Kupffer Cells.

In Chapter 3, we develop a novel DNA barcoding system that allows for the measurement of the functional, cytosolic mRNA delivery of >100 LNPs simultaneously *in vivo*. We utilize this novel system (“FIND”) to evolve two LNP that potently delivered siRNAs, sgRNAs, and mRNAs

to splenic endothelial cells. One of these LNPs also displayed gene editing in wild-type mice upon the co-delivery of Cas9 mRNA and sgRNA.

In Chapter 4, we develop a novel DNA barcoding system that allows for the measurement of the functional, cytosolic siRNA of >100 LNPs simultaneously *in vivo*. We utilize this system to evolve a previously described LNP that targets lung endothelial cells to now target bone marrow endothelial cells, as well as lung endothelial cells.

In Chapter 5, we applied the siRNA functional screen to facilitate the screening of 104 LNPs representing 13 different ionizable lipids structures to 9 cell-type *in vivo*. Utilizing this unbiased screen, we observed siRNA-mediated silencing in T cells isolated from the spleen, and confirmed these results were mediated by LNPs containing a novel ionizable lipid. We then identified and confirmed the chemical motif responsible for this T-cell silencing. Interestingly, LNPs containing this ionizable lipid preferentially mediate functional siRNA delivery to T cells as compared to hepatocytes.

In Chapter 6, we develop two novel oligonucleotide-based anti-CRISPR approach targeting the sgRNA, as well as the 3'UTR of Cas9 mRNA. We display these novel anti-CRISPRs function in a synergistic manner *in vitro* and *in vivo*. We then demonstrate that they can functionally increase the ratio of on- to off- (tissue)target gene editing of a LNP which, without intervention, would edit in both splenic endothelial cells as well as hepatocytes.

CHAPTER 1. A DIRECT COMPARISON OF IN VITRO AND IN VIVO NANOPARTICLE DELIVERY

The work presented here is an excerpt from Paunovska*, K, Sago*, CD, Monaco, C, Hudson, WH, Gamboa Castro, M, Rudoltz, TG, Kalathoor, S, Vanover, D, Santangelo, PJ, Ahmed, R, Bryksin, AV, Dahlman, JE (2018). “A direct comparison of *in vitro* and *in vivo* nucleic acid delivery mediated by hundreds of nanoparticles reveals a weak correlation.” Nano Letters.

1.1 Background

The transport of foreign nucleic acids is carefully regulated, making systemic drug delivery inefficient¹⁻³. To deliver nucleic acids, thousands of chemically distinct lipid nanoparticles (LNPs) have been designed⁴⁻⁹. LNP chemical diversity is imparted 2 ways. First, thousands of distinct biomaterials have been synthesized⁴⁻⁹. Second, each biomaterial can be formulated into hundreds of LNPs by adding poly(ethylene glycol) (PEG), cholesterol, 1,2-dioleoyl-sn-glycero-3-phosphoethanolamine (DOPE), and other constituents at different mole ratios. LNPs are screened *in vitro* before a small number of finalists is tested *in vivo*⁴⁻⁹; in a typical example, we measured how well 2,000 LNPs delivered siRNA to HeLa cells in static cell culture before analyzing 5 LNPs *in vivo*⁵. Similar studies have been performed with LNPs composed of small amine-, sugar-, or peptide-based materials^{4,6-9}.

To successfully deliver nucleic acids after systemic administration, nanoparticles must overcome complex obstacles that are difficult to model *in vitro*. Nanoparticles must protect the DNA or RNA from degradation, avoid clearance, target the desired cell within a complex microenvironment, and gain access to the cytoplasm, without stimulating a

systemic immune response. A significant fraction of the drug can be lost at each point, and as a result, every step is important to model. Physical variables also influence delivery. Cationic nanoparticles can be disassembled by the renal anionic basement membrane¹⁰, and nanoparticles can be blocked from accessing brain parenchyma, due to the capillary tight junctions and glial cells that make up the blood brain barrier¹¹⁻¹⁵. By contrast, nanoparticles can access tissues like the liver via porous ECs and discontinuous basement membranes in the hepatic sinusoids¹¹⁻¹⁵. In addition to these barriers, *in vivo* analysis and mathematical modeling have demonstrated that blood flow rates affect nanoparticle targeting by affecting the likelihood a particle extravasates¹⁶.

Despite these differences, nanoparticles are often screened for delivery *in vitro*. Large scale *in vitro* nanoparticle screens typically utilize cells that are easy to expand (e.g. HeLa)⁴⁻⁹. These cells have genotypes and phenotypes that differ from cells *in vivo*. Cells can also undergo significant changes in gene expression when cultured¹⁷. Many of these changes may be driven by exposure to a combination of foreign serum (e.g., FBS) and static fluid flow, which most cell types are not exposed to *in vivo*. Given that *in vitro* and *in vivo* delivery require the nanoparticle to overcome different physiological obstacles, and that endocytosis is likely to be affected by gene expression changes that occur when cells are removed from their natural microenvironment, we hypothesized that *in vivo* LNP delivery would not be predicted *in vitro* using common cell culture conditions.

The field can currently synthesize nanomaterials at a rate several orders of magnitude higher than the rate at which we can test nanomaterials for drug delivery *in vivo*. Recently, we reported a nanoparticle DNA barcoding system¹⁸ to increase the number of LNPs we could study at once *in vivo*. We used a microfluidic device to barcode LNPs (**Figure**

1.1A)¹⁹; each LNP was formulated to carry a unique DNA barcode. We pooled stable LNPs, administered them to animals, and deep sequenced the barcodes to quantify the delivery of up to 30 LNPs simultaneously¹⁸. This original paper focused exclusively on control experiments designed to characterize the system. Specifically, we demonstrated that barcoded LNPs can be made so they do not mix in solution, that DNA sequencing readouts were linear with respect to the amount of injected DNA, that DNA barcode delivery recapitulates the behavior of previously characterized LNPs, that delivery does not change with DNA sequence, and that delivery of DNA barcodes to hepatocytes *in vivo* modeled siRNA delivery to hepatocytes *in vivo*¹⁸.

We now report that the same LNP barcoding system, herein named JOint Rapid DNA Analysis of Nanoparticles (JORDAN), can elucidate fundamental questions about nanoparticle delivery. We quantified how well 281 LNPs delivered DNA barcodes to endothelial cells and macrophages, both *in vitro* and *in vivo*. We focused on endothelial cells and macrophages for three reasons. First, both cell types are implicated in many diseases^{20,21}. Second, since they are ubiquitous, we could measure delivery to the same cell type in multiple tissues. Third, endothelial cells are more ‘accessible’ upon intravenous injection than tissue macrophages. We reasoned, incorrectly, that delivery to more accessible cells would be more predictable *in vitro*. Our data strongly suggest that *in vitro* LNP delivery to endothelial cells and macrophages using static cell culture does not predict *in vivo* LNP delivery to the same cell types.

We then used the JORDAN system to investigate how different LNPs distribute within a clearance organ (the spleen). By measuring how 85 LNPs delivered barcodes to 8 different splenic cell types, we found that cells derived from myeloid progenitors tended

to be targeted to by similar LNPs; cells derived from lymphoid progenitors tended to be targeted by different LNPs. We then identified LNP1, which delivered barcodes to all 8 cell types we studied in the spleen. We confirmed the splenic targeting of LNP1 using fluorescently labeled DNA. The approach we have described can be extended to study (i) how well any *in vitro* system (e.g., tissue-on-a-chip) predicts delivery *in vivo*, and (ii) how different cells are targeted within a tissue.

1.2 Results

We rationally designed DNA barcodes in order to study the delivery of many LNPs at once (**Figure 1.1A-C**). Each DNA barcode contained phosphorothioate linkages in order to reduce exonuclease activity, and universal primer sites for unbiased PCR amplification (**Figure 1.1C**)¹⁸. The 8 nucleotide ‘barcode’ region was located in the middle of the 56 nucleotide DNA sequence. Of the 4⁸ possible DNA barcode combinations, we designed 240 to work with Illumina sequencing machines (**Figure 1.2A**). We amplified barcodes using universal primers and labeled individual samples with Illumina dual-indexed adapters that enabled sample multiplexing (**Figure 1.2B**). For each experiment, we calculated the ‘normalized delivery’, using the administered LNP solution as a DNA input (**Figure 1.1D, Figure 1.2C**). We also added new LNP quality controls to reduce the likelihood LNPs mixed together. Specifically, we analyzed the size of each individual LNP using dynamic light scattering (DLS). Based on our experience studying LNPs^{5,18,22-25}, we only pooled stable LNPs with good autocorrelation curves and diameters between 20 and 300 nm (**Figure 1.2D**). We then tested whether barcoded LNPs entered cells. We formulated Alexa647-tagged DNA barcodes in a previously characterized^{5,18,22-27} LNP named 7C1. Barcodes entered immortalized mouse aortic endothelial cells (iMAECs)

within 15 minutes, and were observed inside the cell at 1.5 and 72 hours after administration (**Figure 1.1E, Figure 1.2E, F**).

We then formulated 144 LNPs, systematically varying PEG structure. We synthesized 2 biomaterials called ‘lipomers’, which are lipid-amines conjugates created by reacting epoxide, acrylate, or methacrylate-terminated lipids with oligoamines^{5,7,18,28,29}. Both lipomers were formulated into 72 LNPs, using 9 different PEGs, and 8 different PEG mole percentages, for a total of 144 LNPs (**Figure 1.3A, Figure 1.4A**). 112 out of 144 formulations formed stable LNPs and were pooled (**Figure 1.3B**). We administered the 112 stable LNPs, as well as a naked DNA barcode - which served as a negative control - to cells at a total DNA dose of 4, 20, and 100 ng / well, in a 24 well plate. Concurrently, we administered the LNPs to mice via a tail vein injection at a total dose of 0.5 mg / kg DNA. We isolated DNA from cells or tissues 72 hours later, a time point we chose to minimize the influence of dynamic endocytic processes^{5,30-33}. The 4 ng total DNA dose equaled an average DNA dose of 0.035 ng / well / LNP, demonstrating the sensitivity of the DNA barcoding system. We administered the LNPs to immortalized mouse aortic endothelial cells (iMAECs), and mouse macrophages (RAWs). We chose iMAECs since they are isolated directly from the murine heart, and have been shown to recapitulate endothelial cell signaling and function³⁴. We chose RAWs since they are a commonly used cell line.

We examined positive and negative controls to evaluate whether this dataset was robust. The naked barcode (negative control) performed poorly compared to LNP-delivered DNA in all 18 samples (**Figure 1.3C, D**). LNP delivery in iMAECs and RAWs treated with 20 ng total DNA predicted LNP delivery in iMAECs and RAWs treated with

4 or 100 ng DNA with high precision ($R^2 > 0.9$) (**Figure 1.3E, Figure 1.4B-D**). Put another way, in this positive control experiment, delivery to iMAECs *in vitro* at 1 dose predicted delivery to iMAECs at 2 other doses.

We then investigated whether *in vitro* LNP delivery predicted *in vivo* LNP delivery (**Figure 1.5A**). We compared normalized delivery in iMAECs and RAWs to endothelial cells and macrophages isolated from mice injected with LNPs. We isolated endothelial cells and macrophages from mice using a fluorescence activated cell sorting (FACS) protocol we previously established^{5,18,22,26} (**Figure 1.6A-C**). *In vitro* iMAEC delivery did not predict *in vivo* delivery to heart, lung, or bone marrow endothelial cells (**Figure 1.6J-L**). Similarly, delivery to RAW cells *in vitro* did not predict delivery to heart, lung, or bone marrow macrophages (**Figure 1.6S-U**). To validate these results, we synthesized two additional LNP libraries (**Figure 1.6D-G**). Library two consisted of 120 LNPs, of which 105 were found to be stable by DLS, and included (**Figure 1.6E**). In this library, we systematically varied the lipid tail and amine reacted to make the lipomer component of each LNP. Library three consisted of 156 LNPs, of which 64 were found to be stable by DLS, and included (**Figure 1.6G**). In this library, we systematically varied the PEG tail length and molecular weight (MW), using three different tail lengths (C14, C16, C18) and 2 different MWs (350, 2000 Da). Results from libraries two and three recapitulated results from library one; *in vitro* delivery to endothelial cells and macrophages did not predict *in vivo* delivery to the same cell types. In total, we performed three experiments, formulating 420 LNPs, of which 281 were stable and included (**Figure 1.6H-I**). Results from each individual experiment are plotted in Supplementary Figure 1.5J-AA. Combined results from all 3 experiments are plotted in **Figure 1.5B-G**.

We considered the possibility that our results were due to a poor choice of cell line or time-point. To exclude this possibility, we investigated to what extent the (i) cell line and (ii) experimental time point altered the predictivity of *in vitro* delivery. We performed these experiments using library two. We administered library two to iMAECs, RAWs, and mice, and measured delivery 4, 48, and 72 hours after LNP administration (**Figure 1.6M-O, V-X, BB-LL**). At all three time points, we also administered LNPs to three primary human endothelial cell lines: human aortic endothelial cells (HAECs), human aortic vein endothelial cells (HAVECs), and human umbilical vein endothelial cells (HUVECs). We observed no strong relationship between *in vitro* and *in vivo* delivery (**Figure 1.6MM-UU**).

We then analyzed our data set, with the goal of quantifying the ‘efficiency’ of traditional *in vitro* screening. Put another way, if a LNP library is screened *in vitro* and a small number of LNPs is selected for *in vivo* analysis, how likely is it that the best *in vivo* candidate is selected? We first calculated the percentage of an *in vitro* library required to select the top 5, 10, 15, or 20% of *in vivo* LNPs. To ensure the top 5% of *in vivo* LNPs were selected, more than 50% of the *in vitro* library would need to be selected (**Figure 1.7A, Figure 1.8A**). We then analyzed how well the best *in vivo* LNPs performed *in vitro*. We ranked LNPs based on their *in vitro* performance. We then colored the LNPs that performed in the top 10% *in vivo* (**Figure 1.8D**). Some LNPs that performed well *in vivo* also performed well *in vitro*. However, in many cases, LNPs that performed well *in vivo* did not rank highly *in vitro*; these LNPs would likely be discarded after an *in vitro* screen. Third, we evaluated how the top *in vitro* LNPs performed *in vivo*. Top ranked *in vitro* LNPs did not consistently perform well *in vivo* (**Figure 1.7B, Figure 1.8B**). Based on this result, we asked a 4th question: if we selected the top 3, 5, or 20 *in vitro* LNPs, how likely were

we to pick the 1st, 1st and 2nd, or 1st, 2nd, and 3rd ranked *in vivo* LNPs? The odds of finding the top LNP *in vivo* were 11%, 22%, and 44% using the top 3, 5, and 20 *in vitro* LNPs, respectively; the odds of finding the top 2, or top 3 *in vivo* LNPs were lower (**Figure 1.7C**, **Figure 1.8C**). Taken together, these data strongly suggest that *in vitro* delivery may not predict systemic *in vivo* delivery. While they do not directly implicate all *in vitro* systems or all cell types, they do strongly suggest each *in vitro* system should be validated using many nanoparticles before being used as the basis for nanoparticle discovery.

The JORDAN system generates large nanoparticle datasets; the size of these datasets enabled us to analyze the relationship between LNP properties and *in vivo* delivery statistically. We plotted DNA barcode delivery as a function of each material property. In total, we analyzed 309 relationships between LNP structure and *in vivo* delivery. We found that the lipomer alkyl tail length, lipomer amine structure, and PEG molecular weight were most likely to influence LNP delivery (**Figure 1.8E**). These results suggest that the structure of the amine-lipid compound, as well as the degree of LNP PEG both strongly influence LNP targeting. These results provide an important insight into LNP library design and substantiate previously reported nanoparticle research³⁵⁻³⁷. One important limitation is that we were not able to identify a mathematical framework with assumptions that allowed us to analyze how multiple LNP chemical variables interacted with one another. This future work is important, given that changing 1 LNP parameter often impacts another (e.g., adding more PEG to the LNP concomitantly reduces cholesterol).

Nanoparticle biodistribution is quantified using *ex vivo* tissue fluorescence; however, it is still unclear how different cell types within a tissue microenvironment are targeted^{5,16}. More specifically, it is unclear which cell types tend to be targeted by similar LNPs. To address this question, we focused on the spleen; LNPs can deliver nucleic acids to³⁸, and be cleared by¹⁶, the spleen. We formulated a 4th LNP library. Library 4 consisted of 144 LNPs, of which 85 were found to be stable by DLS, and included (**Figure 1.9A, B**). We administered library 4 to RAWs and mice, and isolated 8 different cell types using FACS (**Figure 1.10A, Figure 1.9C**). We performed unbiased Euclidean clustering, which is used to compare how many experimental groups relate to one another. Recapitulating our results from libraries 1-3, Euclidean clustering separated clearly separated *in vivo* delivery to all cell types (including macrophages) from *in vitro* delivery to RAWs (**Figure 1.10B, Figure 1.10C, Figure 1.10G**).

More interestingly, the 7 immune cell sub-types clustered into cells derived from (i) myeloid progenitors and (ii) lymphoid progenitors, respectively. Plasmacytoid and conventional dendritic cells were clustered most closely with one another, and also clustered closely with macrophages and neutrophils (**Figure 1.10B, Figure 1.10C**). All 4 cell types derive from a common progenitor. T cells, B cells, and natural killer cells, which derive from a different progenitor, clustered together (**Figure 1.10B, Figure 1.10C**). To quantify this clustering, we measured the correlation between all 8 *in vivo* cell types and RAWs (**Figure 1.10C**). Conventional DCs and plasmacytoid DCs, which clustered together, were highly correlated (R^2 value = 0.90) (**Figure 1.10C, 5D**), as were B cells and T cells (R^2 value = 0.88) (**Figure 1.10C, 5E**). Cells derived from myeloid progenitors (e.g., conventional DCs) and lymphoid progenitors (e.g., T cells) had a much weaker correlation

(R^2 value = 0.2) (**Fig 5F**). These data demonstrate a unique capability for the JORDAN system; directly comparing how dozens of LNPs deliver nucleic to 7 different cell types would be very challenging using traditional one-by-one methods (e.g., fluorescence).

Using delivery data generated from this screen, we identified two LNPs for additional characterization (**Figure 1.11A**). Barcodes delivered by LNP1 were enriched in all 8 splenic cell types, relative to barcodes delivered by LNP2 (**Figure 1.11B, C**). We formulated LNP1 and LNP2 separately, using a Cy5.5-tagged DNA barcode, and injected mice intravenously with 0.75 mg/kg DNA barcode. LNP1-treated mice had 12.1x more splenic Cy5.5 *ex vivo* fluorescence than LNP2-treated mice, recapitulating the barcode readouts (**Figure 1.11D**).

1.3 Discussion

We found that *in vivo* delivery to macrophages and endothelial cells is not predicted *in vitro* using common cell culture conditions. Modeling all the factors (e.g., blood flow, vascular heterogeneity, systemic and local immune cells, unwanted delivery to clearance organs) that influence nanoparticles *in vivo* is challenging. These results have important implications for nanoparticle design, given that nanoparticles are typically selected *in vitro*. We compared delivery to 5 different cell lines, and 6 different *in vivo* cell types; it will be important to determine whether these results extend to other cell types and cell culture conditions. For example, it was previously shown that delivery in primary hepatocytes was more predictive of *in vivo* delivery than a hepatoma cell line³⁹. At first glance, our results may seem to contradict this work. We believe they do not; both studies underscore the importance of characterizing how well a given *in vitro* system predicts a desired *in vivo*

outcome. To this end, we believe JORDAN is well positioned to optimize organ-on-a-chip⁴⁰ and organoids⁴¹ designed to predict *in vivo* behavior by acting as a positive control.

JORDAN is agnostic to cell type and animal model. This allowed us to easily study drug delivery to 8 different splenic cell types in a single experiment. Testing how many LNPs target several cell types may lead to interesting discoveries. For example, our results suggest cells derived from myeloid progenitors tend to be targeted by the similar LNPs. This provides preliminary evidence that gene expression patterns that promote LNP delivery to phagocytic cells may be identified. However, these results need to be validated using other nanoparticles.

We noticed that there were practical advantages to using the JORDAN system. Testing many nanoparticles at once reduces experimental variation that occurs when experiments performed over months are compared to one another. We previously screened LNPs one by one⁵; it was difficult to ensure kits, reagents, and cell passage number were perfectly consistent. By testing many LNPs on the same day, it is easier to reduce unintentional experimental bias. At the same time, the JORDAN system has limitations. JORDAN is unlikely to work with unstable or toxic LNPs; it is critical to characterize particles before pooling them. JORDAN measures biodistribution, which is required, but not sufficient, for intracellular delivery. It will also be important to prevent PCR contamination. Finally, like all high throughput screening systems, lead candidates need to be independently verified. For example, we identified LNP1, which performed well in our barcode screen, and LNP2, which performed poorly in our barcode screen, before confirming their activity one by one. As part of our original barcoding study¹⁸, we performed a similar confirmation experiment using Factor 7 siRNA.

Despite these caveats, we believe our data demonstrate that JORDAN is a powerful new tool to help researchers understand *in vivo* drug delivery. We also believe the differences between *in vitro* and *in vivo* delivery suggest that *in vivo* screening may accelerate the rate at which clinically relevant LNPs can be discovered. To help other labs use the JORDAN system, we have published an open-source, ‘living’ document, which details reagents, protocols and our LNP bioinformatics pipeline on dahlmanlab.org.

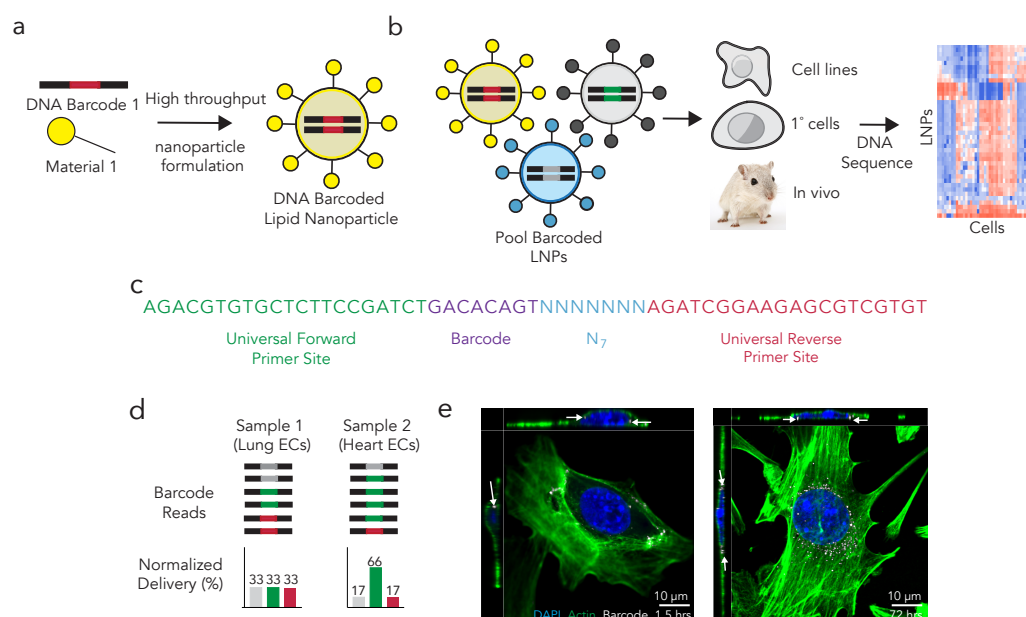


Figure 1.1. JOint Rapid Dna Analysis of Nanoparticles (JORDAN), a system for high throughput *in vivo* nanoparticle analysis. (a) Lipid nanoparticles (LNPs) were formulated to carry DNA barcodes, before (b) stable LNPs were pooled together and administered to cells or mice. Cells were deep sequenced to quantify the relative delivery of all the LNPs simultaneously. (c) The DNA barcode was rationally designed with universal primer sites and a randomized 7 nucleotide region to minimize PCR bias. (d) Normalized delivery for every barcoded LNP was calculated. In this example schematic, all 3 barcodes were equally represented in Sample 1, while in Sample 2, the green barcode was overrepresented. We would hypothesize that the gray LNP delivered DNA more efficiently to Sample 2 than the yellow or blue LNP. The full data analysis to calculate normalized delivery is described in Supplementary Fig. 1C. (e) Alexa-647 fluorescence 1.5 and 72 hours after cells were transfected with 20 ng of Alexa Fluor 647 tagged DNA barcode formulated into the LNP 7C1.

a

Forward Universal Site Barcode 7N Region Reverse Universal Site

A*G*A CGT GTG CTC TTC CGA TCT GAC ACA GTN NNN NNN AGA TCG GAA GAG CGT CGT* G*T

1	GAC ACA GT	43	GCT ACA AC	85	AGT ATG CC	127	CAT CTG CT	169	ACT GCT TG	204	CTT AGG AC
2	GCA TAA CG	44	CCG ATG TA	86	TAC TGC TC	128	CCA ACG AA	170	AGA AGC CT	205	CTT GCT AG
3	ACA GAG GT	45	TAG GAG CT	87	TGC TTG CT	129	CCA GTT GA	171	AGA TCG TC	206	GAA CGG TT
4	CCA CTA AG	46	AAC AAG GC	88	TCC ACG TT	130	CCG GAA TA	172	AGC GTG TA	207	GAA GTG CT
5	TGT TCC GT	47	CTC GGT AA	89	AAC CAG AG	131	CCT ACC TA	173	AGG CAA TG	208	GAC GTC AT
6	GAT ACC TG	48	AGC TTC AG	90	ACG AAC GA	132	CCT ATT GG	174	AGG TTC CT	209	GAG ACC AA
7	AGC CGT AA	49	TCA CCT AG	91	ATA GTC GG	133	CCT TGG AA	175	AGT CGA AG	210	GAG TAG AG
8	CTC CTG AA	50	CAA GTC GT	92	CCA TGA AC	134	CGA ATT GC	176	AGT GGC AA	211	GAT CCA CT
9	ACG AAT CC	51	CTG TAT GC	93	GAG CAA TC	135	CGA GTT AG	177	ATA CTG GC	212	GAT GGA GT
10	AAT GGT CG	52	AGT TCG CA	94	CAA CTT GG	136	CGC TGA TA	178	ATC CTT CC	213	GCA CAC AA
11	CGC TAC AT	53	ATC GGA GA	95	CCA CAA CA	137	CGG CAT TA	179	ATC TCC TG	214	GCA TTG GT
12	CCT AAG TC	54	AAG TCC TC	96	TGG TGA AG	138	CGT CAA GA	180	ATG CGC TT	215	GCC TTC TT
13	TTG CTT GG	55	TGG ATG GT	97	AAC ACG CT	139	CTA AGA CC	181	ATT CCG CT	216	GCT AAG GA
14	CCT GTC AA	56	AGG TGT TG	98	AAC AGG TG	140	CTA GGT TG	182	CAA GCC AA	217	GCT GAA TC
15	AGC CTA TC	57	GAC GAA CT	99	AAC CTA CG	141	CTC ACC AA	183	CAA TGC GA	218	GGA AGA GA
16	TGA TCA CG	58	GTT CTT CG	100	AAG ACA CC	142	CTC GAC TT	184	CAT CAA CC	219	GCA CTA CT
17	CCA CAT TG	59	TTC GCC AT	101	AAG CGA CT	143	CTC TCA GA	178	ATC CTT CC	220	GGA TGT AG
18	TCG AGA GT	60	CAA CTC CA	102	AAT CGC TG	144	CTG ATG AG	179	ATC TCC TG	221	GGA TTC AC
19	GGT CGT AT	61	AAC CGT GT	103	AAT TCC GG	145	TAC CTG CA	180	ATG CGC TT	222	GGT ATA GG
20	ACA GGC AT	62	CGG TTG TT	104	ACA CCT CA	146	CTT ACA GC	181	ATT CCG CT	223	GGT TAG CT
21	GTG ATC CA	63	CTA GCA GT	105	ACA GTT CG	147	CTT CGG TT	182	CAA GCC AA	224	GTA AGC AC
22	TTC GTA CG	64	ACC TCT TC	106	ACC ATG TC	148	GAA CGA AG	183	CAA TGC GA	225	GTA CGA TC
23	ATG ACA GG	65	TAC TAG CG	107	ACC GGT TA	149	GAA GAT CC	184	CAT CAA CC	226	GTC AAC AG
24	CGA CCT AA	66	ACA ACA GC	108	ACG AGA AC	150	GAC CGA TA	185	CAT GAG CA	227	GTC CTT GA
25	TAT GGC AC	67	CGC AAT GT	109	ACG CTT CT	151	GAG AAG GT	186	CCA ACT TC	228	GTC TGA GT
26	ATA ACG CC	68	CAG TGC TT	110	ACT CCT AC	152	GAG GCA TT	187	CCG AAG AT	229	GTG TGT TC
27	GTA GTA CC	69	TCT AGG AG	111	ACT GCG AA	153	GAT CAG AC	188	CCG TAA CT	230	GTT CCA TG
28	CGC GTA TT	70	GAT TGT CC	112	AGA ACC AG	154	GAT GCT AC	189	CCT AGA GA	231	TAA GCG CA
29	ATC CAC GA	71	GGT ACG AA	113	AGA TAC GG	155	AAC AAC CG	190	CCT CAT CT	232	TAC AGA GC
30	TAA CGT CG	72	CTT CAC TG	114	AGC GAG AT	156	AAC AGT CC	191	CGA ACA AC	233	TAG CAG GA
31	CCT TCC AT	73	ATA GGT CC	115	AGG AGG TT	157	AAC GCA CA	192	CGA CAC TT	234	TAG CTT CC
32	GAT CAA GG	74	ACC GAC AA	116	AGG TAG GA	158	AAG ACC GT	193	CGA TCG AT	235	TAG TGC CA
33	AAG CAT CG	75	AAC ACT GG	117	AGT CAG GT	159	AAG CGT TC	194	CGG AGT AT	236	TAT GAC CG
34	AGG ATA GC	76	ACC ATA GG	118	AGT GCA TC	160	AAT GAC GC	195	CGG TAA TC	237	TCA CTC GA
35	GGC TCA AT	77	TCG ATG AC	119	ATA CGC AG	161	ACA AGA CG	196	CGT CCA TT	238	TCA GTA GG
36	TTC ACG GA	78	GAC TTG TG	120	ATC CGT TG	162	ACA CGA GA	197	CTA CAA GG	239	TCC GAT CA
37	GGC GAA TA	79	CCG TTA TG	121	ATC GTG GT	163	ACA GCA AG	198	CTA TCC AC	240	TCG AAC CT
38	AAG TGC AG	80	CAA CGA GT	122	ATG CCT AG	164	ACC GAA TG	199	CTC AGA AG		
39	GCA ATT CC	81	TTA CCG AC	123	ATT AGC CG	165	ACC TAG AC	200	CTC GTT CT		
40	CTT CGC AA	82	GAG AGT AC	124	CAA GAA GC	166	ACG ATC AG	201	CTC TGG AT		
41	CAT TGA CG	83	CTG TAC CA	125	CAA TCA GG	167	ACG GAC TT	202	CTG CCA TA		
42	TCT GGA CA	84	TGA GCT GT	126	CAT ACT CG	168	ACT CGA TC	203	CTG AAC GT		

b

Index Name	Index Sequence	Index Name	Index Sequence
------------	----------------	------------	----------------

N701	TAAGGCCA	S502	ATAGAGAG
N702	CGTACTAG	S503	AGAGGATA
N703	AGGCAGAA	S505	CTCCTTAC
N704	TCCTGAGC	S506	TATGCAGT
N705	GGACTCCT	S507	TACTCCTT
N706	TAGGCATG	S508	AGGCTTAG
N707	CTCTCTAC	S510	ATTAGACG
N710	CGAGGCTG	S511	CGGAGAGA
N711	AAGAGGCA	S513	CTAGTCGA
N712	GTAGAGGA	S515	AGCTAGAA
N714	GCTCATGA	S516	ACTCTAGG
N715	ATCTCAGG	S517	TCTTACGC
N716	ACTCGCTA	S518	CTTAATAG
N718	GGAGCTAC	S520	ATAGCCTT
N719	GCGTAGTA	S521	TAAGGCTC
N720	CGGAGCCT	S522	TCGCATAA
N721	TACGCTGC		
N722	ATGCGCAG		
N723	TAGCGCTC		
N724	ACTGAGCG		
N726	CCTAAGAC		
N727	CGATCAGT		
N728	TGCAGCTA		
N729	TCGACGTC		

Binds to Forward Universal Site

Binds to Reverse Universal Site

Illumina Index

Universal Reverse Primer (N7XX)	AATGATACGGCGACCCGAGATCTACATTAAGGCCAACACTCTTTCCCTACAGCAGCCTCTCCGATCT
Base Forward Primer	TGACTGGAGTTCAGACGTGTGCTCTCCGATCT
Universal Forward Primer (S5XX)	CAAGCAGAAGACGGCATACGAGATATAGACAGTGAAGTTCAAGCGTGTG

C

Step 1) Raw Counts

LNP #	Barcode	Sample Name								
		Heart 1	Heart 2	Heart 3	Lung 1	Lung 2	Lung 3	INPUT 1	INPUT 2	INPUT 3
1	GACACAGT	100	250	200	200	150	100	100	110	150
2	GCATAACG	120	300	150	75	100	120	110	100	190
3	ACAGAGGT	150	260	75	125	90	150	130	150	130
4	CCACTAAG	160	350	100	150	150	175	140	180	150
5	TGTTCCGT	200	100	75	90	200	100	150	190	140
6	GATACCTG	130	150	140	50	55	60	180	200	170
7	AGCCGTAA	300	350	400	100	125	130	120	135	150
8	CTCCTGAA	200	300	250	50	60	55	120	130	135
9	ACGAATCC	100	50	100	300	350	250	115	110	125
10	AATGGTCG	300	350	300	50	60	50	135	130	150

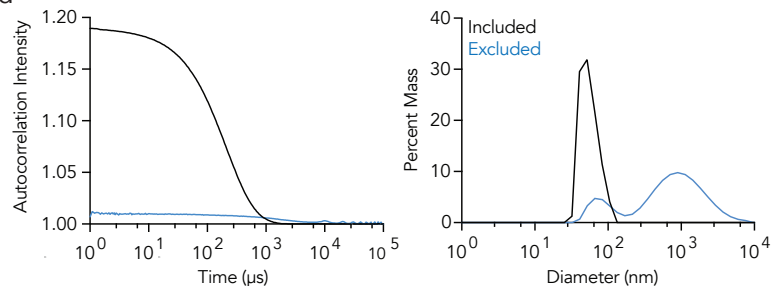
Step 2) Counts Relative to Input Row Mean

LNP #	Barcode	Sample Name						
		Heart 1	Heart 2	Heart 3	Lung 1	Lung 2	Lung 3	INPUT MEAN
1	GACACAGT	0.83	2.08	1.67	1.67	1.25	0.83	120.00
2	GCATAACG	0.90	2.25	1.13	0.56	0.75	0.90	133.33
3	ACAGAGGT	1.10	1.90	0.55	0.91	0.66	1.10	136.67
4	CCACTAAG	1.02	2.23	0.64	0.96	0.96	1.12	156.67
5	TGTTCCGT	1.25	0.63	0.47	0.56	1.25	0.63	160.00
6	GATACCTG	0.71	0.82	0.76	0.27	0.30	0.33	183.33
7	AGCCGTAA	2.22	2.59	2.96	0.74	0.93	0.96	135.00
8	CTCCTGAA	1.56	2.34	1.95	0.39	0.47	0.43	128.33
9	ACGAATCC	0.86	0.43	0.86	2.57	3.00	2.14	116.67
10	AATGGTCG	2.17	2.53	2.17	0.36	0.43	0.36	138.33

Step 3) Counts Normalized to Column Sum + Bioreplicate Mean

LNP #	Barcode	Sample Name							
		Heart Mean	Heart 1	Heart 2	Heart 3	Lung Mean	Lung 1	Lung 2	Lung 3
1	GACACAGT	10.33	6.60	11.70	12.68	13.50	18.52	12.51	9.47
2	GCATAACG	9.44	7.13	12.64	8.56	8.00	6.25	7.51	10.23
3	ACAGAGGT	7.85	8.70	10.69	4.17	9.74	10.16	6.59	12.48
4	CCACTAAG	8.50	8.09	12.55	4.85	10.97	10.64	9.58	12.70
5	TGTTCCGT	5.66	9.91	3.51	3.57	8.62	6.25	12.51	7.11
6	GATACCTG	5.34	5.62	4.60	5.81	3.25	3.03	3.00	3.72
7	AGCCGTAA	18.24	17.61	14.56	22.54	9.48	8.23	9.27	10.95
8	CTCCTGAA	13.43	12.35	13.13	14.82	4.63	4.33	4.68	4.87
9	ACGAATCC	5.24	6.79	2.41	6.52	27.65	28.57	30.02	24.36
10	AATGGTCG	15.96	17.19	14.21	16.49	4.16	4.02	4.34	4.11

d



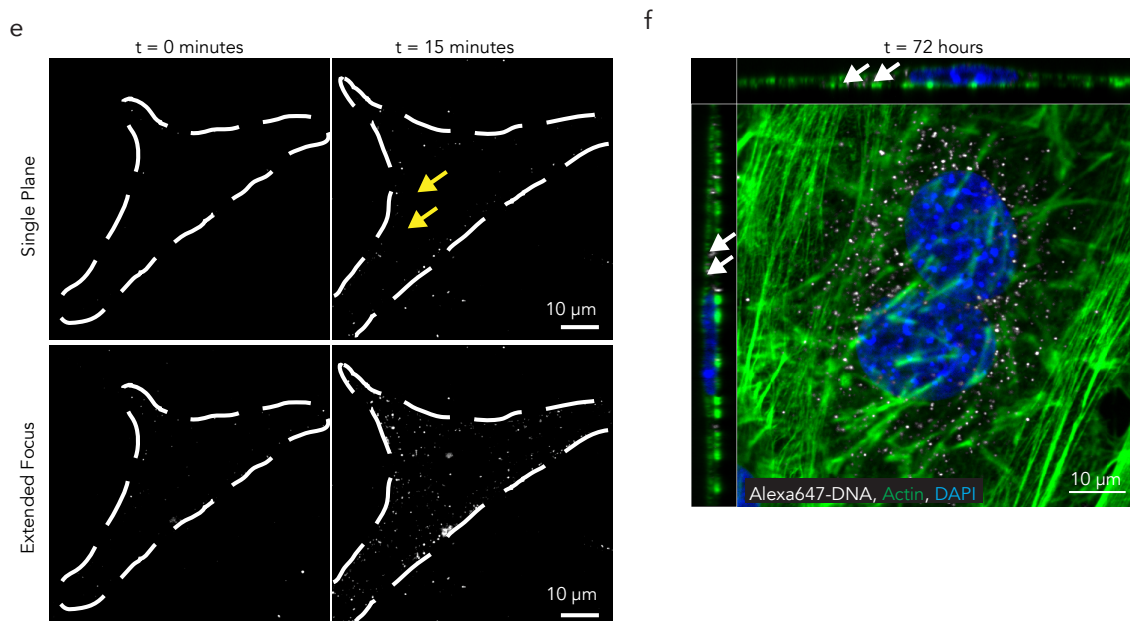


Figure 1.2. JORDAN is a rationally designed system for high throughput *in vivo* LNP analysis. (a) 240 barcode sequences were chosen to comply with the Illumina MiniSeq machine. (b) Primers used to amplify barcodes from *in vitro* and *in vivo* samples. (c) Data from all experiments was normalized using the procedure shown. (d) Pooled LNPs were stable, had good autocorrelation curves, and single-peak diameter distributions between 20 and 300 nm. All other LNPs were discarded. (e) Alexa Fluor 647 tagged DNA barcode localizes to cell surface after 15 minutes and (f) can be seen in the cell cytoplasm after 72 hours.

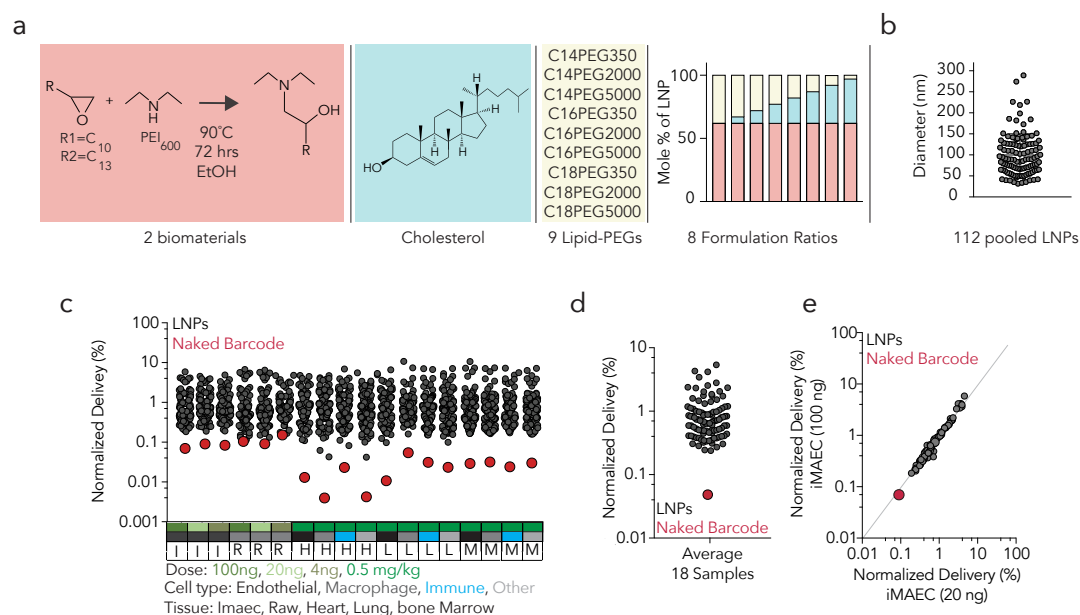
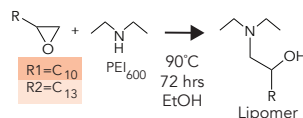


Figure 1.3. To analyze the robustness of our system (a) We formulated 144 chemically distinct LNPs, (b) pooled stable LNPs and administered them to two cell lines (RAWs, iMAECs) and mice. (c) Normalized delivery for all LNPs and naked barcode in 18 cell and tissue types. (d) Average normalized delivery for all 18 samples. The naked barcode delivered DNA less efficiently than all LNPs. (e) Normalized delivery in iMAECs 72 hours after 20 ng or 100 ng total DNA was administered. *In vitro* delivery to iMAECs at 20 ng / well predicted *in vitro* delivery to iMAECs at 100 ng / well.

a

UNP #	Lipomer	Amine	Lipid	Mass Ratio	PEG Chain	PEG MW	Lipomer Mole %	Cholesterol Mole %	PEG Mole %
1	7C1	PEI-600	C15 Epaloy	10	C14	350	62	0	38
2	7C1	PEI-600	C15 Epaloy	10	C14	350	62	5	33
3	7C1	PEI-600	C15 Epaloy	10	C14	350	62	10	28
4	7C1	PEI-600	C15 Epaloy	10	C14	350	62	15	23
5	7C1	PEI-600	C15 Epaloy	10	C14	350	62	20	18
6	7C1	PEI-600	C15 Epaloy	10	C14	350	62	25	13
7	7C1	PEI-600	C15 Epaloy	10	C14	350	62	30	8
8	7C1	PEI-600	C15 Epaloy	10	C14	350	62	35	3
9	104	PEI-600	C12 Epaloy	10	C14	350	62	0	38
10	104	PEI-600	C12 Epaloy	10	C14	350	62	5	33
11	104	PEI-600	C12 Epaloy	10	C14	350	62	10	28
12	104	PEI-600	C12 Epaloy	10	C14	350	62	15	23
13	104	PEI-600	C12 Epaloy	10	C14	350	62	20	18
14	104	PEI-600	C12 Epaloy	10	C14	350	62	25	13
15	104	PEI-600	C12 Epaloy	10	C14	350	62	30	8
16	104	PEI-600	C12 Epaloy	10	C14	350	62	35	3
17	7C1	PEI-600	C15 Epaloy	10	C16	350	62	0	38
18	7C1	PEI-600	C15 Epaloy	10	C16	350	62	5	33
19	7C1	PEI-600	C15 Epaloy	10	C16	350	62	10	28
20	7C1	PEI-600	C15 Epaloy	10	C16	350	62	15	23
21	7C1	PEI-600	C15 Epaloy	10	C16	350	62	20	18
22	7C1	PEI-600	C15 Epaloy	10	C16	350	62	25	13
23	7C1	PEI-600	C15 Epaloy	10	C16	350	62	30	8
24	7C1	PEI-600	C15 Epaloy	10	C16	350	62	35	3
25	104	PEI-600	C12 Epaloy	10	C16	350	62	0	38
26	104	PEI-600	C12 Epaloy	10	C16	350	62	5	33
27	104	PEI-600	C12 Epaloy	10	C16	350	62	10	28
28	104	PEI-600	C12 Epaloy	10	C16	350	62	15	23
29	104	PEI-600	C12 Epaloy	10	C16	350	62	20	18
30	104	PEI-600	C12 Epaloy	10	C16	350	62	25	13
31	104	PEI-600	C12 Epaloy	10	C16	350	62	30	8
32	104	PEI-600	C12 Epaloy	10	C16	350	62	35	3
33	7C1	PEI-600	C15 Epaloy	10	C18	350	62	0	38
34	7C1	PEI-600	C15 Epaloy	10	C18	350	62	5	33
35	7C1	PEI-600	C15 Epaloy	10	C18	350	62	10	28
36	7C1	PEI-600	C15 Epaloy	10	C18	350	62	15	23
37	7C1	PEI-600	C15 Epaloy	10	C18	350	62	20	18
38	7C1	PEI-600	C15 Epaloy	10	C18	350	62	25	13
39	7C1	PEI-600	C15 Epaloy	10	C18	350	62	30	8
40	7C1	PEI-600	C15 Epaloy	10	C18	350	62	35	3
41	104	PEI-600	C12 Epaloy	10	C18	350	62	0	38
42	104	PEI-600	C12 Epaloy	10	C18	350	62	5	33
43	104	PEI-600	C12 Epaloy	10	C18	350	62	10	28
44	104	PEI-600	C12 Epaloy	10	C18	350	62	15	23
45	104	PEI-600	C12 Epaloy	10	C18	350	62	20	18
46	104	PEI-600	C12 Epaloy	10	C18	350	62	25	13
47	104	PEI-600	C12 Epaloy	10	C18	350	62	30	8
48	104	PEI-600	C12 Epaloy	10	C18	350	62	35	3
49	7C1	PEI-600	C15 Epaloy	10	C14	2000	62	0	38
50	7C1	PEI-600	C15 Epaloy	10	C14	2000	62	5	33
51	7C1	PEI-600	C15 Epaloy	10	C14	2000	62	10	28
52	7C1	PEI-600	C15 Epaloy	10	C14	2000	62	15	23
53	7C1	PEI-600	C15 Epaloy	10	C14	2000	62	20	18
54	7C1	PEI-600	C15 Epaloy	10	C14	2000	62	25	13
55	7C1	PEI-600	C15 Epaloy	10	C14	2000	62	30	8
56	7C1	PEI-600	C15 Epaloy	10	C14	2000	62	35	3
57	104	PEI-600	C12 Epaloy	10	C14	2000	62	0	38
58	104	PEI-600	C12 Epaloy	10	C14	2000	62	5	33
59	104	PEI-600	C12 Epaloy	10	C14	2000	62	10	28
60	104	PEI-600	C12 Epaloy	10	C14	2000	62	15	23
61	104	PEI-600	C12 Epaloy	10	C14	2000	62	20	18
62	104	PEI-600	C12 Epaloy	10	C14	2000	62	25	13
63	104	PEI-600	C12 Epaloy	10	C14	2000	62	30	8
64	104	PEI-600	C12 Epaloy	10	C14	2000	62	35	3
65	7C1	PEI-600	C15 Epaloy	10	C16	2000	62	0	38
66	7C1	PEI-600	C15 Epaloy	10	C16	2000	62	5	33
67	7C1	PEI-600	C15 Epaloy	10	C16	2000	62	10	28
68	7C1	PEI-600	C15 Epaloy	10	C16	2000	62	15	23
69	7C1	PEI-600	C15 Epaloy	10	C16	2000	62	20	18
70	7C1	PEI-600	C15 Epaloy	10	C16	2000	62	25	13
71	7C1	PEI-600	C15 Epaloy	10	C16	2000	62	30	8
72	7C1	PEI-600	C15 Epaloy	10	C16	2000	62	35	3
73	104	PEI-600	C12 Epaloy	10	C16	2000	62	0	38
74	104	PEI-600	C12 Epaloy	10	C16	2000	62	5	33
75	104	PEI-600	C12 Epaloy	10	C16	2000	62	10	28
76	104	PEI-600	C12 Epaloy	10	C16	2000	62	15	23
77	104	PEI-600	C12 Epaloy	10	C16	2000	62	20	18
78	104	PEI-600	C12 Epaloy	10	C16	2000	62	25	13
79	104	PEI-600	C12 Epaloy	10	C16	2000	62	30	8
80	104	PEI-600	C12 Epaloy	10	C16	2000	62	35	3
81	7C1	PEI-600	C15 Epaloy	10	C18	2000	62	0	38
82	7C1	PEI-600	C15 Epaloy	10	C18	2000	62	5	33
83	7C1	PEI-600	C15 Epaloy	10	C18	2000	62	10	28
84	7C1	PEI-600	C15 Epaloy	10	C18	2000	62	15	23
85	7C1	PEI-600	C15 Epaloy	10	C18	2000	62	20	18
86	7C1	PEI-600	C15 Epaloy	10	C18	2000	62	25	13
87	7C1	PEI-600	C15 Epaloy	10	C18	2000	62	30	8
88	7C1	PEI-600	C15 Epaloy	10	C18	2000	62	35	3
89	104	PEI-600	C12 Epaloy	10	C18	2000	62	0	38
90	104	PEI-600	C12 Epaloy	10	C18	2000	62	5	33
91	104	PEI-600	C12 Epaloy	10	C18	2000	62	10	28
92	104	PEI-600	C12 Epaloy	10	C18	2000	62	15	23
93	104	PEI-600	C12 Epaloy	10	C18	2000	62	20	18
94	104	PEI-600	C12 Epaloy	10	C18	2000	62	25	13
95	104	PEI-600	C12 Epaloy	10	C18	2000	62	30	8
96	104	PEI-600	C12 Epaloy	10	C18	2000	62	35	3
97	7C1	PEI-600	C15 Epaloy	10	C14	5000	62	0	38
98	7C1	PEI-600	C15 Epaloy	10	C14	5000	62	5	33
99	7C1	PEI-600	C15 Epaloy	10	C14	5000	62	10	28
100	7C1	PEI-600	C15 Epaloy	10	C14	5000	62	15	23
101	7C1	PEI-600	C15 Epaloy	10	C14	5000	62	20	18
102	7C1	PEI-600	C15 Epaloy	10	C14	5000	62	25	13
103	7C1	PEI-600	C15 Epaloy	10	C14	5000	62	30	8
104	7C1	PEI-600	C15 Epaloy	10	C14	5000	62	35	3
105	104	PEI-600	C12 Epaloy	10	C14	5000	62	0	38
106	104	PEI-600	C12 Epaloy	10	C14	5000	62	5	33
107	104	PEI-600	C12 Epaloy	10	C14	5000	62	10	28
108	104	PEI-600	C12 Epaloy	10	C14	5000	62	15	23
109	104	PEI-600	C12 Epaloy	10	C14	5000	62	20	18
110	104	PEI-600	C12 Epaloy	10	C14	5000	62	25	13
111	104	PEI-600	C12 Epaloy	10	C14	5000	62	30	8
112	104	PEI-600	C12 Epaloy	10	C14	5000	62	35	3
113	7C1	PEI-600	C15 Epaloy	10	C16	5000	62	0	38
114	7C1	PEI-600	C15 Epaloy	10	C16	5000	62	5	33
115	7C1	PEI-600	C15 Epaloy	10	C16	5000	62	10	28
116	7C1	PEI-600	C15 Epaloy	10	C16	5000	62	15	23
117	7C1	PEI-600	C15 Epaloy	10	C16	5000	62	20	18
118	7C1	PEI-600	C15 Epaloy	10	C16	5000	62	25	13
119	7C1	PEI-600	C15 Epaloy	10	C16	5000	62	30	8
120	7C1	PEI-600	C15 Epaloy	10	C16	5000	62	35	3
121	104	PEI-600	C12 Epaloy	10	C16	5000	62	0	38
122	104	PEI-600	C12 Epaloy	10	C16	5000	62	5	33
123	104	PEI-600	C12 Epaloy	10	C16	5000	62	10	28
124	104	PEI-600	C12 Epaloy	10	C16	5000	62	15	23
125	104	PEI-600	C12 Epaloy	10	C16	5000	62	20	18
126	104	PEI-600	C12 Epaloy	10	C16	5000	62	25	13
127	104	PEI-600	C12 Epaloy	10	C16	5000	62	30	8
128	104	PEI-600	C12 Epaloy	10	C16	5000	62	35	3
129	7C1	PEI-600	C15 Epaloy	10	C18	5000	62	0	38
130	7C1	PEI-600	C15 Epaloy	10	C18	5000	62	5	33
131	7C1	PEI-600	C15 Epaloy	10	C18	5000	62	10	28
132	7C1	PEI-600	C15 Epaloy	10	C18	5000	62	15	23
133	7C1	PEI-600	C15 Epaloy	10	C18	5000	62	20	18
134	7C1	PEI-600	C15 Epaloy	10	C18	5000	62	25	13
135	7C1	PEI-600	C15 Epaloy	10	C18	5000	62	30	8
136	7C1	PEI-600	C15 Epaloy	10	C18	5000	62	35	3
137	104	PEI-600	C12 Epaloy	10	C18	5000	62	0	38
138	104	PEI-600	C12 Epaloy	10	C18	5000	62	5	33
139	104	PEI-600	C12 Epaloy	10	C18	5000	62	10	28
140	104	PEI-600	C12 Epaloy	10	C18	5000	62	15	23
141	104	PEI-600	C12 Epaloy	10	C18	5000	62	20	18
142	104	PEI-600	C12 Epaloy	10	C18	5000	62	25	13
143	104	PEI-600	C12 Epaloy	10	C18	5000	62	30	8
144	104	PEI-600	C12 Epaloy	10	C18	5000	62	35	3



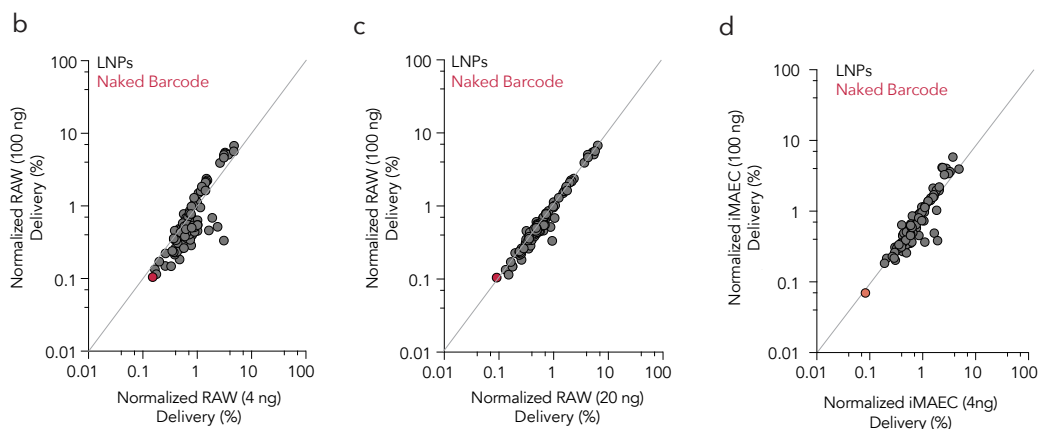


Figure 1.4. The data generated by JORDAN are robust. (a) Library 1 was designed to vary PEG-chain length (C14, C16, C18) and PEG molecular weight (350, 2000, 5000), using two different lipomers. Chemical formulas for lipomers as well as all other LNP components are shown. (b,c) Normalized delivery in RAWs 72 hours after 4 ng, 20 ng, or 100 ng total DNA was administered. (d) Normalized delivery in iMAECs 72 hours after 4 ng or 100 ng total DNA was administered.

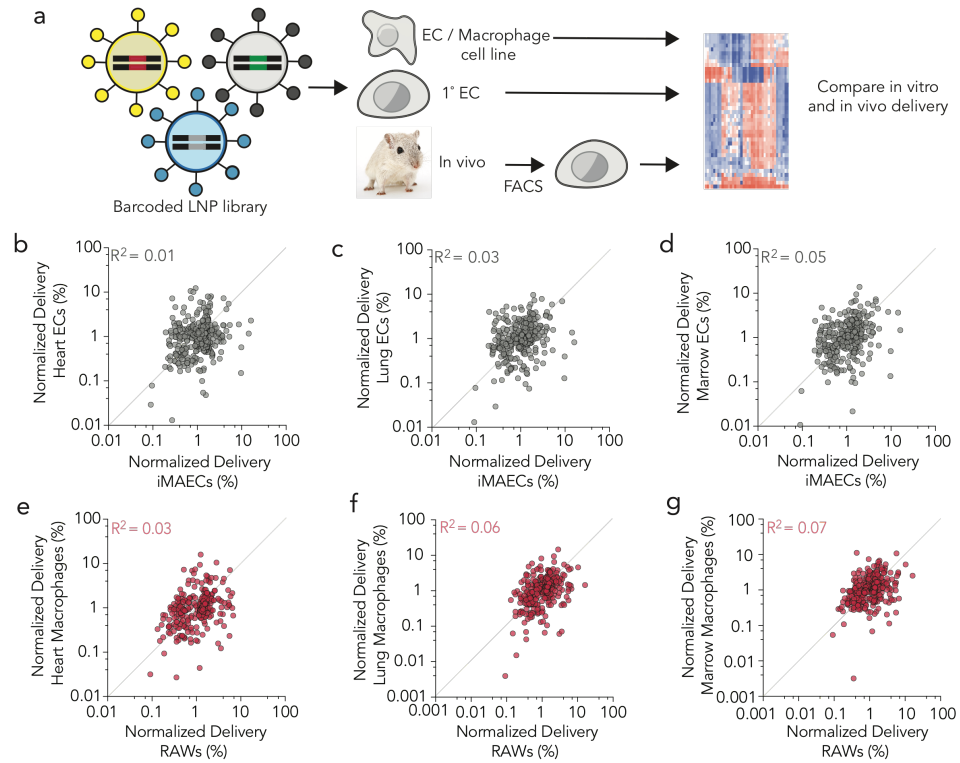
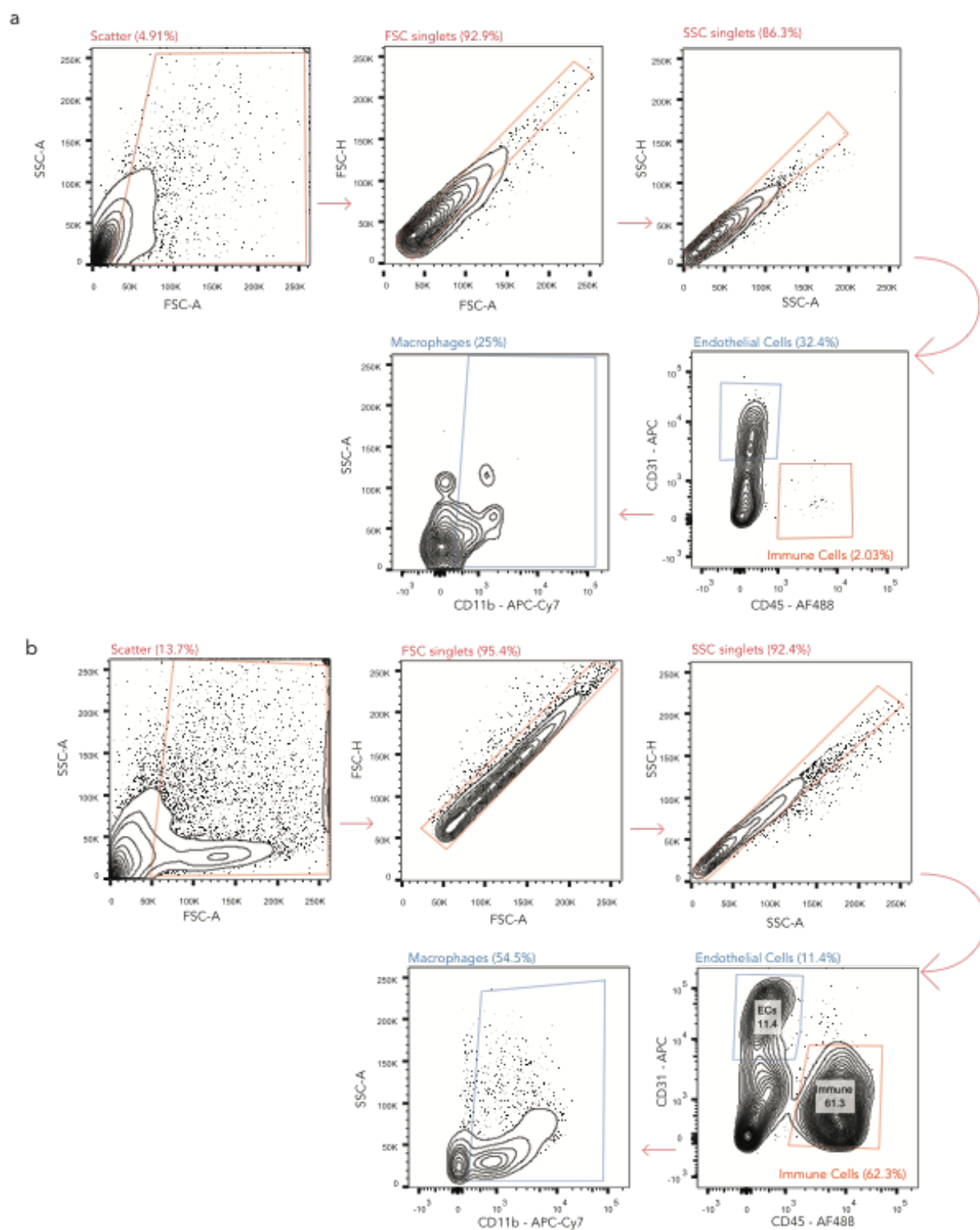
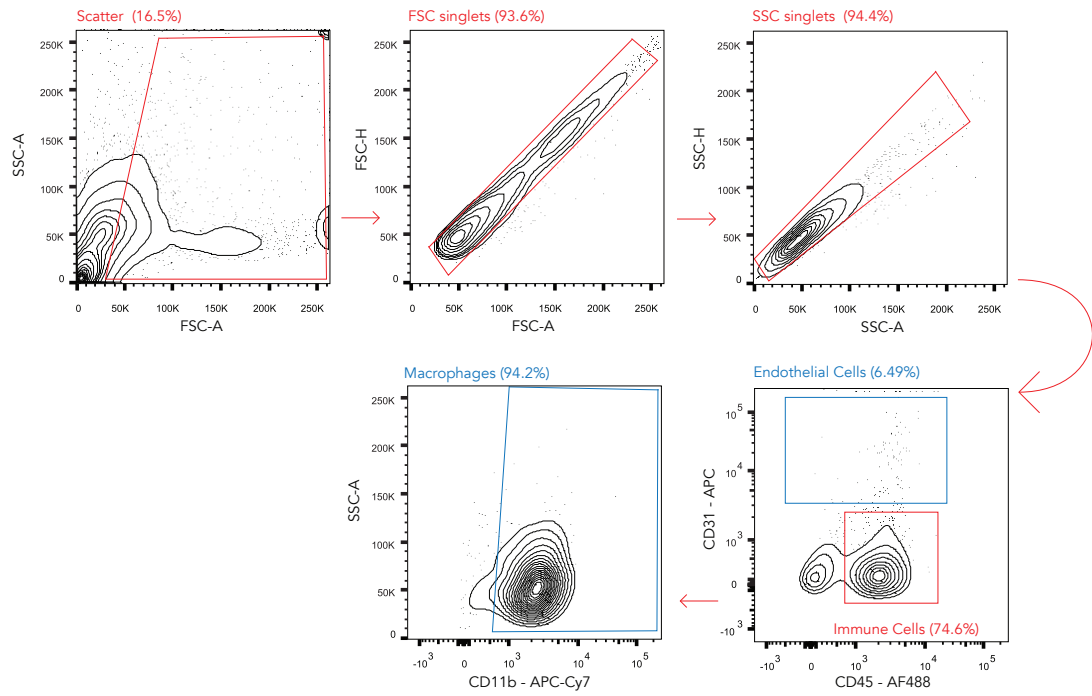


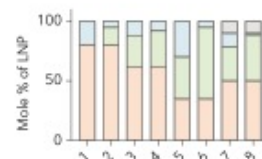
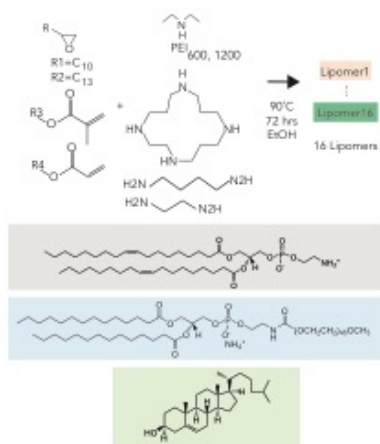
Figure 1.5. A direct comparison between in vitro and in vivo nanoparticle delivery. (a) 420 LNPs were formulated and delivery was compared between in vivo FACS sorted cells, primary cells, and cell lines. (b-d) Normalized delivery of LNPs in iMAECs and heart, lung, and bone marrow endothelial cells. (e-g) Normalized delivery of LNPs in RAWs and heart, lung, and bone marrow macrophages. In both cases, in vitro LNP delivery does not predict in vivo delivery.

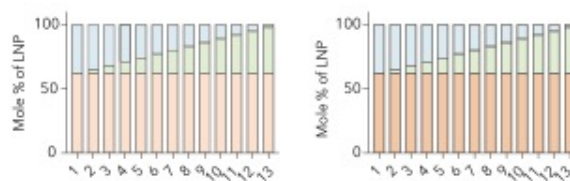
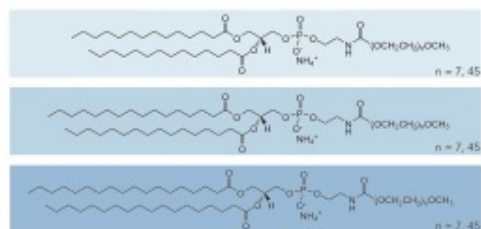
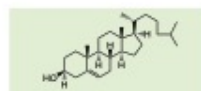


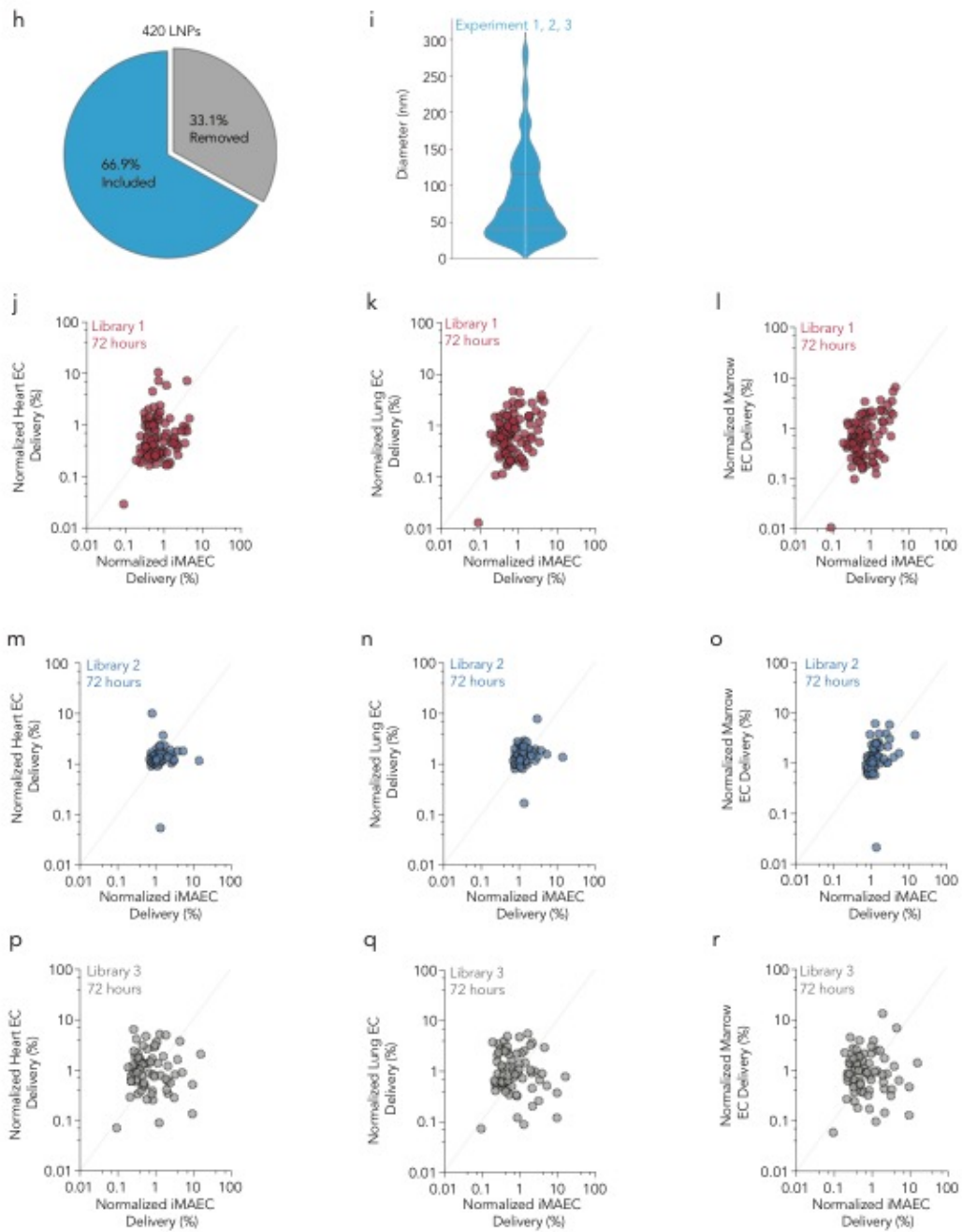
C

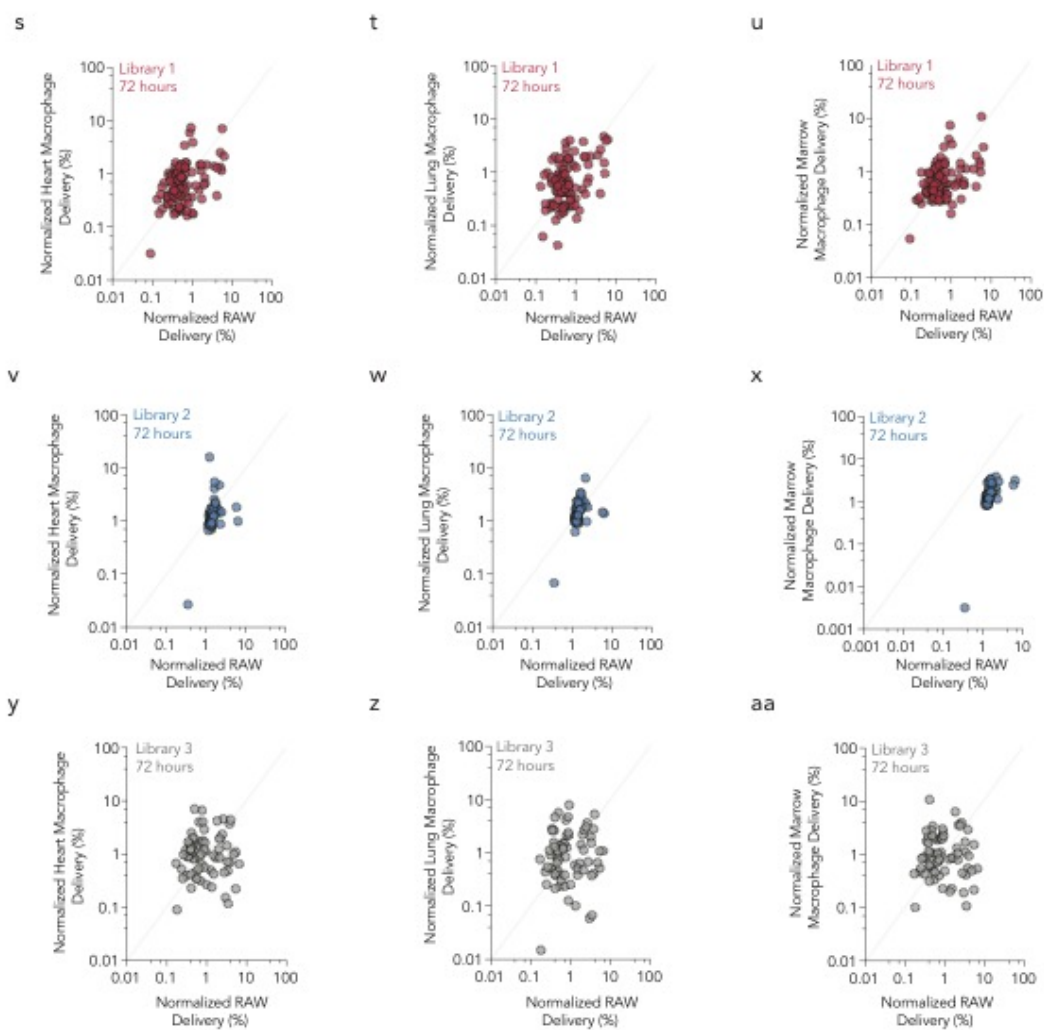


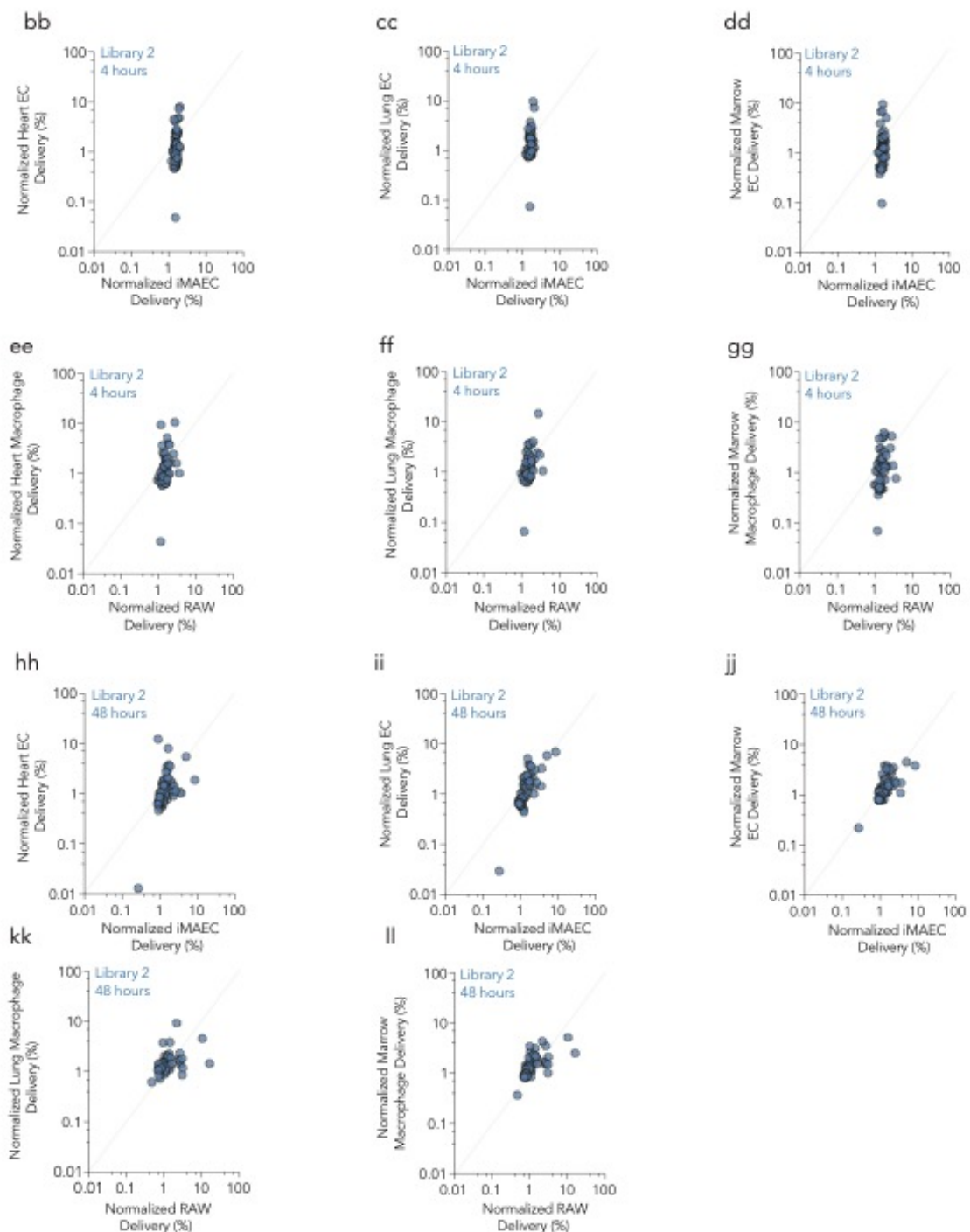
#	PROJ	PROJ NAME	PROJ TYPE	PROJ STATUS	PROJ START	PROJ END	PROJ DURATION	PROJ COST	PROJ REVENUE	PROJ PROFIT	PROJ RISK
1	PROJ1	PROJ1 NAME	PROJ1 TYPE	PROJ1 STATUS	PROJ1 START	PROJ1 END	PROJ1 DURATION	PROJ1 COST	PROJ1 REVENUE	PROJ1 PROFIT	PROJ1 RISK
2	PROJ2	PROJ2 NAME	PROJ2 TYPE	PROJ2 STATUS	PROJ2 START	PROJ2 END	PROJ2 DURATION	PROJ2 COST	PROJ2 REVENUE	PROJ2 PROFIT	PROJ2 RISK
3	PROJ3	PROJ3 NAME	PROJ3 TYPE	PROJ3 STATUS	PROJ3 START	PROJ3 END	PROJ3 DURATION	PROJ3 COST	PROJ3 REVENUE	PROJ3 PROFIT	PROJ3 RISK
4	PROJ4	PROJ4 NAME	PROJ4 TYPE	PROJ4 STATUS	PROJ4 START	PROJ4 END	PROJ4 DURATION	PROJ4 COST	PROJ4 REVENUE	PROJ4 PROFIT	PROJ4 RISK
5	PROJ5	PROJ5 NAME	PROJ5 TYPE	PROJ5 STATUS	PROJ5 START	PROJ5 END	PROJ5 DURATION	PROJ5 COST	PROJ5 REVENUE	PROJ5 PROFIT	PROJ5 RISK
6	PROJ6	PROJ6 NAME	PROJ6 TYPE	PROJ6 STATUS	PROJ6 START	PROJ6 END	PROJ6 DURATION	PROJ6 COST	PROJ6 REVENUE	PROJ6 PROFIT	PROJ6 RISK
7	PROJ7	PROJ7 NAME	PROJ7 TYPE	PROJ7 STATUS	PROJ7 START	PROJ7 END	PROJ7 DURATION	PROJ7 COST	PROJ7 REVENUE	PROJ7 PROFIT	PROJ7 RISK
8	PROJ8	PROJ8 NAME	PROJ8 TYPE	PROJ8 STATUS	PROJ8 START	PROJ8 END	PROJ8 DURATION	PROJ8 COST	PROJ8 REVENUE	PROJ8 PROFIT	PROJ8 RISK
9	PROJ9	PROJ9 NAME	PROJ9 TYPE	PROJ9 STATUS	PROJ9 START	PROJ9 END	PROJ9 DURATION	PROJ9 COST	PROJ9 REVENUE	PROJ9 PROFIT	PROJ9 RISK
10	PROJ10	PROJ10 NAME	PROJ10 TYPE	PROJ10 STATUS	PROJ10 START	PROJ10 END	PROJ10 DURATION	PROJ10 COST	PROJ10 REVENUE	PROJ10 PROFIT	PROJ10 RISK
11	PROJ11	PROJ11 NAME	PROJ11 TYPE	PROJ11 STATUS	PROJ11 START	PROJ11 END	PROJ11 DURATION	PROJ11 COST	PROJ11 REVENUE	PROJ11 PROFIT	PROJ11 RISK
12	PROJ12	PROJ12 NAME	PROJ12 TYPE	PROJ12 STATUS	PROJ12 START	PROJ12 END	PROJ12 DURATION	PROJ12 COST	PROJ12 REVENUE	PROJ12 PROFIT	PROJ12 RISK
13	PROJ13	PROJ13 NAME	PROJ13 TYPE	PROJ13 STATUS	PROJ13 START	PROJ13 END	PROJ13 DURATION	PROJ13 COST	PROJ13 REVENUE	PROJ13 PROFIT	PROJ13 RISK
14	PROJ14	PROJ14 NAME	PROJ14 TYPE	PROJ14 STATUS	PROJ14 START	PROJ14 END	PROJ14 DURATION	PROJ14 COST	PROJ14 REVENUE	PROJ14 PROFIT	PROJ14 RISK
15	PROJ15	PROJ15 NAME	PROJ15 TYPE	PROJ15 STATUS	PROJ15 START	PROJ15 END	PROJ15 DURATION	PROJ15 COST	PROJ15 REVENUE	PROJ15 PROFIT	PROJ15 RISK
16	PROJ16	PROJ16 NAME	PROJ16 TYPE	PROJ16 STATUS	PROJ16 START	PROJ16 END	PROJ16 DURATION	PROJ16 COST	PROJ16 REVENUE	PROJ16 PROFIT	PROJ16 RISK
17	PROJ17	PROJ17 NAME	PROJ17 TYPE	PROJ17 STATUS	PROJ17 START	PROJ17 END	PROJ17 DURATION	PROJ17 COST	PROJ17 REVENUE	PROJ17 PROFIT	PROJ17 RISK
18	PROJ18	PROJ18 NAME	PROJ18 TYPE	PROJ18 STATUS	PROJ18 START	PROJ18 END	PROJ18 DURATION	PROJ18 COST	PROJ18 REVENUE	PROJ18 PROFIT	PROJ18 RISK
19	PROJ19	PROJ19 NAME	PROJ19 TYPE	PROJ19 STATUS	PROJ19 START	PROJ19 END	PROJ19 DURATION	PROJ19 COST	PROJ19 REVENUE	PROJ19 PROFIT	PROJ19 RISK
20	PROJ20	PROJ20 NAME	PROJ20 TYPE	PROJ20 STATUS	PROJ20 START	PROJ20 END	PROJ20 DURATION	PROJ20 COST	PROJ20 REVENUE	PROJ20 PROFIT	PROJ20 RISK
21	PROJ21	PROJ21 NAME	PROJ21 TYPE	PROJ21 STATUS	PROJ21 START	PROJ21 END	PROJ21 DURATION	PROJ21 COST	PROJ21 REVENUE	PROJ21 PROFIT	PROJ21 RISK
22	PROJ22	PROJ22 NAME	PROJ22 TYPE	PROJ22 STATUS	PROJ22 START	PROJ22 END	PROJ22 DURATION	PROJ22 COST	PROJ22 REVENUE	PROJ22 PROFIT	PROJ22 RISK
23	PROJ23	PROJ23 NAME	PROJ23 TYPE	PROJ23 STATUS	PROJ23 START	PROJ23 END	PROJ23 DURATION	PROJ23 COST	PROJ23 REVENUE	PROJ23 PROFIT	PROJ23 RISK
24	PROJ24	PROJ24 NAME	PROJ24 TYPE	PROJ24 STATUS	PROJ24 START	PROJ24 END	PROJ24 DURATION	PROJ24 COST	PROJ24 REVENUE	PROJ24 PROFIT	PROJ24 RISK
25	PROJ25	PROJ25 NAME	PROJ25 TYPE	PROJ25 STATUS	PROJ25 START	PROJ25 END	PROJ25 DURATION	PROJ25 COST	PROJ25 REVENUE	PROJ25 PROFIT	PROJ25 RISK
26	PROJ26	PROJ26 NAME	PROJ26 TYPE	PROJ26 STATUS	PROJ26 START	PROJ26 END	PROJ26 DURATION	PROJ26 COST	PROJ26 REVENUE	PROJ26 PROFIT	PROJ26 RISK
27	PROJ27	PROJ27 NAME	PROJ27 TYPE	PROJ27 STATUS	PROJ27 START	PROJ27 END	PROJ27 DURATION	PROJ27 COST	PROJ27 REVENUE	PROJ27 PROFIT	PROJ27 RISK
28	PROJ28	PROJ28 NAME	PROJ28 TYPE	PROJ28 STATUS	PROJ28 START	PROJ28 END	PROJ28 DURATION	PROJ28 COST	PROJ28 REVENUE	PROJ28 PROFIT	PROJ28 RISK
29	PROJ29	PROJ29 NAME	PROJ29 TYPE	PROJ29 STATUS	PROJ29 START	PROJ29 END	PROJ29 DURATION	PROJ29 COST	PROJ29 REVENUE	PROJ29 PROFIT	PROJ29 RISK
30	PROJ30	PROJ30 NAME	PROJ30 TYPE	PROJ30 STATUS	PROJ30 START	PROJ30 END	PROJ30 DURATION	PROJ30 COST	PROJ30 REVENUE	PROJ30 PROFIT	PROJ30 RISK
31	PROJ31	PROJ31 NAME	PROJ31 TYPE	PROJ31 STATUS	PROJ31 START	PROJ31 END	PROJ31 DURATION	PROJ31 COST	PROJ31 REVENUE	PROJ31 PROFIT	PROJ31 RISK
32	PROJ32	PROJ32 NAME	PROJ32 TYPE	PROJ32 STATUS	PROJ32 START	PROJ32 END	PROJ32 DURATION	PROJ32 COST	PROJ32 REVENUE	PROJ32 PROFIT	PROJ32 RISK
33	PROJ33	PROJ33 NAME	PROJ33 TYPE	PROJ33 STATUS	PROJ3						



[illegible]







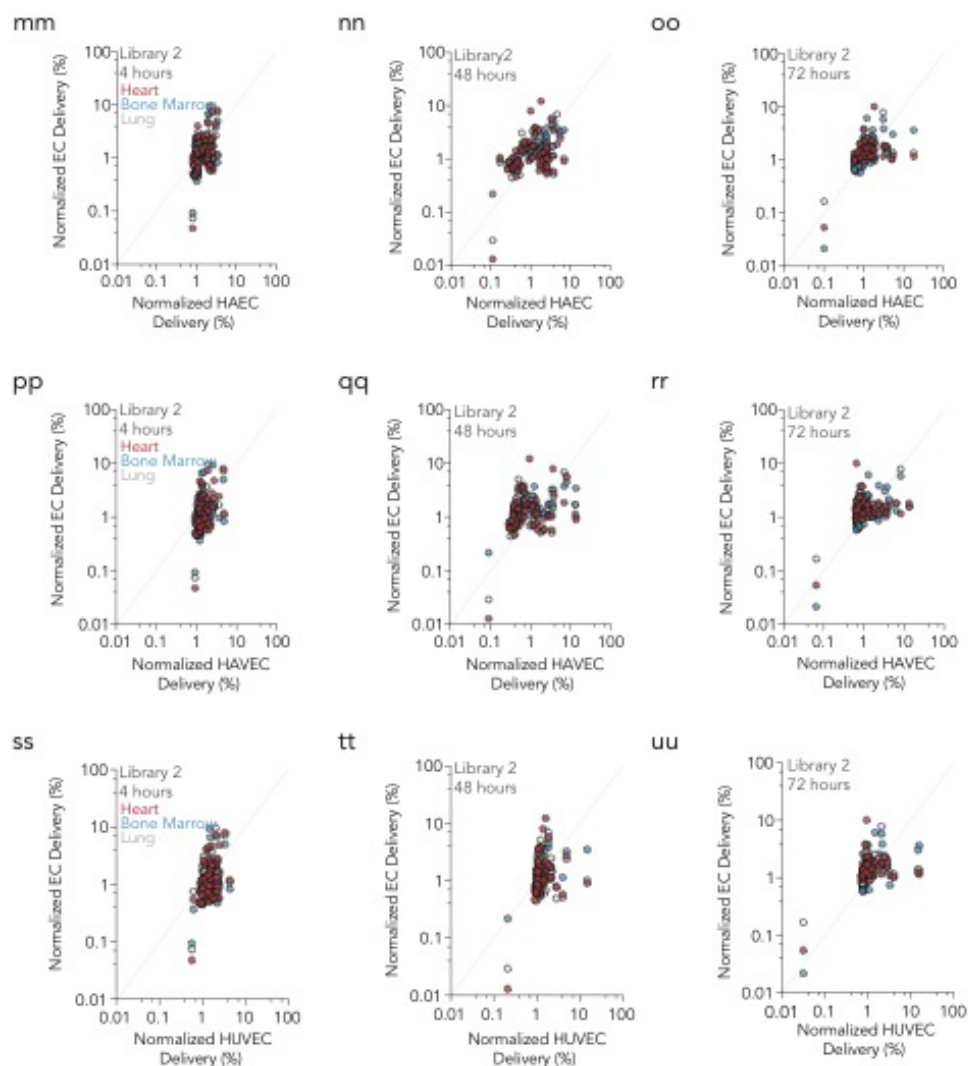


Figure 1.6. Gating strategy for isolation of endothelial cells and macrophages from (a) mouse heart, (b) mouse lung, and (c) mouse bone marrow. (d) Library 2 was designed to test the efficiency of different lipomers. 15 different lipomers were tested at varying lipomer mole percentages. Chemical formulas for lipomers are shown. (e) LNP diameters (nm) for stable pooled LNPs from library 2. (f) Library 3 was designed to further investigate the effect of PEG lipid length (C14, C16, C18) and molecular weight (350, 2000). Chemical formulas for lipomers are shown. (g) LNP diameters

(nm) for stable pooled LNPs from library 3. (h) For experiments in (a), (b), and (c), 420 LNPs were formulated, of which 281 formed stable LNPs and were pooled. (i) Diameter distribution for 281 stable LNPs that were pooled. Lines on violin plot represent 75th quartile, mean, and 25th quartile, respectively. Normalized heart, lung, and bone marrow endothelial cell delivery versus normalized iMAEC delivery for (j-l) library 1, (m-o) library 2, (p-r) library 3. Normalized heart, lung, or bone marrow macrophage delivery versus normalized RAW delivery for (s-u) library 1, (v-x) library 2, (y-aa) library 3. Normalized heart, lung, and bone marrow endothelial cell delivery versus normalized (bb-dd, hh-jj) iMAEC and (ee – gg, kk-ll) RAW delivery 4 hours and 48 hours after LNP administration, respectively. (mm-oo) Normalized HAEC, (pp-rr) HAVEC, and (ss-uu) HUVEC delivery 4 hrs, 48 hrs, and 72 hrs after LNP administration versus heart, lung, and bone marrow macrophages at the same timepoints.

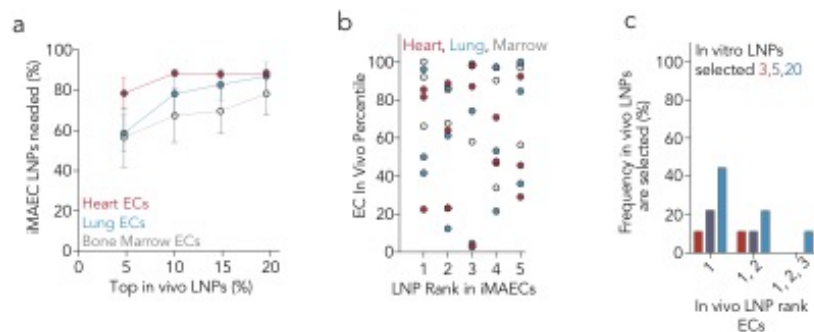
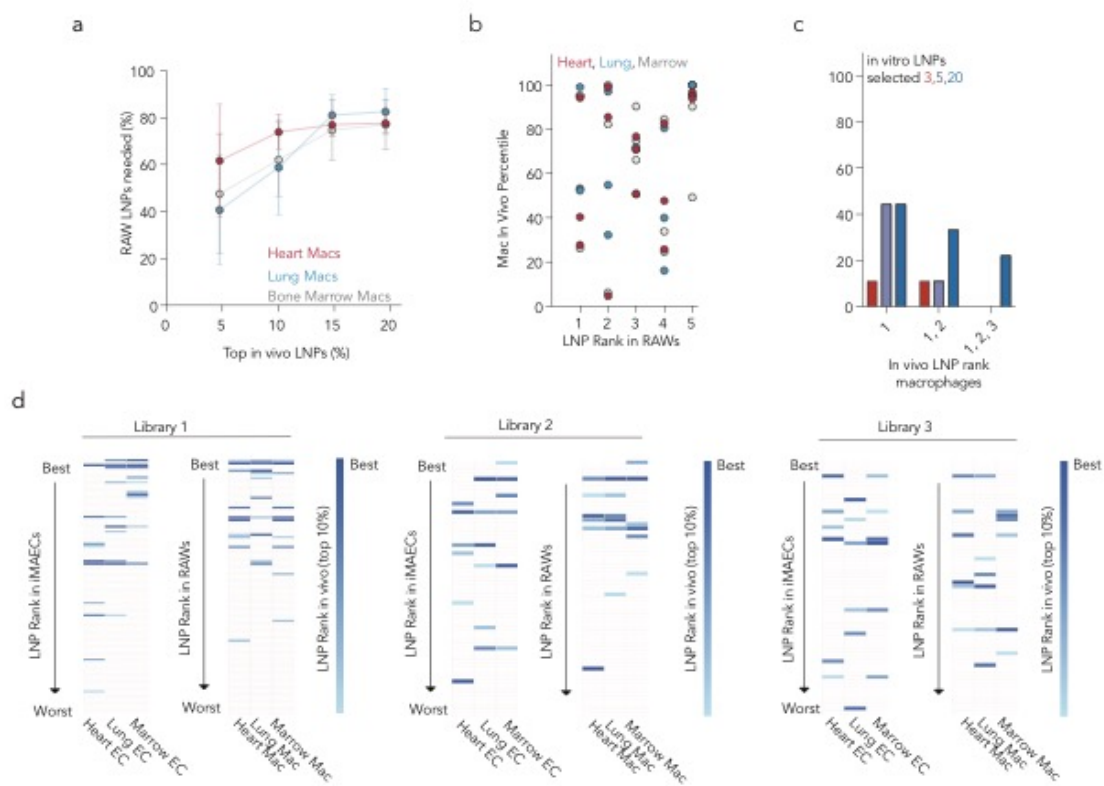


Figure 1.7. Quantifying the efficiency with which *in vitro* screens predict *in vivo* delivery. (a) Percentage of *in vitro* LNPs required to encompass the top 5, 10, 15, and 20% of the LNPs in heart, lung, and bone marrow endothelial cells *in vivo*. For example, over 50% of the *in vitro* library would be required to ensure the top 5% of the *in vivo* LNPs were selected. (b) LNP rank *in vivo* in heart, lung, and bone marrow endothelial cells, for the top 5 *in vitro* ranked LNPs. (c) Frequency with which the 1st, 1st and 2nd, or 1st, 2nd, and 3rd *in vivo* LNPs would be chosen by selecting the top 3, 5, and 20 LNPs *in vitro*.



e

Library 1													
Lipomer	Amine	Lipid	Mass Ratio	PEG Chain	PEG MW	Lipomer Mole %	Cholesterol Mole %	PEG Mole %	Diameter (nm)	IMAC	Heart Ecs	Lung Ecs	Marrow Ecs
7C1	PEI 600	C15 Epoxy	10	C14	350	62	20	18	143.4	1		5	1
7C1	PEI 600	C15 Epoxy	10	C16	350	62	15	23	117.6	3	3	3	2
7C1	PEI 600	C15 Epoxy	10	C14	350	62	5	33	218.8	4		4	4
7C1	PEI 600	C15 Epoxy	10	C16	350	62	20	18	198.7	8			6
7C1	PEI 600	C15 Epoxy	10	C18	5000	62	35	3	83.9	10		8	10
7C1	PEI 600	C15 Epoxy	10	C14	350	62	0	38	120.2	14			7
7C1	PEI 600	C15 Epoxy	10	C18	2000	62	5	33	33.4	15			3
7C1	PEI 600	C15 Epoxy	10	C18	350	62	20	18	136.2	16			8
7C1	PEI 600	C15 Epoxy	10	C18	2000	62	30	8	154.3	24	4	7	
7C1	PEI 600	C15 Epoxy	10	C14	5000	62	20	18	73.8	28		2	9
7C1	PEI 600	C15 Epoxy	10	C14	5000	62	30	8	77.1	30		9	
7C1	PEI 600	C15 Epoxy	10	C18	2000	62	10	28	50.3	35	6		
7C1	PEI 600	C15 Epoxy	10	C14	2000	62	20	18	89.8	36	9		
104	PEI 600	C12 Epoxy	10	C14	2000	62	5	33	144.2	42	2	6	
104	PEI 600	C12 Epoxy	10	C18	350	62	5	33	56.3	43	1	1	5
7C1	PEI 600	C15 Epoxy	10	C18	2000	62	25	13	111.6	59	7		
104	PEI 600	C12 Epoxy	10	C18	2000	62	10	28	47.8	64	5	10	
104	PEI 600	C12 Epoxy	10	C18	350	62	10	28	68.2	82	8		
104	PEI 600	C12 Epoxy	10	C16	350	62	30	8	78.2	95	10		

Library 1													
Lipomer	Amine	Lipid	Mass Ratio	PEG Chain	PEG MW	Lipomer Mole %	Cholesterol Mole %	PEG Mole %	Diameter (nm)	RAWs	Heart Macs	Lung Macs	Marrow Macs
7C1	PEI 600	C15 Epoxy	10	C14	350	62	20	18	143.4	1	7	2	6
7C1	PEI 600	C15 Epoxy	10	C16	350	62	15	23	117.6	2	2	4	1
7C1	PEI 600	C15 Epoxy	10	C14	350	62	5	33	218.8	5	6	1	
7C1	PEI 600	C15 Epoxy	10	C16	350	62	20	18	198.7	6		8	7
7C1	PEI 600	C15 Epoxy	10	C16	350	62	0	38	134.0	8		10	
7C1	PEI 600	C15 Epoxy	10	C18	5000	62	35	3	83.9	16		5	
7C1	PEI 600	C15 Epoxy	10	C18	2000	62	30	8	154.3	20	4		4
104	PEI 600	C12 Epoxy	10	C18	350	62	5	33	56.3	24	1	9	2
104	PEI 600	C12 Epoxy	10	C14	2000	62	5	33	144.2	25	3		3
7C1	PEI 600	C15 Epoxy	10	C14	5000	62	20	18	73.8	31	10	3	
7C1	PEI 600	C15 Epoxy	10	C18	2000	62	10	28	50.3	32	8		10
104	PEI 600	C12 Epoxy	10	C18	2000	62	10	28	47.8	36	5		5
7C1	PEI 600	C15 Epoxy	10	C14	5000	62	25	13	74.6	42		7	
7C1	PEI 600	C15 Epoxy	10	C14	5000	62	30	8	77.1	43		6	
104	PEI 600	C12 Epoxy	10	C14	350	62	30	8	88.5	47			8
7C1	PEI 600	C15 Epoxy	10	C14	2000	62	5	33	67.6	66			9
104	PEI 600	C12 Epoxy	10	C18	350	62	30	8	172.8	74	9		

f

Library 2															
Lipomer	Amine	Lipid	Phospholipid	Mass Ratio	PEG Chain	PEG MW	Lipomer Mole %	Cholesterol Mole %	PEG Mole %	Helper Lipid Mole %	Diameter (nm)	MAEC	Heart Ecs	Lung Ecs	Marrow Ecs
68	PEI 600	Lauryl Acrylate	DOPE	10	C14	2000	35	35	30	0	21.5	1			6
7C1	PEI 600	C15 Epoxy	DOPE	10	C14	2000	80	0	20	0	33.3	5		1	2
58	Spermidine	Lauryl Acrylate	DOPE	10	C14	2000	50	38.5	1.5	10	69.7	9			3
100	Spermine Free Base	C12 Epoxy	DOPE	10	C14	2000	80	15	5	0	37.0	11	4		
78	PEI 1200	Lauryl Acrylate	DOPE	10	C14	2000	35	35	30	0	35.0	13	2	4	4
100	Spermine Free Base	C12 Epoxy	DOPE	10	C14	2000	62	30	8	0	30.3	20	3	2	
58	Spermidine	Lauryl Acrylate	DOPE	10	C14	2000	50	28.5	11.5	10	34.3	22	5		
58	Spermidine	Lauryl Acrylate	DOPE	10	C14	2000	36	60	5	0	31.2	25		6	1
88	Triethylenetetramine	Lauryl Acrylate	DOPE	10	C14	2000	50	28.5	11.5	10	64.0	34	6		
58	Spermidine	Lauryl Acrylate	DOPE	10	C14	2000	62	30	8	0	66.1	40		5	
58	Spermidine	Lauryl Acrylate	DOPE	10	C14	2000	80	15	5	0	53.2	45		3	5
102	Spermidine	C12 Epoxy	DOPE	10	C14	2000	35	35	30	0	26.7	53	1		
Library 2															
Lipomer	Amine	Lipid	Phospholipid	Mass Ratio	PEG Chain	PEG MW	Lipomer Mole %	Cholesterol Mole %	PEG Mole %	Helper Lipid Mole %	Diameter (nm)	RAWs	Heart Macs	Lung Macs	Marrow Macs
68	PEI 600	Lauryl Acrylate	DOPE	10	C14	2000	35	35	30	0	21.5	1			4
8	1,4,8,12-Tetraazacyclopentadecane	Lauryl Acrylate	DOPE	10	C14	2000	80	0	20	0	21.7	17	5	4	2
8	1,4,8,12-Tetraazacyclopentadecane	Lauryl Acrylate	DOPE	10	C14	2000	50	38.5	1.5	10	53.0	19			3
48	Spermine Free Base	Lauryl Acrylate	DOPE	10	C14	2000	80	0	20	0	22.9	16			5
58	Spermidine	Lauryl Acrylate	DOPE	10	C14	2000	50	28.5	11.5	10	34.3	14	2	3	
58	Spermidine	Lauryl Acrylate	DOPE	10	C14	2000	80	15	5	0	53.2	15	4	2	
58	Spermidine	Lauryl Acrylate	DOPE	10	C14	2000	35	60	5	0	31.2	28			6
88	Triethylenetetramine	Lauryl Acrylate	DOPE	10	C14	2000	50	28.5	11.5	10	64.0	33		6	
100	Spermine Free Base	C12 Epoxy	DOPE	10	C14	2000	62	30	8	0	30.3	9	6	5	
102	Spermidine	C12 Epoxy	DOPE	10	C14	2000	35	35	30	0	26.7	51	1		
7C1	PEI 600	C15 Epoxy	DOPE	10	C14	2000	80	0	20	0	33.3	5	3	1	1

Library 3													
Lipomer	Amine	Lipid	Mass Ratio	PEG Chain	PEG MW	Lipomer Mole %	Cholesterol Mole %	PEG Mole %	Diameter (nm)	iMAEC	Heart Ecs	Lung Ecs	Marrow Ecs
7C1	PEI 600	C15 Epoxy	10	C14	2000	62	0	38	72.0	5	5		
7C1	PEI 600	C15 Epoxy	10	C16	350	62	24	14	201.2	7			1
7C1	PEI 600	C15 Epoxy	10	C14	2000	62	18	20	105.6	11		6	
7C1	PEI 600	C15 Epoxy	10	C14	2000	62	9	29	71.6	14	3		2
7C1	PEI 600	C15 Epoxy	10	C14	2000	62	6	32	58.3	16		1	6
104	PEI 600	C12 Epoxy	10	C16	350	62	27	11	108.7	18	2		
7C1	PEI 600	C15 Epoxy	10	C16	350	62	12	26	234.6	19			5
104	PEI 600	C12 Epoxy	10	C18	2000	62	30	8	56.8	21	6		
7C1	PEI 600	C15 Epoxy	10	C16	2000	62	30	8	53.4	22		3	
104	PEI 600	C12 Epoxy	10	C16	350	62	21	17	75.0	29			4
7C1	PEI 600	C15 Epoxy	10	C16	2000	62	15	23	42.6	33			3
104	PEI 600	C12 Epoxy	10	C18	2000	62	9	29	182.2	38		2	
7C1	PEI 600	C15 Epoxy	10	C16	2000	62	6	32	36.8	45		4	
104	PEI 600	C12 Epoxy	10	C14	2000	62	18	20	237.9	52	4		
104	PEI 600	C12 Epoxy	10	C18	2000	62	0	38	150.6	56	1		
104	PEI 600	C12 Epoxy	10	C18	2000	62	18	20	111.5	64		5	
Library 3													
Lipomer	Amine	Lipid	Mass Ratio	PEG Chain	PEG MW	Lipomer Mole %	Cholesterol Mole %	PEG Mole %	Diameter (nm)	RAWs	Heart Macs	Lung Macs	Marrow Macs
7C1	PEI 600	C15 Epoxy	10	C14	2000	62	21	17	135.8	5	4	3	
7C1	PEI 600	C15 Epoxy	10	C14	2000	62	0	38	72.0	14	3		3
7C1	PEI 600	C15 Epoxy	10	C14	2000	62	6	32	58.3	15			5
7C1	PEI 600	C15 Epoxy	10	C16	2000	62	30	8	53.4	16			4
7C1	PEI 600	C15 Epoxy	10	C14	2000	62	24	14	60.4	20	5		2
104	PEI 600	C12 Epoxy	10	C18	2000	62	21	17	186.6	26		1	
104	PEI 600	C12 Epoxy	10	C16	2000	62	12	26	176.3	30		4	
104	PEI 600	C12 Epoxy	10	C16	350	62	27	11	108.7	32	6		
104	PEI 600	C12 Epoxy	10	C18	2000	62	0	38	150.6	33	2	6	
104	PEI 600	C12 Epoxy	10	C14	2000	62	18	20	237.9	45	1	2	6
104	PEI 600	C12 Epoxy	10	C16	350	62	0	38	193.8	51			1
104	PEI 600	C12 Epoxy	10	C14	2000	62	12	26	51.4	53		5	

h

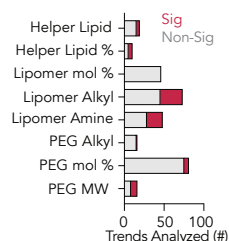
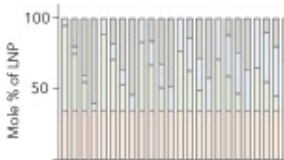
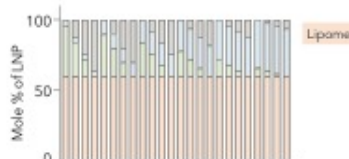
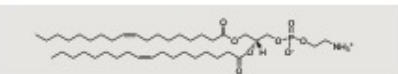
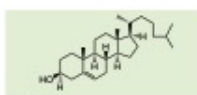
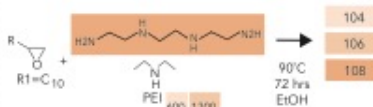
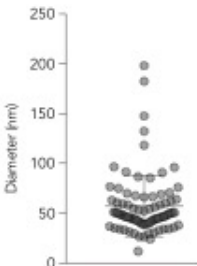


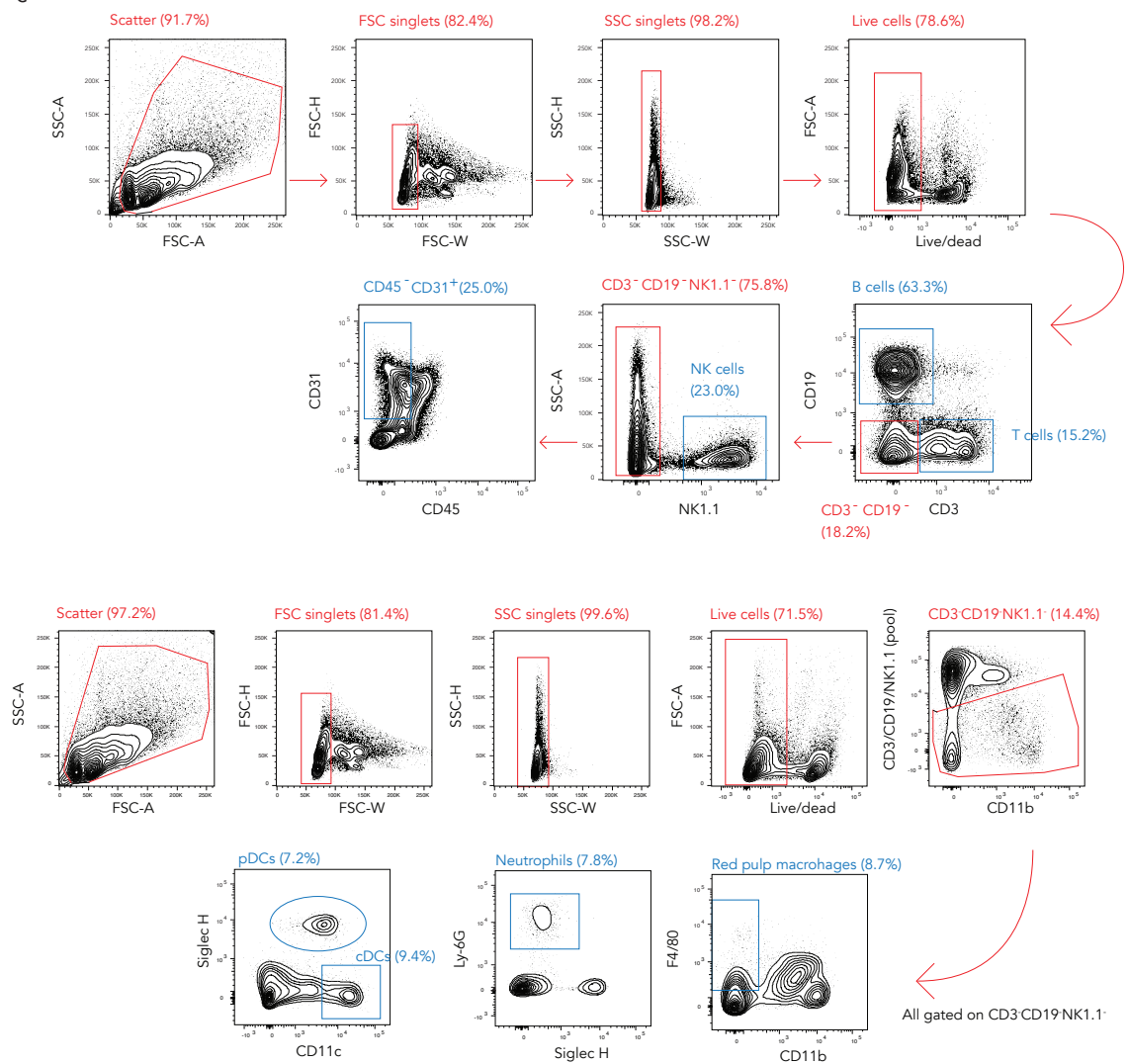
Figure 1.8. (a) The amount (%) of total LNPs from an *in vitro* screen required to encompass the top 5, 10, 15, and 20% of LNPs in heart, lung, and bone marrow macrophages *in vivo*. For example, nearly 60% of the *in vitro* library would be required to ensure that the top 5% of *in vivo* LNPs were found. **(b)** LNP rank *in vivo* in heart, lung, and bone marrow macrophages, for the top 5 *in vitro* performing LNPs. **(c)** Frequency with which the 1, 1 and 2, or 1, 2, and 3 *in vivo* LNPs are chosen when the top 3, 5, and 20 LNPs *in vitro*. **(d)** LNP rank in heart, lung, and bone marrow macrophages, plotted by *in vitro* ranking. The columns are sorted from best (LNP 1) to worst (LNP 104) *in vitro*. Top performing *in vivo* LNPs are colored. **(e)** The number of significant ($p < 0.05$, ANOVA) and non-significant relationships between LNP structure and cell targeting. Lipomer alkyl tail, amine structure, and PEG MW were most likely to influence LNP delivery.

[illegible]

b



C



Flow cytometry plots showing the gating strategy for NK cell isolation. The plots are arranged in a grid, with the top row showing the initial gating and the bottom row showing the final gating. The middle row shows the intermediate gating. The plots are labeled with the following parameters and percentages:

- Top Row (Initial Gating):**
 - Scatter (91.7%)
 - FSC singlets (82.4%)
 - SSC singlets (98.2%)
 - Live cells (78.6%)
- Middle Row (Intermediate Gating):**
 - CD45⁻ CD31⁺ (25.0%)
 - CD3⁻ CD19⁻ NK1.1⁺ (75.8%)
 - B cells (63.3%)
 - T cells (15.2%)
- Bottom Row (Final Gating):**
 - CD3⁻ CD19⁻ (18.2%)
 - CD3⁻ CD19⁻ NK1.1⁺ (14.4%)
 - pDCs (7.2%)
 - Neutrophils (7.8%)
 - Red pulp macrophages (8.7%)

The plots show the relationship between various parameters (FSC-A, FSC-W, SSC-W, Live/dead, CD45, CD31, CD3, CD19, NK1.1, CD11b, Siglec H, Ly-6G, F4/80) and the percentage of cells in each gate. Red gates indicate the selected population, and blue gates indicate the excluded population.

36

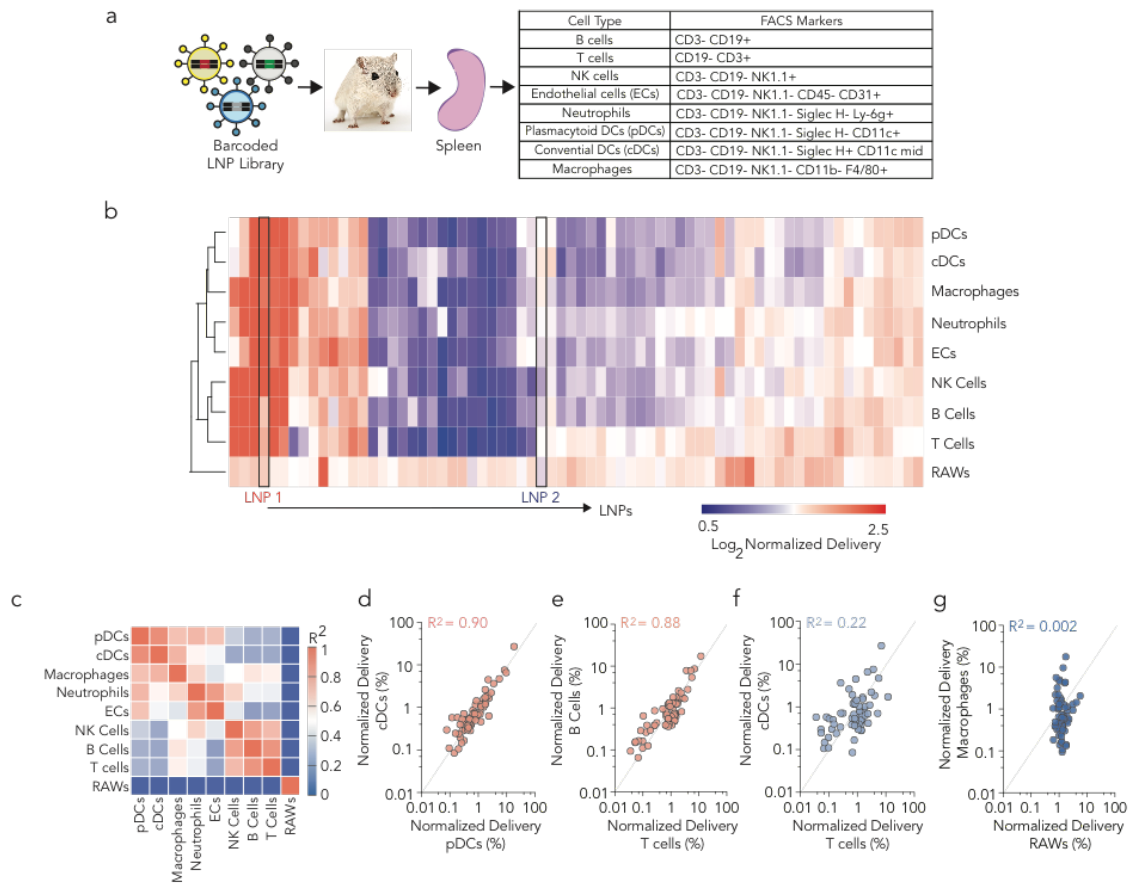


Figure 1.10. High throughput analysis of delivery to splenic microenvironment. (a) 144 LNPs were formulated; 85 stable LNPs were pooled and administered to WT mice. 72 hours later, cell types were isolated from the spleen using FACS. **(b)** Unbiased clustering of LNPs in each cell type, generated by a Euclidean distance algorithm. RAWs (macrophage *in vitro*) clustered separately from all 8 *in vivo* cell types, and both dendritic cell populations clustered together. **(c)** R^2 values for all 8 *in vivo* cell types as well as RAWs. Normalized delivery in **(d)** plasmacytoid and conventional dendritic cells (DCs), **(e)** B cells and T cells, **(f)** conventional DCs and T cells, and **(g)** RAWs and splenic macrophages.

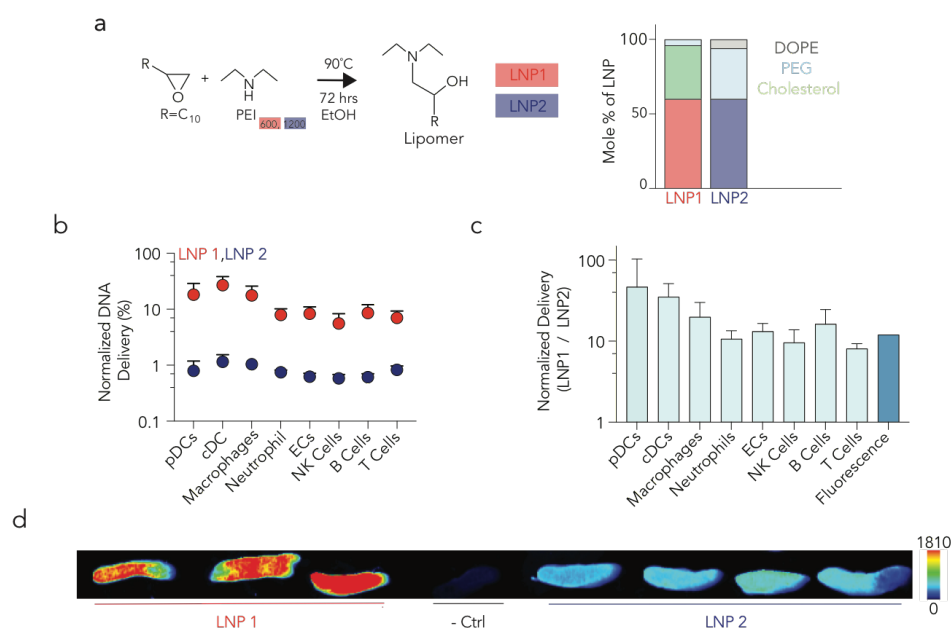


Figure 1.11. (a) Chemical compositions of LNP1 and LNP2. (b) Normalized delivery of 2 LNPs; 1 with high (LNP1) and 1 with low (LNP2) normalized delivery. (c) The ratio of normalized delivery (LNP1/LNP2) in each cell type using barcodes, as well as fluorescence of the spleen whole tissue. (d) Cy5.5 fluorescence in splenic whole tissue 3 hours after mice were injected with either LNP1 or LNP2. LNP1 fluorescence was higher, as predicted by the barcoding data.

a

Library 1			
Strain	Procedure	W (0 hrs) (g)	W (72 hrs) (g)
C57BL/6	IV-pooled NPs	19.2	20.4
C57BL/6	IV-pooled NPs	19.6	19.7
C57BL/6	IV-pooled NPs	17.3	18
C57BL/6	IV-pooled NPs	20.1	21

Library 2			
Strain	Procedure	W (0 hrs) (g)	W (4 hrs) (g)
C57BL/6	IV-pooled LNP Inject	21.4	22.2
C57BL/6	IV-pooled LNP Inject	21.3	21.1
C57BL/6	IV-pooled LNP Inject	23.9	23.3
C57BL/6	IV-pooled LNP Inject	19.1	18.9
Strain	Procedure	W (0 hrs) (g)	W (48 hrs) (g)
C57BL/6	IV-pooled LNP Inject	20.7	22.07
C57BL/6	IV-pooled LNP Inject	22.4	22.6
C57BL/6	IV-pooled LNP Inject	20.7	21.4
C57BL/6	IV-pooled LNP Inject	22.7	22.6
Strain	Procedure	W (0 hrs) (g)	W (72 hrs) (g)
C57BL/6	IV-pooled LNP Inject	20.3	21.7
C57BL/6	IV-pooled LNP Inject	21.7	21.8
C57BL/6	IV-pooled LNP Inject	21.2	21.7
C57BL/6	IV-pooled LNP Inject	21	21.5

Library 3			
Strain	Procedure	W (0 hrs) (g)	W (72 hrs) (g)
C57BL/6	IV-pooled LNP Inject	18.1	19.5
C57BL/6	IV-pooled LNP Inject	19	20
C57BL/6	IV-pooled LNP Inject	19.3	19.3
C57BL/6	IV-pooled LNP Inject	18.5	19.9

Splenic Library			
Strain	Procedure	W (0 hrs) (g)	W (72 hrs)
C57BL/6	IV-pooled LNP Inject	23.8	24.4
C57BL/6	IV-pooled LNP Inject	22.2	22.9
C57BL/6	IV-pooled LNP Inject	24.2	25
C57BL/6	IV-pooled LNP Inject	22.5	23.5

b

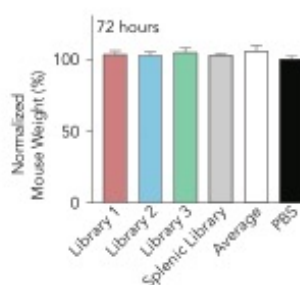


Figure 1.12. (a) Mouse weights before, W (0 hrs), and after injection, W (72 hrs), are shown for each experiment. (b) Normalized mouse weights for each experiment compared to PBS injected mice.

1.4 Methods & Materials

Nanoparticle Formulation. Nanoparticles were formulated in a microfluidic device by mixing DNA with lipomer, PEG, cholesterol, and a helper lipid, as previously described^{5,18,19,22-27,42}. Nanoparticles were made with variable molar ratios of these constituents. The genetic drug (in this case, DNA barcode) was diluted in 10 mM citrate buffer (Teknova), and loaded into a syringe (Hamilton Company). The materials making up the nanoparticle (lipomer, cholesterol, PEG, and helper lipid) were diluted in 100% ethanol, and loaded into a second syringe. The citrate phase and ethanol phase were mixed together in a microfluidic device, at rates of 600 $\mu\text{L}/\text{min}$ and 200 $\mu\text{L}/\text{min}$, respectively, to form LNPs. We used the following helper lipids: DOPE (Avanti Lipids, 850725), and DOPC (Avanti Lipids, 850375).

DNA barcoding. Each chemically distinct LNP was formulated to carry its own unique DNA barcode (**Figure 1.1A, B**). For example, LNP1 carried DNA barcode 1, while the chemically distinct LNP2 carried DNA barcode 2.

The DNA barcodes were designed rationally with several characteristics, as we previously described¹⁸. We purchased 56 nucleotide single stranded DNA sequences from IDT (**Figure 1.1C, Figure 1.2A**). We included 2 universal 21 and 20 nucleotide primer regions in addition to a random 7 nucleotide ('7N') region that is unique to each piece of DNA (**Figure 1.2B**). Barcodes were distinguished using an 8 basepair (bp) sequence in the middle of the barcode. An 8 bp sequence can generate over 1,000,000 (4^8) unique barcodes; we selected 240 barcodes to prevent sequence bleaching on the Illumina MiniSeqTM machine. The 2 nucleotides on the 5' and 3' ends of the 56-nucleotide ssDNA sequence

were modified with phosphorothioate linkages to reduce exonuclease degradation and improve DNA barcode stability.

Nanoparticle Characterization. LNP hydrodynamic diameter was measured using high throughput dynamic light scattering (DLS) (DynaPro Plate Reader II, Wyatt). LNPs were diluted in sterile 1X PBS to a concentration of ~0.0005 mg/mL, and analyzed. LNPs were included if they met 3 criteria: diameter >20 nm, diameter <300 nm, and autocorrelation function with only 1 inflection point. Over the course of our experiments, ~65% of the LNPs we formulated met all 3 criteria. Particles that met these criteria were pooled and dialyzed with 1X phosphate buffered saline (PBS, Invitrogen), and were sterile filtered with a 0.22 μ m filter.

Animal Experiments. All animal experiments were performed in accordance with the Georgia Institute of Technology's Physiological Research Laboratory (PRL) animal care and services policy. Female C57BL/6J (#000664) mice were purchased from the Jackson Laboratory. All mouse weights before and after injection, are shown in (**Figure 1.12A, B**). In all experiments, mice were aged 4-12 weeks, female, and N = 3 – 5 mice per group were injected intravenously via the lateral tail vein with the same pooled LNPs.

Nanoparticle dosing. Mice were injected with a total DNA dose of 0.5 mg/kg. As an example, if an experiment measured 100 nanoparticles, then on average, each nanoparticle was administered at a dose of 0.005 mg/kg. The nanoparticle dose was determined using NanoDrop (Thermo Scientific).

Cell Culture. *In vitro* experiments were performed using mouse macrophage cells (RAW 264.7, ATCC), mouse aortic endothelial cells (provided by Hanjoong Jo at Emory)³⁴,

primary human aortic endothelial cells (HAEC, Lonza), primary human umbilical vein endothelial cells (HUVEC, Lonza), and primary human aortic vein endothelial cells (HAVEC, Lonza).

In all cases, cells were maintained and cultured using previously established conditions. In all cases, cell media was supplemented by penicillin-streptomycin (500 U/mL penicillin G, 0.5 mg/mL streptomycin) (PenStrep, VWR) and 10% (v/v) fetal bovine serum (FBS, VWR). RAW cells were passaged with DMEM F-12 50/50 (Corning). iMAEC cells were passaged using DMEM with 1 g/L glucose, L-glutamine, and sodium pyruvate (Corning), supplemented by 1% (v/v) MEM non-essential amino acid solution (MEMNEAA, Sigma Aldrich), and 25 µg/mL endothelial cell growth supplement (ECGS, Emd Millipore). HAEC and HAVEC cells were passaged with MCDB 131 media without L-glutamine (VWR Scientific), supplemented by 1% (v/v) L-glutamate, 25 µg/mL ECGS, 0.1% (v/v) ascorbic acid, hydrocortisol, and the following growth factors: endothelial growth factor (EGF), vascular-endothelial growth factor (VEGF), fibroblast growth factor (FGF), and insulin-like growth factor (IGF). HUVEC cells were passaged with M199 media with Earle's salts and L-glutamine (Corning), supplemented by 1% (v/v) ECGS, L-glutamine, and 0.2% (v/v) heparin.

In all cases, cells were seeded in a 24-well plate at a density of 40,000 cells/well. 24 hours later, LNPs were added with a total DNA dose of 4, 20, or 100 ng (**Figure 1.3E, Figure 1.4B-D**). Based on these results, cells were treated with 20 ng total DNA in all other experiments. Six hours after transfection, media was removed, and fresh media was added. 72 hours after transfection, media was removed and DNA was isolated using QuickExtract (EpiCentre).

Fixed-cell staining. Cells were plated onto 35 mm glass-bottom dishes (In Vitro Scientific) one day prior to particle delivery. Cells were fixed at the indicated time points with 4% paraformaldehyde (Electron Microscopy Sciences) for 10 min at room temperature before permeabilization with 0.2% Triton X-100 (Sigma-Aldrich) for 5 min at room temperature. To stain actin, cells were then incubated with Phalloidin-488 (Thermo Scientific) for 30 minutes at 37°C. Nuclei were stained with 4',6-diamidino-2-phenylindole (DAPI) (Life Technologies), and coverslips were placed over the cells in the dish and mounted with Prolong Gold (Life Technologies).

Microscopy. Images were acquired with a Hamamatsu Flash 4.0 v2 sCMOS camera on a PerkinElmer UltraView spinning disk confocal microscope mounted to a Zeiss Axiovert 200M body with a 63x NA 1.4 plan-apochromat objective. Images were acquired with Volocity (PerkinElmer) with Z-stacks taken in 0.2 μ m increments. For live-cell images, cells and dishes were kept at 37 °C during imaging by using a Chamlide TC-L live-cell stage-top environment with objective heater (Live Cell Instrument). All images were linearly contrast enhanced. Live-cell images were smoothed with a fine rolling ball filter in Volocity.

Cell Isolation. One time-course experiment was performed; delivery was analyzed 4, 48, and 72 hours after LNPs were administered. In all other cases, tissues and cells were isolated 72 hours after injection with LNPs. In all experiments, mice were perfused with 20 mL of 1X PBS through the right atrium. The heart, lungs, spleen, and bone marrow were isolated immediately following perfusion. Tissues were finely cut, and then placed in a digestive enzyme solution with Collagenase Type I (Sigma Aldrich), Collagenase XI (Sigma Aldrich), and Hyaluronidase (Sigma Aldrich). The digestive enzyme for heart

included Collagenase IV (Sigma Aldrich)²². Tissues were digested for 45 minutes at 37°C and 550 rpm. Digested tissues were passed through a 70 µm filter. Red blood cells were lysed using (RBC) lysis buffer. Cells were resuspended in FACS buffer (2% FBS in 1X PBS).

Heart, Lung, Bone Marrow Cell Staining. Cells were stained to identify specific cell populations and sorted using the BD FACS Fusion and BD FACS Aria IIIu cell sorters in the Georgia Institute of Technology cellular analysis core. Antibodies used for staining were CD31 (Clone 390, BioLegend), CD45.2 (Clone 104, BioLegend), and CD11b (Clone M1/70, BioLegend).

We defined cell populations in the following manner: macrophages (CD31⁻CD45⁺CD11b⁺), heart and lung endothelial cells (CD31⁺CD45⁻), bone marrow endothelial cells (CD31⁺), immune cells excluding macrophages (CD31⁻CD45⁺CD11b⁻), and other cells (CD31⁻CD45⁻) (**S3A-C**).

Splenic Cell Staining and Isolation. Splenocytes were isolated by digesting sliced spleens in 0.1 U/ml collagenase (Sigma Aldrich) in Hank's Balanced Salt Solution (Corning) for 30 minutes at 37°C. Digestion was stopped by addition of EDTA to 5 mM, and the resulting mixture was passed through a cell strainer. Red blood cells were removed with ACK lysing buffer (Lonza), and cells were washed in FACS buffer (PBS supplemented with 2% FBS and 2 mM EDTA; Corning and HyClone) and re-strained.

Cells were stained by conventional methods in FACS buffer as previously described⁴³. Antibodies used for staining were CD19 (clone 1D3, eBioscience), CD3 (clone 17A2, eBioscience), CD31 (clone 390, BioLegend), CD45 (clone 104, BioLegend), NK1.1 (clone

PK136, eBioscience), CD11b (clone M1/70, BioLegend), CD11c (clone N418, BioLegend), Siglec H (clone 551, BioLegend), F4/80 (clone BM8, BioLegend), and Ly-6G (clone 1A8, BioLegend). Cells were also stained with LIVE/DEAD viability dyes (Thermo Fisher) to exclude dead cells.

Described splenocyte cell types (**Figure 1.10A, Figure 1.9D**) from four mice were isolated by FACS on two FACSAria II cell sorters (BD Biosciences) at the Emory University School of Medicine Flow Cytometry Core.

PCR Amplification. All samples were amplified and prepared for sequencing. More specifically, 1 μ L of primers (5 μ M for Final Reverse/Forward, 0.5 μ M for Base Forward) were added to 5 μ L of Kapa HiFi 2X master mix, 3 μ L sterile H₂O, and 1 μ L DNA template. The reaction was run for 30 cycles. When the PCR reaction did not produce clear bands, the primer concentrations, DNA template input, PCR temperature, and number of cycles were optimized for individual samples. The PCR amplicon was isolated with gel extraction.

Deep Sequencing. Illumina deep sequencing was conducted in Georgia Tech's Molecular Evolution core. Runs were performed on an Illumina MiniseqTM. Primers were designed based on Nextera XT adapter sequences.

Data Normalization. Counts for each particle, per tissue, were normalized to unity (**Figure 1.1D**) The DNA counts in each tissue were then normalized to 100%. For example, if a sample (e.g., heart1) had 500,000 total barcode reads, and 50,000 of them came from particle X, while 4,000 came from particle Y, then the normalized delivery for particle X and Y would be 10% and 0.8%, respectively. The barcoded LNP mixture we injected into

the mouse was also sequenced. This ‘input’ DNA was used to normalize DNA counts from the cells and tissues (**Figure 1.2C**).

Data Analysis. Sequencing results were processed using a custom python-based tool to extract raw barcode counts for each tissue. These raw counts were then normalized with an R script prior to further analysis. Statistical analysis was done using GraphPad Prism 7. Correlation analyses were run assuming a Gaussian distribution in order to obtain Pearson correlation coefficients. R^2 values (0 – 1) were computed by squaring Pearson correlation coefficients.

Data Access. The data, analyses, and scripts used to generate all figures in the paper are available upon request to J.E.D. or dahlmanlab.org.

Roles. K.P., C.D.S., and J.E.D. designed experiments. All authors performed the experiments and/or analyzed the data. K.P., C.D.S., and J.E.D. wrote the paper with input from all authors.

1.4 References

1. Blanco, E., Shen, H. & Ferrari, M. Principles of nanoparticle design for overcoming biological barriers to drug delivery. *Nat Biotechnol* **33**, 941-951 (2015).
2. Cheng, C.J., Tietjen, G.T., Saucier-Sawyer, J.K. & Saltzman, W.M. A holistic approach to targeting disease with polymeric nanoparticles. *Nat Rev Drug Discov* **14**, 239-247 (2015).
3. Sahin, U., Kariko, K. & Tureci, O. mRNA-based therapeutics--developing a new class of drugs. *Nat Rev Drug Discov* **13**, 759-780 (2014).
4. Dong, Y., *et al.* Lipopeptide nanoparticles for potent and selective siRNA delivery in rodents and nonhuman primates. *Proceedings of the National Academy of Sciences of the United States of America* **111**, 3955-3960 (2014).
5. Dahlman, J.E., *et al.* In vivo endothelial siRNA delivery using polymeric nanoparticles with low molecular weight. *Nat Nano* **9**, 648-655 (2014).
6. Love, K.T., *et al.* Lipid-like materials for low-dose, in vivo gene silencing. *Proceedings of the National Academy of Sciences of the United States of America* **107**, 1864-1869 (2010).
7. Akinc, A., *et al.* A combinatorial library of lipid-like materials for delivery of RNAi therapeutics. *Nat Biotechnol* **26**, 561-569 (2008).
8. Hao, J., *et al.* Rapid Synthesis of a Lipocationic Polyester Library via Ring-Opening Polymerization of Functional Valerolactones for Efficacious siRNA Delivery. *J Am Chem Soc* **29**, 9206-9209 (2015).
9. Siegwart, D.J., *et al.* Combinatorial synthesis of chemically diverse core-shell nanoparticles for intracellular delivery. *Proceedings of the National Academy of Sciences of the United States of America* **108**, 12996-13001 (2011).
10. Zuckerman, J.E., Choi, C.H., Han, H. & Davis, M.E. Polycation-siRNA nanoparticles can disassemble at the kidney glomerular basement membrane. *Proc Natl Acad Sci U S A* **109**, 3137-3142 (2012).
11. Aird, W.C. Endothelial cell heterogeneity. *Critical care medicine* **31**, S221-S230 (2003).
12. Aird, W.C. Endothelial cell heterogeneity. *Cold Spring Harbor perspectives in medicine* **2**, a006429 (2012).
13. Aird, W.C. Phenotypic heterogeneity of the endothelium. *Circulation research* **100**, 174-190 (2007).

14. Aird, W.C. Phenotypic heterogeneity of the endothelium: II. Representative vascular beds. *Circulation research* **100**, 174-190 (2007).
15. Augustin, H.G. & Koh, G.Y. Organotypic vasculature: From descriptive heterogeneity to functional pathophysiology. *Science* **357**, eaal2379 (2017).
16. Tsoi, K.M., *et al.* Mechanism of hard-nanomaterial clearance by the liver. *Nat Mater* **15**, 1212-1221 (2016).
17. Zhang, Y., *et al.* Purification and Characterization of Progenitor and Mature Human Astrocytes Reveals Transcriptional and Functional Differences with Mouse. *Neuron* **89**, 37-53 (2016).
18. Dahlman, J.E., *et al.* Barcoded nanoparticles for high throughput in vivo discovery of targeted therapeutics. *Proceedings of the National Academy of Sciences of the United States of America* **114**, 2060-2065 (2017).
19. Chen, D., *et al.* Rapid discovery of potent siRNA-containing lipid nanoparticles enabled by controlled microfluidic formulation. *J Am Chem Soc* **134**, 6948-6951 (2012).
20. Carmeliet, P. & Jain, R.K. Molecular mechanisms and clinical applications of angiogenesis. *Nature* **473**, 298-307 (2011).
21. Swirski, F.K. & Nahrendorf, M. Leukocyte behavior in atherosclerosis, myocardial infarction, and heart failure. *Science* **339**, 161-166 (2013).
22. Sager, H.B., *et al.* RNAi targeting multiple cell adhesion molecules reduces immune cell recruitment and vascular inflammation after myocardial infarction. *Science translational medicine* **8**, 342ra380-342ra380 (2016).
23. Yun, S., *et al.* Interaction between integrin $\alpha 5$ and PDE4D regulates endothelial inflammatory signalling. *Nat Cell Biol* (2016).
24. Xue, W., *et al.* Small RNA combination therapy for lung cancer. *Proceedings of the National Academy of Sciences* **111**, E3553-E3561 (2014).
25. Platt, R.J., *et al.* CRISPR-Cas9 knockin mice for genome editing and cancer modeling. *Cell* **159**, 440-455 (2014).
26. Sager, H.B., *et al.* Proliferation and Recruitment Contribute to Myocardial Macrophage Expansion in Chronic Heart Failure. *Circ Res* **119**, 853-864 (2016).

27. White, K., *et al.* Genetic and hypoxic alterations of the microRNA-210-ISCU1/2 axis promote iron-sulfur deficiency and pulmonary hypertension. *EMBO Mol Med* **7**, 695-713 (2015).
28. Khan, O.F., *et al.* Dendrimer-Inspired Nanomaterials for the in Vivo Delivery of siRNA to Lung Vasculature. *Nano Lett* **15**, 3008-3016 (2015).
29. Khan, O.F., *et al.* Ionizable amphiphilic dendrimer-based nanomaterials with alkyl-chain-substituted amines for tunable siRNA delivery to the liver endothelium in vivo. *Angew Chem Int Ed Engl* **53**, 14397-14401 (2014).
30. Wittrup, A., *et al.* Visualizing lipid-formulated siRNA release from endosomes and target gene knockdown. *Nat Biotechnol* (2015).
31. Gilleron, J., *et al.* Image-based analysis of lipid nanoparticle-mediated siRNA delivery, intracellular trafficking and endosomal escape. *Nat Biotechnol* **31**, 638-646 (2013).
32. Geary, R.S., Norris, D., Yu, R. & Bennett, C.F. Pharmacokinetics, biodistribution and cell uptake of antisense oligonucleotides. *Adv Drug Deliv Rev* **87**, 46-51 (2015).
33. Crooke, S.T., Wang, S., Vickers, T.A., Shen, W. & Liang, X.H. Cellular uptake and trafficking of antisense oligonucleotides. *Nat Biotechnol* **35**, 230-237 (2017).
34. Ni, C.W., Kumar, S., Ankeny, C.J. & Jo, H. Development of immortalized mouse aortic endothelial cell lines. *Vascular cell* **6**, 7 (2014).
35. Kumar, V., *et al.* Shielding of Lipid Nanoparticles for siRNA Delivery: Impact on Physicochemical Properties, Cytokine Induction, and Efficacy. *Mol Ther Nucleic Acids* **3**, e210 (2014).
36. Tao, W., *et al.* Noninvasive imaging of lipid nanoparticle-mediated systemic delivery of small-interfering RNA to the liver. *Mol Ther* **18**, 1657-1666 (2010).
37. Mui, B.L., *et al.* Influence of Polyethylene Glycol Lipid Desorption Rates on Pharmacokinetics and Pharmacodynamics of siRNA Lipid Nanoparticles. *Mol Ther Nucleic Acids* **2**, e139 (2013).
38. Kranz, L.M., *et al.* Systemic RNA delivery to dendritic cells exploits antiviral defence for cancer immunotherapy. *Nature* **534**, 396-401 (2016).
39. Whitehead, K.A., *et al.* In vitro-in vivo translation of lipid nanoparticles for hepatocellular siRNA delivery. *ACS nano* **6**, 6922-6929 (2012).
40. Bhatia, S.N. & Ingber, D.E. Microfluidic organs-on-chips. *Nat Biotechnol* **32**, 760-772 (2014).

41. Fatehullah, A., Tan, S.H. & Barker, N. Organoids as an in vitro model of human development and disease. *Nat Cell Biol* **18**, 246-254 (2016).
42. Koga, J., *et al.* Macrophage Notch Ligand Delta-Like 4 Promotes Vein Graft Lesion Development: Implications for the Treatment of Vein Graft Failure. *Arteriosclerosis, thrombosis, and vascular biology* **35**, 2343-2353 (2015).
43. Araki, K., *et al.* Translation is actively regulated during the differentiation of CD8⁺ effector T cells. *Nature immunology* **18**, 1046-1057 (2017).

CHAPTER 2. QUANTATIVE UNBIASED ANALYSIS OF NANOPARTICLE TRAFFICKING

The work presented here is an excerpt from Sago*, CD, Lokugamage*, MP, Lando, GN, Djeddar, N, Shah, NN, Syed, C, Bryksin, AV, Dahlman, JE (2018). “Modifying a commonly expressed endocytic receptor retargets nanoparticles *in vivo*.” Nano Letters.

2.1 Background

Small interfering RNAs (siRNAs) delivered to hepatocytes have treated disease in patients¹⁻³, but delivery to other cell types remains challenging⁴. The liver exhibits physiological advantages that promote nanoparticle accumulation^{5,6}, and as a result, rational approaches will be required to minimize unwanted liver delivery. An ideal approach would involve (i) synthesizing hundreds of nanoparticles with diverse chemical structures, and (ii) analyzing them *in vivo* using an animal model that (iii) tests a specific biological hypothesis (e.g., gene X alters delivery) *in vivo*. However, the current gold standard is to study nanoparticles *in vitro*. Thousands of nanoparticles can be synthesized for nucleic acid delivery, but they are screened *in vitro*⁷⁻¹², which can be a poor predictor of *in vivo* delivery¹³. Genes that alter nanoparticle delivery *in vitro* have been identified¹⁴⁻¹⁷; genes that affect systemic nanoparticle delivery *in vivo* remain much more difficult to study. Exceptions to this¹⁸⁻²¹ have provided valuable insights, but have focused on soluble factors in serum^{18,19} or receptors on hepatocytes¹⁹⁻²¹. Whether a commonly expressed gene can exert cell type-specific effects on nanoparticle delivery *in vivo* remains unexplored.

Nanomedicines are often delivered using ligands that bind receptors expressed on target cells²². For example, the asialoglycoprotein receptor (ASGPR) is expressed on hepatocytes; GalNAc has targeted ASGPR²³, leading to delivery in animals and patients. Other receptors include epidermal growth factor (EGFR)²⁴, folate receptor²⁵, transferrin receptor²⁶, VCAM-1²⁷, and ICAM-1²⁸. Given that few receptors are (i) highly expressed on one cell type and (ii) induce nanomedicine endocytosis upon binding, we envisioned an alternative approach: manipulating an endocytosis receptor expressed on many cells. An ideal receptor would inhibit delivery to cell type A more than cell type B, promoting delivery to cell type B. This approach is timely. Our understanding of cell heterogeneity is progressing; RNA-seq²⁹ has revealed that gene expression varies with disease state³⁰ and within cell populations previously believed to be homogeneous^{31,32}. Large scale approaches like the Human Cell Atlas³³ are likely to uncover endocytic genes whose importance varies with cell type. Since hundreds of genes are involved in endocytosis³⁴, and many genes are regulated by disease- and microenvironment-derived cues^{35,36}, it is foreseeable that manipulating 1 gene could alter delivery in a tissue- or disease-specific manner. To test the hypothesis that manipulating a commonly expressed receptor can affect nanoparticle delivery in cell type-dependent manner, we focused on Caveolin 1 (Cav1), a gene involved in caveolin-mediated endocytosis³⁷. Caveolin can endocytose nanoparticles *in vitro*³⁸ and *in vivo*³⁹. Its expression changes with fibrosis⁴⁰⁻⁴³, lung disease⁴⁴, cancer⁴⁵⁻⁴⁸, neurological disease^{49,50}, and other pathologies⁵¹⁻⁵³, demonstrating that its expression is regulated by microenvironmental signals and disease.

2.2 Results

Given that *in vitro* nanoparticle delivery can be a poor predictor of *in vivo* delivery¹³ and that gene expression can change when cells are cultured *in vitro*⁵⁴, we tested our hypothesis *in vivo*, eventually testing 226 chemically distinct lipid nanoparticles (LNPs). This approach is distinct from previous studies for 2 reasons. First, LNP studies typically evaluate many nanoparticles *in vitro* before selecting a small number to test *in vivo*⁷⁻¹². Second, most LNP studies focus on hepatocytes, not macrophages⁸⁻¹².

We used microfluidics⁵⁵ to formulate a validated ionizable LNP that has delivered siRNAs *in vivo*^{7,56-60}. The LNP carried a single stranded DNA (ssDNA) (**Figure 2.1a**) that was chemically modified with phosphorothioates to reduce exonuclease degradation, and fluorescently tagged with Alexa-647. We chose Alexa-647 since it was significantly brighter than Alexa488 (**Figure 2.1b**). One hour after intravenously injecting wildtype (WT) or Cav1 deficient (Cav1^{-/-}) mice with the clinically relevant³ dose of 0.5 mg / kg DNA, we quantified Alexa-647 mean fluorescence intensity (MFI) in 13 cell types (**Figure 2.1c**) using flow cytometry (**Figure 2.1d,e**). In WT mice, >75% of the MFI signal was found in Kupffer cells or hepatic endothelial cells; we could not reliably quantify delivery in other cell types. The same was true for Cav1^{-/-} mice, suggesting Cav1 did not change LNP biodistribution (**Figure 2.1f**).

Given the role of Cav1 in nanoparticle endocytosis⁶¹, the fact caveolin inhibitors affect this LNP *in vitro*⁷, and the fact this LNP delivers siRNA and sgRNA to pulmonary and cardiovascular endothelial cells *in vivo*^{7,56-60}, we hypothesized that our Alexa-647 biodistribution data were inaccurate. Our hypothesis was recently strengthened by demonstrations that the fluorescent biodistribution of small molecules delivered by nanoparticles can change in ways that do not reflect delivery⁶². Since nucleic acids are

degraded by nucleases that cleave phosphodiester bonds⁶³ - and fluorophores are not – we reasoned the fluorescent signal may not track with the nucleic acid. To test this, we engineered a novel biodistribution assay named QUAntitative Analysis of Nucleic acid Therapeutics (QUANT); QUANT utilizes digital droplet PCR (ddPCR) – a technique used to quantify rare genomic events⁶⁴ – to quantify the biodistribution of the nucleic acid itself with high sensitivity, allowing us to directly compare it to the biodistribution of the fluorescent readout. This is important since fluorescent biodistribution studies are ubiquitously used throughout to measure nucleic acid biodistribution.

Since ddPCR requires efficient DNA amplification, we rationally designed QUANT DNA barcodes to increase DNA polymerase access (**Figure 2.2a,b, Figure 2.1a**). We minimized DNA 2° structure on the forward and reverse primer sites and minimized G-quadruplex formation by separating our randomized 7 nucleotide region^{13,65} into semi-randomized NWNH and NWH sites. We flanked the primer sites with 3 additional phosphorothioate-modified nucleotides to reduce exonuclease degradation of the primer site. Finally, we identified universal primer binding sites that would not amplify mouse or human genomic DNA (gDNA). Specifically, we designed primers with similar melting temperatures (within 1°C) and added them to human and mouse gDNA without barcode template (**Figure 2.3a**). We identified primers that did not amplify gDNA after 40 cycles (**Figure 2.3b**), but amplified barcode templates with 20 cycles. Based on these results, we added the ‘no gDNA background’ primer sites to our barcodes. We then optimized the ddPCR protocol (**Figure 2.3c-g**) by varying annealing temperatures, primer concentrations, and probe concentrations. We increased the signal: noise ratio 14-fold compared to current standard protocols⁶⁴. As a control, we scrambled the ddPCR probe

site; no signal was generated, demonstrating that the signal required specific barcode-probe interactions (**Figure 2.3h**).

Standard curve experiments revealed QUANT was highly sensitive. QUANT ddPCR signal was linear (with respect to the DNA added) when barcodes were diluted in Tris-EDTA buffer to a concentration between 750 aM and 12 fM ($R^2 = 1.00$) and was detected at 300 aM (**Figure 2.2c, d**). As a control, we reduced the concentration to 30 aM, and did not observe readouts above an untreated baseline. QUANT was also highly sensitive *in vitro*. We fluorescently tagged QUANT barcodes and administered them to immortalized aortic endothelial cells (iMAECs)⁶⁶ in 96 well plates with Lipofectamine 2000 (L2K) at doses between 1 pg and 400 ng / well. Twenty-four hours later, we quantified biodistribution using flow cytometry, and observed measurable (but non-linear) increases in MFI above 10 pg / well (**Figure 2.4a**). Separately, we administered QUANT barcodes without a fluorophore at doses between 60 and 16,000 zeptogram (zg) / well. ddPCR readouts were linear ($R^2 = 0.91$) between 120 and 8000 zg / well (**Figure 2.2e**), 10^8 x lower than the minimum dose required for a fluorescent signal. We then formulated QUANT barcodes into validated LNPs⁷ using microfluidics⁵⁵; LNPs carrying barcodes formed nanoparticles with an average hydrodynamic diameter of 53 nm. We intravenously administered them at 0.5 mg / kg, isolated lung endothelial cells using fluorescence activated cell sorting (FACS) 24 hours later, and quantified barcode delivery using ddPCR. We compared samples immediately after completing the experiment to samples analyzed after storage at -20°C for 20 or 31 days. Readouts were consistent when performed by different individuals using different reagent stocks (**Figure 2.2f**).

We hypothesized that fluorescent biodistribution would yield different results than QUANT. We formulated the same LNP⁷ with QUANT barcodes that were, or were not, fluorescently tagged with Alexa-647. One hour after intravenously administering 0.5 mg / kg, we isolated the same 13 cell types (**Figure 2.1c**) using FACS and quantified LNP delivery using Alexa-647 MFI or QUANT (**Figure 2.5a**). 87% of the Alexa-647 signal was found in liver cells; the remaining 10 cell types only generated 13% of the total fluorescent signal (**Figure 2.5b-d**). QUANT biodistribution was different; only 56% of the ddPCR signal derived from the liver (**Figure 2.5b-d**). We compared delivery in all 13 cell types and found statistically significant differences in 7 of them (**Figure 2.5e**). In Figure 2E, we normalized delivery to Kupffer cells, which readily clear nanoparticles^{5,6}. Notably, in all cases, fluorescence overestimated liver biodistribution. To exclude the possibility these results were due to a specific timepoint, we performed a pharmacokinetics experiment in 5 cell types: liver endothelial cells, Kupffer cells, hepatocytes, lung endothelial cells, and lung macrophages. We intravenously injected mice with 0.5 mg / kg QUANT barcodes, and sacrificed mice 0.4, 0.75, 1.25, 12, 24, and 36 hours later (**Figure 2.6a**). At the 0.4, 0.75, and 1.25 hour timepoints, fluorescent biodistribution was localized to liver cells; only 1 of 6 non-liver signals (2 cell types, 3 timepoints) were statistically significant compared to untreated mice. At later timepoints, fluorescent biodistribution was not significantly above PBS-treated mice in any cell type. Out 30 potential data points (5 cell types, 6 time points), only 6 generated a fluorescent signal that was statistically significant compared to untreated mice (**Figure 2.6b**). By contrast, QUANT-based biodistribution was observed in all 30 data points (**Fig 3b**). We calculated under the curve (**Figure 2.6c**) and the maximum DNA delivery (**Figure 2.6d**); once again, the results suggested Alexa-647 fluorescence

overestimated delivery to the liver. Finally, we investigated how robust QUANT readouts were across experiments. We compared the absolute ddPCR values from all 5 cell types in the first QUANT biodistribution experiment (**Figure 2.5**) and the pharmacokinetic experiment (**Figure 2.6**) at similar timepoints (1 and 1.25 hours, respectively). ddPCR readouts were reproducible ($R^2=0.98$) between experiments (**Fig 2.6e**). Figures 1-3 demonstrate that QUANT is a sensitive and repeatable method of quantifying nanoparticle biodistribution.

QUANT enabled us to measure LNP delivery with increased sensitivity; we took advantage of this to test the hypothesis Cav1 affects LNP delivery in a cell type-specific manner *in vivo*. To ensure our results were not specific to 1 LNP chemical structure, we exploited a second advantage of QUANT: it can be multiplexed so the distribution of >100 LNPs is analyzed at once. Multiplexed analysis of nanoparticle delivery has been reported by our group^{13,65} and others⁶⁷, but critically, these barcoding systems can only quantify delivery of LNP-1 relative to LNP-2 within the same sample; it cannot quantify absolute delivery. Without the ability to quantify absolute delivery, it is difficult to directly compare readouts (i) between different tissues, (ii) between different mouse models (e.g., WT and Cav1^{-/-}), or (iii) between ddPCR and fluorescence.

We performed 2 high throughput *in vivo* LNP screens. We formulated LNP-1, with chemical structure 1, so it carried QUANT barcode 1; we formulated LNP-N, with chemical structure N, to carry QUANT barcode N (**Figure 2.7a-c**). The 8 nucleotide barcode region on the QUANT DNA sequence - located in the center - can generate 65,536 unique barcodes; we designed 156 that were compatible with one another on Illumina sequencing machines (**Figure 2.8a**). Each barcode has a base distance of 3 or more, which

means every 8 nucleotide barcode sequence is different from all other 8 nucleotide barcode at 3 of the 8 positions (or more). We used microfluidics⁵⁵ to formulate LNPs with QUANT barcodes^{13,65}. We analyzed the hydrodynamic diameter of each LNP individually using dynamic light scattering and pooled LNPs together if they met 2 inclusion criteria: (i) hydrodynamic diameters between 20 and 200 nm, and (ii) an autocorrelation curve with 1 inflection point (**Figure 2.7d, Figure 2.8b**); We also included a naked DNA barcode, which served as a negative control. We selected these LNP criteria and the control based on experience with a different barcoding system¹³. We studied 2 LNP libraries; as expected, the normalized delivery of the naked DNA barcode was lower than the normalized delivery for barcodes carried by LNPs in library 1 (**Figure 2.7e, f**) and library 2 (**Figure 2.8c, d**). Normalized delivery quantifies how well a LNP performs, relative to all other LNPs in a given sample (**Figure 2.7a, Figure 2.8e**). It is analogous to counts per million in RNA-seq²⁹, and can describe nanoparticle biodistribution^{13,65}.

We intravenously administered the LNPs to WT and Cav1^{-/-} mice at a total DNA dose of 0.5 mg / kg and used FACS to isolate 10 cell types 24 hours after administering the LNPs (**Figure 2.8f**). We focused on endothelial cells and macrophages since they exist in every tissue; this allowed us to study cell- and tissue-level effects. In LNP library 1, we formulated 128 LNPs; 111 met our 2 inclusion criteria and were pooled together (**Figure 2.7c,d, Figure 2.8g,h**). Multiple lines of evidence suggested Cav1 influenced nanoparticle delivery in a tissue- and cell-type dependent way. First, the ‘total experimental’ biodistribution – defined as the total ddPCR counts in the 10 tested cell types – was reduced in Cav1^{-/-} mice, relative to WT mice (**Figure 2.9a**). In these pie charts, the area corresponds to total ddPCR counts. It is important to note this pie chart is not equal to the total clearance

for the organ, since we did not measure the clearance in every cell type, and the values are not weighted by the percentage of a given cell type within the organ. We chose not to weight the values since the percentage of each cell type within an organ, for all tested organs, was not available.

The decrease in ddPCR counts was not constant across different tissues; Cav1 exerted tissue-specific changes on LNP delivery. For example, the biodistribution to the liver was predominant in WT mice but was much less so in Cav1^{-/-} mice (**Figure 2.9a**). The decrease in liver delivery was substantial; the total number of ddPCR counts in the liver of (**Figure 2.9b**) Cav1^{-/-} mice decreased by 93%. The Cav1^{-/-} counts in lung and kidney were reduced by 43% and 27%, respectively, relative to WT mice (**Figure 2.9c,d**). We then analyzed this effect at the cellular level in all 3 organs. In the liver, most of the decrease in Cav1^{-/-} barcode readouts were due to decreased Kupffer cell delivery (**Figure 2.9e**). Delivery to hepatic endothelial cells also decreased, but delivery to hepatocytes was not impacted significantly (**Figure 2.9b,e**).

The data above describe the average change in barcode counts for all LNPs. We then quantified how all 111 individual LNPs were affected by Cav1 expression. We multiplied the ddPCR readouts by the normalized delivery, to calculate absolute delivery for each LNP. We then plotted absolute delivery for each LNP in WT and Cav1^{-/-} mice for 3 cell types in the liver (**Figure 2.9f**). Delivery to Kupffer cells in Cav1^{-/-} mice was visibly lower than delivery to Kupffer cells in WT mice, even when plotted on a Log₁₀ scale (**Figure 2.9f**). Delivery to Kupffer cells was affected more than endothelial cells and hepatocytes. Notably, the high throughput analysis of absolute delivery has not been reported before; it is not possible to generate these plots using previous LNP DNA barcoding technologies.

We repeated this experiment using a second LNP library. We rationally designed LNP library 2 to be similar to LNP library 1, with an important distinction: In library 1, LNPs contained the 7C1 lipid, cholesterol, PEG, and the helper lipid 1,2-distearoyl-sn-glycero-3-phosphocholine (DSPC); in library 2, LNPs contained the 7C1 lipid, cholesterol, and PEG. We omitted DSPC to exclude the possibility that the effects we observed in macrophages were due to changes in CD36 expression. CD36 is expressed by macrophages; it acts as a receptor for phosphocholine, which is present in DSPC⁶⁸. Critically, CD36 expression can be modulated by Cav1⁶⁹. We formulated 120 LNPs, of which 115 were stable, pooled, and injected (**Figure 2.8i-k**). Most of the observations we made with LNP library 1 were consistent in LNP library 2. The ‘total experimental’ biodistribution was – once again - reduced in Cav1^{-/-} mice, relative to WT mice (**Figure 2.10a**). There was a pronounced change in delivery to the liver (72% reduction) (**Figure 2.10b**), and very little change in the kidney (**Figure 2.10c**). Unlike library 1, in library 2, delivery to the lung was also reduced (**Figure 2.10d**). When we measured the cell type-specific changes in the liver, we found that Kupffer cell delivery was reduced again, strongly suggesting any effects we observed did not require the phosphocholine group in the LNPs (**Figure 2.10b,e**). Delivery to hepatic endothelial cells and hepatocytes were decreased significantly (**Figure 2.10e**). Finally, we calculated the delivery for all 115 individual LNPs, and were able to visually observe the differences in Kupffer cells more so than hepatic endothelial cells and hepatocytes.

Given the consistent results in Kupffer cells, we investigated whether Cav1 similarly affected pulmonary and renal macrophages (**Figure 2.11a**). The total ddPCR counts in pulmonary macrophages did not change with Cav1 expression; renal macrophage delivery

decreased, but not significantly. When assessing absolute delivery in WT Kupffer cells as well as pulmonary and renal macrophages, we observed that average nanoparticle delivery was ~10-fold higher in Kupffer cells than in lung and renal macrophages (**Figure 2.11b**). To exclude the possibility the Kupffer cell reduction was due to (i) fewer Kupffer cells or (ii) differences in Kupffer cell phenotype in Cav1^{-/-} mice, we measured the (i) number of Kupffer cells / total liver immune cells, and (ii) the expression of CD86 and CD206, 2 markers for Kupffer cell activation in livers of WT and Cav1^{-/-} mice after they were injected with a 1 mg / kg dose of the same previously validated 7C1 LNP we used in our QUANT studies (**Figs. 2,3**). In all previous experiments, we injected 0.5 mg / kg; in this experiment, we injected a 1 mg / kg dose to increase the chance we would observe immune activation. We reasoned this was the most clinically relevant experiment, since all 226 LNPs included the 7C1 compound. The LNPs contained a siRNA that did not target any murine gene (siLuciferase) to minimize the chance gene silencing affected Kupffer cell behavior. We found no differences between number and phenotype of Kupffer cells in WT and Cav1^{-/-} mice (**Figure 2.11c-e**). Taken together, these results suggest that caveolin-mediated endocytosis of nanomedicines by macrophages varies with tissue type.

We also observed that Cav1 exerted cell type-specific effects on endothelial cell delivery. We first quantified the ddPCR counts in different endothelial cell beds in WT mice, and found LNPs were delivered to liver, lung, heart, and kidney endothelial cells with differential efficiency (**Figure 2.12a**). We then calculated the barcode delivery in Cav1^{-/-} mice, and normalized to delivery in WT mice (**Figure 2.12b**). Cav1^{-/-} had a statistically significant impact on barcode delivery in liver, lung, and heart endothelial cells. Interestingly, delivery to kidney endothelial cells was impacted less. We next

measured the individual biodistribution of all 226 LNPs tested in both wild-type and Cav1^{-/-} and found that barcode delivery to endothelial cells was consistently impaired in Cav1^{-/-} mice (**Figure 2.12c-e**).

2.3 Discussion

Here we show that Cav1 affects LNP delivery in a cell type-specific manner *in vivo*. Delivery to Kupffer cells was significantly altered, leading to changes in nanoparticle biodistribution. Interestingly, Kupffer cell delivery was affected more than delivery to lung or kidney macrophages. These results suggest that Caveolin plays a more prominent role in LNP clearance in Kupffer cells, relative to other macrophage populations. These results are important for drug delivery systems, given that macrophages clear administered LNPs. Given that LNPs are lipid-like nanomaterials with compositions that can be similar HDL, LDL, and VLDL, it will be interesting to evaluate whether the observations we made here extend to these ‘natural’ nanoscale carriers^{20,70}. If so, these results could elucidate how cholesterol is trafficked to different tissues.

These results suggest macrophage uptake changes with tissue type. If future studies elucidate the cell signaling pathways that govern these differences, these cell signaling pathways could be manipulated to alter nanoparticle targeting. Although these data were generated with genetically engineered mice devoid of Cav1, future studies will alter delivery by transiently manipulating an endocytosis gene with small molecules or antibodies. Given the fundamental role endocytosis plays in health and disease, it will be critical that any perturbations made to improve drug delivery are transient. Nonetheless,

our results provide a biological rationale for future experiments designed to redirect nanoparticles by manipulating commonly expressed genes.

Independent of the Cav1 results, we believe the discovery of QUANT is an important advance. More specifically, we found that a rationally designed ddPCR-based barcode system can quantify delivery with very high sensitivity. We anticipate future studies further improving the design of QUANT barcodes by incorporating different patterns of chemical modification. Moreover, given that QUANT was able to read out delivery to all tested cell types here, we anticipate it will help scientists identify nanoparticles that target stem cells, immune cells, neurons, and other hard-to-target cell types.

We found that fluorescent biodistribution overestimated delivery to the liver, compared to readouts of the nucleic acid itself. Our results were consistent over several experiments, and echo results generated by scientists studying small molecule delivery⁶². Given that the known mechanisms of nucleic acid degradation⁶³ are different than the mechanisms that degrade fluorophores, we hypothesize the degradation of the nucleic acid is different from the degradation of the fluorophore. Further studies will be required to confirm or disprove this hypothesis. If confirmed, our results will be important, since most LNPs are thought to preferentially target the liver – often based on fluorescent biodistribution assays. These results could have important implications for nanoparticle discovery pipelines.

It is important note the limitations of our work. First, we only used 1 nucleic acid size; changing the size of QUANT barcodes may better model different classes of nucleic acid drugs. Second, toxic or unstable LNPs will not work with QUANT. Nonetheless,

QUANT enables new types of nanoparticle studies that will help elucidate the biological factors that affect LNP targeting and provides proof of principle data that manipulating one gene can be used to retarget nanomedicines.

a

G*A*T*GCTCTCATACGAACCTCGTCNNHWCCTGCTAGTCACGTCCTCATGTCCACCNWNHTGATATTGNWHGTGGTTAGTCGAGCAGAGAC*T*A*G

Red = phosphorothioate linkages (*) act to increase resistance to exonucleases.

Green = Universal primer binding sites allow for amplification from cells/tissues and linkage to next generation sequence adapters

Blue = Probe binding site. This functionality is used in ddPCR

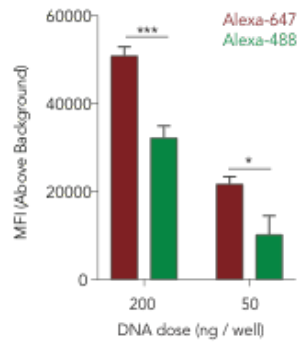
Orange = 8nt Barcode. This 8nt sequence is referenced to identify nanoparticle composition and track nanoparticle distribution.

Light Blue = 4nt primer used to prevent steric blocking of universal forward primer and probe in ddPCR.

Black = Random nucleotide region used to minimize PCR bias.

N= A, T, G, or C; W= A or T; H= A, T, or C.

b



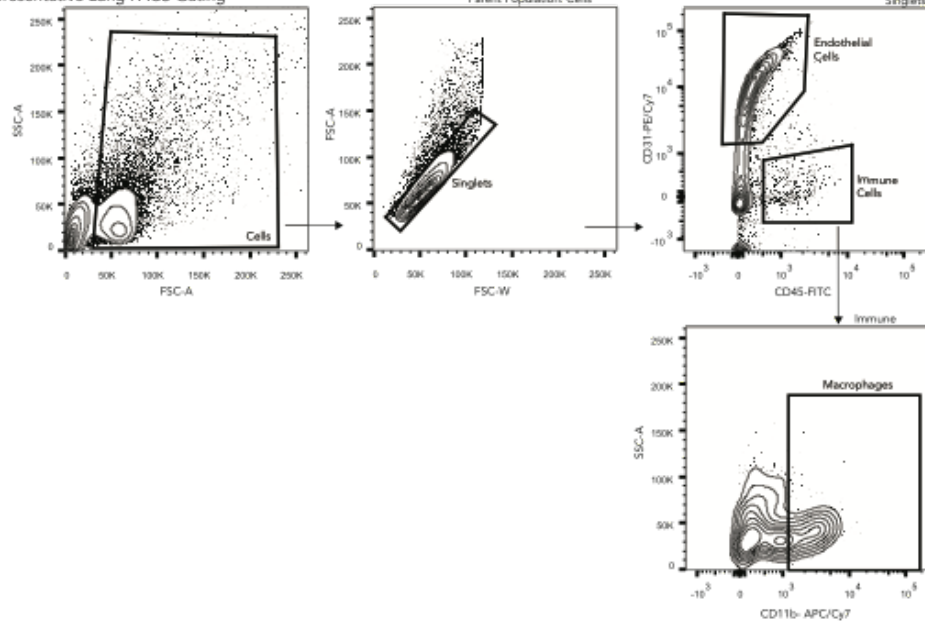
c

Cell Type	FACS Markers	Tissue
B cells	CD3- CD19+	S
T cells	CD19- CD3+	S
Macrophages	CD31- CD45+ CD11b+	L,K
Kupffer Cells	CD31- CD45+ CD68+	v
Endothelial cells	CD31+ CD45-	v,H,L,K
Immune	CD31- CD45+ CD11b-	v,L,K
Hepatocytes	CD31- CD45-	v

Liver, Heart, Lung, Spleen, Kidney

d

Representative Lung FACS Gating



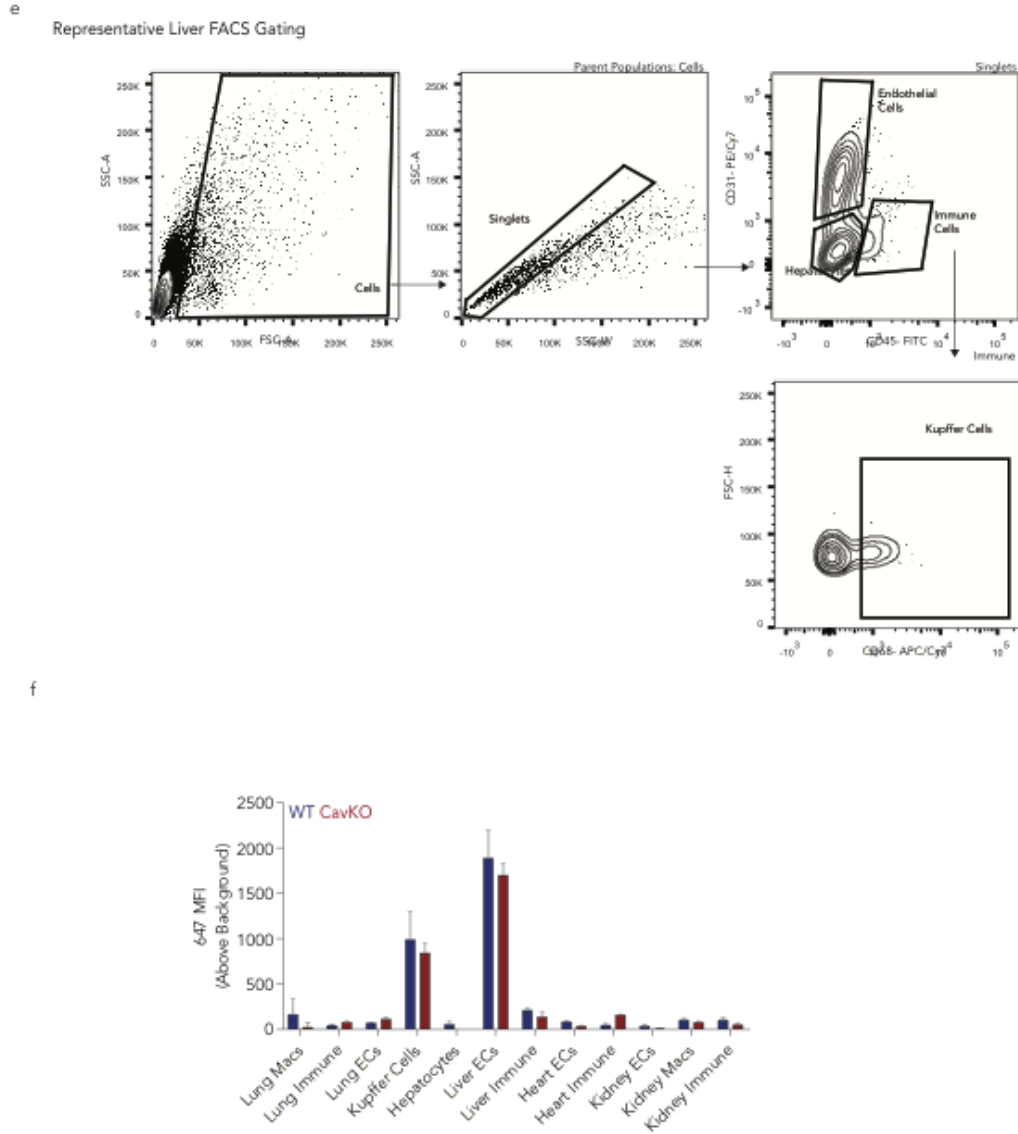


Figure 2.1. (a) QUANT Barcode Design. (b) Comparison of Mean Fluorescent Intensity (MFI) of barcodes conjugated with Alexa-488 and Alexa-647 at 200ng and 50ng per well. * $p < 0.05$, * $p < 0.001$, 2 tailed t-test. (c) Cell types in the liver, heart, lung, spleen, and kidney were sorted based on the following FACS Markers. (d) Representative FACS gating for lung. We isolated endothelial cell ($CD31^+CD45^-$) and macrophages ($CD31^-CD45^+CD11b^+$). (e) Representative FACS gating for liver. We isolated endothelial cells ($CD31^+CD45^-$), Kupffer cells ($CD31^-CD45^+CD68^+$), and Hepatocytes ($CD31^-CD45^-CD68^-$). (f) MFI of barcodes conjugated with Alexa-647 in wild-type and $Cav1^{-/-}$ mice.**

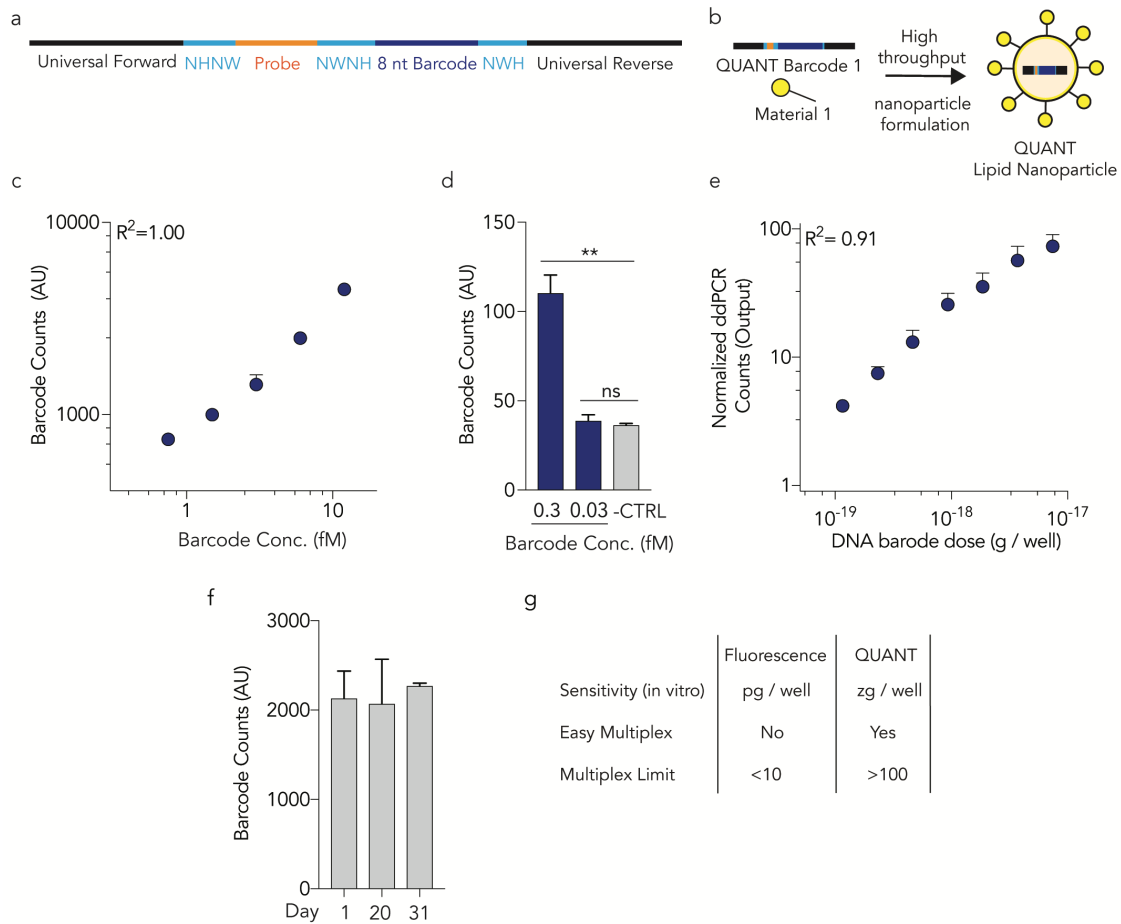
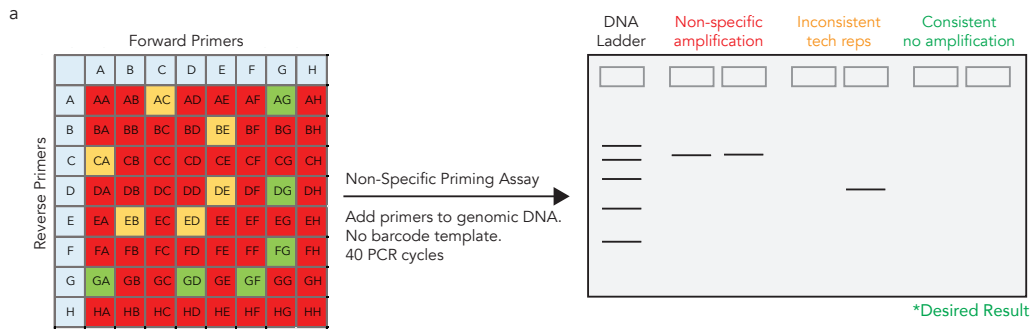
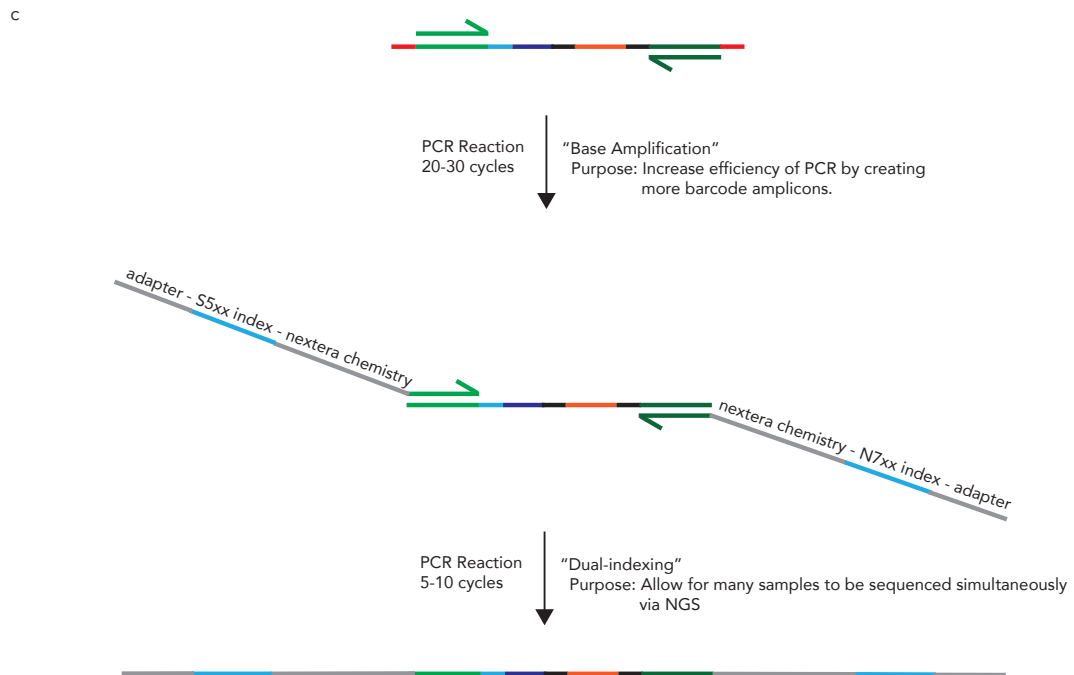


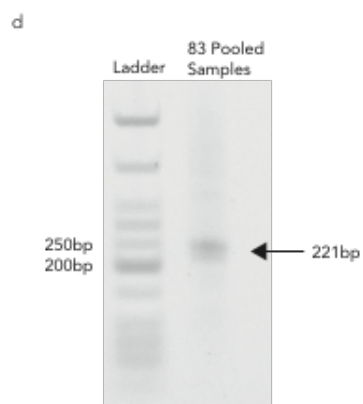
Figure 2.2. QUANT barcodes are rationally designed to provide highly sensitive readouts of nanoparticle delivery. (a) QUANT barcodes contain universal primer sites, an 8 nucleotide barcode region, a probe binding site, and split semi-randomized regions. These designs reduce DNA secondary structure and increase DNA polymerase access. **(b)** Barcodes can be formulated into chemically distinct lipid nanoparticles using high throughput microfluidics. **(c)** Standard curve of QUANT barcodes diluted in TE buffer; **(d)** barcodes can be identified above background at 300 aM concentrations. ****p<0.01, 2 tailed t-test.** **(e)** An *in vitro* standard curve; barcodes were quantified 24 hours after being delivered to cell using Lipofectamine 2000. **(f)** QUANT barcode readouts immediately after DNA was isolated from cells following *in vivo* nanoparticle delivery, or after the samples were stored at -20°C for 20 or 31 days. Each experiment was performed using different stock reagents, demonstrating the repeatability of the assay. **(g)** Comparison of fluorescence and QUANT-based methods of analyzing nanoparticle biodistribution.



b

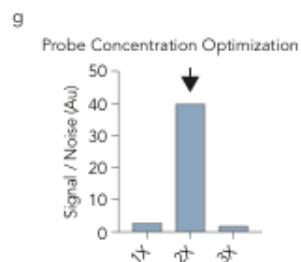
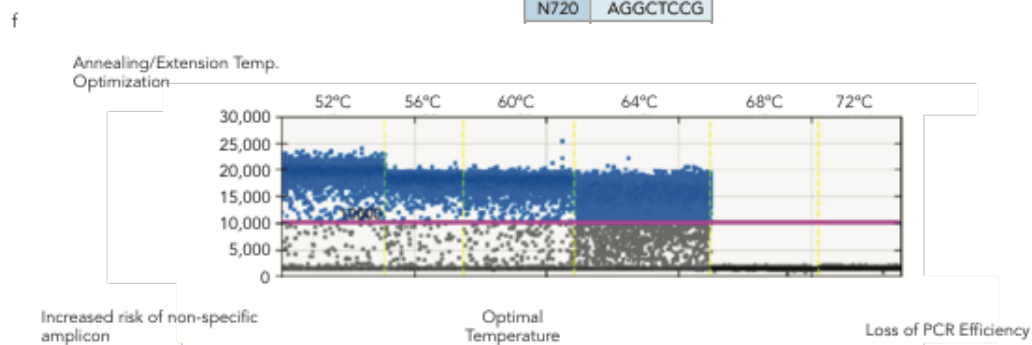
A	GCACGCCTTACGACTCATCT	Forward Primer
B	GCTCAATACTGTTCCACCGC	
C	ACTCACTTCGCATTAGCCGC	
D	GCTCTCATACGAACGCTCC	
E	GCACACGCTCTTCGAATCT	Reverse Primer
F	ATCTCTCGCACTCTCAACGG	
G	GTCTCTGCTCGACTAACCAC	
H	ATCACTCCGCACCGCTTATG	





e

N701	TCGCCTTA	S502	CTCTCTAT
N702	CTAGTACG	S503	TATCCTCT
N703	TTCTGCCT	S505	GTAAGGAG
N704	GCTCAGGA	S506	ACTGCATA
N705	AGGAGTCC	S507	AAGGAGTA
N706	CATGCCTA	S508	CTAAGCCT
N707	GTAGAGAG	S510	CGTCTAAT
N710	CAGCCTCG	S511	TCTCTCCG
N711	TGCCTCTT	S513	TCGACTAG
N712	TCCTCTAC	S515	TTCTAGCT
N714	TCATGAGC	S516	CCTAGAGT
N715	CCTGAGAT	S517	GCGTAAGA
N716	TAGCGAGT		
N718	GTAGCTCC		
N719	TACTACGC		
N720	AGGCTCCG		



h

Scrambled Probe Site: 5'- ACCAACGCCGTATCCGTCTTCCG -3'
Correct Probe Site: 5'- CCTGCTAGTCCACGTCCATGTCCACC -3'

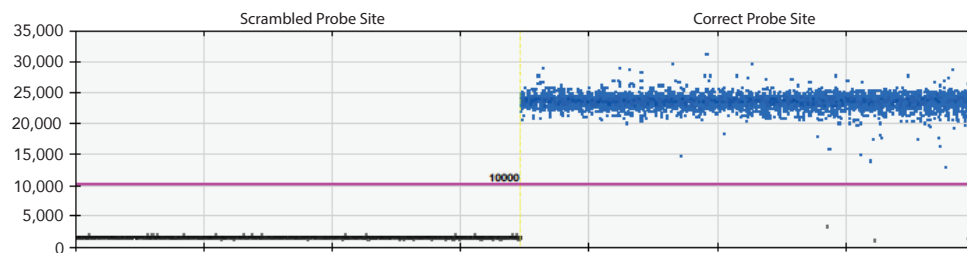


Figure 2.3. A multi-step approach to optimizing the signal generated by ddPCR QUANT barcodes. (a) Primer combinations were tested to avoid non-specific amplification by genomic DNA (gDNA). Different primer pairs were added to mouse and human gDNA without any barcode template. (b) Primers that did not amplify gDNA were selected. (c) A two-step PCR adds Illumina nextera chemistry regions, indices, and Illumina adapters for Illumina sequencing and (d) produces a clear product. (e) Dual indices allow for multiplexed Illumina sequencing. (f) ddPCR was optimized using an annealing temperature of 60°C and (g) probe concentration 2x more than the ddPCR standard protocol concentration. (h) A scrambled probe site was tested to verify the specificity of the probe-based signal.

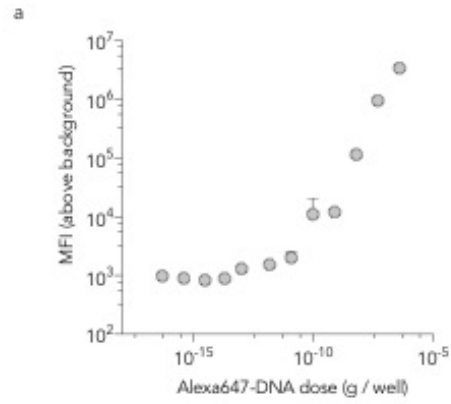


Figure 2.4. (a) Alexa-647 fluorescence 24 hours after fluorescently labeled QUANT barcodes were administered *in vitro* to iMAECs with Lipofectamine 2000 and analyzed with flow cytometry.

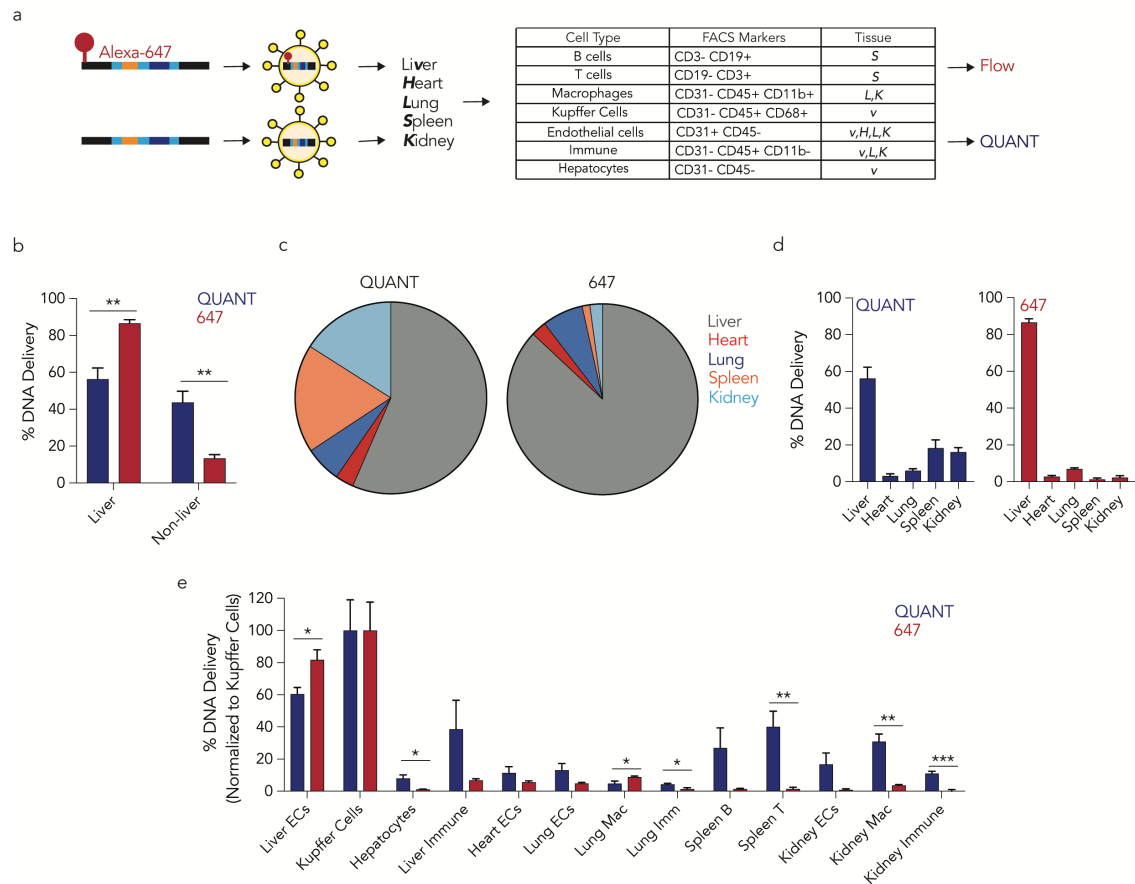


Figure 2.5. A direct comparison of fluorescent- and ddPCR-based biodistribution *in vivo* reveals differences. (a) QUANT barcodes with (or without) a fluorophore were formulated into a LNP and injected intravenously. Five tissues were isolated and barcode delivery to 13 cell types isolated by FACS was measured by QUANT or fluorescence. (b) Cumulative biodistribution measured by QUANT or fluorescence in liver and non-liver cell types. ** $p < 0.01$, 2 tailed t-test. (c,d) Cumulative biodistribution within the 5 tissues examined by QUANT and fluorescence. Fluorescence readouts overestimate liver delivery. (e) Comparison of biodistribution in the 13 cell types examined by QUANT and fluorescence. * $p < 0.05$, ** $p < 0.01$, * $p < 0.001$, 2 tailed t-test. ECs; endothelial cells. Mac; macrophage. Imm; immune.**

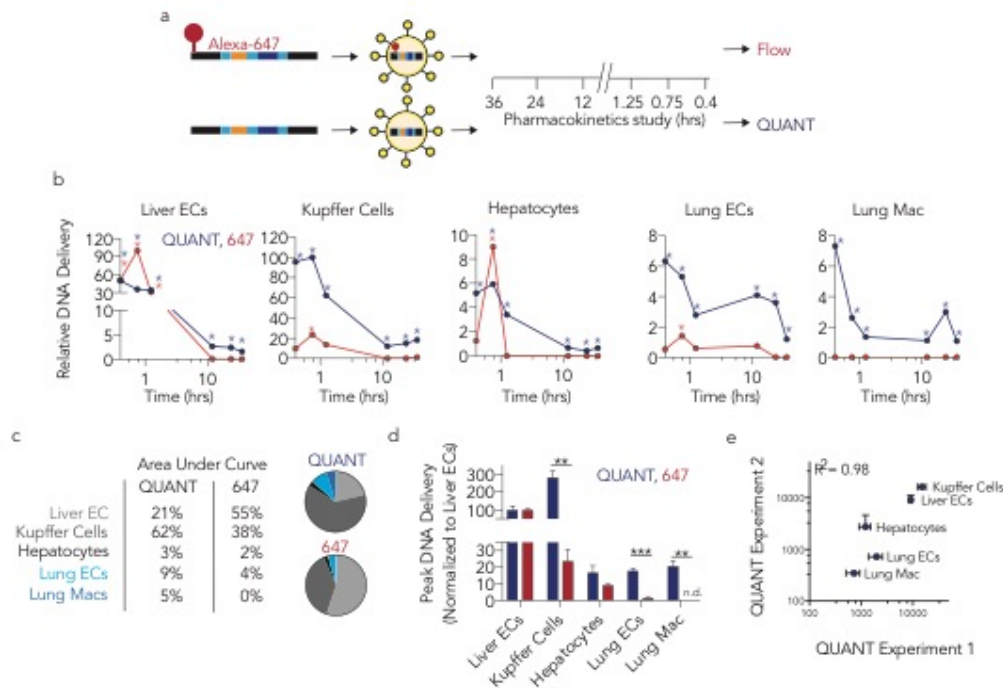


Figure 2.6. QUANT biodistribution is more sensitive than fluorescence *in vivo*. (a) QUANT barcodes with (or without) a fluorophore were formulated into LNPs, injected intravenously, and isolated at different timepoints. Nanoparticle distribution was measured using QUANT or fluorescence. (b) Relative nanoparticle biodistribution (normalized to maximal signal in any cell type) 0.4, 0.75, 1.25, 12, 24, and 36 hours after administration of a LNP carrying 647-QUANT barcode or QUANT barcodes at a dose of 0.5 mg / kg. Asterisk denotes a signal that was significantly different than PBS-treated mice. (c) Comparisons of area under the curve as measured by QUANT or fluorescence. Delivery to the lungs was underestimated by >3 fold by fluorescence. (d) Peak DNA delivery (normalized to liver ECs) as measured by QUANT and fluorescence. No fluorescent signal was detected in lung macrophages. ** $p < 0.01$, *** $p < 0.001$ 2 tailed t-test. (e) R^2 analysis of QUANT absolutely counts from the 1 hour timepoint (Figure 2) and the 1.25 hour timepoint (Figure 3) across two experiments performed on separate days.

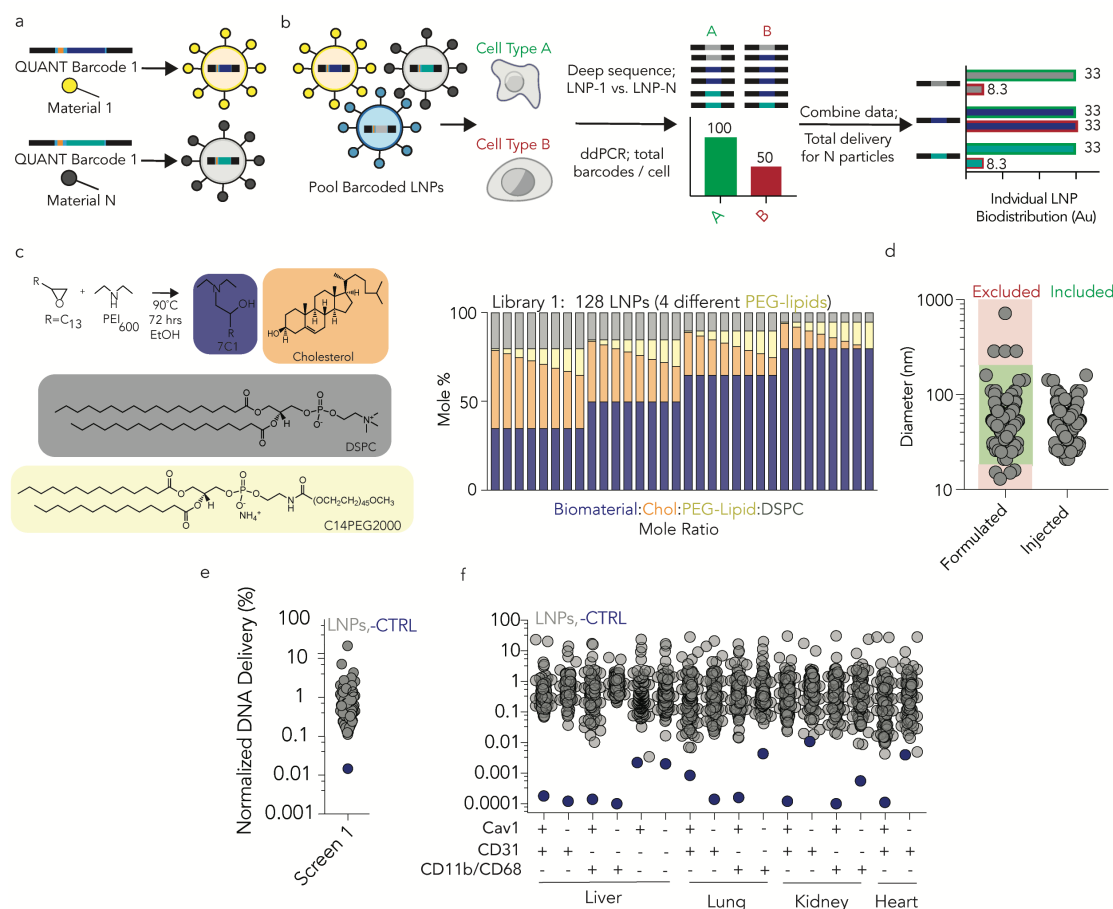
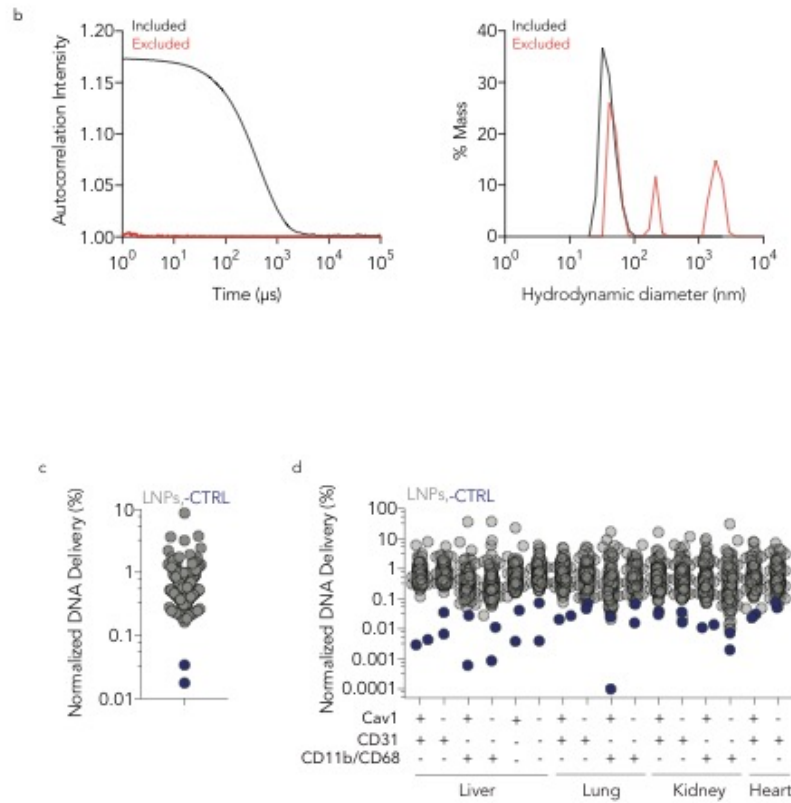


Figure 2.7. QUANT quantifies how over 100 LNPs deliver nucleic acids in wild-type and Cav1^{-/-} mice. (a) Unique QUANT barcodes can be formulated into chemically distinct nanoparticles. (b) QUANT ddPCR readouts can be coupled with deep sequencing to measure absolute delivery mediated by >100 LNPs at once *in vivo*. (c) LNP library 1 was synthesized with the amine 7C1, Cholesterol, DSPC, and PEG compounds at variable molar ratios; 128 different LNPs were formulated for screen 1. (d) The diameter of each LNP in screen 1 was measured individually; stable LNPs, with diameters between 20 and 200 nm were included. (e) The average normalized delivery from all LNPs and the naked barcode (negative control) from screen 1. (f) As expected, the naked barcode – which was the negative control – was delivered less efficiently than barcodes carried by LNPs in every cell type, both in WT mice and Cav1^{-/-} mice.

a

G*A*T*GCTCTCATACGAACTCGTCNNHWCCTGCTAGTCCACGTCCATGTCCACCNWNH-8nt Barcode Seq-NWHGTGGTGTAGTCGAGCAGAGAC*T*A*G

BC #	Seq	BC #	Seq	BC #	Seq	BC #	Seq
1	TGATATTG	40	TCTAACTG	79	ATCAATTG	118	CGCTTAAC
2	GACGCAAT	41	TATGCCCT	80	GGTCGGTC	119	CTGACCGC
3	GCGAGTAT	42	GTAATTGC	81	TTGGATCC	120	TGACCAGG
4	ACCTAATC	43	GTCTCCGT	82	ATTGGTTC	121	CTCATAGG
5	AGGCGCTA	44	TGCATGGT	83	GATGGCCT	122	CCGTAAGC
6	GATCTACC	45	AGTCCGGT	84	TTATAGCA	123	CGAGACGT
7	CTACTGAT	46	TCCTGATG	85	GTCAATCT	124	GACGATAA
8	TGATCTAT	47	ATCGTCTA	86	CGCTCCGG	125	CCGCTGCT
9	ATGAGATG	48	GGACGTCC	87	ACTCAAGT	126	GGTTAGAA
10	GCGAATTC	49	CTACGAGG	88	CCGTCGGG	127	TTATCCGG
11	GATTCCGG	50	CAATCCGT	89	CCGCAGAG	128	AGTAGGTA
12	ATAATATA	51	GGCGCTTG	90	CGGTATCT	129	CGTACTAC
13	AGCATGCG	52	GTCCGTTA	91	TTATTAAT	130	AACTAGCG
14	GATTCAAC	53	GCCTCTCG	92	AGGCTCAT	131	TGCTCCTT
15	TACCTGCT	54	GAGAGTTG	93	TAGTACGT	132	TCGCCAAC
16	GCTAATCG	55	CATAATAG	94	AATATACG	133	CGCGGCTC
17	CTCCTTCG	56	TCTAGAGT	95	CGATGCTT	134	AAGGCGGT
18	ACGCTAGC	57	AAGTCTAG	96	CCAAGATT	135	GTAATGAG
19	GCAGGACT	58	ATTCGAGA	97	TCCATTAT	136	AGATACTA
20	ATTGCTCT	59	CTACCATT	98	AATACCAT	137	GAATCGTC
21	TACGCTCG	60	GTTAGTCA	99	CTGCGACC	138	AGGAAGAG
22	ACGCTCCA	61	ATAGAATC	100	GACTTGAG	139	CAGGTACC
23	CGGTCAAT	62	CTCAACTA	101	CAGAAGCA	140	TAGATAGC
24	CGCCTATT	63	CTTACGTC	102	TCTCTTAA	141	AGAGTAAG
25	TTGCGTTG	64	TGAGTTCG	103	CTGAGCCA	142	TCATTCCG
26	TCCTAAGA	65	ATGGTAGA	104	TCCTGCGC	143	CGGCGTCG
27	CAAGAAGG	66	TCCAGGCG	105	CGAACGCC	144	ATCAAGCA
28	TAGAATTA	67	CTCAGCAT	106	CTGCTCTA	145	TTGGCGTA
29	GGCGCCAA	68	TGCGTATA	107	GCCTACCA	146	CGTCCGCA
30	TAGATCCG	69	AATGCTAC	108	GGATGAAG	147	AGGACCGA
31	CGAGCAGC	70	CGCGAGGC	109	CTATATAC	148	CCTCGATC
32	TAAGATGA	71	GTCGAAGT	110	CGAATATG	149	TATCTGAG
33	AGCTCGGA	72	ACTATCTC	111	ACGCATTA	150	CGGAGTAA
34	TAACCGAA	73	GTCGCCTC	112	GGTAGACC	151	AGAATGAA
35	TATATCTA	74	AGTTACCG	113	CGTTATGC	152	AATCGGTT
36	AAGAGGAT	75	GAGTATAC	114	TCTGCGGA	153	CATCGCCA
37	ACGTCGAA	76	GGCAGTAG	115	CCTTGCAT	154	TATTGACT
38	CATCATTA	77	TGGAGACG	116	ATTATAGT	155	GTAGGCGG
39	TTGCAACT	78	ATTAGGAC	117	CTCGTAAT	156	GTTCTGAT



e

		Raw Counts Lung Endothelial Cells			Raw Counts Kidney Endothelial Cells			
LNP	Barcode	Mouse 1	Mouse 2	Mouse 3	Mouse 1	Mouse 2	Mouse 3	Input
1	GACACAGT	100	80	200	300	200	250	100
2	GCATAACG	50	45	110	100	60	70	120
3	ACAGAGGT	120	105	250	150	90	110	110
Total Counts		270	230	560	550	350	430	330

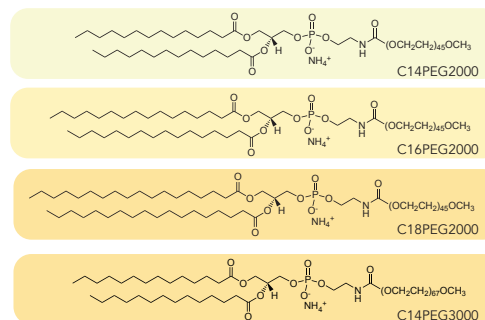
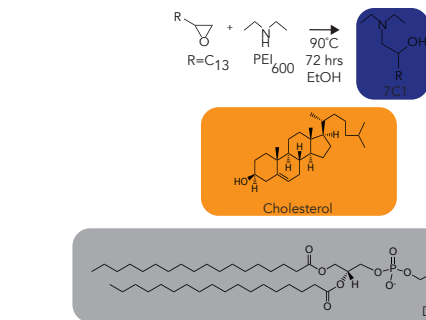
		Normalized Counts Lung ECs (%)			Normalized Counts Kidney ECs (%)			
LNP	Barcode	Mouse 1	Mouse 2	Mouse 3	Mouse 1	Mouse 2	Mouse 3	Input
1	GACACAGT	37	35	36	55	57	58	30
2	GCATAACG	19	20	20	18	17	16	36
3	ACAGAGGT	44	46	45	27	26	26	33
Total (%)		100	100	100	100	100	100	100

		Normalized to Input Counts Lung ECs (%)			Normalized to Input Counts Kidney ECs (%)			
LNP	Barcode	Mouse 1	Mouse 2	Mouse 3	Mouse 1	Mouse 2	Mouse 3	
1	GACACAGT	40	38	39	58	60	61	
2	GCATAACG	17	18	18	16	15	14	
3	ACAGAGGT	44	45	44	26	25	24	
Total (%)		100	100	100	100	100	100	

f

Cell Type	FACS Markers	Tissue
Endothelial cells	CD31+ CD45-	v, <i>H</i> , <i>L</i> , <i>K</i>
Macrophages	CD31-CD45+CD11b+	<i>L</i> , <i>K</i>
Kupffer Cells	CD31- CD45+ CD68+	v
Immune Cells	CD31- CD45+ CD11b-	<i>L</i> , <i>K</i>
Hepatocytes	CD31- CD45- CD68-	v

Liver, *Heart*, *Lung*, *Kidney*



h

Library 1: 128 LNPs (4 PEG-lipids)

[illegible]

Number	Language	Chd Type	MSI Ed.	MSI Name	Licensor	Chd's	MSI %	%	Comment
65	PCI	Chd	CI-BREF	2000	DISC	65	24	10	13
67	PCI	Chd	CI-BREF	2000	DISC	65	22	3	10
68	PCI	Chd	CI-BREF	2000	DISC	65	18	7	12
69	PCI	Chd	CI-BREF	2000	DISC	65	18	7	12
70	PCI	Chd	CI-BREF	2000	DISC	65	14	9	10
72	PCI	Chd	CI-BREF	2000	DISC	65	14	11	10
73	PCI	Chd	CI-BREF	2000	DISC	65	12	13	10
74	PCI	Chd	CI-BREF	2000	DISC	65	10	15	10
75	PCI	Chd	CI-BREF	2000	DISC	80	14	1	10
76	PCI	Chd	CI-BREF	2000	DISC	80	12	3	5
78	PCI	Chd	CI-BREF	2000	DISC	80	10	5	5
79	PCI	Chd	CI-BREF	2000	DISC	80	8	9	5
80	PCI	Chd	CI-BREF	2000	DISC	80	6	9	5
81	PCI	Chd	CI-BREF	2000	DISC	80	6	9	5
82	PCI	Chd	CI-BREF	2000	DISC	80	6	11	5
83	PCI	Chd	CI-BREF	2000	DISC	80	6	13	5
84	PCI	Chd	CI-BREF	2000	DISC	80	6	13	5
85	PCI	Chd	CI-BREF	2000	DISC	80	6	13	5
86	PCI	Chd	CI-BREF	2000	DISC	80	6	13	5
87	PCI	Chd	CI-BREF	2000	DISC	80	6	13	5
88	PCI	Chd	CI-BREF	2000	DISC	80	6	13	5
89	PCI	Chd	CI-BREF	2000	DISC	80	6	13	5
90	PCI	Chd	CI-BREF	2000	DISC	80	6	13	5
91	PCI	Chd	CI-BREF	2000	DISC	80	6	13	5
92	PCI	Chd	CI-BREF	2000	DISC	80	6	13	5
93	PCI	Chd	CI-BREF	2000	DISC	80	6	13	5
94	PCI	Chd	CI-BREF	2000	DISC	80	6	13	5
95	PCI	Chd	CI-BREF	2000	DISC	80	6	13	5
96	PCI	Chd	CI-BREF	2000	DISC	80	6	13	5
97	PCI	Chd	CI-BREF	2000	DISC	80	6	13	5
98	PCI	Chd	CI-BREF	2000	DISC	80	6	13	5
99	PCI	Chd	CI-BREF	2000	DISC	80	6	13	5
100	PCI	Chd	CI-BREF	2000	DISC	80	6	13	5
101	PCI	Chd	CI-BREF	2000	DISC	80	6	13	5
102	PCI	Chd	CI-BREF	2000	DISC	80	6	13	5
103	PCI	Chd	CI-BREF	2000	DISC	80	6	13	5
104	PCI	Chd	CI-BREF	2000	DISC	80	6	13	5
105	PCI	Chd	CI-BREF	2000	DISC	80	6	13	5
106	PCI	Chd	CI-BREF	2000	DISC	80	6	13	5
107	PCI	Chd	CI-BREF	2000	DISC	80	6	13	5
108	PCI	Chd	CI-BREF	2000	DISC	80	6	13	5
109	PCI	Chd	CI-BREF	2000	DISC	80	6	13	5
110	PCI	Chd	CI-BREF	2000	DISC	80	6	13	5
111	PCI	Chd	CI-BREF	2000	DISC	80	6	13	5
112	PCI	Chd	CI-BREF	2000	DISC	80	6	13	5
113	PCI	Chd	CI-BREF	2000	DISC	80	6	13	5
114	PCI	Chd	CI-BREF	2000	DISC	80	6	13	5
115	PCI	Chd	CI-BREF	2000	DISC	80	6	13	5
116	PCI	Chd	CI-BREF	2000	DISC	80	6	13	5
117	PCI	Chd	CI-BREF	2000	DISC	80	6	13	5
118	PCI	Chd	CI-BREF	2000	DISC	80	6	13	5
119	PCI	Chd	CI-BREF	2000	DISC	80	6	13	5
120	PCI	Chd	CI-BREF	2000	DISC	80	6	13	5

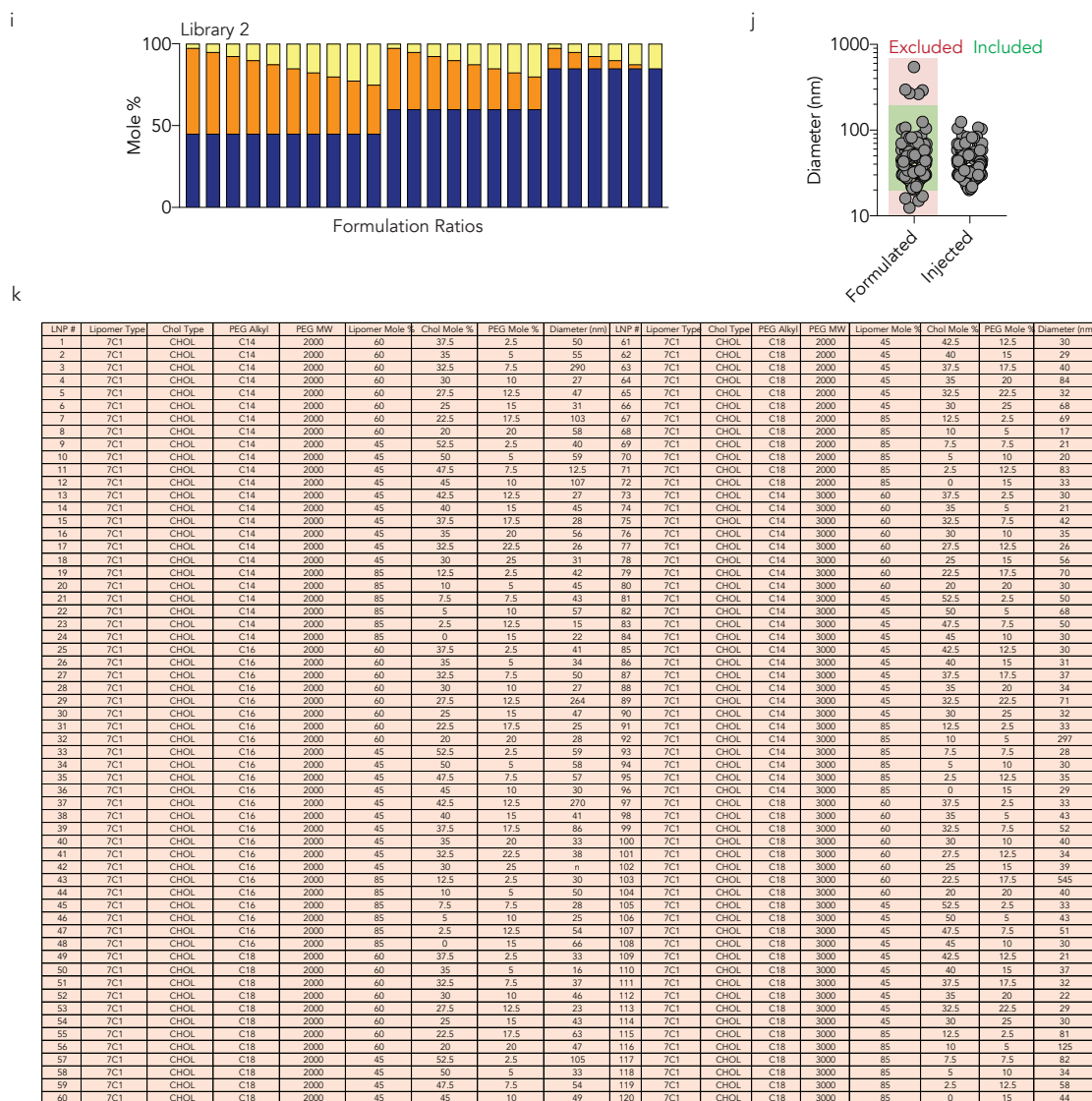


Figure 2.8. (a) 156 8-nucleotide barcode sequences were rationally selected for their ability to be multiplexed on Illumina Miniseq Machines. (b) Using dynamic light scattering (DLS), LNPs were included if they met the following inclusion criteria: autocorrelation curves with 1 inflection point and hydrodynamic diameters between 20 nm and 200 nm. (c) Average normalized delivery of each LNP from library 2. (d) In all samples of library 2, naked barcode – the negative control – was delivered less efficiently than barcodes carried by LNPs, as expected. (e) The following example illustrates how our deep sequencing data was normalized. (f) Cells were sorted on the indicated FACS markers. (g) LNPs libraries for screens 1 and 2 were synthesized with the LNP 7C1, Cholesterol, DSPC, and variable PEG compounds at variable molar

ratios. (h) The formulation ratios and diameter of each LNP for screen 1. (i) Nanoparticle formulation ratios for screen 2; in this screen, we formulated 120 different LNPs. (j) Stable LNPs with diameters between 20 and 200 nm were included. (k) The formulation ratios and diameter of each LNP for screen 2.

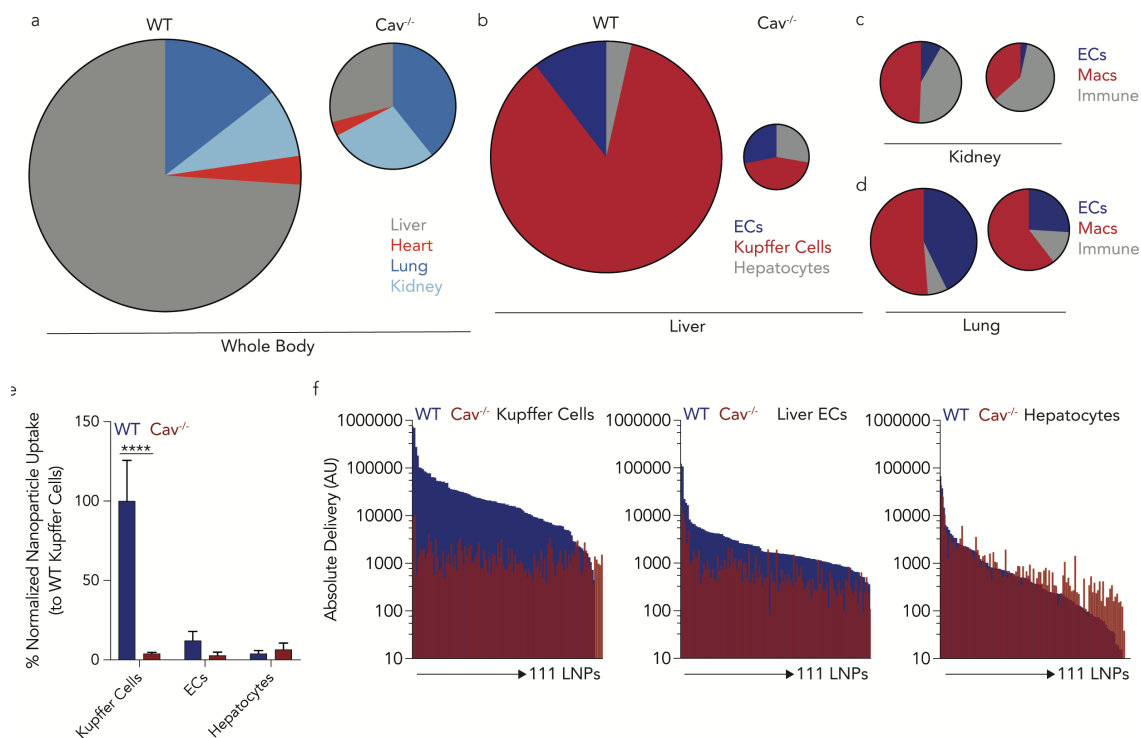


Figure 2.9. High throughput QUANT studies reveal Caveolin1 affects delivery in a tissue- and cell-type dependent manner *in vivo*. (a) The total ddPCR counts in all tested cell types – which are equal to the area of the circle - were used to determine the ‘total experimental’ biodistribution in WT and Cav1^{-/-} mice. (b) The total ddPCR counts were determined in different cell-types from the liver, (c) lung and (d) kidney. Compared to cells isolated from wild-type mice, ddPCR counts from Cav1^{-/-} decreased, with the most dramatic effect in the liver. (e) Within the liver cell-types, normalized library 1 nanoparticle biodistribution demonstrates that Kupffer cells in Cav1^{-/-} uptake less nucleic acids when compared to Kupffer cells from wild-type mice. ****p<0.0001 2-way ANOVA. (f) Combined sequencing data and ddPCR results shows the absolute delivery of 111 nanoparticles for each LNP in the liver in wild type (blue) and Cav1^{-/-} (red) mice, from library 1, in Kupffer cells, liver endothelial cells, and hepatocytes.

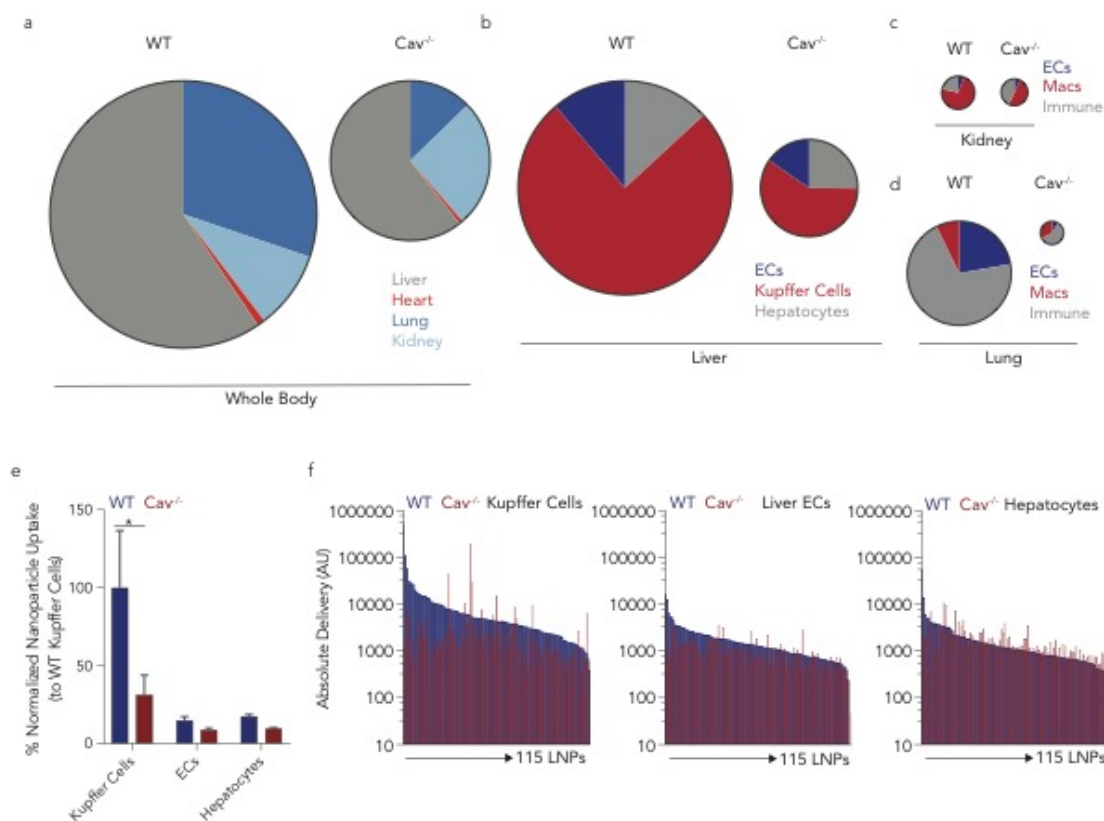


Figure 2.10. (a) Total ddPCR barcode counts for library 2 – equal to the area of the circle - were used to determine the overall biodistribution from the LNP screens previously described across multiple organs from wild-type and *Cav1*^{-/-} mice. **(b)** The total ddPCR counts were determined in different cell-types from the liver, **(c)** lung and **(d)** kidney. **(e)** Within the liver cell-types, normalized nanoparticle biodistribution demonstrates that Kupffer cells in *Cav1*^{-/-} uptake less nucleic acids when compared to Kupffer cells from wild-type mice. **p*<0.05 2-way ANOVA. **(f)** Combined sequencing data and ddPCR results shows the absolute delivery of 115 nanoparticles for each LNP in the liver in wild type (blue) and *Cav1*^{-/-} (red) mice, from library 1, in Kupffer cells, liver endothelial cells, and hepatocytes.

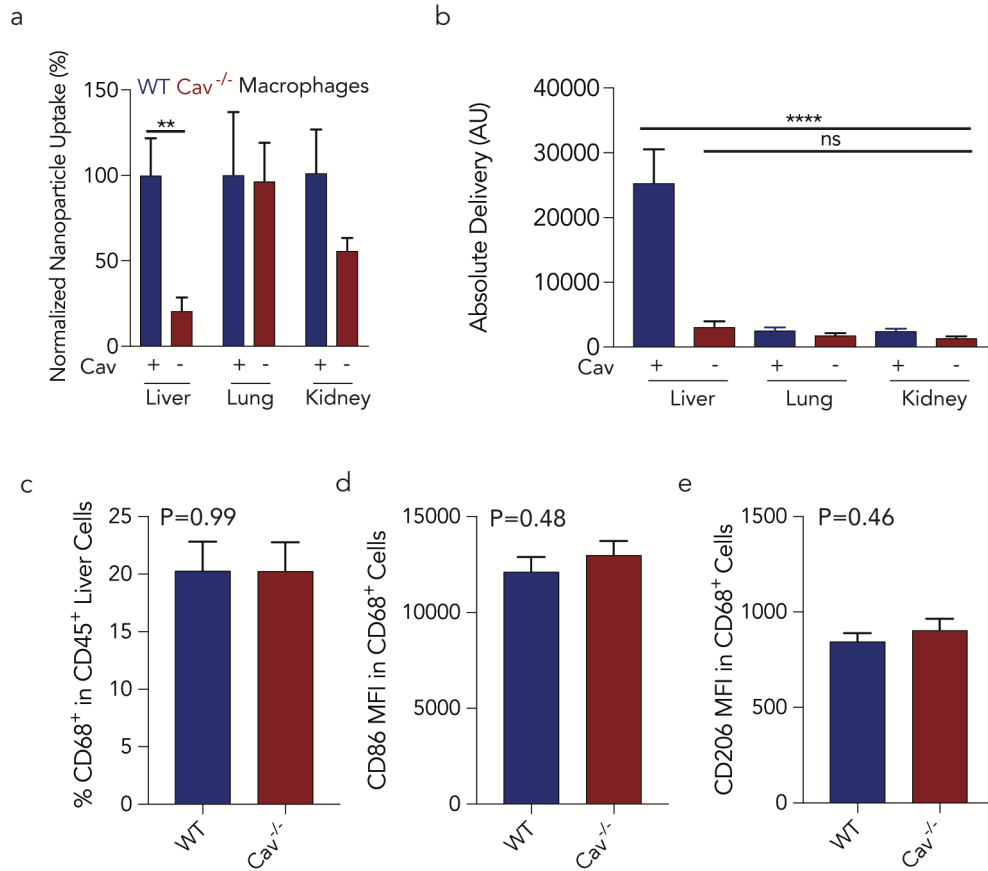


Figure 2.11. Caveolin1 significantly affects delivery in Kupffer cells *in vivo*. (a) Nanoparticle biodistribution in macrophages were isolated from multiple tissues from wild-type and Cav1^{-/-} mice. Lung and kidney macrophages were less impacted by the loss of caveolin. **p<0.01 1-tailed t-test. (b) Absolute nanoparticle delivery to wild-type and Cav1^{-/-} macrophages in the liver, lung, and kidney. Kupffer cells were statistically significant compared to other macrophage beds. ****p<0.0001 One-way ANOVA. (c) The percentage of Kupffer cells (CD68⁺ CD45⁺) within the immune cell population (CD45⁺) in wild-type and Cav1^{-/-} mice were similar. Phenotype variations in wild-type and Cav1^{-/-} Kupffer (CD68⁺ CD45⁺) cells populations were determined by MFI of (d) CD86 and (e) CD206.

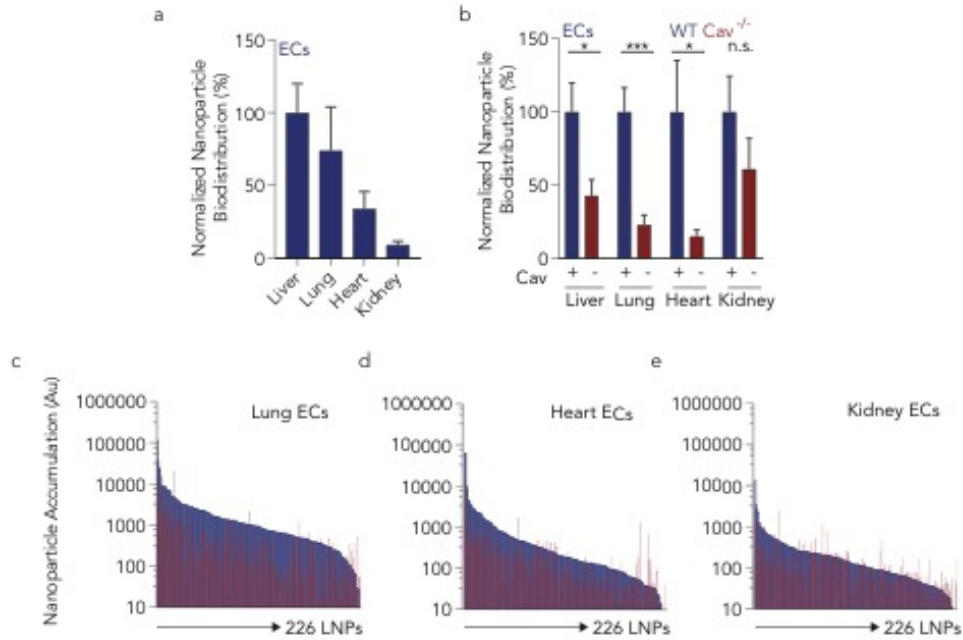


Figure 2.12. (a) Normalized nanoparticle biodistribution across two screens (226 LNPs) in liver, lung, heart, and kidney endothelial cells. (b) QUANT demonstrates that endothelial cells in Cav^{1-/-} uptake less QUANT barcodes than endothelial cells in wild-type mice. * $p < 0.05$, * $p < 0.001$ 1 tailed t-test. (c) Combined sequencing data and ddPCR results for each LNP in lung endothelial cells in wild type (blue) and Cav^{1-/-} (red) mice from screen 1 and screen 2 in lung, (d) heart, and (e) kidney endothelial cells.**

2.4 Methods & Materials

Nanoparticle Formulation. Nanoparticles were formulated using a microfluidic device as previously described²⁶. Briefly, nucleic acids (DNA barcodes) were diluted in 10mM citrate buffer (Teknova) while lipid-amine compounds, alkyl tailed PEG, cholesterol, and helper lipids were diluted in ethanol. All PEGs, cholesterol, and helper lipids were purchased from Avanti Lipids. Citrate and ethanol phases were combined in a microfluidic device by syringes (Hamilton Company) at a flow rate of 600 $\mu\text{L}/\text{min}$ and 200 $\mu\text{L}/\text{min}$, respectively.

DNA Barcoding. Each chemically distinct LNP was formulated to carry its own unique DNA barcode (**Figure 2.2a-b**). For example, LNP1 carried DNA barcode 1, while the chemically distinct LNP2 carried DNA barcode 2. 91 nucleotide long single stranded DNA sequences were purchased as ultramers from Integrated DNA Technologies (IDT). Three nucleotides on the 5' and 3' ends were modified with phosphorothioates to reduce exonuclease degradation and improve DNA barcode stability. To ensure equal amplification of each sequence, the we included universal forward and reverse primer regions on all barcodes. Each barcode was distinguished using a unique 8nt sequence. An 8nt sequence can generate over 4^8 (65,536) distinct barcodes. We used 156 distinct 8nt sequences designed by to prevent sequence bleaching on the Illumina MiniSeqTM sequencing machine. A 26nt probe was purchased from IDT with 5' FAM as the fluorophore, while internal Zen and 3' Iowa Black FQ were used as quenchers. Fluorescent barcode was purchased from IDT with AlexaFluor647 or AlexaFluor488 conjugated to the 5' end.

In Vitro L2K. Immortalized Mouse Aortic Endothelial Cells (IMAECs) were seeded at 10,000 cells per well in a 96-well plate. 24 hours after seeding, QUANT barcodes or Alexa-647-barcodes were transfected using Lipofectamine 2000. 24 hours after transfection, DNA was isolated from cells treated with QUANT barcodes and fluorescent barcodes were measured using a DN Accuri C6 flow cytometer.

Nanoparticle Characterization. LNP hydrodynamic diameter was measured using high throughput dynamic light scattering (DLS) (DynaPro Plate Reader II, Wyatt). LNPs were diluted in sterile 1X PBS to a concentration of $\sim 0.06 \mu\text{g/mL}$, and analyzed. To avoid using unstable LNPs, and to enable sterile purification using a $0.22 \mu\text{m}$ filter, LNPs were included only if they met the criteria of monodisperse population with diameter between 20 and 200nm. Particles that met these criteria were dialyzed with 1X phosphate buffered saline (PBS, Invitrogen), and were sterile filtered with a $0.22 \mu\text{m}$ filter.

Animal Experiments. All animal experiments were performed in accordance with the Georgia Institute of Technology IACUC. C57BL/6J (#000664) and Caveolin1^{-/-} (#007083) mice were purchased from The Jackson Laboratory and used between 5-8 weeks of age. In all *in vitro* and *in vivo* experiments, we used N=3-5 group. Mice were injected intravenously via the lateral tail vein. The nanoparticle concentration was determined using NanoDrop (Thermo Scientific). For *in vivo* nanoparticle screens, mice were administered at a dose of 0.5 mg/kg.

Cell Isolation & Staining. Cells were isolated 24 (for screens) or 96 (for *in vivo* gene editing) hours after injection with LNPs unless otherwise noted. Mice were perfused with 20 mL of 1X PBS through the right atrium. Tissues were finely cut, and then placed in a

digestive enzyme solution with Collagenase Type I (Sigma Aldrich), Collagenase XI (Sigma Aldrich) and Hyaluronidase (Sigma Aldrich) at 37 °C at 550 rpm for 45 minutes. The digestive enzyme for heart and spleen included Collagenase IV^{7,56,58}. Cell suspension was filtered through 70µm mesh and red blood cells were lysed. Cells were stained to identify specific cell populations and sorted using the BD FACS Fusion and BD FACS Aria IIIu cell sorters in the Georgia Institute of Technology Cellular Analysis Core. For *in vitro* flow cytometry experiments, a BD Accuri C6 was used in the Georgia Institute of Technology Cellular Analysis Core. The antibody clones used were: anti-CD31 (390, BioLegend), anti-CD45.2 (104, BioLegend), anti-CD68 (FA-11, Biolegend), and anti-CD11b (M1/70, Biolegend). Representative flow gates are located in Supplementary Figure 1.

ddPCR. The QX200™ Droplet Digital™ PCR System (Bio-Rad) was used to prep and analyze all ddPCR results. All PCR samples were prepared with 10µL ddPCR with ddPCR™ Supermix for Probes (Bio-Rad), 1µL of primer and probe mix (solution of 10µM of target probe and 20µM of Reverse/Forward Primers), 1µL of template/TE buffer, and 8µL water. 20µL of each reaction and 70µL of Droplet Generation Oil for Probes (Bio-Rad) were loaded into DG8™ Cartridges and covered with DG8™ Gaskets. Cartridges were placed in the QX200™ Droplet Generator to create water-oil emulsion droplets. Cycle conditions for PCR were as follows: 1 cycle of 95° for 10 minutes, followed by 40 cycles of 94°C for 30 seconds, 60°C for 1 minute, and 1 cycle of 95°C for 10 minutes. Plates were stored at 4°C until run on the QX200™ Droplet Digital™ PCR System. For each biological rep, 3 technical repetitions were completed. In all cases, technical reps were

averaged. Technical reps were only excluded if they saturated the detection or showed inconsistent positive event amplitudes.

PCR Amplification for Illumina Sequencing. All samples were amplified and prepared for sequencing using a two-step, nested PCR protocol (**Figure 1.1**). More specifically, 2 μ L of primers (10 uM for Base Reverse/Forward) were added to 5 μ L of Kapa HiFi 2X master mix, and 3 μ L template DNA/water. This first PCR reaction was ran for 20-30 cycles. The second PCR, to add Nextera XT chemistry, indices, and i5/i7 adapter regions was ran for 5-10 cycles and used the product from ‘PCR 1’ as template. Dual-indexed samples were ran on a 2% agarose gel to ensure that PCR reaction occurred before being pooled and purified using BluePippin (Sage Science).

Deep Sequencing. Illumina sequencing was conducted in Georgia Institute of Technology’s Molecular Evolution core. Runs were performed on an Illumina Miniseq. Primers were designed based on Nextera XT adapter sequences.

Barcode Sequencing Normalization. Counts for each particle, per cell type, were normalized to the barcoded LNP mixture applied to cells or injected into the mouse.

Endothelial RNA interference. C57BL/6J and Caveolin1^{-/-} mice were injected with 7C1 carrying 1 mg/kg siCTRL (siLuc) (AxoLabs). In all cases, siRNAs were chemically modified at the 2’ position to increase stability and negate immunostimulation. 72 hours after injection, tissues were isolated and protein expression was determined via flow cytometry. ICAM2 MFI in siLuc-treated mice (for each background) was normalized to 100 percent.

Data Analysis & Statistics. Sequencing results were processed using a custom R script to extract raw barcode counts for each tissue. These raw counts were then normalized with an R script prior for further analysis. Statistical analysis was done using GraphPad Prism 7; more specifically, 1-tail T-test, Paired 2-tail T-test, or One-way ANOVAs were used where appropriate. Data is plotted as mean \pm standard error mean unless otherwise stated.

Data Access. The data, analyses, and scripts used to generate all figures in the paper are available upon request to james.dahlman@bme.gatech.edu.

2.5 References

1. Pasi, K.J., *et al.* Targeting of Antithrombin in Hemophilia A or B with RNAi Therapy. *N Engl J Med* **377**, 819-828 (2017).
2. Adams, D., *et al.* Patisiran, an RNAi Therapeutic, for Hereditary Transthyretin Amyloidosis. *N Engl J Med* **379**, 11-21 (2018).
3. Coelho, T., *et al.* Safety and efficacy of RNAi therapy for transthyretin amyloidosis. *N Engl J Med* **369**, 819-829 (2013).
4. Lorenzer, C., Dirin, M., Winkler, A.M., Baumann, V. & Winkler, J. Going beyond the liver: progress and challenges of targeted delivery of siRNA therapeutics. *J Control Release* **203**, 1-15 (2015).
5. Tsoi, K.M., *et al.* Mechanism of hard-nanomaterial clearance by the liver. *Nat Mater* **15**, 1212-1221 (2016).
6. Zhang, Y.N., Poon, W., Tavares, A.J., McGilvray, I.D. & Chan, W.C.W. Nanoparticle-liver interactions: Cellular uptake and hepatobiliary elimination. *J Control Release* **240**, 332-348 (2016).
7. Dahlman, J.E., *et al.* In vivo endothelial siRNA delivery using polymeric nanoparticles with low molecular weight. *Nat Nano* **9**, 648-655 (2014).
8. Hao, J., *et al.* Rapid Synthesis of a Lipocationic Polyester Library via Ring-Opening Polymerization of Functional Valerolactones for Efficacious siRNA Delivery. *J Am Chem Soc* **29**, 9206-9209 (2015).
9. Dong, Y., *et al.* Lipopeptide nanoparticles for potent and selective siRNA delivery in rodents and nonhuman primates. *Proceedings of the National Academy of Sciences of the United States of America* **111**, 3955-3960 (2014).
10. Siegwart, D.J., *et al.* Combinatorial synthesis of chemically diverse core-shell nanoparticles for intracellular delivery. *Proceedings of the National Academy of Sciences of the United States of America* **108**, 12996-13001 (2011).
11. Love, K.T., *et al.* Lipid-like materials for low-dose, in vivo gene silencing. *Proceedings of the National Academy of Sciences of the United States of America* **107**, 1864-1869 (2010).
12. Akinc, A., *et al.* A combinatorial library of lipid-like materials for delivery of RNAi therapeutics. *Nat Biotechnol* **26**, 561-569 (2008).

13. Paunovska, K., *et al.* A Direct Comparison of in Vitro and in Vivo Nucleic Acid Delivery Mediated by Hundreds of Nanoparticles Reveals a Weak Correlation. *Nano Lett* **18**, 2148-2157 (2018).
14. Patel, S., *et al.* Boosting Intracellular Delivery of Lipid Nanoparticle-Encapsulated mRNA. *Nano Lett* **17**, 5711-5718 (2017).
15. Sahay, G., *et al.* Efficiency of siRNA delivery by lipid nanoparticles is limited by endocytic recycling. *Nat Biotechnol* **31**, 653-658 (2013).
16. Wittrup, A., *et al.* Visualizing lipid-formulated siRNA release from endosomes and target gene knockdown. *Nat Biotechnol* (2015).
17. Gilleron, J., *et al.* Image-based analysis of lipid nanoparticle-mediated siRNA delivery, intracellular trafficking and endosomal escape. *Nat Biotechnol* **31**, 638-646 (2013).
18. Bertrand, N., *et al.* Mechanistic understanding of in vivo protein corona formation on polymeric nanoparticles and impact on pharmacokinetics. *Nature communications* **8**, 777 (2017).
19. Akinc, A., *et al.* Targeted delivery of RNAi therapeutics with endogenous and exogenous ligand-based mechanisms. *Mol Ther* **18**, 1357-1364 (2010).
20. Paunovska, K., Sago, C.D., Lokugamage, M., Bryksin, A.V. & Dahlman, J.E. Analyzing 2,000 in vivo data points reveals that cholesterol structure affects nanoparticle delivery. *In press, ACS Nano* (2018).
21. Willoughby, J.L.S., *et al.* Evaluation of GalNAc-siRNA Conjugate Activity in Pre-clinical Animal Models with Reduced Asialoglycoprotein Receptor Expression. *Mol Ther* **26**, 105-114 (2018).
22. Wang, M. & Thanou, M. Targeting nanoparticles to cancer. *Pharmacological research* **62**, 90-99 (2010).
23. Ostergaard, M.E., *et al.* Efficient Synthesis and Biological Evaluation of 5'-GalNAc Conjugated Antisense Oligonucleotides. *Bioconjug Chem* (2015).
24. El-Sayed, I.H., Huang, X. & El-Sayed, M.A. Selective laser photo-thermal therapy of epithelial carcinoma using anti-EGFR antibody conjugated gold nanoparticles. *Cancer letters* **239**, 129-135 (2006).
25. Stevens, P.J., Sekido, M. & Lee, R.J. A folate receptor-targeted lipid nanoparticle formulation for a lipophilic paclitaxel prodrug. *Pharmaceutical research* **21**, 2153-2157 (2004).

26. Davis, M.E., *et al.* Evidence of RNAi in humans from systemically administered siRNA via targeted nanoparticles. *Nature* **464**, 1067-1070 (2010).
27. Kheirilomoom, A., *et al.* Multifunctional Nanoparticles Facilitate Molecular Targeting and miRNA Delivery to Inhibit Atherosclerosis in ApoE(-/-) Mice. *ACS nano* **9**, 8885-8897 (2015).
28. Muro, S., *et al.* Control of endothelial targeting and intracellular delivery of therapeutic enzymes by modulating the size and shape of ICAM-1-targeted carriers. *Mol Ther* **16**, 1450-1458 (2008).
29. Conesa, A., *et al.* A survey of best practices for RNA-seq data analysis. *Genome biology* **17**, 13 (2016).
30. Lee, M.N., *et al.* Common genetic variants modulate pathogen-sensing responses in human dendritic cells. *Science* **343**, 1246980 (2014).
31. Vanlandewijck, M., *et al.* A molecular atlas of cell types and zonation in the brain vasculature. *Nature* **554**, 475-480 (2018).
32. Zeisel, A., *et al.* Brain structure. Cell types in the mouse cortex and hippocampus revealed by single-cell RNA-seq. *Science* **347**, 1138-1142 (2015).
33. Rozenblatt-Rosen, O., Stubbington, M.J.T., Regev, A. & Teichmann, S.A. The Human Cell Atlas: from vision to reality. *Nature* **550**, 451-453 (2017).
34. Collinet, C., *et al.* Systems survey of endocytosis by multiparametric image analysis. *Nature* **464**, 243-249 (2010).
35. Sigismund, S., *et al.* Endocytosis and signaling: cell logistics shape the eukaryotic cell plan. *Physiological reviews* **92**, 273-366 (2012).
36. Palm, W. & Thompson, C.B. Nutrient acquisition strategies of mammalian cells. *Nature* **546**, 234-242 (2017).
37. Doherty, G.J. & McMahon, H.T. Mechanisms of endocytosis. *Annu Rev Biochem* **78**, 857-902 (2009).
38. Voigt, J., Christensen, J. & Shastri, V.P. Differential uptake of nanoparticles by endothelial cells through polyelectrolytes with affinity for caveolae. *Proceedings of the National Academy of Sciences of the United States of America* **111**, 2942-2947 (2014).
39. Shamay, Y., *et al.* Quantitative self-assembly prediction yields targeted nanomedicines. *Nat Mater* **17**, 361-368 (2018).

40. Cheng, Z., *et al.* Hypoxia Activates Src and Promotes Endocytosis Which Decreases MMP-2 Activity and Aggravates Renal Interstitial Fibrosis. *International journal of molecular sciences* **19**(2018).
41. Shihata, W.A., Putra, M.R.A. & Chin-Dusting, J.P.F. Is There a Potential Therapeutic Role for Caveolin-1 in Fibrosis? *Frontiers in pharmacology* **8**, 567 (2017).
42. Gvaramia, D., Blaauboer, M.E., Hanemaaijer, R. & Everts, V. Role of caveolin-1 in fibrotic diseases. *Matrix biology : journal of the International Society for Matrix Biology* **32**, 307-315 (2013).
43. Yokomori, H., *et al.* Increases in endothelial caveolin-1 and caveolins correlate with cirrhosis progression. *Micron (Oxford, England : 1993)* **76**, 52-61 (2015).
44. Maniatis, N.A., Chernaya, O., Shinin, V. & Minshall, R.D. Caveolins and lung function. *Advances in experimental medicine and biology* **729**, 157-179 (2012).
45. Sotgia, F., *et al.* Understanding the Warburg effect and the prognostic value of stromal caveolin-1 as a marker of a lethal tumor microenvironment. *Breast cancer research : BCR* **13**, 213 (2011).
46. Witkiewicz, A.K., *et al.* An absence of stromal caveolin-1 expression predicts early tumor recurrence and poor clinical outcome in human breast cancers. *Am J Pathol* **174**, 2023-2034 (2009).
47. Yang, G., Truong, L.D., Wheeler, T.M. & Thompson, T.C. Caveolin-1 expression in clinically confined human prostate cancer: a novel prognostic marker. *Cancer Res* **59**, 5719-5723 (1999).
48. Wiechen, K., *et al.* Down-regulation of caveolin-1, a candidate tumor suppressor gene, in sarcomas. *Am J Pathol* **158**, 833-839 (2001).
49. Gaudreault, S.B., Dea, D. & Poirier, J. Increased caveolin-1 expression in Alzheimer's disease brain. *Neurobiology of aging* **25**, 753-759 (2004).
50. Kassan, A., *et al.* Caveolin-1 regulation of disrupted-in-schizophrenia-1 as a potential therapeutic target for schizophrenia. *Journal of neurophysiology* **117**, 436-444 (2017).
51. Chand, S., *et al.* Caveolin-1 single-nucleotide polymorphism and arterial stiffness in non-dialysis chronic kidney disease. *Nephrology, dialysis, transplantation : official publication of the European Dialysis and Transplant Association - European Renal Association* **31**, 1140-1144 (2016).

52. Tourkina, E., *et al.* Altered monocyte and fibrocyte phenotype and function in scleroderma interstitial lung disease: reversal by caveolin-1 scaffolding domain peptide. *Fibrogenesis & tissue repair* **4**, 15 (2011).
53. Del Galdo, F., Lisanti, M.P. & Jimenez, S.A. Caveolin-1, transforming growth factor-beta receptor internalization, and the pathogenesis of systemic sclerosis. *Current opinion in rheumatology* **20**, 713-719 (2008).
54. Zhang, Y., *et al.* Purification and Characterization of Progenitor and Mature Human Astrocytes Reveals Transcriptional and Functional Differences with Mouse. *Neuron* **89**, 37-53 (2016).
55. Chen, D., *et al.* Rapid discovery of potent siRNA-containing lipid nanoparticles enabled by controlled microfluidic formulation. *J Am Chem Soc* **134**, 6948-6951 (2012).
56. Sager, H.B., *et al.* RNAi targeting multiple cell adhesion molecules reduces immune cell recruitment and vascular inflammation after myocardial infarction. *Science translational medicine* **8**, 342ra380-342ra380 (2016).
57. Yun, S., *et al.* Interaction between integrin alpha5 and PDE4D regulates endothelial inflammatory signalling. *Nat Cell Biol* (2016).
58. Sager, H.B., *et al.* Proliferation and Recruitment Contribute to Myocardial Macrophage Expansion in Chronic Heart Failure. *Circ Res* **119**, 853-864 (2016).
59. White, K., *et al.* Genetic and hypoxic alterations of the microRNA-210-ISCU1/2 axis promote iron-sulfur deficiency and pulmonary hypertension. *EMBO Mol Med* **7**, 695-713 (2015).
60. Platt, R.J., *et al.* CRISPR-Cas9 knockin mice for genome editing and cancer modeling. *Cell* **159**, 440-455 (2014).
61. Sahay, G., Alakhova, D.Y. & Kabanov, A.V. Endocytosis of nanomedicines. *J Control Release* **145**, 182-195 (2010).
62. Meng, F., Wang, J., Ping, Q. & Yeo, Y. Quantitative Assessment of Nanoparticle Biodistribution by Fluorescence Imaging, Revisited. *ACS nano* (2018).
63. Yang, W. Nucleases: diversity of structure, function and mechanism. *Quarterly reviews of biophysics* **44**, 1-93 (2011).
64. Hindson, C.M., *et al.* Absolute quantification by droplet digital PCR versus analog real-time PCR. *Nat Methods* **10**, 1003-1005 (2013).

65. Dahlman, J.E., *et al.* Barcoded nanoparticles for high throughput in vivo discovery of targeted therapeutics. *Proceedings of the National Academy of Sciences of the United States of America* **114**, 2060-2065 (2017).
66. Ni, C.W., Kumar, S., Ankeny, C.J. & Jo, H. Development of immortalized mouse aortic endothelial cell lines. *Vascular cell* **6**, 7 (2014).
67. Yaari, Z., *et al.* Theranostic barcoded nanoparticles for personalized cancer medicine. *Nature communications* **7**, 13325 (2016).
68. Podrez, E.A., *et al.* Identification of a novel family of oxidized phospholipids that serve as ligands for the macrophage scavenger receptor CD36. *J Biol Chem* **277**, 38503-38516 (2002).
69. Mattern, H.M., Raikar, L.S. & Hardin, C.D. The effect of caveolin-1 (Cav-1) on fatty acid uptake and CD36 localization and lipotoxicity in vascular smooth muscle (VSM) cells. *International journal of physiology, pathophysiology and pharmacology* **1**, 1-14 (2009).
70. Kuai, R., Li, D., Chen, Y.E., Moon, J.J. & Schwendeman, A. High-Density Lipoproteins (HDL) – Nature’s Multi-Functional Nanoparticles. *ACS nano* **10**, 3015-3041 (2016).

CHAPTER 3. FAST IDENTIFICATION OF NANOPARTICLE DELIVERY

The work presented here is an excerpt from Sago, CD, Lokugamage, MP, Paunovska, K, Vanover, DA, Monaco, CM, Shah, NN, Gamboa Castro, M, Anderson, SE, Rudoltz, TG, Lando, GN, Tiwari, P, Kirschman, JL, Willett, N, Jang, Y, Santangelo, PJ, Bryksin, AV, Dahlman, JE (2018). “A high throughput *in vivo* screen of functional mRNA delivery identifies nanoparticles for endothelial cell gene editing.” Proceedings of the National Academy of Science.

3.1 Background

A lipid nanoparticle (LNP) siRNA therapy targeted to hepatocytes (1, 2) has been approved by the FDA. This advance is exciting, but its long-term implications are tempered by the fact that clinical LNP therapies have targeted hepatocytes (when administered systemically) (1, 3) and muscle (when administered locally) (4). In mice, nanoparticles have delivered Cas9 mRNA and ribonucleoproteins via systemic or local injection (5-12). Systemically administered Cas9 delivery to non-liver tissues remains a challenge. When LNPs are administered systemically, they display an affinity for the liver; this is thought to be driven by natural physiological advantages including slow blood flow (13, 14) and discontinuous vasculature in hepatic sinusoids (15). One additional reason most LNPs target the liver may be the process by which they are selected. LNPs are screened *in vitro* before a few LNPs are tested *in vivo*. *In vitro* LNP delivery can predict *in vivo* LNP delivery to hepatocytes (16), but *in vitro* nanoparticle can be a poor predictor of *in vivo* delivery to endothelial cells and macrophages (17). Moreover, LNP siRNA delivery is often tested *in vivo* using the FVII assay, which predicts hepatocyte delivery; this assay is enhanced by its ease, as well as the fact that validated, potent siRNA targeting FVII is available (18, 19).

It is possible that LNPs target hepatocytes in part because established assays select for hepatocyte delivery.

We reasoned that measuring hundreds of distinct LNPs *in vivo* would provide the best chance of identifying nanoparticles that deliver mRNA to new cell types. Using DNA barcodes (17, 20-22), we previously quantified how >350 LNPs distributed *in vivo*. However, biodistribution is necessary, but not sufficient, for functional RNA delivery. Over 96% of RNA delivered into the endosome of a target cell can be degraded (23, 24), and cell type-specific changes in endosomal escape are not understood (25). It is not possible to predict functional delivery using biodistribution. As a result, a high throughput method to quantify functional, cytosolic delivery of mRNA *in vivo* could accelerate the discovery of clinically relevant LNPs.

An ideal system would (i) enable scientists to test many LNPs simultaneously, (ii) utilize commonly available animal models, (iii) rely on a robust signal, and (iv) measure functional RNA delivery to any combinations of cell types *in vivo*. Measuring delivery to ‘on-target’ cells and ‘off-target cells’ would enable iterative screens to improve LNP specificity. We designed a system named Fast Identification of Nanoparticle Delivery (FIND) that meets these criteria. FIND measures cytosolic mRNA delivery by >100 LNPs *in vivo* to any combination of cell types. We quantified how >250 LNPs functionally delivered mRNA to multiple cell types *in vivo* and identified 2 novel formulations that deliver RNA to endothelial beds. FIND is the first system that facilitates high throughput screens of functional mRNA delivery and may identify LNPs with novel tropisms.

3.2 Results

FIND combined rationally designed DNA barcodes and the Cre-Lox system to generate a multiplexed readout of functional mRNA delivery. FIND is distinct from previous barcoding systems we developed, which measure biodistribution (**Figure 3.1a**). Using high throughput microfluidics (26), we co-formulated LNPs with Cre mRNA and a unique DNA barcode. LNP-1, with chemical structure 1, carried DNA barcode 1 and Cre mRNA; LNP-N, with chemical structure N, carried DNA barcode N and Cre mRNA (**Figure 3.1a-c**). We characterized the size and stability of each LNP using dynamic light scattering (DLS), and discarded LNPs that did not meet 2 criteria: (i) diameters between 20 and 200 nm, and (ii) an autocorrelation curve with 1 inflection point (**Figure 3.2A**). LNPs that met these criteria were pooled together and administered to Lox-Stop-Lox-tdTomato (Ai14) mice (27). Ai14 cells fluoresce if Cre mRNA is translated into Cre protein, which then translocates to the nucleus and edits target DNA. We isolated tdTomato⁺ cells with fluorescence activated cell sorting (FACS), and deep sequenced the cells to identify LNPs that delivered mRNA. We reasoned the co-delivery of mRNA and a 56-nucleotide single stranded DNA (ssDNA) could approximate the co-delivery of a mRNA encoding a nuclease and guide RNA (28-30). After sequencing tdTomato⁺ cells (**Figure 3.1c**), we ranked LNPs by calculating the ‘normalized delivery’ of each barcode. Normalized delivery is analogous to counts per million in RNA-seq data (**Figure 3.1d**, **Figure 3.2B**). We used barcodes we previously described and validated with a number of control experiments (**Figure 3.2C-E**) (17, 20, 21).

We characterized FIND using *in vitro* and *in vivo* experiments. First, we cultured HEK.293 cells that expressed LoxP-GFP-Stop-LoxP-RFP (LGSL-RFP) under a CMV

promoter (**Figure 3.1b**). These cells became RFP⁺ 72 hours after treatment with Cre mRNA carried by Lipofectamine 2000 (L2K), but not with naked Cre mRNA, which served as the negative control (**Figure 3.1e, Figure 3.2F**). The number of RFP⁺ cells after L2K treatment increased with dose and time, up to 3 days (**Figure 3.2G**). We then co-formulated L2K with Cre mRNA and an Alexa647-labeled DNA barcode. After 24 hours, 62, 36, 2, and 0% of the cells were 647⁺RFP⁻, 647⁺RFP⁺, 647⁻RFP⁻, and 647⁻RFP⁺ positive, respectively. This indicates that biodistribution is required, but not sufficient for functional cytosolic delivery, as we expected (**Figure 3.1f**). Untreated cells – used to control for autofluorescence – were 647⁻RFP⁻ (**Figure 3.1f, Figure 3.2H**).

We then formulated 54 chemically distinct LNPs (**Figure 3.2I,J**) carrying Cre mRNA and a unique DNA barcode. We administered the LNPs to LGSL-RFP cells with mRNA doses of 10, 100, or 1000 ng, and a mRNA: DNA barcode mass ratio of 10: 1. We observed a dose-dependent increase in RFP⁺ cells, with over 80% of the cells RFP⁺ 3 days after the 1000 ng transfection (**Figure 3.1g**). We sequenced barcodes at all 3 doses, reasoning that barcode delivery at the lowest dose (4% RFP⁺ cells) would predict delivery at the middle dose (20% RFP⁺ cells); we observed a strong correlation ($R^2 > 0.9$) between normalized delivery at 10 ng and 100 ng doses, suggesting this was the case (**Figure 3.1h**). As a control, we sequenced cells treated with 1000 ng mRNA; in this case, the system was saturated (>80% of the cells were RFP⁺). As expected, the correlation between 1000 ng and either 10 or 100 ng was weaker (**Figure 3.2K**) than the correlation between the 2 lower doses; importantly, these data indicate that FIND can become saturated as the percent of RFP⁺ increases. Varying the dose by the potency of the nanoparticles pooled may be critical. We then evaluated whether the number of RFP⁺ cells decreased after pre-treatment

with chlorpromazine, genistein, or ethylisopropyl amiloride (EIPA), which inhibit clathrin-, caveolin-, and macropinocytosis-mediated endocytosis, respectively. Compared to control cells that were not treated with inhibitors, RFP⁺ cells decreased by 40-60%, recapitulating results previously obtained with individual LNPs (24, 31) (**Figure 3.1i**). Taken together, these results led us to conclude that FIND could analyze mRNA delivery *in vitro*.

We investigated whether FIND could identify nanoparticles that deliver mRNA *in vivo* (**Figure 3.3a,b**). We formulated 112 LNPs, varying 4 chemical traits that influence LNP delivery *in vitro*: the lipid-amine compound, the molar amount of PEG, the structure of PEG, and the molar amount of cholesterol (**Figure 3.3c Figure 3.4A,B**). Seventy-one LNPs met our 2 criteria for inclusion and were pooled (**Figure 3.3d**). Naked DNA barcode, which should not be delivered as efficiently as DNA barcodes in LNPs, was included as a negative control. We intravenously injected the pooled LNPs and naked barcode into Ai14 mice at a 1.5 mg/kg total mRNA dose (0.021 mg / kg / particle). Three days later, we isolated tdTomato⁺ lung and kidney endothelial cells (tdTomato⁺CD31⁺CD45⁻). Separately, we injected 1.0 mg/kg total mRNA into mice intramuscularly, and isolated immune (tdTomato⁺CD45⁺) and non-immune (tdTomato⁺CD45⁻) cells from muscle. We gated on PBS-injected Ai14 mice for intravenously injected mice and the contralateral limb for intramuscular administration. It was important to gate on untreated Ai14 mice instead of C57BL/6J mice; gating on C57BL/6J mice could lead to inflated values of tdTomato⁺ cells (**Figure 3.4C**). Separately, we administered the same LNPs to LGSL-RFP cells *in vitro*. Several lines of evidence suggested the data were robust. In all routes of administration, the naked barcode was delivered less efficiently than every LNP (**Figure**

3.3e). Second, 7C1-based LNPs, which we previously optimized for *in vivo* RNA delivery (32), were enriched in the top 20% LNPs, compared to the other 6 lipid-amine compounds. (**Figure 3.4D,E**) Finally, we reasoned that the route of administration would affect delivery; Euclidean clustering, a common bioinformatics technique (33) that compares how similar / dissimilar groups are to one another, and can be used to study nanoparticles *in vivo* (17, 20), separated intravenous, intramuscular, and *in vitro* delivery into three distinct clusters, as expected (**Figure 3.3f**).

We formulated a second LNP library to study how PEG, cholesterol, and helper lipids (e.g. DOPE) influence delivery to cells *in vivo*. We focused on 7C1-based LNPs, since 7C1 was enriched in the first screen. We varied the PEG molar amount, as well as the alkyl length on the PEG-lipid (**Figure 3.4F**). Seventy-eight out of 108 LNPs met our 2 criteria for inclusion; we intravenously administered the pool to the mice at a total mRNA dose of 1.5 mg/kg. Three days later, we sequenced barcodes from tdTomato⁺ lung and kidney endothelial cells. LNPs containing C₁₄ alkyl PEG were enriched in lung endothelial cells whereas LNPs containing C₁₈ alkyl PEG were enriched in kidney endothelial cells (**Figure 3.4G,H**). To validate the relationship between lung delivery, kidney delivery, and PEG structure, we formulated a third LNP library. We formulated 158 LNPs designed to improve lung delivery relative to kidney delivery by only using C₁₄ alkyl tail PEG varying helper lipid composition (**Figure 3.4I**). We found 3.75x more lung endothelial cells were tdTomato⁺ than kidney endothelial cells, a ratio that was significantly higher than the second screen (**Figure 3.4J**), as expected. Consistent with previous results (17, 20), we did not observe a relationship between LNP size and delivery to endothelial cells between the range of 20 to 200 nm (**Figure 3.4K**). The poor performance of the naked barcode,

enrichment of 7C1, fact that unbiased clustering separated the 3 routes of administration, and the PEG data convinced us FIND was capable of quantifying delivery *in vivo*.

After completing these *in vitro* and *in vivo* validation experiments, we selected 2 LNPs (named 7C2 and 7C3) for more thorough characterization (**Figure 3.5a,b, Figure 3.6A,B**). 7C2 was formulated with 7C1 : Cholesterol : C14-PEG2000 : 18:1 Lyso PC at a molar ratio of 50: 23.5: 6.5: 20. 7C3 was formulated with 7C1 : Cholesterol : C14-PEG2000 : DOPE at a molar ratio of 60: 10: 25: 5. 7C2 and 7C3 formed stable LNPs with average diameters between 50 and 80 nm when formulated with siRNA, sgRNA, or mRNA (**Figure 3.6C,D**). The *in vitro* endocytosis and functional Cre mRNA delivery of both LNPs in LGSL-RFP cells decreased by at least 40% when cells were pre-treated with Chlorpromazine and Genistein, relative to cells that were not treated with inhibitors. EIPA impacted LNP uptake but did not significantly decrease functional delivery *in vitro* (**Figure 3.6E-H**). These results suggest 7C2 and 7C3 are endocytosed *in vitro* via several pathways. To study biodistribution, 7C2 and 7C3 were formulated with a Cy5.5-conjugated DNA barcode and intravenously injected into separate mice at a dose of 0.75 mg/kg DNA. Three hours later – a timepoint that is sufficiently long for LNPs to be cleared from the blood (34) - Cy5.5 *ex vivo* fluorescence, normalized by tissue weight, was highest in the spleen, kidney, and liver, suggesting 7C2 and 7C3 distributed to these tissues (**Figure 3.5c, Figure 3.6I**).

We tested whether 7C2 and 7C3 functionally delivered siRNA, sgRNA, and mRNA, which are all clinically relevant. We performed our individual LNP proof of concept experiments with nucleic acids targeting ICAM-2. We chose this target for three reasons. First, ICAM-2 is related to a number of inflammatory diseases (35, 36). Second, ICAM-2

expression is robust on endothelial cells. Third, there is a well validated monoclonal antibody to ICAM-2, which allows us to quantify protein expression robustly using FACS.

First, we formulated the LNPs to carry siRNA targeting ICAM-2. Three days after intravenously injecting mice with PBS, 2.0 mg/kg siGFP (a higher dose was used to test tolerability), or 1.0 mg/kg siICAM-2, we quantified ICAM-2 protein mean fluorescent intensity (MFI) in lung, kidney, and splenic endothelial cells using flow cytometry (32, 37). Both siRNAs were previously validated and chemically modified to reduce immunostimulation and promote on-target mRNA degradation (32, 37) (**Figure 3.6J**). ICAM-2 MFI was constant in PBS- and siGFP-treated mice but decreased by 60% in lung endothelial cells isolated from mice injected with siICAM-2. 7C2-mediated delivery of siRNA reduced ICAM-2 expression in lung endothelial cells more than splenic endothelial cells, whereas 7C3 silencing was more robust in splenic endothelial cells (**Figure 3.5d**, **Figure 3.6K**). Compared to PBS-treated mice, mice injected with 2.0 mg/kg siGFP did not show any weight loss, or changes in organ weight (**Figure 3.6L-N**).

We then quantified 7C2- and 7C3-mediated sgRNA delivery. We co-formulated 2 sgRNAs that were chemically modified at the 5' and 3' termini (38), and injected each at a dose of 0.75 mg/kg into mice that constitutively express SpCas9 (39) (**Figure 3.6O**). After 3 injections, ICAM-2 MFI decreased by up to 90%, 75%, and 59% in lung, spleen, and kidney endothelial cells, respectively for 7C2 (**Figure 3.5e**). To confirm protein silencing was mediated by gene editing, we measured (40) ICAM-2 insertions and deletions (indels) in lung, spleen, and kidney endothelial cells, and found between 30 and 70% editing per locus, leading to overall ICAM-2 indel percentages of 135%, 95%, and 123% indel, respectively for 7C2 (**Figure 3.5f,g**, **Figure 3.6P,Q**). In these experiments, we

utilized 2 sgRNAs per gene; thus, the total indel percentage was 200% (100% per site). Compared to PBS mice, mice treated with LNPs did not lose weight (**Figure 3.6R,S**). Based on these experiments, we concluded that 7C2 potentially delivered small RNAs to pulmonary endothelial cells *in vivo*.

In our siRNA and sgRNA experiments, 7C2 outperformed 7C3, and potentially delivered RNAs to pulmonary endothelial cells. We then investigated whether the same observations were true for the delivery of large RNAs (mRNA). We formulated 7C2 and 7C3 to carry Cre mRNA and injected the LNPs into separate mice at a dose of 1.5 mg / kg mRNA (**Figure 3.7a**). Three days later, we isolated tdTomato⁺ immune cells and endothelial cells from the spleen, kidney, heart, lung, and liver, as well as hepatocytes. We made 2 interesting observations. First, contrasting the small RNA delivery experiments, 7C3 outperformed 7C2. Second, splenic endothelial cells were targeted efficiently (**Figure 3.7b**). Notably, relative to splenic endothelial cells, very few immune cells and hepatocytes were tdTomato⁺ (**Figure 3.6T,U**). Given this degree of specificity has not been reported to date, we repeated the experiment using 34 Ai14 mice over the course of several months. 7C3 delivered Cre mRNA to splenic endothelial cells in every experiment (**Figure 3.7c**). However, we did observe batch-to-batch variability with respect to hepatocyte targeting (**Figure 3.7c,d**). In 22 of the 34 mice, a low percentage of hepatocytes were tdTomato⁺ (<13%); in 12 of the 34 mice, we observed high percentages of tdTomato⁺ cells. Averaging data from all 34 mice, the number of tdTomato⁺ splenic endothelial cells (43%) was 2.2x higher than the number of tdTomato⁺ hepatocytes (20%) (**Figure 3.7d**). Splenic endothelial cell delivery was also dose dependent (**Figure 3.6V**). The variable delivery to hepatocytes was unlikely to be driven by toxicity; throughout our studies, we injected 34 mice with

7C3, and did not observe changes in mouse weight or obvious signs of toxicity (**Figure 3.6W**). We were unable to identify the source of batch variability; however we hypothesize it is driven by the polymeric backbone of 7C3, and the resulting heterogeneous chemical structure. Our data strongly suggest that future FIND screens should focus on compounds with defined chemical structures, which may be less likely to exhibit biological heterogeneity. The data also demonstrate that 7C3 can efficiently deliver mRNA to splenic endothelial cells *in vivo*. Importantly, the 7C2 and 7C3 formulations both included the lipomer 7C1 but had variable molar compositions of helper lipids (18:1 Lyso PC and DOPE), which distinguished them chemically from previously described endothelial-targeting nanoparticles. The differences in delivery between 7C2 and 7C3 provide interesting preliminary evidence that suggests changing the composition of helper lipids added to a given ionizable amine can alter tropism. The compositions and efficacy of 7C2 and 7C3 are included in Figure 3.8.

Given the difference between small and large RNA delivery, we quantified how LNPs co-delivered CRISPR-Cas9 mRNA and sgRNA. We formulated Cas9 mRNA and 2 guides targeting ICAM-2 into LNPs at a 3:1 mass ratio and injected a 2.0 mg/kg total intravenously on day 0 and 2. On day 7, we isolated endothelial cells from the spleen, lung, kidney, and liver, as well as hepatocytes (**Figure 3.9A**). Splenic endothelial cell editing mediated by 7C3 was more robust than editing in hepatocytes (**Figure 3.9B**). Mice injected with 7C2 and 7C3 did not lose weight, as compared to PBS-treated mice (**Figure 3.9C**). These studies were also conducted with sgRNAs that were chemically modified at the 5' and 3' termini (38); during the course of the experiments, 2 groups demonstrated that heavily modified sgRNAs improved *in vivo* editing (7, 8). We re-designed sgICAM2b with

‘enhanced’ modifications (8) (referred to as e-sgICAM2) (**Figure 3.9D**) and formulated 7C3 to carry Cas9 mRNA and e-sgICAM2. Given that e-sgICAM2 was more likely to resist degradation *in vivo* (8), we hypothesized that the optimal mass ratio of Cas9 mRNA:sgRNA would decrease from 3:1, which is the optimized ratio with minimally stabilized sgRNAs. To test this, we formulated 7C3 with Cas9 mRNA:e-sgRNA ratios of 5:1, 3:1, and 1:1, keeping the total injected dose constant at 2.0 mg / kg. After injecting mice intravenously with 2.0 mg / kg total RNA (Cas9 mRNA + sgRNA) on day 0 and 2, we isolated splenic endothelial cells and hepatocytes using FACS on day 7. We observed gene editing in splenic endothelial cells and hepatocytes at all mRNA to sgRNA ratios, with an average of 20% editing in the 1:1 mass ratio group (**Figure 3.7e,f**). As expected, the lower Cas9 mRNA:e-sgRNA mass ratio led to increased editing. Once again, mice injected with 7C3 did not lose weight compared to PBS-treated controls (**Figure 3.9E**). This is the first demonstration of systemic Cas9-mediated editing of endothelial cells in wildtype mice. These data demonstrate that systemically administered nanoparticles can edit endothelial cells, and that the ideal Cas9: sgRNA ratio will depend on the relative stability of the 2 molecules.

3.3 Discussion

FIND is the first high throughput method to quantify functional mRNA delivery mediated by LNPs. The distinction between biodistribution and functional delivery is significant; >96% of delivered RNA does not escape the endosome (23, 24), and endosomal escape may vary with cell type or disease state (41), making it hard to predict functional delivery using biodistribution. Notably, Cre mRNA must be translated in the cytoplasm, translocate into the nucleus, and edit target DNA. The similarity between these steps the

steps required for nuclease-mediated gene editing is 1 reason we selected a Cre-based FIND system. We also chose the Cre-lox system because Ai14 mice are well validated and commonly available (27). Moreover, the Cre-mediated signal is strong and does not vary dramatically with time; by contrast a GFP-based system would have a signal that varies hour by hour, making FACS gates impossible to interpret during a long experimental day.

Although we focused on endothelial cells, FIND is agnostic to cell type; we envision FIND studies that identify LNPs targeting other cells. Ai14 mice have recently been used to monitor LNP-mediated delivery to immune populations at a cellular resolution (42). Given that on- and off-target cells can be isolated from the same mouse, FIND may also be used to identify (or iteratively evolve) LNPs with high therapeutic windows. To further increase the ratio of splenic endothelial cell: hepatocyte delivery, we could incorporate endothelial cell targeting ligands (43, 44).

More generally, this new ability to study how hundreds of LNPs target combinations of cells *in vivo* may elucidate relationships between LNP structure and *in vivo* functional delivery. In this case, FIND enabled us to quickly identify 2 lead LNPs. This is the first report of preferential delivery to splenic endothelial cells by any RNA *in vivo*, and the first report of systemic non-viral gene editing in endothelial cells. Here we delivered sgRNAs targeting the inflammation related gene ICAM-2. However, the long-term utility of FIND will be defined by its ability to identify nanoparticles for *in vivo* gene editing more efficiently than the current gold standard, which is *in vitro* screening. Relatedly, to fully utilize the large *in vivo* datasets generated by FIND, efforts will need to be made to develop high throughput ways of characterizing LNP characterizations zeta-potential, pKa, and lipid bilayer structure. We believe that, in time, these advances will

help FIND is positioned to help facilitate the discovery of structure-activity relationships to non-liver tissues. In future studies, it will also be important to further improve the efficiency of gene editing in endothelial cells beyond 20%.

We did not observe noticeable experimental variability within a given FIND screening experiment. We quantified the consistency of the sequencing readouts by analyzing the normalized DNA delivery values between bioreplicates. In all cell types, in each of the three screens, there was no overt differences between bioreplicates, suggesting the precision of the sequencing was high (**Figure 3.10**). In individual LNP testing, we did observe variability in hepatocyte delivery when 7C3 was administered over several batches to a total of 34 mice. Notably, delivery to splenic ECs was consistent, as was the (lack of) delivery to all other tested cell types. We were unable to identify the chemical variations that led to batch variability in hepatocyte targeting. Two possibilities that will require further investigation include variable LNP chemical structure and variable mRNA activity. Performing FIND screens with well-defined compounds could minimize batch to batch variability.

We note that when testing many new LNP, batch variability may be observed since the formulations are not yet optimized. However, this issue is not related to FIND or to pooled LNP screens; it is just as likely to occur when LNPs are tested individually. We believe FIND may actually minimize unwanted error in 2 ways. First, Cre-based reporters quantify deliver at the level of cell type. Identifying the cell type with batch issues is much easier than with two common approaches used in the field today: mRNA encoding Luciferase or erythropoietin, which quantifies protein production at the tissue- and organism-level, respectively. Second, when nanoparticles are screened individually,

missed injections, small changes in timepoints, mouse age, and other variables can introduce ‘silent’ experimental variability that affects how LNP1 performs, relative to LNP2. Here, we inject all the nanoparticles into the same mouse, which helps to reduce these sources of unintentional experimental variance. At the same time, FIND has several important limitations. LNPs must be stable, and must be well tolerated. Like all DNA-based screens, it is imperative to prevent DNA contamination.

Finally, we note that the doses of mRNA or gene editing constructs that are well tolerated after systemic administration to patients has not yet been established. In one related example, the FDA approved ONPATRO therapeutic, which is a siRNA systemically administered in a LNP, at a dose of 0.3 mg / kg. This may provide an initial estimate of the mRNA doses that are tolerated in the clinic. However, Cas9 mRNA is >100x larger than a single siRNA duplex (~4,500nt ssRNA vs. 21nt dsRNA). As a result, there is still a need to further improve the potency of the drug delivery systems and as well as the mRNA drugs, in order to advance novel Cas9 therapies into the clinic. Despite these caveats, FIND is a novel and robust method to quantify how hundreds of LNPs deliver mRNA to any combination of cell types *in vivo*. We believe FIND is well positioned to help identify LNPs with novel tropisms, which could lead to improved non-liver RNA drugs.

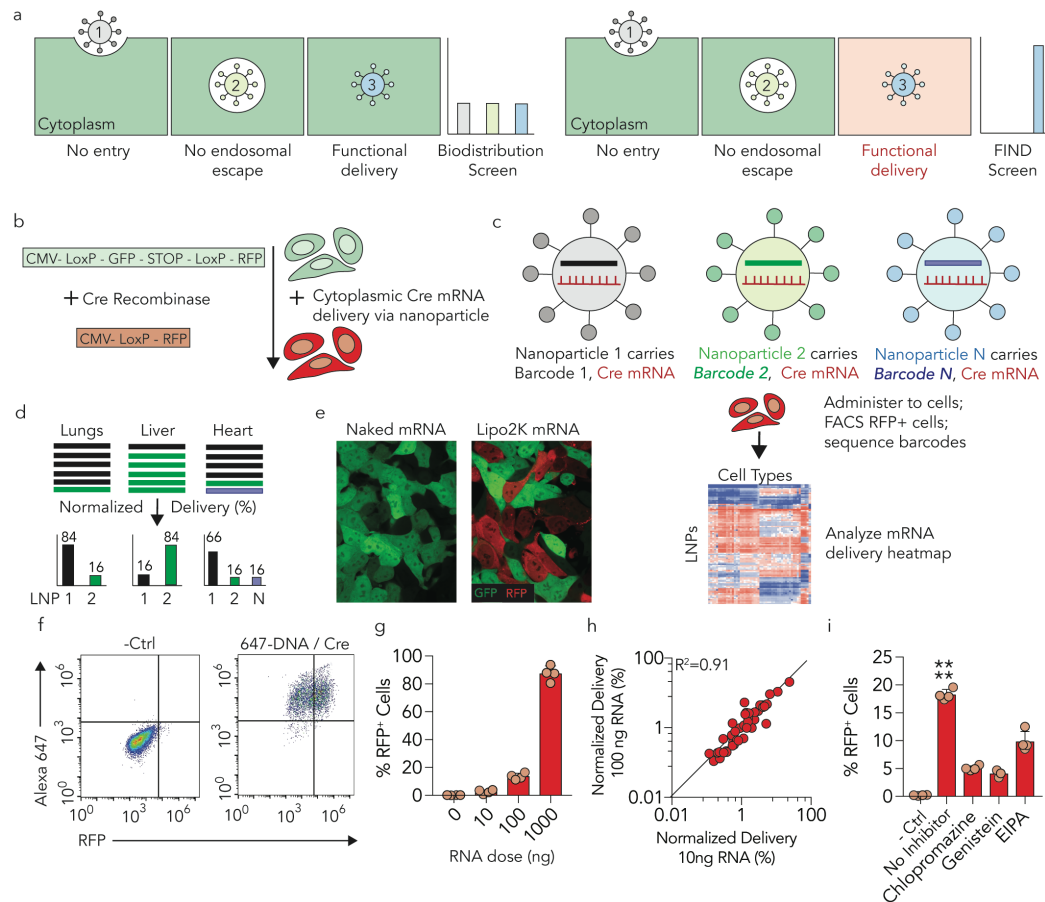
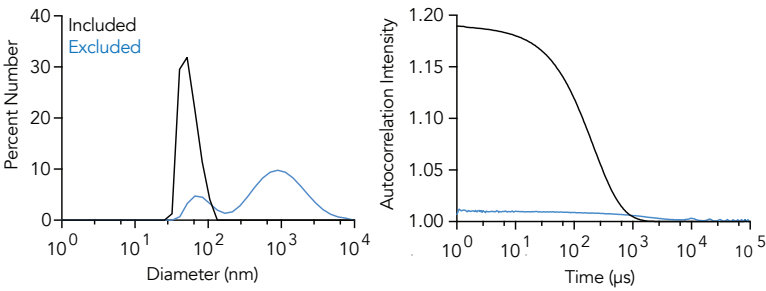


Figure 3.1. FIND is a high throughput screen for functional mRNA delivery. (a) Unlike previous biodistribution screens, which cannot distinguish between bound particles, particles stuck in endosomes, and particles that delivered RNA into the cytoplasm, FIND identifies LNPs that functionally deliver RNA. **(b,c)** Nanoparticles were formulated to carry Cre mRNA and a DNA barcode, before they were administered to Cre reporter cell lines or mice. Cells that underwent Cre-mediated genetic changes were isolated using FACS, and the DNA barcode was sequenced to identify the LNP that delivered the mRNA. **(d)** LNP barcodes were ranked by ‘normalized delivery’; each sample (e.g. Lung 1 vs. Heart 1) was analyzed individually on a single sequencing run. Using these data, we would hypothesize that LNP-1 delivered nucleic acids more efficiently to the lungs than LNP-2 and LNP-N. **(e)** LGSRL-R cells were treated with naked Cre mRNA or Cre mRNA carried by Lipofectamine 2000 (L2K). RFP expression indicates cytoplasmic Cre mRNA delivery. **(f)** Alexa-647 and RFP intensities after treatment with L2K carrying Cre mRNA and Alexa-647 labeled DNA barcode. Compared to untreated cells, there are no Alexa647-RFP+ cells, demonstrating that biodistribution is necessary, but not sufficient, for cytoplasmic delivery. **(g)** RFP+ HEK cells as a function of the administered Cre mRNA, which was delivered with L2K. **(h)** Normalized DNA barcode delivery for 54 LNPs sequenced from RFP+ HEK cells after the administration of 10 ng or 100 ng total mRNA. A high degree of correlation between

samples suggests that LNPs which deliver mRNA at the first dose deliver mRNA at the second dose. (i) RFP+ HEK cells following the administration of 54 LNPs (100 ng total mRNA), after cells were treated with endocytosis inhibitors. N= 3-4 wells / group. **p<0.01, **p<0.0001, 2 tailed t-test.**

a

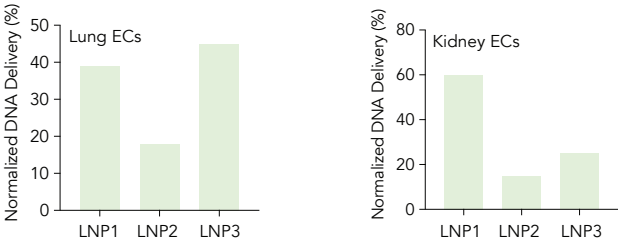


b

		Raw Counts Lung Endothelial Cells			Raw Counts Kidney Endothelial Cells			
LNP	Barcode	Mouse 1	Mouse 2	Mouse 3	Mouse 1	Mouse 2	Mouse 3	Input
1	GACACAGT	100	80	200	300	200	250	100
2	GCATAACG	50	45	110	100	60	70	120
3	ACAGAGGT	120	105	250	150	90	110	110
Total Counts		270	230	560	550	350	430	330

		Normalized Counts Lung ECs (%)			Normalized Counts Kidney ECs (%)			
LNP	Barcode	Mouse 1	Mouse 2	Mouse 3	Mouse 1	Mouse 2	Mouse 3	Input
1	GACACAGT	37	35	36	55	57	58	30
2	GCATAACG	19	20	20	18	17	16	36
3	ACAGAGGT	44	46	45	27	26	26	33
Total (%)		100	100	100	100	100	100	100

		Normalized to input Counts Lung ECs (%)			Normalized to input Counts Kidney ECs (%)			
LNP	Barcode	Mouse 1	Mouse 2	Mouse 3	Mouse 1	Mouse 2	Mouse 3	
1	GACACAGT	40	38	39	58	60	61	
2	GCATAACG	17	18	18	16	15	14	
3	ACAGAGGT	44	45	44	26	25	24	
Total (%)		100	100	100	100	100	100	



c

AGACGTGTGCTCTTCCGATCTGAGGGTACTTNNNNNNNAGATCGGAAGAGCGTCGTGT
Universal primer site 8 nt barcode N₇ Universal primer site

Phosphorothioate modification

d

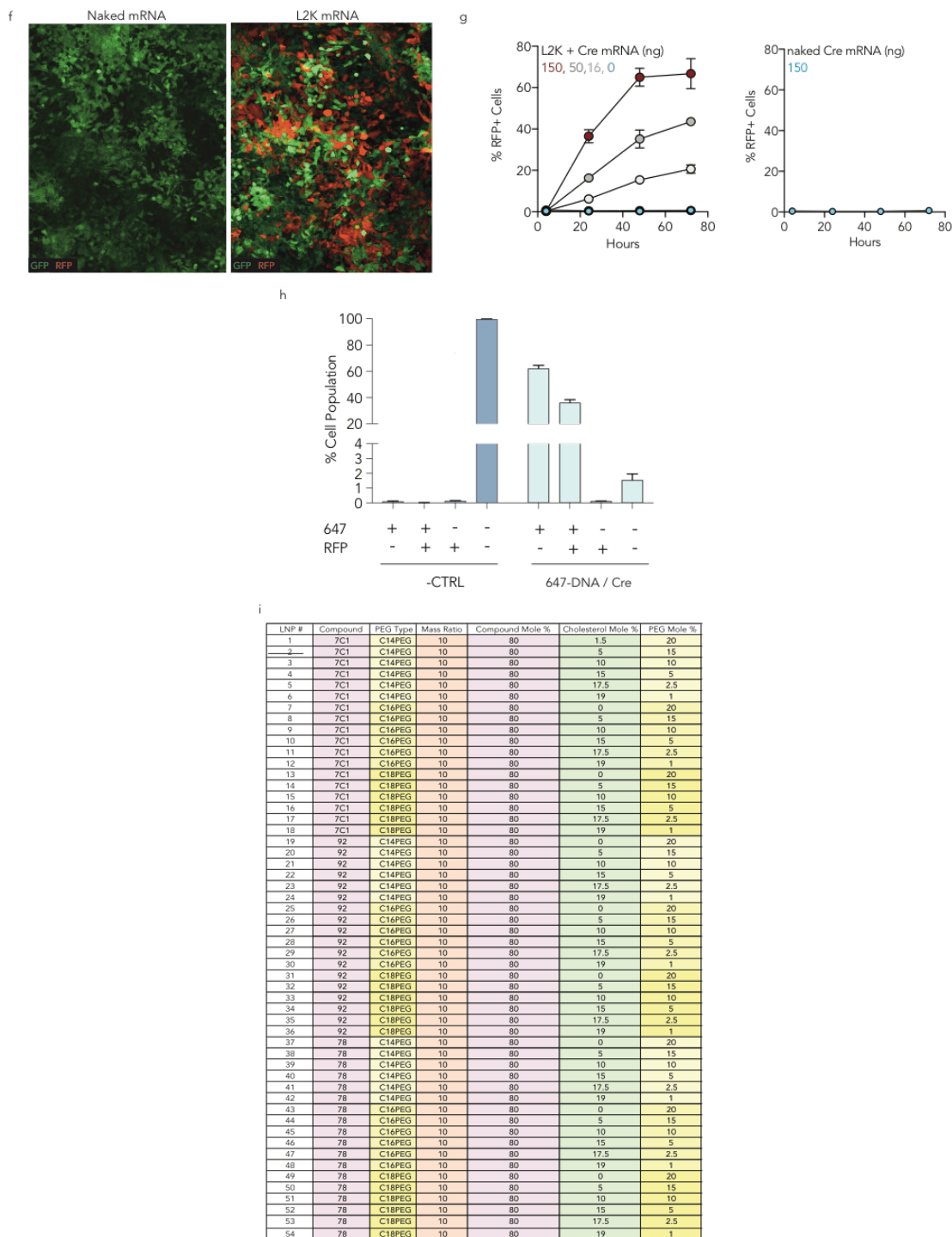
Barcode Sequences

1	GAC ACA GT	43	GCT ACA AC	85	AGT ATG CC	127	CAT CTG CT	169	ACT GCT TG	204	CTT AGG AC
2	GCA TAA CG	44	CCG ATG TA	86	TAC TGC TC	128	CCA ACG AA	170	AGA AGC CT	205	CTT GCT AG
3	ACA GAG GT	45	TAG GAG CT	87	TGC TTG CT	129	CCA GTT GA	171	AGA TCG TC	206	GAA CGG TT
4	CCA CTA AG	46	AAC AAG GC	88	TCC ACG TT	130	CCG GAA TA	172	AGC GTG TA	207	GAA GTG CT
5	TGT TCC GT	47	CTC GGT AA	89	AAC CAG AG	131	CCT ACC TA	173	AGG CAA TG	208	GAC GTC AT
6	GAT ACC TG	48	AGC TTC AG	90	ACG AAC GA	132	CCT ATT GG	174	AGG TTC CT	209	GAG ACC AA
7	AGC CGT AA	49	TCA CCT AG	91	ATA GTC GG	133	CCT TGG AA	175	AGT CGA AG	210	GAG TAG AG
8	CTC CTG AA	50	CAA GTC GT	92	CCA TGA AC	134	CGA ATT GC	176	AGT GGC AA	211	GAT CCA CT
9	ACG AAT CC	51	CTG TAT GC	93	GAG CAA TC	135	CGA GTT AG	177	ATA CTG GC	212	GAT GGA GT
10	AAT GGT CG	52	AGT TCG CA	94	CAA CTT GG	136	CGC TGA TA	178	ATC CTT CC	213	GCA CAC AA
11	CGC TAC AT	53	ATC GGA GA	95	CCA CAA CA	137	CGG CAT TA	179	ATC TCC TG	214	GCA TTG GT
12	CCT AAG TC	54	AAG TCC TC	96	TGG TGA AG	138	CGT CAA GA	180	ATG CGC TT	215	GCC TTC TT
13	TTG CTT GG	55	TGG ATG GT	97	AAC ACG CT	139	CTA AGA CC	181	ATT CCG CT	216	GCT AAG GA
14	CCT GTC AA	56	AGG TGT TG	98	AAC AGG TG	140	CTA GGT TG	182	CAA GCC AA	217	GCT GAA TC
15	AGC CTA TC	57	GAC GAA CT	99	AAC CTA CG	141	CTC ACC AA	183	CAA TGC GA	218	GGA AGA GA
16	TGA TCA CG	58	GTT CTT CG	100	AAG ACA CC	142	CTC GAC TT	184	CAT CAA CC	219	GGA CTA CT
17	CCA CAT TG	59	TTC GCC AT	101	AAG CGA CT	143	CTC TCA GA	178	ATC CTT CC	220	GGA TGT AG
18	TCG AGA GT	60	CAA CTC CA	102	AAT CGC TG	144	CTG ATG AG	179	ATC TCC TG	221	GGA TTC AC
19	GGT CGT AT	61	AAC CGT GT	103	AAT TCC GG	145	TAC CTG CA	180	ATG CGC TT	222	GGT ATA GG
20	ACA GGC AT	62	CGG TTG TT	104	ACA CCT CA	146	CTT ACA GC	181	ATT CCG CT	223	GGT TAG CT
21	GTG ATC CA	63	CTA GCA GT	105	ACA GTT CG	147	CTT CGG TT	182	CAA GCC AA	224	GTA AGC AC
22	TTC GTA CG	64	ACC TCT TC	106	ACC ATG TC	148	GAA CGA AG	183	CAA TGC GA	225	GTA CGA TC
23	ATG ACA GG	65	TAC TAG CG	107	ACC GGT TA	149	GAA GAT CC	184	CAT CAA CC	226	GTC AAC AG
24	CGA CCT AA	66	ACA ACA GC	108	ACG AGA AC	150	GAC CGA TA	185	CAT GAG CA	227	GTC CTT GA
25	TAT GGC AC	67	CGC AAT GT	109	ACG CTT CT	151	GAG AAG GT	186	CCA ACT TC	228	GTC TGA GT
26	ATA ACG CC	68	CAG TGC TT	110	ACT CCT AC	152	GAG GCA TT	187	CCG AAG AT	229	GTG TGT TC
27	GTA GTA CC	69	TCT AGG AG	111	ACT GCG AA	153	GAT CAG AC	188	CCG TAA CT	230	GTT CCA TG
28	CGC GTA TT	70	GAT TGT CC	112	AGA ACC AG	154	GAT GCT AC	189	CCT AGA GA	231	TAA GCG CA
29	ATC CAC GA	71	GGT ACG AA	113	AGA TAC GG	155	AAC AAC CG	190	CCT CAT CT	232	TAC AGA GC
30	TAA CGT CG	72	CTT CAC TG	114	AGC GAG AT	156	AAC AGT CC	191	CGA ACA AC	233	TAG CAG GA
31	CCT TCC AT	73	ATA GGT CC	115	AGG AGG TT	157	AAC GCA CA	192	CGA CAC TT	234	TAG CTT CC
32	GAT CAA GG	74	ACC GAC AA	116	AGG TAG GA	158	AAG ACC GT	193	CGA TCG AT	235	TAG TGC CA
33	AAG CAT CG	75	AAC ACT GG	117	AGT CAG GT	159	AAG CGT TC	194	CGG AGT AT	236	TAT GAC CG
34	AGG ATA GC	76	ACC ATA GG	118	AGT GCA TC	160	AAT GAC GC	195	CGG TAA TC	237	TCA CTC GA
35	GGC TCA AT	77	TGG ATG AC	119	ATA CGC AG	161	ACA AGA CG	196	CGT CCA TT	238	TCA GTA GG
36	TTC ACG GA	78	GAC TTG TG	120	ATC CGT TG	162	ACA CGA GA	197	CTA CAA GG	239	TCC GAT CA
37	GGC GAA TA	79	CCG TTA TG	121	ATC GTG GT	163	ACA GCA AG	198	CTA TCC AC	240	TCG AAC CT
38	AAG TGC AG	80	CAA CGA GT	122	ATG CCT AG	164	ACC GAA TG	199	CTC AGA AG		
39	GCA ATT CC	81	TTA CCG AC	123	ATT AGC CG	165	ACC TAG AC	200	CTC GTT CT		
40	CTT CGC AA	82	GAG AGT AC	124	CAA GAA GC	166	ACG ATC AG	201	CTC TGG AT		
41	CAT TGA CG	83	CTG TAC CA	125	CAA TCA GG	167	ACG GAC TT	202	CTG CCA TA		
42	TCT GGA CA	84	TGA GCT GT	126	CAT ACT CG	168	ACT CGA TC	203	CTG AAC GT		

e

Index Name	Index Sequence	Index Name	Index Sequence
N701	TAAGGCCA	S502	ATAGAGAG
N702	CGTACTAG	S503	AGAGGATA
N703	AGGCAGAA	S505	CTCCTTAC
N704	TCCTGAGC	S506	TATGCAGT
N705	GGACTCCT	S507	TACTCCTT
N706	TAGGCATG	S508	AGGCTTAG
N707	CTCTCTAC	S510	ATTAGACG
N710	CGAGGCTG	S511	CGGAGAGA
N711	AAGAGGCA	S513	CTAGTCGA
N712	GTAGAGGA	S515	AGCTAGAA
N714	GCTCATGA	S516	ACTCTAGG
N715	ATCTCAGG	S517	TCTTACGC
N716	ACTCGCTA	S518	CTTAATAG
N718	GGAGCTAC	S520	ATAGCCTT
N719	GCGTAGTA	S521	TAAGGCTC
N720	CGGAGCCT	S522	TCGCATAA
N721	TACGCTGC		
N722	ATGCGCAG		
N723	TAGCGCTC		
N724	ACTGAGCG		
N726	CCTAAGAC		
N727	CGATCAGT		
N728	TGACGCTA		
N729	TCGACGTC		

Binds to Forward Universal Site	
Binds to Reverse Universal Site	
Universal Reverse Primer (N7XX)	AATGATACGGCGACCACCGAGATCTACACTAAGGCCAACACTCTTTCCTACACGACGCTCTCCGATCT
Base Forward Primer	TGACTGGAGTTCAAGCGTGTGCTCTCCGATCT
Universal Forward Primer (S5XX)	CAAGCAGAAGACGGCATACGAGATATAGAGAGGTGACTGGAGTTCAAGCGTGTG



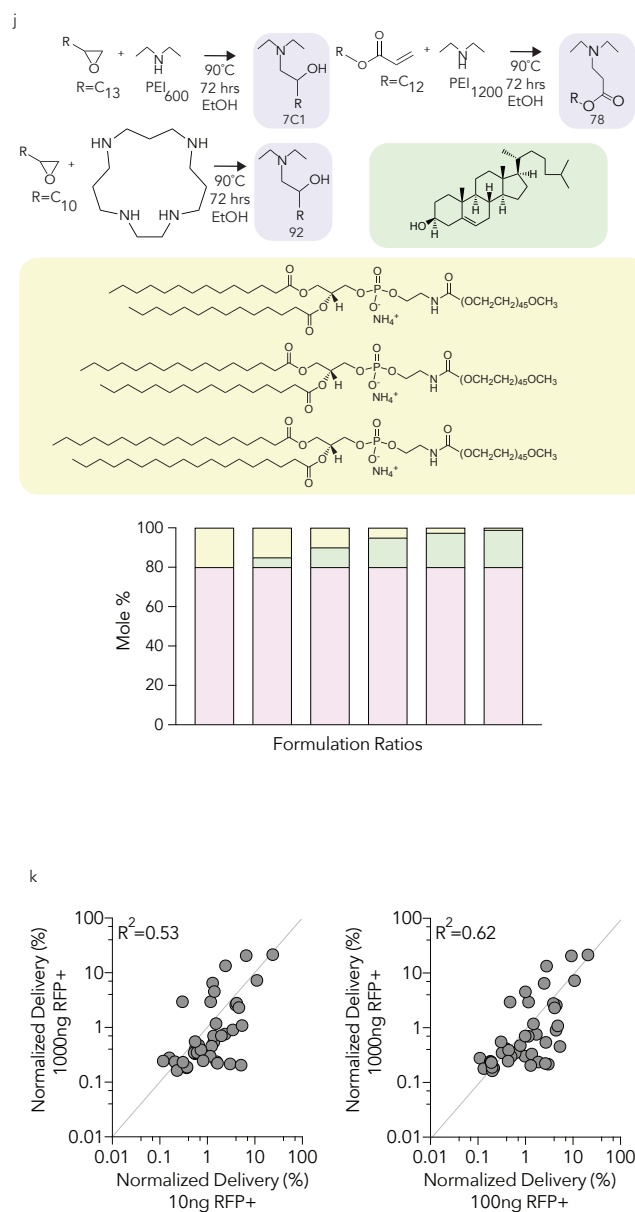


Figure 3.2. (a) LNP inclusion criteria. After formulating up to 158 LNPs in a single day, each LNP is individually using high throughput DLS. LNPs that do not form stable LNPs with a single population less than 200 nm are discarded. **(b) Normalized delivery example calculation.** In the first step, the total barcode counts in a given sample are summed. In the second step, the normalized counts for each barcode are calculated as Barcode1 / Sum (Barcode 1-->N). In the third step, these normalized counts are normalized a second time by the input DNA. In all cases, data from the third step are plotted as normalized delivery. **(c) DNA barcode design;** DNA barcodes were designed to reduce exonuclease activity and PCR bias. **(d) 8 nucleotide barcode sequences and (e) dual indices designed for multiplexed Illumina sequencing. (f) GFP**

and RFP expression 72 hours after LoxP-GFP-Stop-LoxP-RFP HEK cells were transfected with naked Cre mRNA (negative ctrl) or Cre mRNA carried by L2K. (g) RFP expression at various time points after LoxP-GFP-Stop-LoxP-RFP HEK cells were transfected with 150ng naked Cre mRNA (negative ctrl) or various doses of Cre mRNA carried by L2K. (h) Co-localization of Alexa-647+ (647) and RFP+ cells after treatment with a negative control or L2K carrying Cre mRNA and Alexa-647 labeled DNA barcode. (i) LNP library used for in vitro assay. (j) Synthesis used to the compounds 7C1, 78, and 92. We selected epoxide-, acrylate-, and methacrylate-based chemistries because we, and others have used them before to synthesize LNPs. (k) Comparing normalized DNA barcode readouts from RFP+ cells after cells were treated with 10, 100, or 1000 ng mRNA.

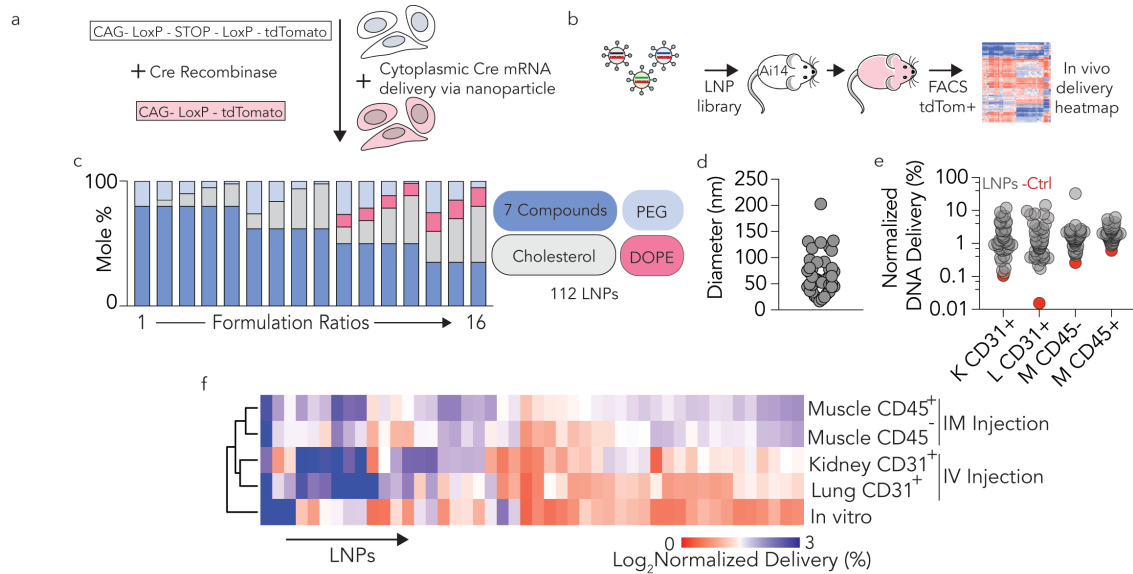
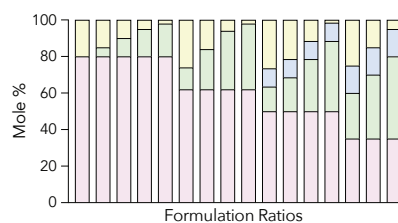
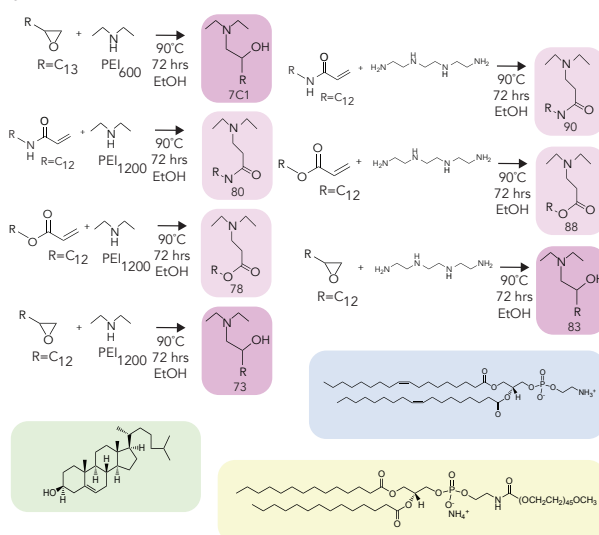


Figure 3.3. FIND can quantify LNP delivery *in vivo*. (a) Cre recombinase leads to the deletion of a stop codon allowing for the expression of tdTomato driven by a CAG promoter. (b) Libraries of LNPs containing Cre mRNA and DNA barcodes are administered to LSL-tdTom (Ai14) mice. tdTomato⁺ cells are isolated by FACS and DNA barcodes are sequenced. (c) Screen 1 consisted of a library of 112 distinct LNPs created by formulating 7 compounds with cholesterol, DOPE, and C14-PEG2000 at 16 different mole ratios. (d) Dynamic light scattering analysis of all 112 LNPs from this library; 71 formed stable LNPs and were included. (e) Normalized DNA delivery in kidney and lung endothelial cells (CD31⁺CD45⁻) after LNPs were intravenously injected, as well as CD45⁺ and CD45⁻ cells isolated following intramuscular injection. (f) *In vivo* LNP targeting heatmap generated by unbiased, Euclidean clustering. *In vitro* LNP delivery, *in vivo* intramuscular delivery, and *in vivo* intravenous delivery cluster separately, as expected.

a

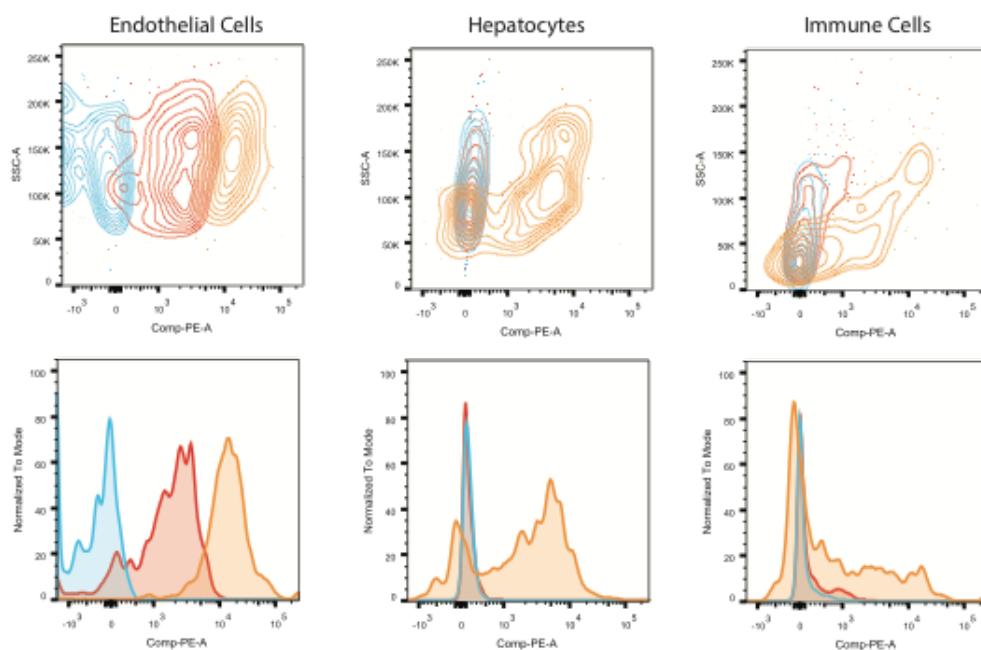
LNP #	Compound	PEG Type	Mass Ratio	Compound Mole %	Cholesterol Mole %	PEG Mole %	DOPE Mole %
1	7C1	CH4PEG	10	80	0	20	0
2	7C1	CH4PEG	10	80	5	15	0
3	7C1	CH4PEG	10	80	10	10	0
4	7C1	CH4PEG	10	80	15	5	0
5	7C1	CH4PEG	10	80	18	2	0
6	7C1	CH4PEG	10	62	12	26	0
7	7C1	CH4PEG	10	62	22	16	0
8	7C1	CH4PEG	10	62	32	6	0
9	7C1	CH4PEG	10	62	36	2	0
10	7C1	CH4PEG	10	50	38.5	1.5	10
11	7C1	CH4PEG	10	50	28.5	11.5	10
12	7C1	CH4PEG	10	50	18.5	21.5	10
13	7C1	CH4PEG	10	50	13.5	26.5	10
14	7C1	CH4PEG	10	35	25	25	15
15	7C1	CH4PEG	10	35	35	15	15
16	7C1	CH4PEG	10	35	45	5	15
17	90	CH4PEG	10	80	0	20	0
18	90	CH4PEG	10	80	5	15	0
19	90	CH4PEG	10	80	10	10	0
20	90	CH4PEG	10	80	15	5	0
21	90	CH4PEG	10	80	18	2	0
22	90	CH4PEG	10	62	12	26	0
23	90	CH4PEG	10	62	22	16	0
24	90	CH4PEG	10	62	32	6	0
25	90	CH4PEG	10	62	36	2	0
26	90	CH4PEG	10	50	38.5	1.5	10
27	90	CH4PEG	10	50	28.5	11.5	10
28	90	CH4PEG	10	50	18.5	21.5	10
29	90	CH4PEG	10	50	13.5	26.5	10
30	90	CH4PEG	10	35	25	25	15
31	90	CH4PEG	10	35	35	15	15
32	90	CH4PEG	10	35	45	5	15
33	88	CH4PEG	10	80	0	20	0
34	88	CH4PEG	10	80	5	15	0
35	88	CH4PEG	10	80	10	10	0
36	88	CH4PEG	10	80	15	5	0
37	88	CH4PEG	10	80	18	2	0
38	88	CH4PEG	10	62	12	26	0
39	88	CH4PEG	10	62	22	16	0
40	88	CH4PEG	10	62	32	6	0
41	88	CH4PEG	10	62	36	2	0
42	88	CH4PEG	10	50	38.5	1.5	10
43	88	CH4PEG	10	50	28.5	11.5	10
44	88	CH4PEG	10	50	18.5	21.5	10
45	88	CH4PEG	10	50	13.5	26.5	10
46	88	CH4PEG	10	35	25	25	15
47	88	CH4PEG	10	35	35	15	15
48	88	CH4PEG	10	35	45	5	15
49	83	CH4PEG	10	80	0	20	0
50	83	CH4PEG	10	80	5	15	0
51	83	CH4PEG	10	80	10	10	0
52	83	CH4PEG	10	80	15	5	0
53	83	CH4PEG	10	80	18	2	0
54	83	CH4PEG	10	62	12	26	0
55	83	CH4PEG	10	62	22	16	0
56	83	CH4PEG	10	62	32	6	0
57	83	CH4PEG	10	62	36	2	0
58	83	CH4PEG	10	50	38.5	1.5	10
59	83	CH4PEG	10	50	28.5	11.5	10
60	83	CH4PEG	10	50	18.5	21.5	10
61	83	CH4PEG	10	50	13.5	26.5	10
62	83	CH4PEG	10	35	25	25	15
63	83	CH4PEG	10	35	35	15	15
64	83	CH4PEG	10	35	45	5	15
65	80	CH4PEG	10	80	0	20	0
66	80	CH4PEG	10	80	5	15	0
67	80	CH4PEG	10	80	10	10	0
68	80	CH4PEG	10	80	15	5	0
69	80	CH4PEG	10	80	18	2	0
70	80	CH4PEG	10	62	12	26	0
71	80	CH4PEG	10	62	22	16	0
72	80	CH4PEG	10	62	32	6	0
73	80	CH4PEG	10	62	36	2	0
74	80	CH4PEG	10	50	38.5	1.5	10
75	80	CH4PEG	10	50	28.5	11.5	10
76	80	CH4PEG	10	50	18.5	21.5	10
77	80	CH4PEG	10	50	13.5	26.5	10
78	80	CH4PEG	10	35	25	25	15
79	80	CH4PEG	10	35	35	15	15
80	80	CH4PEG	10	35	45	5	15
81	78	CH4PEG	10	80	0	20	0
82	78	CH4PEG	10	80	5	15	0
83	78	CH4PEG	10	80	10	10	0
84	78	CH4PEG	10	80	15	5	0
85	78	CH4PEG	10	80	18	2	0
86	78	CH4PEG	10	62	12	26	0
87	78	CH4PEG	10	62	22	16	0
88	78	CH4PEG	10	62	32	6	0
89	78	CH4PEG	10	62	36	2	0
90	78	CH4PEG	10	50	38.5	1.5	10
91	78	CH4PEG	10	50	28.5	11.5	10
92	78	CH4PEG	10	50	18.5	21.5	10
93	78	CH4PEG	10	50	13.5	26.5	10
94	78	CH4PEG	10	35	25	25	15
95	78	CH4PEG	10	35	35	15	15
96	78	CH4PEG	10	35	45	5	15
97	73	CH4PEG	10	80	0	20	0
98	73	CH4PEG	10	80	5	15	0
99	73	CH4PEG	10	80	10	10	0
100	73	CH4PEG	10	80	15	5	0
101	73	CH4PEG	10	80	18	2	0
102	73	CH4PEG	10	62	12	26	0
103	73	CH4PEG	10	62	22	16	0
104	73	CH4PEG	10	62	32	6	0
105	73	CH4PEG	10	62	36	2	0
106	73	CH4PEG	10	50	38.5	1.5	10
107	73	CH4PEG	10	50	28.5	11.5	10
108	73	CH4PEG	10	50	18.5	21.5	10
109	73	CH4PEG	10	50	13.5	26.5	10
110	73	CH4PEG	10	35	25	25	15
111	73	CH4PEG	10	35	35	15	15
112	73	CH4PEG	10	35	45	5	15
113	n	n	n	n	n	n	n

b

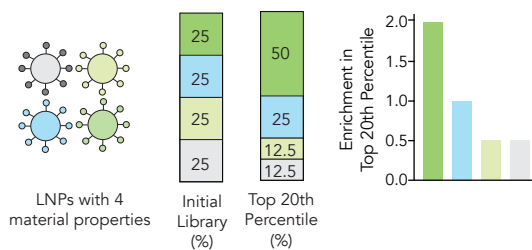


c

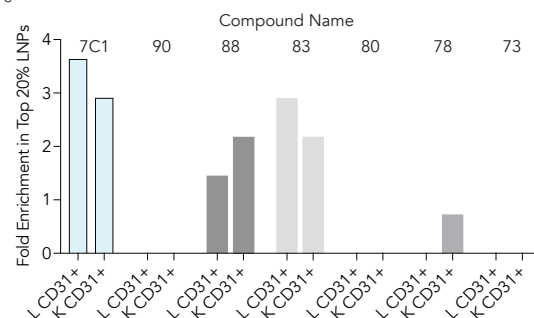
We observe tissue- and cell-type specific tdTomato autofluorescence in Ai14 mice.
Exemplified below are from the liver. C57BL/6J + PBS Ai14 + PBS Ai14 + LNP w/ Cre mRNA



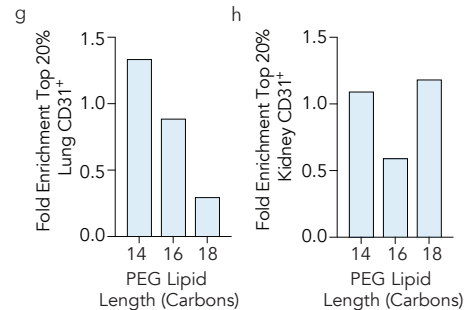
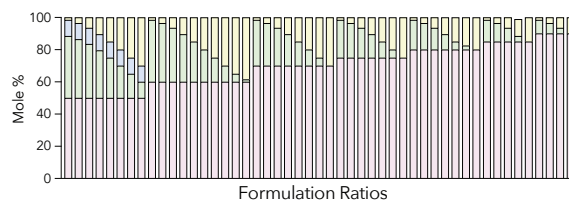
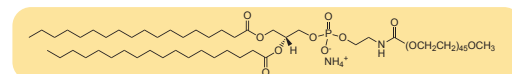
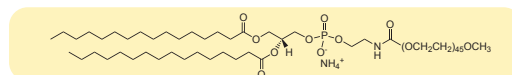
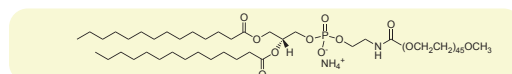
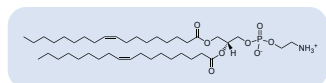
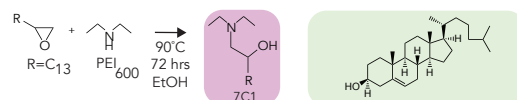
d



e

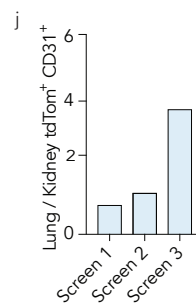
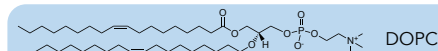
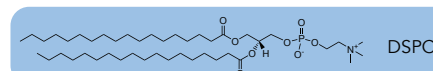
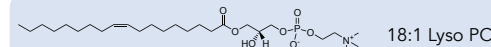
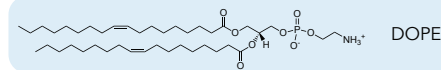
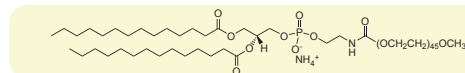
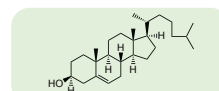
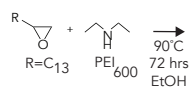


LNP #	Compound	PEG Type	Mass Ratio	Compound Mole %	Cholesterol Mole %	PEG Mole %	DOPE Mole %
1	7C1	C14PEG	10	50	38.5	1.5	10
2	7C1	C14PEG	10	50	36.5	3.5	10
3	7C1	C14PEG	10	50	33.5	6.5	10
4	7C1	C14PEG	10	50	29.5	10.5	10
5	7C1	C14PEG	10	50	25	15	10
6	7C1	C14PEG	10	50	20	20	10
7	7C1	C14PEG	10	50	15	25	10
8	7C1	C14PEG	10	50	10	30	10
9	7C1	C14PEG	10	60	38.5	1.5	0
10	7C1	C14PEG	10	60	36.5	3.5	0
11	7C1	C14PEG	10	60	33.5	6.5	0
12	7C1	C14PEG	10	60	29.5	10.5	0
13	7C1	C14PEG	10	60	25	15	0
14	7C1	C14PEG	10	60	20	20	0
15	7C1	C14PEG	10	60	15	25	0
16	7C1	C14PEG	10	60	10	30	0
17	7C1	C14PEG	10	60	5	35	0
18	7C1	C14PEG	10	60	1.5	38.5	0
19	7C1	C14PEG	10	70	28.5	1.5	0
20	7C1	C14PEG	10	70	26.5	3.5	0
21	7C1	C14PEG	10	70	23.5	6.5	0
22	7C1	C14PEG	10	70	19.5	10.5	0
23	7C1	C14PEG	10	70	15	15	0
24	7C1	C14PEG	10	70	10	20	0
25	7C1	C14PEG	10	70	5	25	0
26	7C1	C14PEG	10	70	0	30	0
27	7C1	C14PEG	10	75	23.5	1.5	0
28	7C1	C14PEG	10	75	21.5	3.5	0
29	7C1	C14PEG	10	75	18.5	6.5	0
30	7C1	C14PEG	10	75	14.5	10.5	0
31	7C1	C14PEG	10	75	10	15	0
32	7C1	C14PEG	10	75	5	20	0
33	7C1	C14PEG	10	75	0	25	0
34	7C1	C14PEG	10	80	18.5	1.5	0
35	7C1	C14PEG	10	80	16.5	3.5	0
36	7C1	C14PEG	10	80	13.5	6.5	0
37	7C1	C14PEG	10	80	9.5	10.5	0
38	7C1	C14PEG	10	80	5	15	0
39	7C1	C14PEG	10	80	2.5	17.5	0
40	7C1	C14PEG	10	80	0	20	0
41	7C1	C14PEG	10	85	13.5	1.5	0
42	7C1	C14PEG	10	85	11.5	3.5	0
43	7C1	C14PEG	10	85	8.5	6.5	0
44	7C1	C14PEG	10	85	4.5	10.5	0
45	7C1	C14PEG	10	85	0	15	0
46	7C1	C14PEG	5	80	0	20	0
47	7C1	C14PEG	7	80	0	20	0
48	7C1	C14PEG	12	80	0	20	0
49	7C1	C14PEG	10	90	8.5	1.5	0
50	7C1	C14PEG	10	90	6.5	3.5	0
51	7C1	C14PEG	10	90	3.5	6.5	0
52	7C1	C14PEG	10	90	0	10	0
53	7C1	C14PEG	12	50	28.5	11.5	10
54	7C1	C14PEG	10	50	28.5	11.5	10
55	7C1	C14PEG	8	50	28.5	11.5	10
56	7C1	C14PEG	5	50	28.5	11.5	10
57	7C1	C18PEG	10	50	38.5	1.5	10
58	7C1	C18PEG	10	50	36.5	3.5	10
59	7C1	C18PEG	10	50	33.5	6.5	10
60	7C1	C18PEG	10	50	29.5	10.5	10
61	7C1	C18PEG	10	50	25	15	10
62	7C1	C18PEG	10	50	20	20	10
63	7C1	C18PEG	10	50	15	25	10
64	7C1	C18PEG	10	50	10	30	10
65	7C1	C18PEG	10	80	18.5	1.5	0
66	7C1	C18PEG	10	80	16.5	3.5	0
67	7C1	C18PEG	10	80	13.5	6.5	0
68	7C1	C18PEG	10	80	9.5	10.5	0
69	7C1	C18PEG	10	80	5	15	0
70	7C1	C18PEG	10	80	2.5	17.5	0
71	7C1	C18PEG	10	80	0	20	0
72	7C1	C18PEG	10	60	38.5	1.5	0
73	7C1	C18PEG	10	60	36.5	3.5	0
74	7C1	C18PEG	10	60	33.5	6.5	0
75	7C1	C18PEG	10	60	29.5	10.5	0
76	7C1	C18PEG	10	60	25	15	0
77	7C1	C18PEG	10	60	20	20	0
78	7C1	C18PEG	10	60	15	25	0
79	7C1	C18PEG	10	60	10	30	0
80	7C1	C16PEG	10	50	38.5	1.5	10
81	7C1	C16PEG	10	50	36.5	3.5	10
82	7C1	C16PEG	10	50	33.5	6.5	10
83	7C1	C16PEG	10	50	29.5	10.5	10
84	7C1	C16PEG	10	50	25	15	10
85	7C1	C16PEG	10	50	20	20	10
86	7C1	C16PEG	10	50	15	25	10
87	7C1	C16PEG	10	50	10	30	10
88	7C1	C16PEG	10	80	18.5	1.5	0
89	7C1	C16PEG	10	80	16.5	3.5	0
90	7C1	C16PEG	10	80	13.5	6.5	0
91	7C1	C16PEG	10	80	9.5	10.5	0
92	7C1	C16PEG	10	80	5	15	0
93	7C1	C16PEG	10	80	2.5	17.5	0
94	7C1	C16PEG	10	80	0	20	0
95	7C1	C16PEG	10	60	38.5	1.5	0
96	7C1	C16PEG	10	60	36.5	3.5	0
97	7C1	C16PEG	10	60	33.5	6.5	0
98	7C1	C16PEG	10	60	29.5	10.5	0
99	7C1	C16PEG	10	60	25	15	0
100	7C1	C16PEG	10	60	20	20	0
101	7C1	C14PEG	10	60	15	25	0
102	7C1	C14PEG	10	60	10	30	0
103	n	n	n	n	n	n	n



i

UMP#	Compound	PEG Type	Mass Ratio	Helper Lipid Type	Compound Mole %	Cholesterol Mole %	PEG Mole %	Helper Lipid Mole %
1	ZC1	CHAPES	10	DOPE	50	28.5	1.5	0
2	ZC1	CHAPES	10	DOPE	50	28.5	1.5	20
3	ZC1	CHAPES	10	DOPE	50	28.5	1.5	0
4	ZC1	CHAPES	10	DOPE	50	28.5	1.5	10
5	ZC1	CHAPES	10	DOPE	50	28.5	1.5	20
6	ZC1	CHAPES	10	DOPE	50	28.5	1.5	0
7	ZC1	CHAPES	10	DOPE	50	33.5	4.5	10
8	ZC1	CHAPES	10	DOPE	50	33.5	4.5	20
9	ZC1	CHAPES	10	DOPE	50	43.5	4.5	0
10	ZC1	CHAPES	10	DOPE	50	28.5	10.5	10
11	ZC1	CHAPES	10	DOPE	50	28.5	10.5	20
12	ZC1	CHAPES	10	DOPE	50	28.5	10.5	0
13	ZC1	CHAPES	10	DOPE	50	1.5	2.5	0
14	ZC1	CHAPES	10	DOPE	50	1.5	2.5	20
15	ZC1	CHAPES	10	DOPE	50	2.5	2.5	0
16	ZC1	CHAPES	10	DOPE	50	28.5	1.5	10
17	ZC1	CHAPES	10	DOPE	50	28.5	1.5	20
18	ZC1	CHAPES	10	DOPE	50	28.5	1.5	0
19	ZC1	CHAPES	10	DOPE	50	28.5	3.5	10
20	ZC1	CHAPES	10	DOPE	50	28.5	3.5	20
21	ZC1	CHAPES	10	DOPE	50	28.5	3.5	0
22	ZC1	CHAPES	10	DOPE	50	33.5	4.5	10
23	ZC1	CHAPES	10	DOPE	50	33.5	4.5	20
24	ZC1	CHAPES	10	DOPE	50	43.5	4.5	0
25	ZC1	CHAPES	10	DOPE	50	28.5	10.5	10
26	ZC1	CHAPES	10	DOPE	50	28.5	10.5	20
27	ZC1	CHAPES	10	DOPE	50	28.5	10.5	0
28	ZC1	CHAPES	10	DOPE	50	1.5	2.5	0
29	ZC1	CHAPES	10	DOPE	50	1.5	2.5	20
30	ZC1	CHAPES	10	DOPE	50	2.5	2.5	0
31	ZC1	CHAPES	10	DOPE	50	28.5	1.5	10
32	ZC1	CHAPES	10	DOPE	50	28.5	1.5	20
33	ZC1	CHAPES	10	DOPE	50	28.5	1.5	0
34	ZC1	CHAPES	10	DOPE	50	28.5	3.5	10
35	ZC1	CHAPES	10	DOPE	50	28.5	3.5	20
36	ZC1	CHAPES	10	DOPE	50	28.5	3.5	0
37	ZC1	CHAPES	10	DOPE	50	33.5	4.5	10
38	ZC1	CHAPES	10	DOPE	50	33.5	4.5	20
39	ZC1	CHAPES	10	DOPE	50	43.5	4.5	0
40	ZC1	CHAPES	10	DOPE	50	28.5	10.5	10
41	ZC1	CHAPES	10	DOPE	50	28.5	10.5	20
42	ZC1	CHAPES	10	DOPE	50	28.5	10.5	0
43	ZC1	CHAPES	10	DOPE	50	1.5	2.5	10
44	ZC1	CHAPES	10	DOPE	50	1.5	2.5	20
45	ZC1	CHAPES	10	DOPE	50	2.5	2.5	0
46	ZC1	CHAPES	10	18:1 Lyso PC	50	28.5	1.5	10
47	ZC1	CHAPES	10	18:1 Lyso PC	50	28.5	1.5	20
48	ZC1	CHAPES	10	18:1 Lyso PC	50	28.5	1.5	0
49	ZC1	CHAPES	10	18:1 Lyso PC	50	28.5	3.5	10
50	ZC1	CHAPES	10	18:1 Lyso PC	50	28.5	3.5	20
51	ZC1	CHAPES	10	18:1 Lyso PC	50	28.5	3.5	0
52	ZC1	CHAPES	10	18:1 Lyso PC	50	33.5	4.5	10
53	ZC1	CHAPES	10	18:1 Lyso PC	50	33.5	4.5	20
54	ZC1	CHAPES	10	18:1 Lyso PC	50	43.5	4.5	0
55	ZC1	CHAPES	10	18:1 Lyso PC	50	28.5	10.5	10
56	ZC1	CHAPES	10	18:1 Lyso PC	50	28.5	10.5	20
57	ZC1	CHAPES	10	18:1 Lyso PC	50	28.5	10.5	0
58	ZC1	CHAPES	10	18:1 Lyso PC	50	1.5	2.5	10
59	ZC1	CHAPES	10	18:1 Lyso PC	50	1.5	2.5	20
60	ZC1	CHAPES	10	18:1 Lyso PC	50	2.5	2.5	0
61	ZC1	CHAPES	10	DOPE	50	1.5	2.5	10
62	ZC1	CHAPES	10	DOPE	50	0	35	15
63	ZC1	CHAPES	10	DOPE	50	1.5	2.5	0
64	ZC1	CHAPES	10	DOPE	60	28.5	1.5	10
65	ZC1	CHAPES	10	DOPE	60	28.5	1.5	20
66	ZC1	CHAPES	10	DOPE	60	28.5	1.5	0
67	ZC1	CHAPES	10	DOPE	60	33.5	3.5	10
68	ZC1	CHAPES	10	DOPE	60	33.5	3.5	20
69	ZC1	CHAPES	10	DOPE	60	43.5	3.5	0
70	ZC1	CHAPES	10	DOPE	60	28.5	10.5	10
71	ZC1	CHAPES	10	DOPE	60	28.5	10.5	20
72	ZC1	CHAPES	10	DOPE	60	28.5	10.5	0
73	ZC1	CHAPES	10	DOPE	60	1.5	2.5	10
74	ZC1	CHAPES	10	DOPE	60	1.5	2.5	20
75	ZC1	CHAPES	10	DOPE	60	2.5	2.5	0
76	ZC1	CHAPES	10	DOPE	60	0	35	15
77	ZC1	CHAPES	10	DOPE	60	1.5	2.5	0
78	ZC1	CHAPES	10	DOPE	60	33.5	1.5	10
79	ZC1	CHAPES	10	DOPE	60	33.5	1.5	20
80	ZC1	CHAPES	10	DOPE	60	43.5	1.5	0
81	ZC1	CHAPES	10	DOPE	60	28.5	3.5	10
82	ZC1	CHAPES	10	DOPE	60	28.5	3.5	20
83	ZC1	CHAPES	10	DOPE	60	33.5	3.5	0
84	ZC1	CHAPES	10	DOPE	60	28.5	10.5	10
85	ZC1	CHAPES	10	DOPE	60	28.5	10.5	20
86	ZC1	CHAPES	10	DOPE	60	28.5	10.5	0
87	ZC1	CHAPES	10	DOPE	60	1.5	2.5	10
88	ZC1	CHAPES	10	DOPE	60	1.5	2.5	20
89	ZC1	CHAPES	10	DOPE	60	2.5	2.5	0
90	ZC1	CHAPES	10	DOPE	60	0	35	15
91	ZC1	CHAPES	10	DOPE	60	1.5	2.5	0
92	ZC1	CHAPES	10	DOPE	60	0	35	15
93	ZC1	CHAPES	10	DOPE	60	1.5	2.5	10
94	ZC1	CHAPES	10	DOPE	60	1.5	2.5	20
95	ZC1	CHAPES	10	DOPE	60	2.5	2.5	0
96	ZC1	CHAPES	10	DOPE	60	33.5	1.5	10
97	ZC1	CHAPES	10	DOPE	60	33.5	1.5	20
98	ZC1	CHAPES	10	DOPE	60	43.5	1.5	0
99	ZC1	CHAPES	10	DOPE	60	28.5	3.5	10
100	ZC1	CHAPES	10	DOPE	60	28.5	3.5	20
101	ZC1	CHAPES	10	DOPE	60	33.5	3.5	0
102	ZC1	CHAPES	10	DOPE	60	28.5	10.5	10
103	ZC1	CHAPES	10	DOPE	60	28.5	10.5	20
104	ZC1	CHAPES	10	DOPE	60	28.5	10.5	0
105	ZC1	CHAPES	10	DOPE	60	1.5	2.5	10
106	ZC1	CHAPES	10	DOPE	60	1.5	2.5	20
107	ZC1	CHAPES	10	DOPE	60	2.5	2.5	0
108	ZC1	CHAPES	10	DOPE	60	0	35	15
109	ZC1	CHAPES	10	DOPE	60	1.5	2.5	0
110	ZC1	CHAPES	10	18:1 Lyso	50	0	35	15
111	ZC1	CHAPES	10	18:1 Lyso	50	1.5	2.5	0
112	ZC1	CHAPES	10	18:1 Lyso	60	28.5	1.5	10
113	ZC1	CHAPES	10	18:1 Lyso	60	28.5	1.5	20
114	ZC1	CHAPES	10	18:1 Lyso	60	33.5	1.5	0
115	ZC1	CHAPES	10	18:1 Lyso	60	33.5	1.5	10
116	ZC1	CHAPES	10	18:1 Lyso	60	28.5	3.5	0
117	ZC1	CHAPES	10	18:1 Lyso	60	28.5	3.5	10
118	ZC1	CHAPES	10	18:1 Lyso	60	43.5	3.5	0
119	ZC1	CHAPES	10	18:1 Lyso	60	28.5	10.5	10
120	ZC1	CHAPES	10	18:1 Lyso	60	28.5	10.5	20
121	ZC1	CHAPES	10	18:1 Lyso	60	33.5	10.5	0
122	ZC1	CHAPES	10	18:1 Lyso	60	1.5	2.5	10
123	ZC1	CHAPES	10	18:1 Lyso	60	1.5	2.5	20
124	ZC1	CHAPES	10	18:1 Lyso	60	2.5	2.5	0
125	ZC1	CHAPES	10	DOPE	80	0	20	0
126	ZC1	CHAPES	10	DOPE	90	3.5	1.5	5
127	ZC1	CHAPES	10	DOPE	90	3.5	1.5	0
128	ZC1	CHAPES	10	DOPE	90	1.5	3.5	5
129	ZC1	CHAPES	10	DOPE	90	6.5	3.5	0
130	ZC1	CHAPES	10	DOPE	90	0	10	0
131	ZC1	CHAPES	10	DOPE	80	0	20	0
132	ZC1	CHAPES	10	DOPE	90	3.5	1.5	5
133	ZC1	CHAPES	10	DOPE	90	8.5	1.5	0
134	ZC1	CHAPES	10	DOPE	90	1.5	3.5	5
135	ZC1	CHAPES	10	DOPE	90	3.5	3.5	0
136	ZC1	CHAPES	10	DOPE	90	0	10	0
137	ZC1	CHAPES	10	DOPE	90	28.5	1.5	0
138	ZC1	CHAPES	10	DOPE	50	28.5	3.5	10
139	ZC1	CHAPES	10	DOPE	50	28.5	3.5	20
140	ZC1	CHAPES	10	DOPE	50	28.5	3.5	0
141	ZC1	CHAPES	10	DOPE	70	1.5	1.5	10
142	ZC1	CHAPES	10	DOPE	90	0	10	0
143	ZC1	CHAPES	10	DOPE	90	0.5	3.5	5
144	ZC1	CHAPES	10	DOPE	90	8.5	1.5	0
145	ZC1	CHAPES	10	DOPE	90	28.5	10.5	10
146	ZC1	CHAPES	10	DOPE	90	5	3.5	0
147	ZC1	CHAPES	10	DOPE	60	28.5	10.5	10
148	ZC1	CHAPES	10	DOPE	80	0	20	0
149	ZC1	CHAPES	10	DOPE	80	0	20	0
150	ZC1	CHAPES	10	DOPE	80	0	20	0
151	ZC1	CHAPES	10	DOPE	80	0	20	0
152	ZC1	CHAPES	10	DOPE	80	0	20	0
153	ZC1	CHAPES	10	DOPE	50	28.5	11.5	10
154	ZC1	CHAPES	10	DOPE	50	28.5	11.5	20
155	ZC1	CHAPES	10	DOPE	50	28.5	11.5	0
156	ZC1	CHAPES	10	DOPE	50	28.5	11.5	10
157	ZC1	CHAPES	10	DOPE	50	28.5	11.5	20



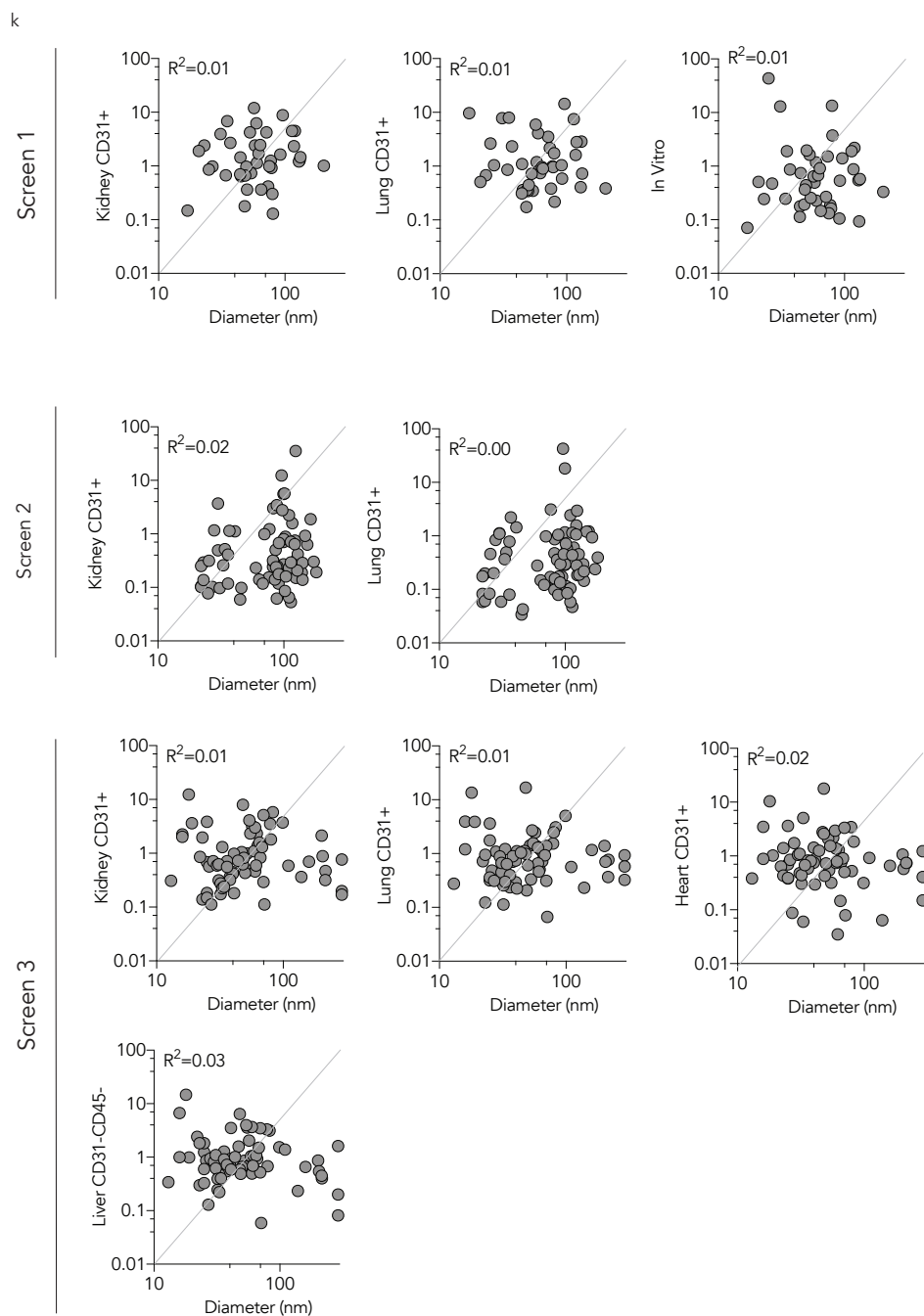


Figure 3.4. (a) LNP library used for first *in vivo* experiment. (b) Synthesis used to the compounds 7C1, 78, and 92. We selected epoxide- and acrylate-based chemistries

reacting various alkyl lengths and PEI600, PEI1200, and triethyltetramine. (c) PBS-treated Ai14 mice display higher levels of tdTomato autofluorescence compared to PBS-treated C57BL/6J mice in some cell types. PBS-treated Ai14 mice are used as negative control for all FIND experiments. (d) Enrichment criteria. Material properties from the top 20% of LNPs in a tissue are divided by the materials properties present in the initial library formulation. These enrichment criteria encompasses both formulation stability as well as *in vivo* performance. (e) Enrichment of all compounds in Top 20% LNPs in lung and kidney endothelial cells in screen 1. 7C1 was significantly enriched. (f) LNP library used for second *in vivo* experiment. PEG alkyl length was varied. (g,h) Enrichment analysis for lung and kidney endothelial cells in an iterative, second LNP screen. Data suggested that lipids with C18 performed poorly in lung endothelial cells. (i) LNP library used for third *in vivo* experiment. Helper lipid type was varied. (j) The ratio of Lung / Kidney endothelial cell delivery for all 3 LNP screens. (k) Correlation between LNP diameter and normalized counts in select cell types in screens 1, 2, and 3.

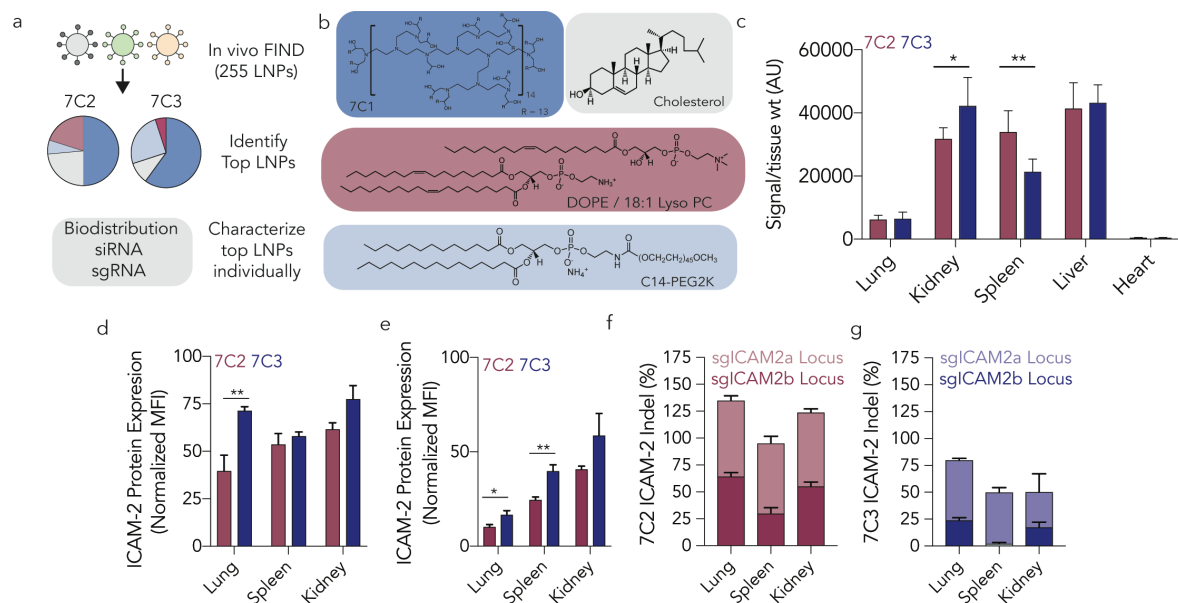
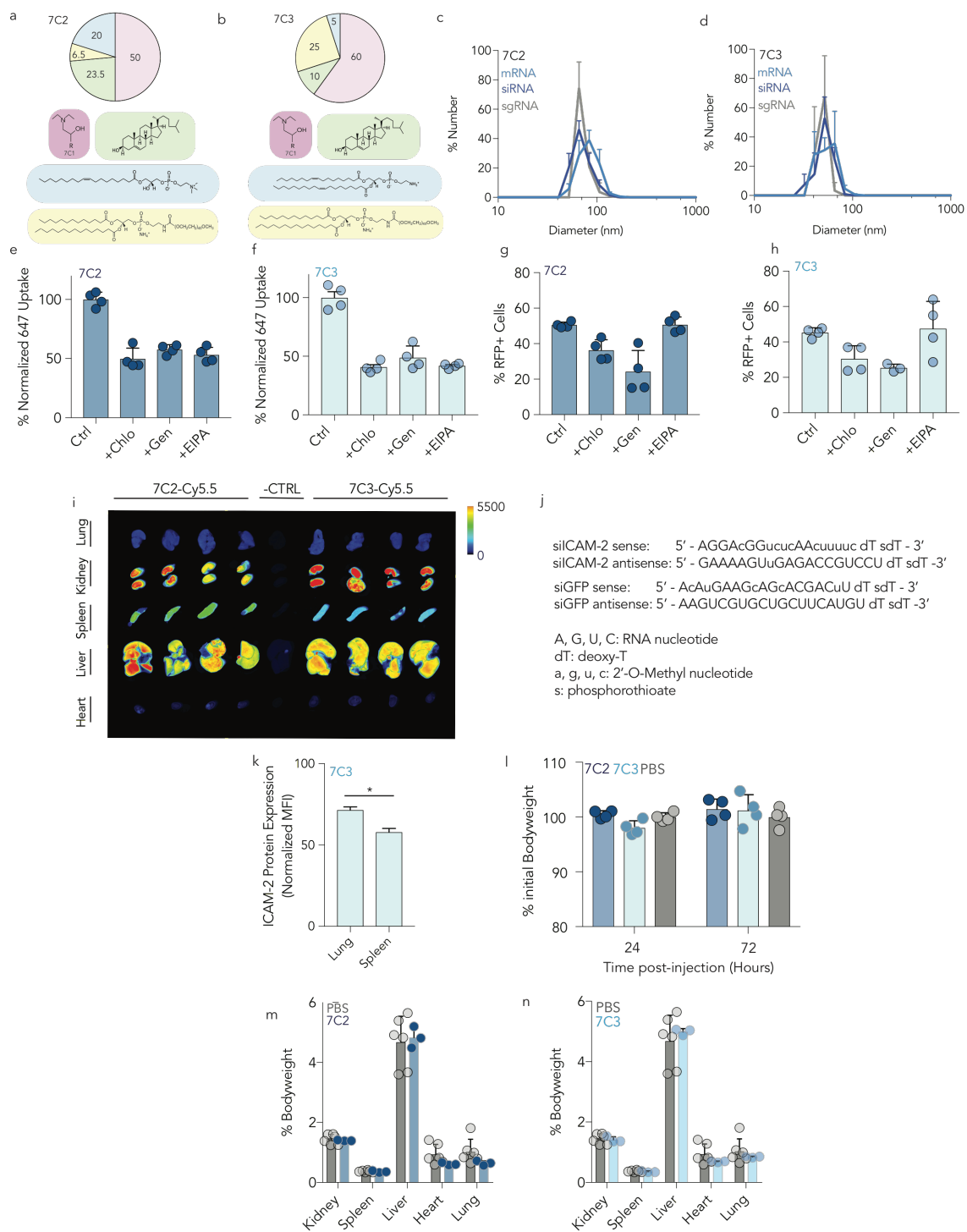


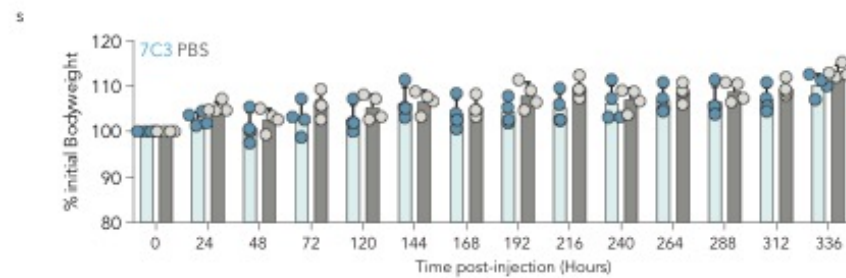
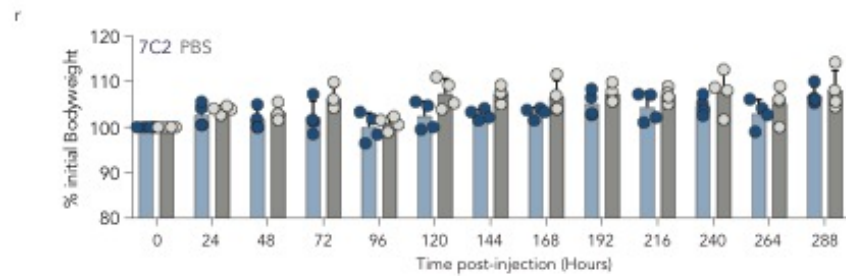
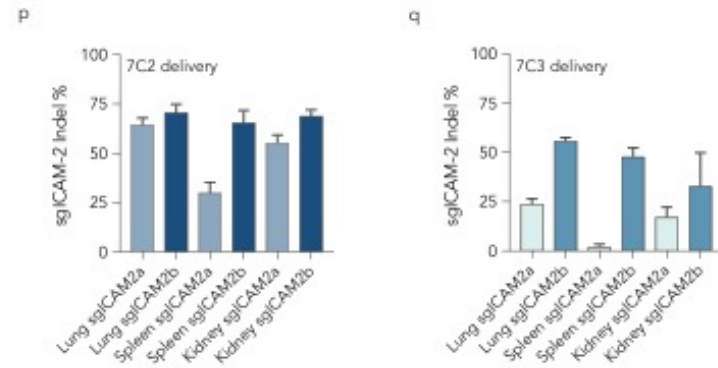
Figure 3.5. Characterization of lead nanoparticles discovered by FIND. (a) Top 2 particles, 7C2 and 7C3, discovered following three rounds of FIND are characterized by measuring biodistribution, delivery of siRNA, sgRNA. (b) 7C2 and 7C3 were comprised of 7C1 compound, cholesterol, C14-PEG2000 and helper lipids, 18:1 Lyso PC and DOPE, respectively. (c) Following a 0.75 mg / kg Barcode-Cy5.5 administration, biodistribution of 7C2 and 7C3 was quantified and normalized to tissue weight. (n=4 mice / group) *p<0.05, **p<0.01, 2-way ANOVA. (d) Following a 1 mg / kg siICAM2 administration, both 7C2 and 7C3 induced ICAM2 protein silencing in endothelial cells by flow cytometry. 7C2 demonstrates more robust protein silencing in lung endothelial cells than 7C3. (n=4 mice / group) **p<0.01, 2 tailed t-test. (e-g) Following repeat administration of 7C2 and 7C3 at 1.5 mg / kg sgICAM2a and sgICAM2b, ICAM2 (e) protein and (f,g) indels were measured in endothelial cells isolated from multiple organs using FACS. (n=3-4 mice / group) *p<0.05, **p<0.01, 2 tailed t-test.



o

sg-ICAM2a 5' gscsusUACCUGGGCUGUAGAACGUUUUAGAGCUAGAA
 AUAGCAAGUAAAAUAAGGCUAGUCCGUUAUCAACUUG
 AAAAAGUGGCACCGAGUCGGUGCusususU 3'

sg-ICAM2b 5' asasgsACGGACAGGCACCUACGGUUUUAGAGCUAGAA
 AUAGCAAGUAAAAUAAGGCUAGUCCGUUAUCAACUUG
 AAAAAGUGGCACCGAGUCGGUGCusususU 3'



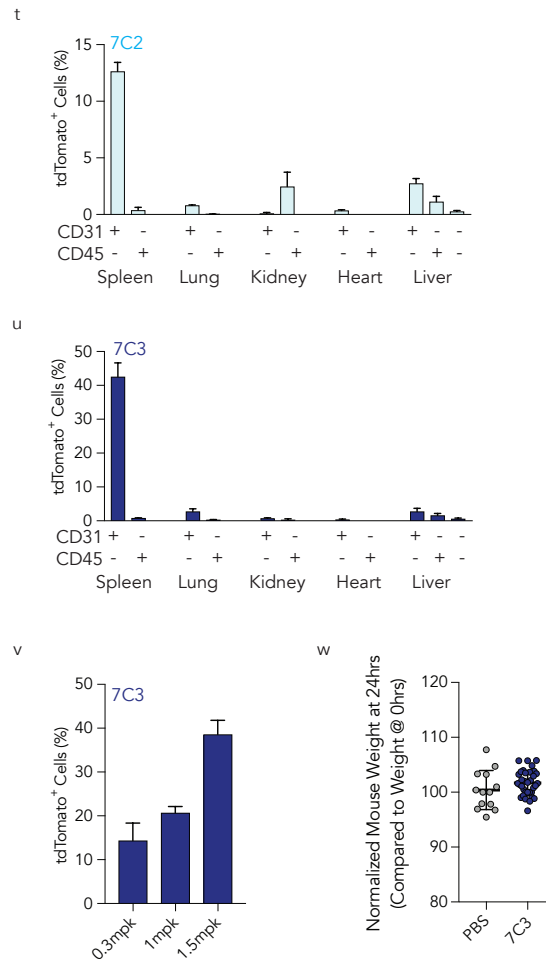


Figure 3.6. (a,b) Compositions of 7C2 and 7C3. (c,d) DLS Spectra of 7C2 and 7C3 encapsulating mRNA, siRNA, and sgRNA. (e,f) Endocytosis of AlexaFluor-647 barcode uptake encapsulated by 7C2 and 7C3 in the presence of chlorpromazine, genistein, and EIPA. (g,h) Delivery of Cre mRNA is inhibited for both 7C2 and 7C3 in the presence of chlorpromazine and genistein, but not EIPA. (i) Barcode-Cy5.5 biodistribution of 7C2 and 7C3 measured in lung, kidney, spleen, liver, and heart by whole tissue *ex vivo* imaging. (j) Sequences and modification patterns of siICAM2 and siGFP used. (k) 7C3 mediates more potent silencing in splenic endothelial cells than lung endothelial cells as measured by ICAM2 MFI 3 days after the administration of 1mg / kg siICAM2 (n= 4 mice / group) *p<0.05, two-tail T-test. (l) Normalized mouse weights 24 and 72hrs after administration of PBS or 2 mg / kg siGFP in 7C2 and 7C3. (m,n) Organ weight comparing PBS to 7C2 and 7C3 72hrs after a 2 mg / kg injection. (o) Sequences of sgICAM2a and sgICAM2b used. (p,q) 7C2 and 7C3 facilitated indel formation at multiple targeting loci of the ICAM-2 gene in endothelial cells of multiple organs when delivering sgRNAs to mice constitutively expressing Cas9. (r,s) Mouse weights for the duration of repeat administration of 7C2- and 7C3- carrying 1.5 mg/

kg sgICAM2ab in mice constitutively expressing cas9. (t) Percentage of tdTomato⁺ cells after a 1.5 mg / kg injection of 7C2 carrying Cre-mRNA. (u) Percentage of tdTomato⁺ cells after a 1.5 mg / kg injection of 7C3 carrying Cre-mRNA. (v) Cre mRNA delivery mediated by 7C3 is dose dependent in splenic ECs. (w) Normalized weights of 34 Ai14 mice injected with 7C3 carrying 1.5 mg / kg of Cre mRNA, comparing weights 24hr after injections to weights immediately prior to injections.

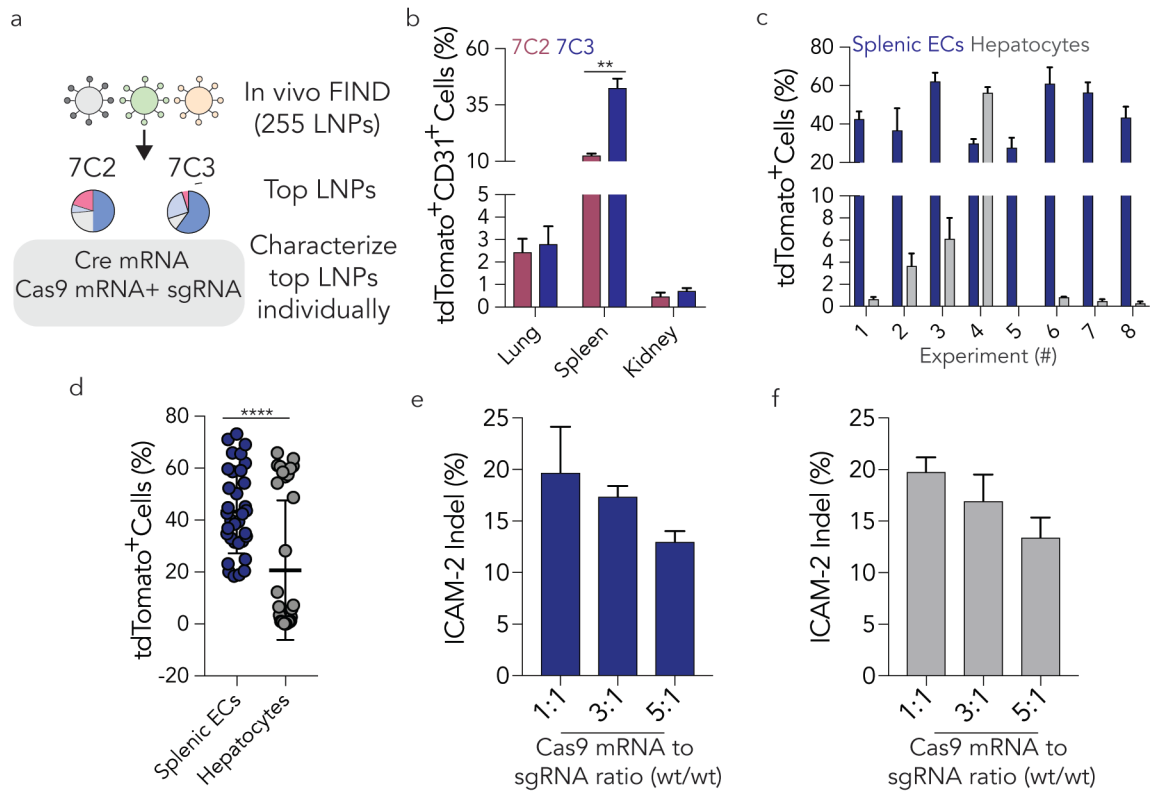


Figure 3.7. (a) Top 2 particles, 7C2 and 7C3, are characterized by delivery of Cre mRNA and co-delivery of Cas9 mRNA & sgRNA. (b) Percentage of tdTomato⁺ endothelial cells in LSL-Tom mice 72 hours after a single 1.5 mg / kg injection of Cre mRNA delivered by 7C2 or 7C3. (n=4 mice / group) **p<0.01, 2 tailed t-test. (c) Percentage of tdTomato⁺ splenic endothelial cells and hepatocytes in LSL-Tom mice following a single 1.5 mg / kg injection of Cre mRNA delivered by 7C3 from 8 independent experiments representing 34 mice. (d) Percentages from all 8 experiments of tdTomato⁺ splenic endothelial cells and hepatocytes in LSL-Tom mice following a single 1.5 mg / kg injection of Cre mRNA delivered by 7C3 (n=34) **p<0.0001, 2 tailed t-test. (e) Indel % in splenic ECs following two injections of 7C3 carrying Cas9 mRNA and e-sgICAM2 at a mass ratio of 1:1, 3:1, and 5:1. (f) Indel % in hepatocytes following two injections of 7C3 carrying Cas9 mRNA and e-sgICAM2 at a mass ratio of 1:1, 3:1, and 5:1.**

a

LNP Name	Compound	PEG Type	Helper Lipid Type	Formulation Ratio (Comp : Chol : PEG : HL)	siRNA induced protein silencing (%)			sgRNA indel rate (%; 2 Loci)			mRNA % TdTom ⁺
					Lung	Spleen	Kidney	Lung	Spleen	Kidney	Spleen ECs
7C2	7C1	C ₁₄ PEG2K	18:1 Lyso PC	50 : 23.5 : 6.5 : 20	60%	47%	34%	135%	95%	124%	13%
7C3	7C1	C ₁₄ PEG2K	DOPE	60 : 10 : 25 : 5	29%	43%	23%	80%	50%	50%	43%

Figure 3.8. (a) Table of composition and efficacy of 7C2 and 7C3.

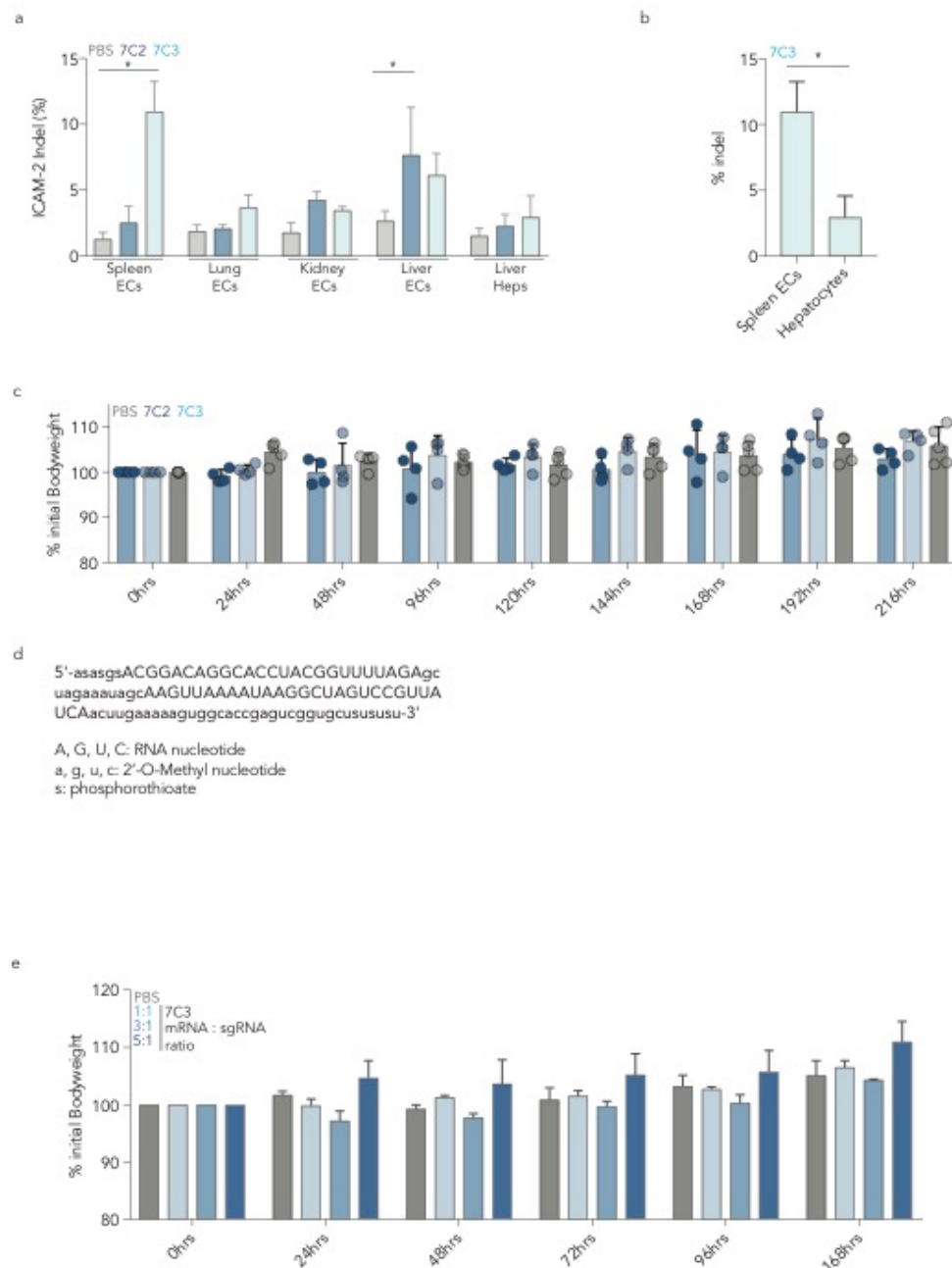


Figure 3.9. (a) ICAM-2 indel percentages following co-delivery of cas9 mRNA and 5' & 3' modified sgICAM2 guides. (b) ICAM-2 indel percentages in splenic endothelial cells and hepatocytes following co-delivery of cas9 mRNA and sgICAM2 guides. 7C3 facilitates more efficient editing in splenic endothelial cells than in hepatocytes. (c) Mouse weights for the duration of repeat administration of 7C2- and 7C3- co-delivering cas9 mRNA and gRNA. (d) Modification pattern of enhanced-sgICAM2

(e-sgICAM2) sequence. (e) Mouse weights for the duration of repeat administration of 7C3- co-delivering cas9 mRNA and hm-sgRNA.

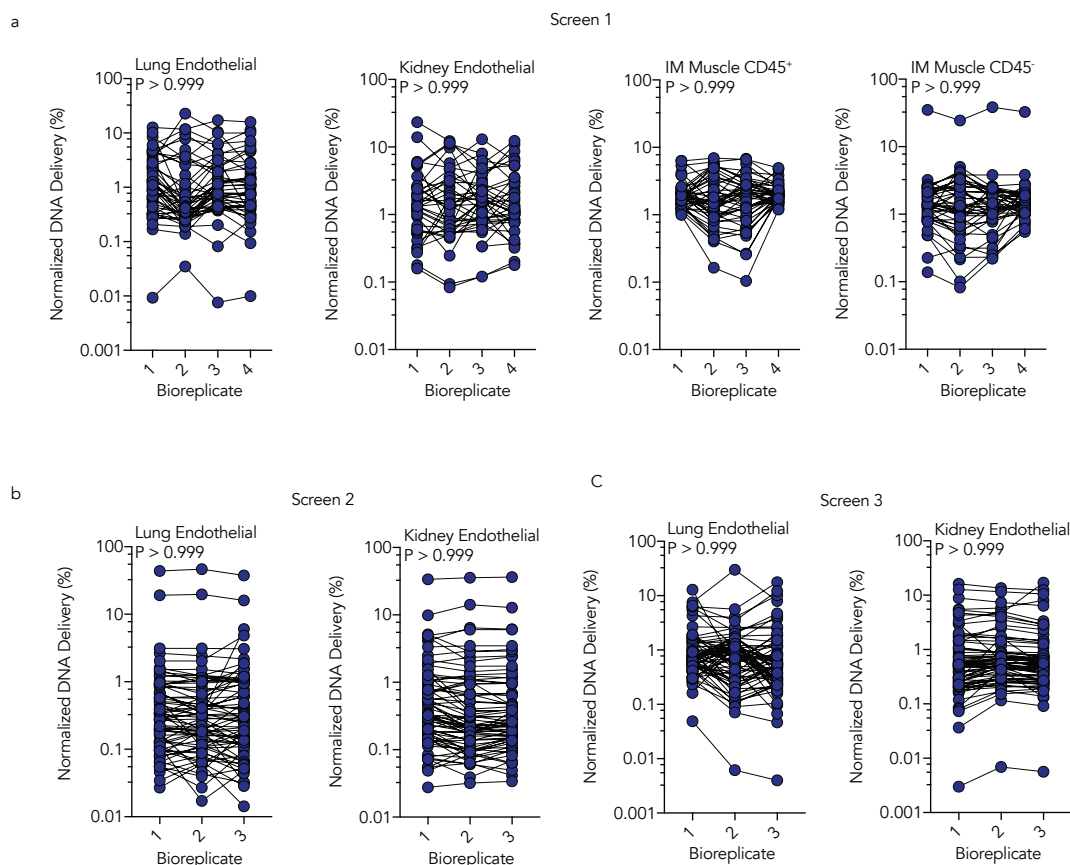


Figure 3.10. Normalized DNA Delivery from all bioreplicates were very similar in (a) Screen 1, (b) Screen 2, and (c) Screen 3. Paired One-Way ANOVA.

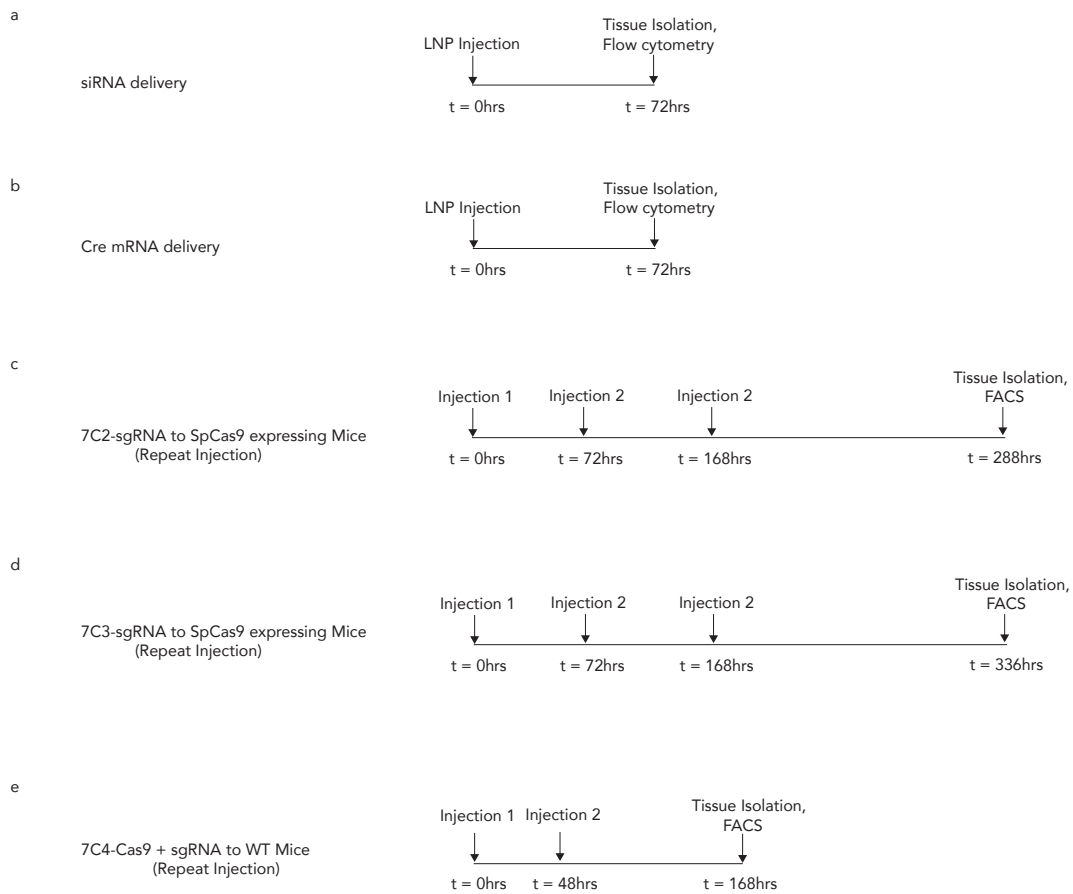


Figure 3.11. Timing of injecting and cell isolation for (a) siRNA injection into C57BL/6 mice, (b) Cre mRNA into Ai14 mice, (c,d) sgRNA injection into mice constitutively expressing SpCas9, and (e) Cas9 mRNA + sgRNA injection into C57BL/6 mice.

a

Representative gating for measuring %tdTomato+ ECs (CD31+CD45-).
Data from ATL2-Cre mRNA Repeat Administration in Spleen.

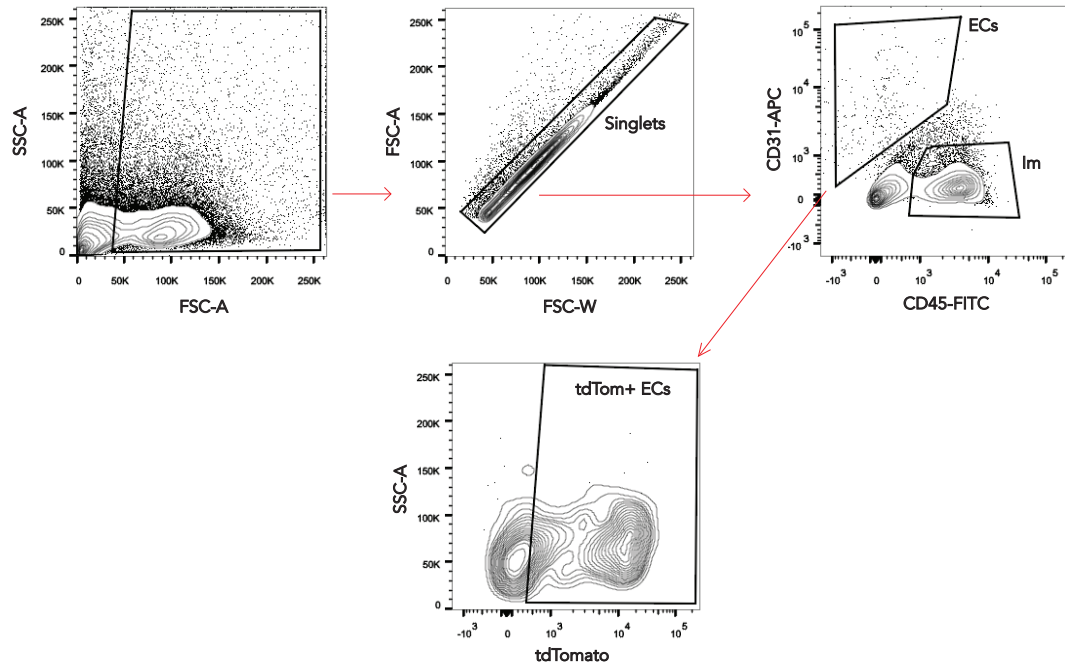


Figure 3.12. (a) Representative gating for measuring %tdTomato+ ECs (CD31+CD45-)

3.4 Methods & Materials

Nanoparticle Formulation. Nanoparticles were formulated using a microfluidic device as previously described²⁶. Briefly, nucleic acids (mRNA, DNA barcodes, siRNA, sgRNA) were diluted in 10mM citrate buffer (Teknova) while lipid-amine compounds, alkyl tailed PEG, cholesterol, and helper lipids were diluted in ethanol. For nanoparticle screens, Cre mRNA and DNA barcodes were mixed at a 10:1 mass ratio. Citrate and ethanol phases were combined in a microfluidic device by syringes (Hamilton Company) at a flow rate of 600 $\mu\text{L}/\text{min}$ and 200 $\mu\text{L}/\text{min}$, respectively. All PEGs, cholesterol, and helper lipids were purchased from Avanti Lipids.

DNA Barcoding. Each chemically distinct LNP was formulated to carry its own unique DNA barcode (**Figure 3.1**). For example, LNP1 carried DNA barcode 1, while the chemically distinct LNP2 carried DNA barcode 2. DNA barcodes were designed rationally with several characteristics, as we previously described (20). 56 nucleotide long single stranded DNA sequences were purchased from Integrated DNA Technologies. The 2 nucleotides on the 5' and 3' ends of the 56-nucleotide ssDNA were modified with phosphorothioates to reduce exonuclease degradation and improve DNA barcode stability. To ensure equal amplification of each sequence, the we included universal forward and reverse primer regions on all barcodes. To monitor for PCR bias, each barcode was also designed with 7 random nucleotides. Each barcode was distinguished using a unique 8 bp sequence. An 8 bp sequence can generate over 4^8 (65,536) distinct barcodes. We used 240 distinct 8 bp sequences designed by to prevent sequence bleaching on the Illumina MiniSeqTM sequencing machine.

Nanoparticle Characterization. LNP hydrodynamic diameter was measured using high throughput dynamic light scattering (DLS) (DynaPro Plate Reader II, Wyatt). LNPs were diluted in sterile 1X PBS to a concentration of $\sim 0.06 \mu\text{g/mL}$, and analyzed. To avoid using unstable LNPs, and to enable sterile purification using a $0.22 \mu\text{m}$ filter, LNPs were included only if they met 3 criteria: diameter $>20 \text{ nm}$, diameter $<200 \text{ nm}$, and correlation function with 1 inflection point. Particles that met these criteria were dialyzed with 1X phosphate buffered saline (PBS, Invitrogen), and were sterile filtered with a $0.22 \mu\text{m}$ filter.

Cell Culture. *In vitro* experiments were performed using HEK.293 cells (GenTarget) stably transduced with a CMV-lox-GFP-stop-lox-RFP construct cultured in DMEM/F-12 50/50 media (Corning) supplemented by 10% (v/v) FBS (VWR) and 1% (v/v) penicillin-streptomycin (VWR). Cells were seeded in a 6-well plate at a density of 300k cells / well. 24 hours later, LNPs were added with a total mRNA dose of 100 ng. 6 hours after transfection, media was refreshed. DNA was isolated using $50 \mu\text{L}$ of QuickExtract (EpiCentre).

Endocytosis Inhibition. For experiments shown in Figure 1 and Supp. Figure 3e-h, cells were incubated with endocytosis inhibitors. Specifically, 1 hour prior to incubation with pooled LNPs, inhibitors of clathrin-mediated endocytosis (chlorpromazine, $100 \mu\text{M}$, Alfa Aesar), caveolae-mediated endocytosis (genistein, $100 \mu\text{M}$, TCI America), and macropinocytosis (5-(N-Ethyl-N-isopropyl) Amiloride, EIPA, $50 \mu\text{M}$, Toronto Research Chemicals) were added to cells.

Animal Experiments. All animal experiments were performed in accordance with the Georgia Institute of Technology's IACUC. LSL-Tomato (#007914), C57BL/6J (#000664)

and constitutive SpCas9 (#026179) mice were purchased from The Jackson Laboratory and used between 5-12 weeks of age. In all experiments, we used N=3-5 mice/group. Mice were injected intravenously via the lateral tail vein or intramuscularly into the quadriceps, tibialis anterior and gastrocnemius. The nanoparticle concentration was determined using NanoDrop (Thermo Scientific). For *in vivo* nanoparticle screens, mice were administered 1.5 mg/kg for intravascular and 1 mg/kg for intramuscular administration. The dosing schedule for each experiment is located in **Figure 3.11**.

Cell Isolation & Staining. Cells were isolated 72 hours after injection with LNPs unless otherwise noted. Mice were perfused with 20 mL of 1X PBS through the right atrium. Tissues were finely cut, and then placed in a digestive enzyme solution with Collagenase Type I (Sigma Aldrich), Collagenase XI (Sigma Aldrich) and Hyaluronidase (Sigma Aldrich) at 37 °C at 550 rpm for 45 minutes. The digestive enzyme for heart and spleen included Collagenase IV (32, 37, 45). Cell suspension was filtered through 70µm mesh and red blood cells were lysed. Cells were stained to identify specific cell populations and sorted using the BD FACS Fusion and BD FACS Aria IIIu cell sorters in the Georgia Institute of Technology Cellular Analysis Core. For *in vitro* experiments, BD Accuri C6 and BD FACS Fusion were used. The antibody clones used were: anti-CD31 (390, BioLegend), anti-CD45.2 (104, BioLegend), anti-CD102 (3C4, BioLegend). PE anti-mCD47 (miap301, BioLegend) was used for tdTomato compensation. Representative flow gates are located in **Figure 3.12**. PBS-injected Ai14 mice were used to gate tdTomato populations for intravenous administration, while contralateral limbs were used to gate for intramuscular experiments.

Biodistribution. LNPs encapsulating Cy5.5-tagged DNA Barcode were administered at 0.75 mg/kg. After 3 hours, tissues were isolated without perfusion, weighed individually, and imaged using the Licor Odyssey CLx imaging system. Signal intensity was normalized to tissue weight.

Endothelial RNA interference. C57BL/6J Mice were injected with 7C2 and 7C3 with PBS, 2 mg/kg siCTRL (siGFP-647) (AxoLabs), or 1 mg/kg siICAM2 (AxoLabs). In all cases, siRNAs were chemically modified at the 2' position to increase stability and negate immunostimulation. Both siGFP and siICAM2 sequences have been previously reported several times(32, 37, 45). 72 hours after injection, tissues were isolated and protein expression was determined via flow cytometry. ICAM2 MFI in PBS-treated mice was normalized to 100 percent, and all treated groups were compared to this control group.

Endothelial Gene Editing. Mice constitutively expressing SpCas9 were injected 3 times with 7C2 or 7C3 carrying 1.5 mg/kg of 2 chemically-modified sgRNAs with three nucleotides modified on the 5' and 5' ends (TriLink Biotechnologies) targeting ICAM2 (sgICAM2ab) (1:1 mass ratio). Separately, C57BL/6J mice were injected 2 times with 2 mg/kg with 7C2 and 7C3 formulated to carry both SpCas9 mRNA (Trilink Biotechnology, L-7206) and sgICAM2ab at a 3:1 mass ratio. 5 days after the last injection, tissues were isolated, and ICAM2 protein expression was measured concurrently while ~20,000 cells were sorted into QuickExtract. Next, C57BL/6J mice were injected 2 times with 2 mg/kg with 7C3 formulated to carry both SpCas9 mRNA (Trilink Biotechnology, L-7206) and e-sgICAM2 (AxoLabs) at a 1:1, 3:1, and 5:1 mass ratio. 5 days after the last injection, tissues were isolated, and ICAM2 protein expression was measured concurrently while

~20,000 cells were sorted into QuickExtract. Indel formation was measured by TIDE (<https://tide-calculator.nki.nl>).

Tissue Immunostaining. Excised organs were fixed overnight in 4% paraformaldehyde (Electron Microscopy Systems) in PBS. Tissues were washed twice in PBS and cryoprotected in 30% sucrose in PBS until the organs sank to the bottom of the container. Organs were then embedded in OCT (Tissue-Tek) and cryosectioned (10 μ m) onto slides. Antigen retrieval was performed on slides for 10 min in a pressure cooker using low pH antigen retrieval solution (Life Technologies). Sections were then permeabilized with 0.2% Triton X-100 (Sigma-Aldrich) in PBS for 10 min at RT before being blocked for nonspecific binding with 5% donkey serum (Sigma-Aldrich) in PBS for 1 hr at RT. Sections were incubated with anti-VE cadherin (BV13, Biolegend), diluted to 0.5 μ g/mL in PBS, overnight at 4 °C. After 3 washes with PBS, sections were incubated at RT with AlexaFluor 647 conjugated donkey anti-rat (Thermo Fisher) diluted in PBS for 2 h. After 2 PBS washes, nuclei were stained with 4',6-diamidino-2-phenylindole (DAPI) (Life Technologies), and coverslips were mounted using Prolong Gold (Life Technologies).

Microscopy. Images were acquired with a Hamamatsu Flash 4.0 v2 sCMOS camera on a PerkinElmer UltraView spinning disk confocal microscope mounted to a Zeiss Axiovert 200M body. Single cell images were acquired using Volocity (PerkinElmer) with Z-stacks taken in 0.2 μ m increments with a 63x NA 1.4 plan-apochromat objective. Stitched images were acquired using a 20x NA 0.8 objective with an automated XY stage (ASI) controlled by Volocity and set to 20% overlap. All images were linearly contrast enhanced.

PCR Amplification. All samples were amplified and prepared for sequencing using a one-step PCR protocol as previously described(20). More specifically, 1 μ L of primers (5 uM for Final Reverse/Forward, 0.5 uM for Base Forward) were added to 5 μ L of Kapa HiFi 2X master mix, and 4 μ L template DNA/water. The reaction was run for 30 cycles. When the PCR reaction did not produce clear bands, the primer concentrations, DNA template input, PCR temperature, and number of cycles were optimized for individual samples.

Deep Sequencing. Illumina deep sequencing was conducted in Georgia Tech's Molecular Evolution core. Runs were performed on an Illumina MiniseqTM. Primers were designed based on Nextera XT adapter sequences.

Data Normalization. Counts for each particle, per tissue, were normalized to the barcoded LNP mixture we injected into the mouse. This 'input' DNA provided the DNA counts, and was used to normalize DNA counts from the cells and tissues.

Data Analysis & Statistics. Sequencing results were processed using a custom python-based tool to extract raw barcode counts for each tissue. These raw counts were then normalized with an R script prior for further analysis. Statistical analysis was done using GraphPad Prism 7; more specifically, 1-tail T-test or One-way ANOVAs were used where appropriate. Data is plotted as mean \pm standard error mean unless otherwise stated.

Data Access. The data, analyses, and scripts used to generate all figures in the paper are available upon request from J.E.D. or dahlmanlab.org.

3.5 References

1. Coelho T, *et al.* (2013) Safety and efficacy of RNAi therapy for transthyretin amyloidosis. *N Engl J Med* 369(9):819-829.
2. Adams D, *et al.* (2018) Patisiran, an RNAi Therapeutic, for Hereditary Transthyretin Amyloidosis. *N Engl J Med* 379(1):11-21.
3. Rizk M & Tuzmen S (2017) Update on the clinical utility of an RNA interference-based treatment: focus on Patisiran. *Pharmacogenomics and personalized medicine* 10:267-278.
4. Bahl K, *et al.* (2017) Preclinical and Clinical Demonstration of Immunogenicity by mRNA Vaccines against H10N8 and H7N9 Influenza Viruses. *Mol Ther* 25(6):1316-1327.
5. Miller JB, *et al.* (2017) Non-Viral CRISPR/Cas Gene Editing In Vitro and In Vivo Enabled by Synthetic Nanoparticle Co-Delivery of Cas9 mRNA and sgRNA. *Angew Chem Int Ed Engl* 56(4):1059-1063.
6. Jiang C, *et al.* (2017) A non-viral CRISPR/Cas9 delivery system for therapeutically targeting HBV DNA and pcsk9 in vivo. *Cell research* 27(3):440-443.
7. Yin H, *et al.* (2017) Structure-guided chemical modification of guide RNA enables potent non-viral in vivo genome editing. *Nat. Biotechnol.*
8. Finn JD, *et al.* (2018) A Single Administration of CRISPR/Cas9 Lipid Nanoparticles Achieves Robust and Persistent In Vivo Genome Editing. *Cell Rep* 22(9):2227-2235.
9. Lee B, *et al.* (2018) Nanoparticle delivery of CRISPR into the brain rescues a mouse model of fragile X syndrome from exaggerated repetitive behaviours. *Nature biomedical engineering*.
10. Lee K, *et al.* (2017) Nanoparticle delivery of Cas9 ribonucleoprotein and donor DNA in vivo induces homology-directed DNA repair. *Nature biomedical engineering* 1:889-901.
11. Gao X, *et al.* (2018) Treatment of autosomal dominant hearing loss by in vivo delivery of genome editing agents. *Nature* 553(7687):217-221.
12. Zuris JA, *et al.* (2015) Cationic lipid-mediated delivery of proteins enables efficient protein-based genome editing in vitro and in vivo. *Nat Biotechnol* 33(1):73-80.
13. Tsoi KM, *et al.* (2016) Mechanism of hard-nanomaterial clearance by the liver. *Nat Mater* 15(11):1212-1221.

14. Zhang YN, Poon W, Tavares AJ, McGilvray ID, & Chan WCW (2016) Nanoparticle-liver interactions: Cellular uptake and hepatobiliary elimination. *J Control Release* 240:332-348.
15. Augustin HG & Koh GY (2017) Organotypic vasculature: From descriptive heterogeneity to functional pathophysiology. *Science* 357(6353).
16. Whitehead KA, *et al.* (2014) Degradable lipid nanoparticles with predictable in vivo siRNA delivery activity. *Nature communications* 5:4277.
17. Paunovska K, *et al.* (2018) A Direct Comparison of in Vitro and in Vivo Nucleic Acid Delivery Mediated by Hundreds of Nanoparticles Reveals a Weak Correlation. *Nano Lett* 18(3):2148-2157.
18. Love KT, *et al.* (2010) Lipid-like materials for low-dose, in vivo gene silencing. *Proceedings of the National Academy of Sciences of the United States of America* 107(5):1864-1869.
19. Semple SC, *et al.* (2010) Rational design of cationic lipids for siRNA delivery. *Nat Biotechnol* 28(2):172-176.
20. Dahlman JE, *et al.* (2017) Barcoded nanoparticles for high throughput in vivo discovery of targeted therapeutics. *Proceedings of the National Academy of Sciences of the United States of America* 114(8):2060-2065.
21. Paunovska K, *et al.* (2018) Analyzing 2000 in Vivo Drug Delivery Data Points Reveals Cholesterol Structure Impacts Nanoparticle Delivery. *ACS nano*.
22. Lokugamage MP, Sago CD, & Dahlman JE (2018) Testing thousands of nanoparticles in vivo using DNA barcodes. *Current Opinion in Biomedical Engineering*.
23. Gilleron J, *et al.* (2013) Image-based analysis of lipid nanoparticle-mediated siRNA delivery, intracellular trafficking and endosomal escape. *Nat Biotechnol* 31(7):638-646.
24. Wittrup A, *et al.* (2015) Visualizing lipid-formulated siRNA release from endosomes and target gene knockdown. *Nat Biotechnol*.
25. Akinc A & Battaglia G (2013) Exploiting endocytosis for nanomedicines. *Cold Spring Harb Perspect Biol* 5(11):a016980.
26. Chen D, *et al.* (2012) Rapid discovery of potent siRNA-containing lipid nanoparticles enabled by controlled microfluidic formulation. *J Am Chem Soc* 134(16):6948-6951.

27. Madisen L, *et al.* (2010) A robust and high-throughput Cre reporting and characterization system for the whole mouse brain. *Nat Neurosci* 13(1):133-140.
28. Zetsche B, *et al.* (2015) Cpf1 is a single RNA-guided endonuclease of a class 2 CRISPR-Cas system. *Cell* 163(3):759-771.
29. Doudna JA & Charpentier E (2014) Genome editing. The new frontier of genome engineering with CRISPR-Cas9. *Science* 346(6213):1258096.
30. Hsu PD, Lander ES, & Zhang F (2014) Development and applications of CRISPR-Cas9 for genome engineering. *Cell* 157(6):1262-1278.
31. Sahay G, *et al.* (2013) Efficiency of siRNA delivery by lipid nanoparticles is limited by endocytic recycling. *Nat Biotechnol* 31(7):653-658.
32. Dahlman JE, *et al.* (2014) In vivo endothelial siRNA delivery using polymeric nanoparticles with low molecular weight. *Nat Nano* 9(8):648-655.
33. Ronan T, Qi Z, & Naegle KM (2016) Avoiding common pitfalls when clustering biological data. *Science signaling* 9(432):re6.
34. Mui BL, *et al.* (2013) Influence of Polyethylene Glycol Lipid Desorption Rates on Pharmacokinetics and Pharmacodynamics of siRNA Lipid Nanoparticles. *Mol Ther Nucleic Acids* 2:e139.
35. Geijtenbeek TB, *et al.* (2000) DC-SIGN-ICAM-2 interaction mediates dendritic cell trafficking. *Nature immunology* 1(4):353-357.
36. Huang MT, *et al.* (2006) ICAM-2 mediates neutrophil transmigration in vivo: evidence for stimulus specificity and a role in PECAM-1-independent transmigration. *Blood* 107(12):4721-4727.
37. Sager HB, *et al.* (2016) RNAi targeting multiple cell adhesion molecules reduces immune cell recruitment and vascular inflammation after myocardial infarction. *Science translational medicine* 8(342):342ra380-342ra380.
38. Hendel A, *et al.* (2015) Chemically modified guide RNAs enhance CRISPR-Cas genome editing in human primary cells. *Nat Biotechnol* 33(9):985-989.
39. Platt RJ, *et al.* (2014) CRISPR-Cas9 knockin mice for genome editing and cancer modeling. *Cell* 159(2):440-455.
40. Brinkman EK, Chen T, Amendola M, & van Steensel B (2014) Easy quantitative assessment of genome editing by sequence trace decomposition. *Nucleic Acids Res* 42(22):e168.

41. Palm W & Thompson CB (2017) Nutrient acquisition strategies of mammalian cells. *Nature* 546(7657):234-242.
42. Kauffman KJ, *et al.* (2018) Rapid, Single-Cell Analysis and Discovery of Vectored mRNA Transfection In Vivo with a loxP-Flanked tdTomato Reporter Mouse. *Mol Ther Nucleic Acids* 10:55-63.
43. Kheirloomoom A, *et al.* (2015) Multifunctional Nanoparticles Facilitate Molecular Targeting and miRNA Delivery to Inhibit Atherosclerosis in ApoE(-/-) Mice. *ACS nano* 9(9):8885-8897.
44. Greineder CF, *et al.* (2018) Site-Specific Modification of Single-Chain Antibody Fragments for Bioconjugation and Vascular Immunotargeting. *Bioconjug Chem* 29(1):56-66.
45. Sager HB, *et al.* (2016) Proliferation and Recruitment Contribute to Myocardial Macrophage Expansion in Chronic Heart Failure. *Circ Res* 119(7):853-864.

CHAPTER 4. DIRECTED EVOLUTION OF LNPS FOR DELIVERY TO BONE MARROW

The work presented here is an excerpt from Sago, CD, Lokugamage, MP, Islam, FZ, Krupczak, BR, Sato, M, Dahlman, JE (2018). “Nanoparticles that deliver RNA to bone marrow identified by *in vivo* directed evolution.” Journal of the American Chemical Society XYZ.

4.1 Background

Small interfering RNAs (siRNAs) can elucidate how genes cause disease. In a typical example, a lipid nanoparticle (LNP) delivers siRNA that inhibits a target gene *in vivo*; this circumvents the need to breed inducible genetic knockout mice, which can take over a year. Nanoparticles that efficiently deliver siRNA to hepatocytes¹⁻³, lung and heart endothelial cells⁴, and immune cells⁵⁻⁸ have been used in this way. For example, a LNP with tropism to hepatocytes delivered siRNAs targeting endolysosomal genes; this uncovered how Rab5 influenced endocytosis⁹. Similar approaches have been applied to hypertension¹⁰, heart disease¹¹⁻¹³, extracellular matrix signaling¹⁴, cancer¹⁵⁻¹⁶, glucose homeostasis¹⁷, and other phenotypes¹⁸⁻¹⁹. In addition to its utility as an *in vivo* scientific reagent, siRNA has treated disease in patients. A systemically administered LNP¹ that delivers siRNA to hepatocytes halted a previously fatal disease in Phase III clinical trials²⁰; clinical programs using other hepatocyte-targeting siRNA delivery systems have generated promising data as well²¹.

These examples underscore the scientific and therapeutic potential of siRNAs when they can be delivered to target cells. However, most cell types cannot be targeted by systemically administered nanoparticles. Foremost amongst these is bone marrow

endothelial cells (BMECs). LNPs can target lung and heart endothelial cells in mice⁴, but nanoparticles have not efficiently delivered siRNA to BMECs in mice. BMECs are important target cells for several reasons. They signal to pericytes, immune cells, and hematopoietic stem cells (HSCs) in the bone marrow microenvironment²² (**Figure 4.1A**). By modulating the bone marrow niche, BMECs may impact heart disease²³, aging²⁴, and other phenotypes. Moreover, BMECs signal differently than hepatic or pulmonary endothelial cells; tissue-specific ‘angiocrine’ signaling is implicated in many diseases but is poorly understood²⁵⁻²⁶. BMECs are difficult to study in large part because manipulating gene expression *in vivo* is challenging.

A method to directly evolve LNPs with novel tropisms *in vivo* would facilitate *in vivo* studies and RNA therapies. However, most LNPs display an affinity for the liver; this is thought to be driven by physiological advantages including slow blood flow²⁷⁻²⁸ and discontinuous vasculature in hepatic sinusoids²⁵. As a result, systemically administered RNA delivery to non-liver organs remains challenging²⁹. One unexplored contributor to LNP liver tropism is the process by which LNPs are selected. Like all nanoparticles, LNPs are initially tested *in vitro*, before a few lead LNPs are tested *in vivo*. However, *in vivo* LNP delivery is influenced by factors absent in cell culture³⁰⁻³¹: liver / kidney / spleen / immune clearance, blood flow²⁷, and physical structures that disassemble nanoparticles³². We compared *in vitro* and *in vivo* nanoparticle biodistribution mediated by >300 LNPs and found no relationship in endothelial cells or macrophages³³. However, *in vitro* nanoparticle delivery can predict hepatocyte delivery³⁴. If *in vitro* delivery predicts hepatocyte delivery (but not endothelial cell delivery), this may help explain why LNPs selected *in vitro* target hepatocytes *in vivo*.

Testing hundreds of LNPs *in vivo* could accelerate the discovery of LNPs targeting new cell types. Our lab^{33, 35-36} and others³⁷ have designed *in vivo* nanoparticle screens with DNA barcodes. Barcoding studies have identified liposomes for tumor delivery³⁷, compared *in vitro* and *in vivo* delivery³³, and uncovered how cholesterol structure influences LNP targeting. However, these studies quantify the delivery of chemotherapeutic small molecule delivery into the tumor, or alternatively, nanoparticle biodistribution. An ideal system would quantify how many LNPs functionally deliver small RNA into the cytoplasm of target cells. The distinction between nanoparticle biodistribution (where the LNP goes) and cytosolic delivery (where the RNA drug works) is crucial; over 95% of the siRNA that reaches a target cell is degraded or exocytosed³⁸⁻³⁹. Since endosomal escape is inefficient and cell-type dependent⁴⁰, it is difficult to predict functional delivery using biodistribution.

Here we report the first screening system capable of simultaneously quantifying how >100 LNPs functionally deliver siRNA to cells *in vivo*. We studied 160 LNPs over the course of 2 experiments, using bioinformatics to ‘evolve’ a LNP that targets BMECs. BMEC targeting did not depend on LNP size; instead, LNPs were targeted to BMECs by varying the chemical structure of a poly(ethylene glycol) (PEG) and the helper lipid 1,2-distearoyl-sn-glycero-3-phosphocholine (DSPC). The LNP, named BM1, is the first nanoparticle to efficiently deliver siRNA and sgRNA to BMECs *in vivo*, demonstrating that directed evolution can identify LNPs with novel tropisms.

4.2 Results

We performed a literature search (**Figure 4.2A**) to identify nanoparticles that systemically delivered siRNA to endothelial cells in different tissues. We found multiple nanoparticles that have been reported to deliver siRNA to endothelial cells in the lung, heart, kidney, liver, lymph nodes, spleen, brain, and pancreas. An ionizable LNP named 7C1 we reported⁴ was the most efficient siRNA delivery vehicle for lung, heart, and kidney endothelial cells in our search, silencing target genes by 50% after systemic siRNA doses as low as 0.02 mg / kg (**Figure 4.1B**). No LNPs in our search targeted BMECs after systemic administration. Based on this, we synthesized the 7C1 lipid as we described⁴, and investigated whether the ‘original’ 80: 20 formulation silenced BMECs *in vivo*. We formulated LNPs by combining the 7C1 ionizable lipid (**Figure 4.2B**) with C₁₄PEG₂₀₀₀ at a molar ratio of 80: 20; the mass ratio of 7C1 and PEG to siRNA was 5:1 as reported. We injected mice with siRNA targeting Luciferase (siLuc, the control group) or ICAM-2 (siICAM-2). Both validated^{4, 11-12} siRNAs were chemically modified to minimize off-target gene silencing and reduce immunostimulation (**Figure 4.2C**). We injected mice intravenously with a 1.0 mg / kg dose of siRNA, waited 3 days, isolated endothelial cells (CD31⁺CD45⁻) from bone marrow, lung, and heart using fluorescence activated cell sorting (FACS), and quantified ICAM-2 protein expression using mean fluorescent intensity (MFI) (**Figure 4.2D**). As expected, ICAM-2 protein expression was reduced in lung and heart endothelial cells isolated from mice treated with siICAM-2, relative to mice treated with the siLuc control. ICAM-2 protein expression did not change in BMECs (**Figure 4.1C**), demonstrating the 80: 20 7C1 formulation did not target BMECs.

We hypothesized BMEC tropism could be impacted by the (i) size of the 7C1 LNP or the (ii) chemical composition of the PEG and ‘helper lipids’ added into the LNP. The chemical composition hypothesis was substantiated by evidence that PEG structure influences pharmacokinetics of liver-targeting LNPs *in vivo*⁴¹. Given that *in vitro* nanoparticle delivery to endothelial cells does not predict *in vivo* nanoparticle delivery to endothelial cells³³, we tested our hypothesis *in vivo*. We reasoned that – like AAV delivery systems - *in vivo* directed evolution could identify LNPs efficiently by refining the ‘chemical space’ which we were investigating (**Figure 4.1D**). This approach has been an important advance in AAVs; directed evolution has identified viruses that deliver genes to the brain⁴², eye⁴³, liver⁴⁴, and other tissues⁴⁵. Refining the LNP chemical space is important; between 100 million and 200 billion chemically distinct LNPs could be formulated with validated chemistries⁴⁶.

We designed and validated a high throughput barcoding system to simultaneously quantify how >100 LNPs functionally delivered siRNA *in vivo*. This screening system is distinct from previous barcoding approaches, which quantify biodistribution (**Figure 4.3A**). We used a validated high throughput microfluidics platform to formulate LNP-1, with chemical structure 1, so it carried siICAM-2 and barcode 1. We repeated this process N times, formulating LNP-N, with chemical structure N, to carry siICAM-2 and barcode N. The size and stability of all N LNPs was tested individually using dynamic light scattering (DLS); stable LNPs with hydrodynamic diameters between 20 and 200 nm were pooled together (other LNPs were discarded). The mass ratio of the siRNA: DNA barcode was 10:1. To identify LNPs that functionally delivered siICAM-2 into the cytoplasm, we pooled the stable LNPs together, administered them to mice intravenously, waited 3 days,

and isolated ICAM-2^{Low} endothelial cells (i.e., cells with low ICAM-2 MFI) from bone marrow using FACS. We isolated and amplified the barcodes using universal primers and performed deep sequencing to identify barcode sequences that were enriched in the ICAM-2^{Low} cells (**Figure 4.3A**). We quantified ‘normalized delivery’ of each barcode; normalized delivery is a calculation of the times each individual barcode is found in a sample, divided by the sum of all barcode counts in that sample (**Figure 4.2E**). Normalized delivery is analogous to counts per million in RNA-seq experiments and can be used to quantify LNP biodistribution^{33, 35}. Normalized DNA delivery is different than the % dose injected / g tissue, a common parameter used to quantify nanoparticle biodistribution. Specifically, normalized delivery quantifies how efficiently a barcode was delivered, relative to all other nanoparticles tested. For example, if barcode 10 is twice as abundant as barcode 11, then we hypothesize nanoparticle 10 delivered the barcode twice as efficiently as barcode 11.

We rationally designed the DNA barcodes (**Figure 4.2F**). Specifically, we designed DNA barcodes with minimal 2° structure and G-quadruplex formation by separating our previously reported randomized 7 nucleotide region³⁵ into semi-randomized NWNH and NWH site. This increased DNA polymerase access during barcode amplification. We also included universal primer sites so all the barcodes were amplified with 1 set of primers (**Figure 4.2G**). The ‘barcode region’ of the DNA barcode was 8 nucleotides and located in the middle of the sequence. We designed the barcodes with a base distance of 3; each barcode was distinct from all other barcodes at 3 of the 8 positions. Using a QC score of 30, this reduced the odds of a ‘false call’ by the Illumina Sequencing machines to less than 1 / 10⁹. Of the 65,536 (i.e., 4⁸) potential barcode combinations, we selected 156 which

would work together on Illumina sequencers. We also flanked the primer sites with 3 additional phosphorothioate-modified nucleotides to reduce exonuclease degradation.

We performed control experiments to evaluate whether co-formulating the barcode and a siRNA into the LNP would affect delivery. First, we formulated LNPs with siRNA or siRNA + barcode, and measured size with DLS; there was no difference (**Figure 4.2H**). As a second control experiment, we formulated the '80: 20' 7C1 formulation with barcodes and a control siRNA (siLuc) or barcodes and siICAM-2. Control mice were injected with 1.5 mg / kg total nucleic acid, while experimental mice were injected with a total nucleic acid dose of either 1.5, 0.5, or 0.16 mg / kg. Seventy-two hours after injection, lung endothelial cells were isolated and ICAM-2 protein expression was quantified as MFI using flow cytometry. As expected, we observed a dose-dependent increase in ICAM-2 protein silencing as the siICAM-2 dose increased (**Figure 4.3B,C**). We also observed an increase in the number of endothelial cells that were ICAM-2^{Low} (**Figure 4.3D**). These data suggested that LNP-mediated delivery of siICAM-2 and barcode silenced target genes as expected *in vivo*.

To test the hypothesis that BMEC tropism was impacted by altering LNP size or LNP chemical composition of the PEG and 'helper lipids', we designed a library of LNPs consisting of 7C1, cholesterol, and 5 different lipid-PEGs (**Figure 4.4A,B**, **Figure 4.5A**). We investigated how PEG molecular weight (2000 and 3000 Da) affected delivery; PEG molecular weight can change PEG conformation at the LNP surface, which can alter interactions between nanoparticles and the body⁴⁷. We also varied the lipid tails in the PEG (fully saturated with 14, 16, or 18 carbons). This can change 'on / off kinetics' of PEG by altering the stability with which the hydrophilic PEG is 'anchored' into the LNP

membrane⁴¹. Each PEG type was formulated into 24 distinct formulations with 7C1 and Cholesterol (**Figure 4.4C**). Of the 120 LNPs formulated to carry siRNA and barcode, 115 were stable, with diameters between 20 and 200nm. These 115 LNPs were pooled together and intravenously injected at a total nucleic acid dose of 1.5 mg / kg. As a control, we compared the diameter of the pooled LNPs (53 nm) to the individual LNPs making up the pool, and found they were similar (**Figure 4.4D**). We included 2 additional negative controls, which were 2 naked barcodes. As expected, the normalized delivery of both naked barcode controls in ICAM2^{Low} BMECs was lower than the normalized delivery for all barcodes delivered by LNPs (**Figure 4.4E**).

We tested the hypothesis that LNP size affected BMEC tropism. We plotted normalized delivery against the diameter for all 115 LNPs and observed no correlation ($R^2=0.06$) (**Figure 4.4F**). To exclude the possibility these results were an artifact of testing many LNPs, we plotted normalized delivery against diameter for the top and bottom 10%; once again, we found no relationship (**Figure 4.4G**). Finally, we plotted the size of the top and bottom 10% and found no statistical difference (**Figure 4.4H**). Taken together, this evidence did not support our size-based hypothesis. We then tested the hypothesis that LNP chemical composition affected BMEC tropism. We analyzed the material characteristics of top performing LNPs. Specifically, we looked for material properties that were enriched in the top 10% LNPs. An example calculation (which does not include real data) for enrichment is shown in **Figure 4.5B**. In top-performing LNPs, we observed an enrichment of nanoparticles with either low (1-2.5%) or high (15-20%) PEG mole percent (**Figure 4.6A**). Additionally, we observed that nanoparticles containing either C₁₆PEG₂₀₀₀ or C₁₈PEG₂₀₀₀ were enriched (**Figure 4.6B**). To further confirm that PEG structure influenced

delivery, we performed a paired analysis, comparing normalized delivery of LNPs that had identical ratios of 7C1, cholesterol, and PEG, but had either C₁₈PEG₂₀₀₀ or C₁₈PEG₃₀₀₀. C₁₈PEG₂₀₀₀ performed significantly better compared to C₁₈PEG₃₀₀₀ (**Figure 4.6C**). Taken together, this provided preliminary evidence to support the hypothesis that LNP composition affected BMEC targeting more than size. To confirm that our screening methodology could be used to identify LNPs that functionally deliver siRNA to BMECs, we formulated the top performing LNP to carry both siLuc and siICAM-2 (**Figure 4.5C**). We intravenously injected mice with 1.0 mg / kg siRNA and measured ICAM-2 MFI on BMECs by flow cytometry. We observed a 16% reduction in ICAM-2 MFI with the winner from screen 1 (**Figure 4.5D**), which was 2.2-fold more potent (**Figure 4.5E**) than the ‘original’ 80:20 formulation (**Figure 4.1B**).

To further identify LNPs with improved potency in BMECs, we designed a second LNP library that was evolved from the first; the second library was informed by our PEG enrichment data. More specifically, LNPs for library 2 were made with 7C1, cholesterol, and either C₁₆PEG₂₀₀₀ or C₁₈PEG₂₀₀₀. In some formulations, we also included DSPC (**Figure 4.7A**, **Figure 4.5F**), since DSPC may improve the encapsulation of nucleic acids⁴⁸, and may alter how nanoparticles interact with serum proteins in the ‘protein corona’⁴⁸. We formulated LNPs with 20 distinct molar ratios (**Figure 4.7B**). Of the 40 formulated, 31 formed stable nanoparticles with diameters between 20 and 200 nm. These stable LNPs were pooled together; as a control, we compared the diameter of the pooled LNPs (43 nm) to the individual LNPs, and found they were similar (**Figure 4.5G**). Pooled LNPs were administered to mice at a total nucleic acid dose of 1.5 mg / kg. Three days later, we isolated ICAM-2^{Low} BMECs using FACS, and sequenced the barcodes. We made several

observations that gave us confidence in the results. The first observation was that ICAM-2 silencing in the second library was ~1.5x more robust than the first library (**Figure 4.7C**). This suggested our second library contained more potent LNPs than the first. We noted that the experimental variance in potency of the second library was larger than the variance in the first; we analyzed mouse weight, sex, and age (**Figure 4.5H**), but were unable to come up with a specific hypothesis for this observation except for normal experimental variance *in vivo*; furthermore, the delivery of individual LNPs to ICAM-2^{Low} BMECs was consistent between technical replicates in both library 1 and 2 by paired One-way ANOVA (**Figure 4.5I,J**). Both library 1 and 2 were well tolerated (**Figure 4.5K,L**)

The second observation was that both negative controls (naked barcodes) once again had lower normalized delivery than all barcodes carried by LNPs (**Figure 4.7D**). Third, we observed size and chemical composition results that were consistent with library 1. Specifically, we analyzed the relationship between LNP size and delivery, and observed no correlation between the size of all 31 LNPs and delivery (**Figure 4.7E**). We did not observe any relationship between the normalized delivery and size for the top and bottom 10% (**Figure 4.7F**), and there was no statistical difference in size between the top and bottom 10% (**Figure 4.7G**). We next analyzed which chemical characteristics were enriched in the top 10% of LNPs. When we analyzed LNP chemical composition, we found LNPs with high PEG percentages (15 to 20%) were enriched (**Figure 4.7H**), as were LNPs with C₁₈PEG₂₀₀₀ (**Figure 4.7I**). Additionally, LNPs formulated with 80 mole % 7C1 (**Figure 4.7J**), 0% DSPC (**Figure 4.7K**), and 0.1 – 10 % cholesterol were enriched (**Figure 4.7L**). These enrichment data suggested that a 7C1-based nanoparticle with formulation molar ratio of 80% 7C1 : 0.1-10 % cholesterol : 15 – 20% C₁₈PEG₂₀₀₀ would be highly

active in BMECs. We then tested the top 3 LNPs found in screen 2 (**Figure 4.8A**). Notably, all 3 reduced ICAM-2 expression in BMECs more than (i) 7C1 and (ii) the top performing LNP from screen 1 (**Figure 4.8B**).

Interestingly, we noticed that the chemical composition of the top performing individual LNP (BM1) exactly matched the enriched chemical characteristics from Figure 5 (**Figure 4.9A**). We then selected the top performing LNP from library 2, and compared its (i) chemical composition, (ii) physical traits, (iii) *in vitro* uptake mechanism, and most importantly, (iv) ability to functionally deliver siRNA / sgRNA that manipulate BMEC gene expression *in vivo* (**Figure 4.9**) to that of ‘original’ 80:20 7C1. Both 7C1 and BM1 formed stable LNPs with diameters between 45-50 nm and had a narrow polydispersity index (PDI) (**Figure 4.9B**). BM1 was also stable for over 10 days when stored at 4°C (**Figure 4.8C**). Additionally, the pKa of each LNP was between 6.45 and 6.55, indicating that each has a net neutral charge in blood (pH = 7.4) (**Figure 4.9B, Figure 4.8D,E**), but could become cationic in early endosomes. To measure how ‘original’ 7C1 and BM1 are endocytosed *in vitro*, we formulated both ‘original’ 80:0:20 7C1 and BM1 to carry siGFP tagged with AlexaFluor647 and applied each LNP at a dose of 20 nM siRNA to Immortalized Mouse Aortic Endothelial Cells (iMAECs). iMAECs are endothelial cells that are freshly isolated from mice; they recapitulate important endothelial phenotypes⁴⁹. After 1 hour, cells were washed and siRNA uptake was measured by flow cytometry. BM1 endocytosis was 40% less than 7C1 (**Figure 4.9C**). When cells were pre-treated by genistein (caveolin-inhibitor) and chlorpromazine (clathrin-inhibitor), endocytosis of 7C1 decreased by at least 40%; however, BM1 endocytosis only decreased in the presence of chlorpromazine, relative to cells not treated with inhibitors (**Figure 4.9D, Figure 4.8F,G**).

We next tested the potency of BM1 at delivering siRNA to BMECs *in vivo*. We intravenously injected BM1 at a dose of 1 mg / kg siRNA; after 3 days, we isolated bone marrow and measured ICAM-2 MFI using flow cytometry. Compared to BMECs from mice treated with BM1 carrying siLuc, mice treated with BM1 carrying siICAM-2 showed 37% protein silencing (**Figure 4.9E,F**). This represents a 4.8x increase in potency compared to original 7C1.

Given that we specifically evolved BM1 to target BMECs, we compared its potency to original 7C1 in lung and heart endothelial cells. We observed no difference in potency between 7C1 and BM1 in these tissues (**Figure 4.9G**). We then quantified biodistribution of 7C1 and BM1 using QUANT, a highly sensitive ddPCR-based method⁵⁰. Specifically, we quantified DNA barcode biodistribution in lung, heart, and bone marrow ECs, as well as CD34⁺ hematopoietic stem and progenitor cells (HSPCs) in the bone marrow (**Figure 4.8H,I**). Biodistribution to BMECs increased 4.7x in mice treated with BM1, relative to original 7C1 formulation (**Figure 4.8J**). We did not observe significant differences in biodistribution in the other analyzed cell types. These biodistribution data were similar to the relative siRNA-mediated gene silencing we observed.

Confident that BM1 could potentially deliver siRNA to BMECs, we next tested if it could also deliver sgRNA. We formulated BM1 at a dose of 1 mg / kg carrying an sgRNA targeting ICAM-2 and intravenously injected into mice constitutively expressing SpCas9⁵¹. This sgRNA was chemically modified with three phosphorothioates on each termini and 2'-O-methyl ribose modifications at select positions (**Figure 4.8K**)⁵². Five days after injection, we isolated BMECs and CD34⁺ HSPCs and measured indels at ICAM-2 via Tracking Indels by Decomposition (TIDE). BM1 led to a 15% indel (insertions and

deletions) rate in BMECs (**Figure 4.9H**) and undetectable levels of indels in CD34⁺ HSPCs (**Figure 4.8L**). BM1 was well tolerated in mice with both siRNA and sgRNA (**Figure 4.8M, N**).

4.3 Discussion

The first systemically administered siRNA therapy was approved in August 2018²⁰. In this system, siRNAs are delivered to hepatocytes using an ionizable LNP¹. This illustrates the clinical potential of RNA therapeutics and highlights the need for ‘non-liver’ RNA delivery vehicles. The nanomedicine field is well positioned to make advances in non-liver delivery; thanks to important advances in nanoparticle synthesis, between 100 million and 200 billion chemically distinct nanoparticles can be formulated using available materials. However, nanoparticles must still be tested laboriously 1 by 1 *in vivo*. And as a result, most nanoparticles are only tested *in vitro*, which leaves many potential therapeutic molecules undiscovered.

Here we report that co-formulating a DNA barcode and siRNA into the same LNP can facilitate high throughput screens that quantify functional cytoplasmic siRNA delivery. This approach can help scientists in several ways. First, over the course of several experiments, it is possible to study thousands of nanoparticles deliver siRNA to any combination of cells. This could accelerate the discovery of new nanomedicines. Notably, we predict that it will eventually be feasible to study how up to 500 LNPs deliver siRNA in a single mouse. Second, we envision studies designed to systematically identify the traits that alter nanoparticle targeting directly *in vivo*. In this example, we tested two hypotheses: LNP (1) size or (2) chemical properties affect targeting. Over the course of our

experiments, we consistently found no evidence to support hypothesis 1 and multiple lines of evidence to support hypothesis 2. Interestingly, our data suggested that making seemingly small changes to the LNP formulation – in our case changing the lipid tail of the PEG, and adding cholesterol - altered nanoparticle tropism. Notably, minor changes to PEG composition have altered the pharmacokinetics and function of liver-targeting LNPs⁴¹. However, the mechanisms mediating this effect remain unclear. In future studies, we hope to test two hypotheses. First, that PEG on / off rates in serum are altered by changing the lipid tail of the PEG. Second, that the inclusion of cholesterol alters the serum lipoproteins to which the LNP binds. It is also possible that both hypotheses are incorrect, and instead, that an yet to be discovered, multivariate effect is causing these effects. Broadly, these data suggest that LNP targeting can be altered making small changes to the chemical composition, which may offer a simple alternative⁵² to traditional approaches, which rely on active targeting ligands⁵³⁻⁵⁵. These data substantiated by other recent reports^{41, 56}, but need to be validated in other labs. If vascular tropism can be altered by simple changes to the LNPs, then these data will be helpful by informing the number of physical and chemical variables that need to be considered when formulating chemically diverse nanoparticle libraries.

It is important to note several limitations with the current study. First, this screening system will not work with toxic or unstable nanoparticles. Second, like all DNA-based screens, it is important to include all the controls we have described herein. Third, we only used two iterative libraries; we believe future iterative libraries will be able to identify LNPs with even greater BMEC tropism. Finally, given the size of these datasets, it will be important to collaborate with ‘big data’ scientists, to understand which new, cutting edge

bioinformatic approaches can be applied to these *in vivo* delivery datasets. Even with these nuances, we believe this methodology offers a solution to many technical / practical issues that impede the translation of new nanoparticles into the clinic.

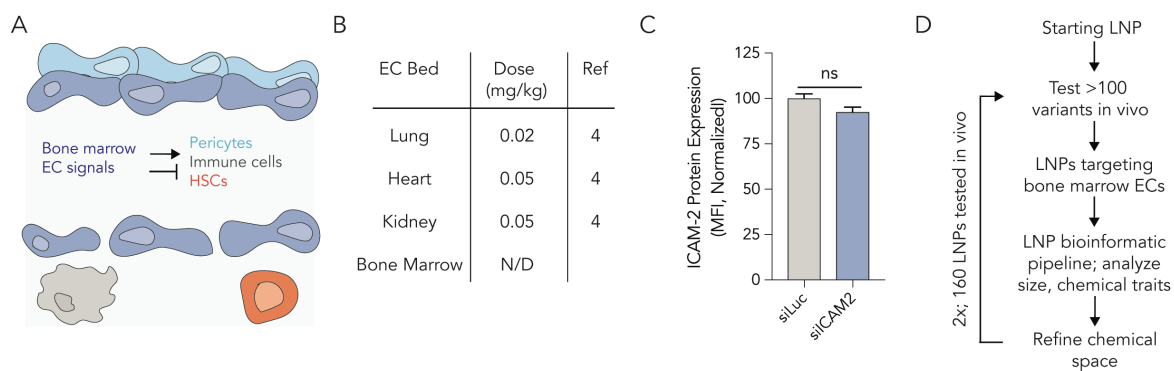


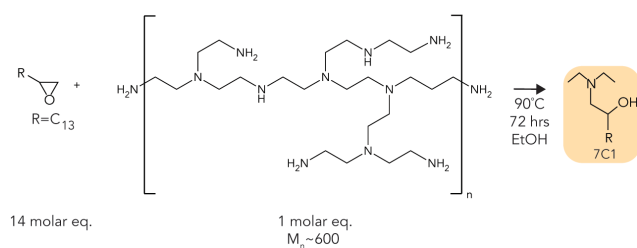
Figure 4.1. Systemically delivering RNA to bone marrow endothelial cells (BMECs) is challenging. (A) BMECs release local signals that regulate pericytes, immune cells, and hematopoietic stem cells in the bone marrow ‘niche’. (B) The dose (mg / kg siRNA) required to silence target gene expression in different vascular beds *in vivo*. BMECs are targeted much less efficiently than other vascular beds. (C) ICAM-2 protein expression after mice were treated with siLuciferase or siICAM-2 carried by the nanoparticle 7C1; the ‘original 80: 20’ 7C1 formulation does not deliver siRNA to BMECs. (D) A methodology to improve LNP delivery to BMECs; this utilizes an iterative high throughput *in vivo* screening method.

Citation	Lung	Heart	Kidney	Target	Protein or mRNA
https://onlinelibrary.wiley.com/doi/epdf/10.1002/adhm.201400054	65% @ 1.25 mg / kg	-	-	Tie2	mRNA
https://onlinelibrary.wiley.com/doi/abs/10.1002/anie.201408221	35% @ 2.5 mg / kg	-	-	Tie2	mRNA
https://pubs.acs.org/doi/pdf/10.1021/nl5048972	95% @ 2.5 mg / kg	-	-	Tie2	mRNA
https://www.nature.com/articles/nnano.2014.84	90% @ 0.05 mg / kg	85% @ 0.6 mg / kg	80% @ 0.6 mg / kg	ICAM2	mRNA
https://www.ncbi.nlm.nih.gov/pmc/articles/PMC3982492/	80% @ 2.8 mg / kg	20% @ 2.8 mg / kg	25% @ 2.8 mg / kg	Tie2	mRNA
https://pubs.acs.org/doi/abs/10.1021/acsnano.8b03640	-	-	-	ICAM2	Pro
https://www.nature.com/articles/3302777	60% @ 1.9 mg / kg	30% @ 1.9 mg / kg	-	Tie2	mRNA
https://www.cell.com/action/showPdf?pii=S1525-0016%2816%2932706-X	-	-	-	OAT3	mRNA

Citation	Liver	Spleen	Pancreas	Target	Protein or mRNA
https://onlinelibrary.wiley.com/doi/epdf/10.1002/adhm.201400054	60% @ 1.25 mg / kg	50% @ 1.25 mg / kg	-	Tie2	mRNA
https://onlinelibrary.wiley.com/doi/abs/10.1002/anie.201408221	80% @ 1 mg / kg	25% @ 2.5 mg / kg	-	Tie2	mRNA
https://pubs.acs.org/doi/pdf/10.1021/nl5048972	-	85% @ 2.5 mg / kg	50% @ 2.5 mg / kg	Tie2	mRNA
https://www.nature.com/articles/nnano.2014.84	40% @ 0.15 mg / kg	-	-	ICAM2	mRNA
https://www.ncbi.nlm.nih.gov/pmc/articles/PMC3982492/	40% @ 2.8 mg / kg	-	-	Tie2	mRNA
https://pubs.acs.org/doi/abs/10.1021/acsnano.8b03640	75% @ 1.5 mg / kg	-	-	ICAM2	Pro
https://www.nature.com/articles/3302777	70% @ 1.9 mg / kg	-	-	Tie2	mRNA
https://www.cell.com/action/showPdf?pii=S1525-0016%2816%2932706-X	-	-	-	OAT3	mRNA

Citation	Lymph Node	Brain	Target	Protein or mRNA
https://onlinelibrary.wiley.com/doi/epdf/10.1002/adhm.201400054	-	-	Tie2	mRNA
https://onlinelibrary.wiley.com/doi/abs/10.1002/anie.201408221	-	-	Tie2	mRNA
https://pubs.acs.org/doi/pdf/10.1021/nl5048972	-	-	Tie2	mRNA
https://www.nature.com/articles/nnano.2014.84	40% (pro) @ 1.6 mg / kg	-	ICAM2	mRNA / Pro
https://www.ncbi.nlm.nih.gov/pmc/articles/PMC3982492/	-	-	Tie2	mRNA
https://pubs.acs.org/doi/abs/10.1021/acsnano.8b03640	-	-	ICAM2	Pro
https://www.nature.com/articles/3302777	-	-	Tie2	mRNA
https://www.cell.com/action/showPdf?pii=S1525-0016%2816%2932706-X	-	50% @ 30 mg / kg	OAT3	mRNA

b

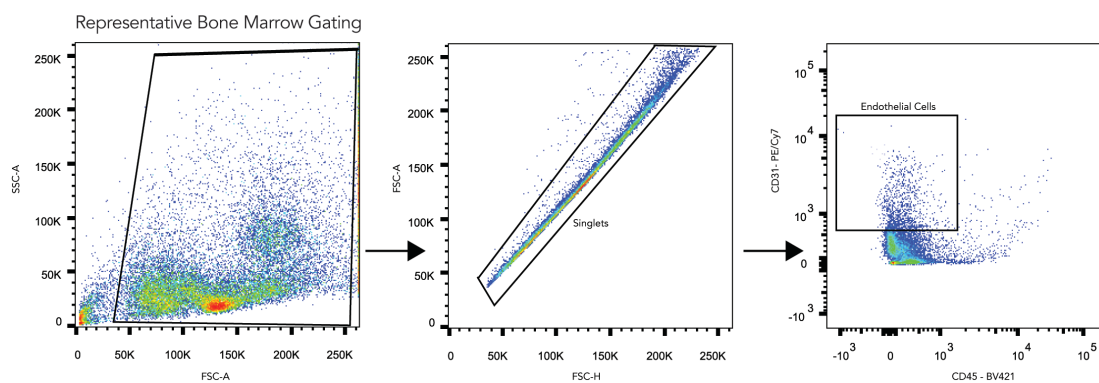


c

siCAM-2 sense: 5' - AGGAcGGucucAAcuuuucdTsdT - 3'
 siCAM-2 antisense: 5' - GAAAAGUuGAGACCGUCCUdTsdT -3'
 siLuciferase sense: 5' - cuuAcGcuGAGuAcuucGAdTsdT - 3'
 siLuciferase antisense: 5' - UCGAAGuACUcAGCGuAAGdTsdT -3'

A, G, U, C: RNA nucleotide
 dT: deoxy-T
 a, g, u, c: 2'-O-Methyl nucleotide
 s: phosphorothioate

d



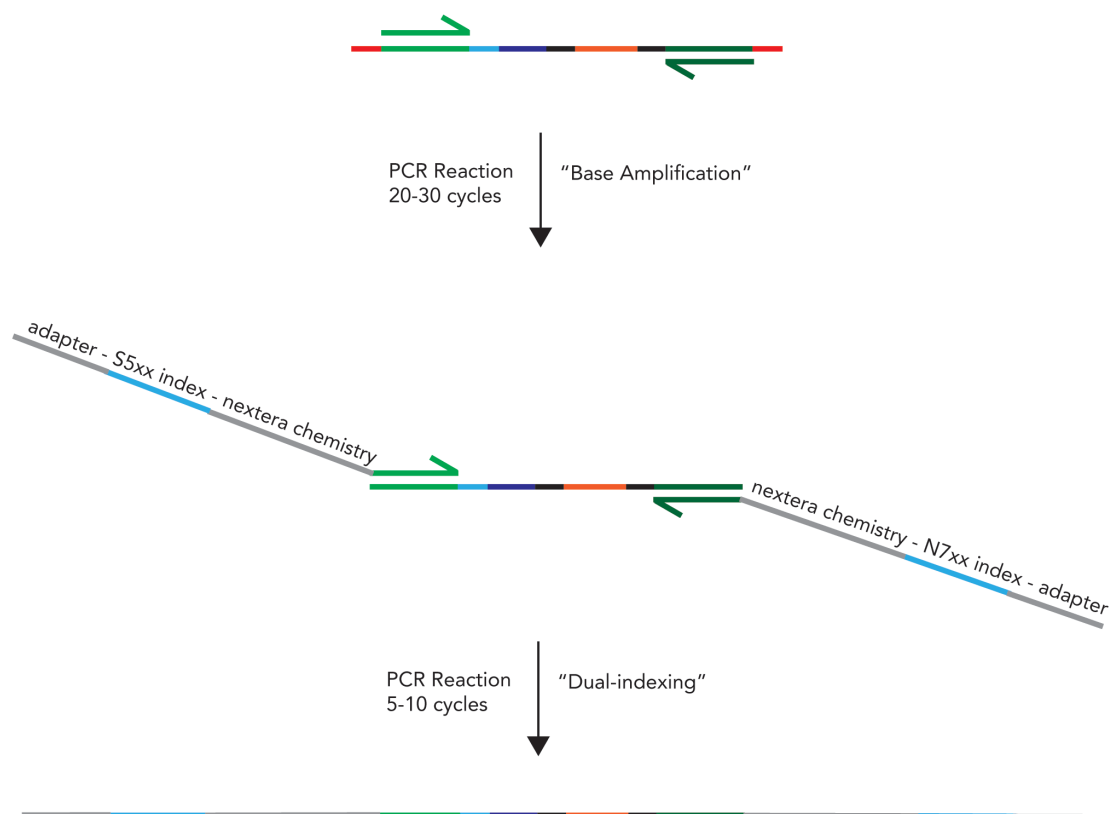
E

		Raw Counts BMECs			
LNP		Mouse 1	Mouse 2	Mouse 3	Input
1	GACACAGT	200	80	200	100
2	GCATAACG	100	45	110	120
3	ACAGAGGT	240	105	250	110
Total Counts		540	230	560	330

		Normalized Counts BMECs (%)			
LNP		Mouse 1	Mouse 2	Mouse 3	Input
1	GACACAGT	37	34	36	30
2	GCATAACG	19	3	20	36
3	ACAGAGGT	44	46	45	33
Total (%)		100	100	100	100

		Normalized Counts BMECs (%)		
LNP		Mouse 1	Mouse 2	Mouse 3
1	GACACAGT	40	38	39
2	GCATAACG	17	18	18
3	ACAGAGGT	44	45	44
Total (%)		100	100	100

G



H

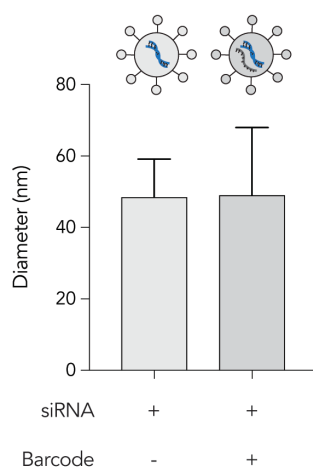


Figure 4.2. (A) Literature review of 8 papers reporting nanoparticles delivering siRNA to endothelial cells in various tissues *in vivo*. Efficacy is reported in either mRNA or protein silencing, as indicated. (B) Synthesis scheme for 7C1 lipomer. (C) Sequence and chemical modification pattern for siICAM-2 and siLuciferase. (D) Representative FACS gating to isolate bone marrow endothelial cells. (E) Example of how normalized delivery is calculated. Barcode counts are normalized within a sample, and then to the DNA barcode input. This process is analogous to normalizing

RNA-seq data. (F) Design of 91 nucleotide barcode used in this study, including 156 example 8 nucleotide DNA barcode sequences that are compatible on the same sequencing run. (G) Representation of two-step PCR scheme to amplify DNA barcodes and add identifiers for Illumina sequencing. (H) Diameters of 7C1 LNP formulated to either siRNA only or siRNA + DNA barcode. The siRNA: DNA barcode mass ratio is 10: 1.

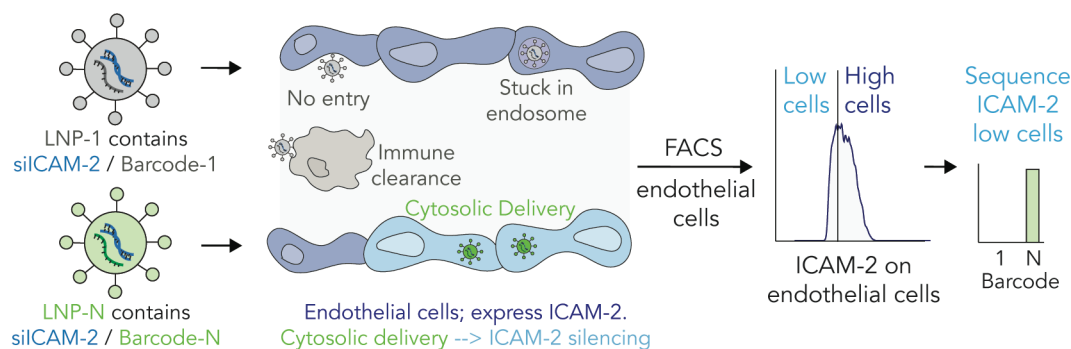


Figure 4.3. Nanoparticles co-formulated with siRNA and a DNA barcode can be used to readout quantify how >100 different LNPs functionally deliver RNA into the cytoplasm of target cells in a single mouse. (A) Unlike previous biodistribution screens, which cannot distinguish between bound particles, particles stuck in endosomes, and particles that delivered RNA into the cytoplasm, our method identifies LNPs that functionally deliver siRNA. We do so by isolating cells that are ICAM^{Low} and sequencing barcodes in those cells. (B,C) ICAM-2 protein expression in lung endothelial cells after mice were treated with 7C1 carrying a barcode and either siLuc or siICAM-2. ICAM-2 protein expression decreased in a dose-dependent manner. (D) siRNA-mediated silencing also led to a dose-dependent increase in ICAM^{Low} lung endothelial cells.

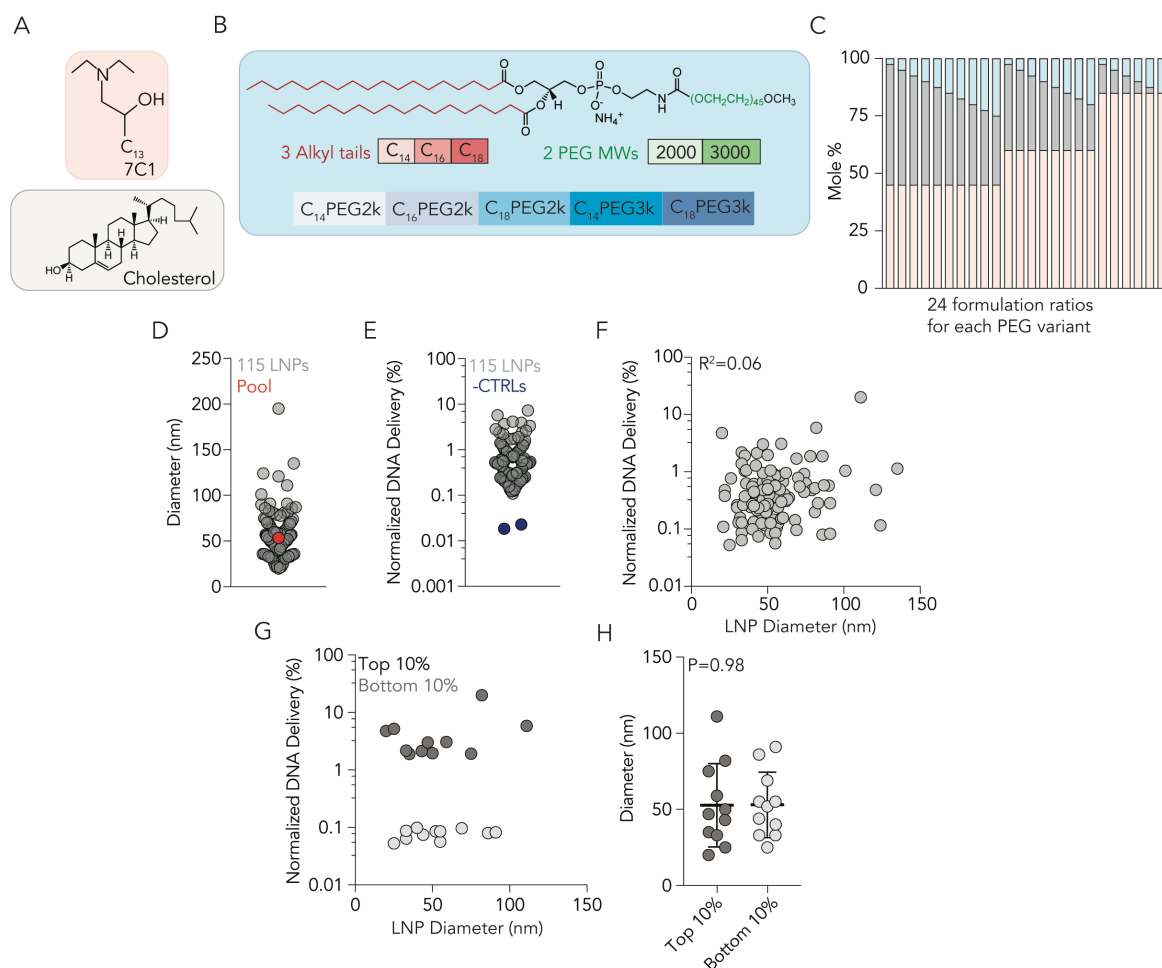


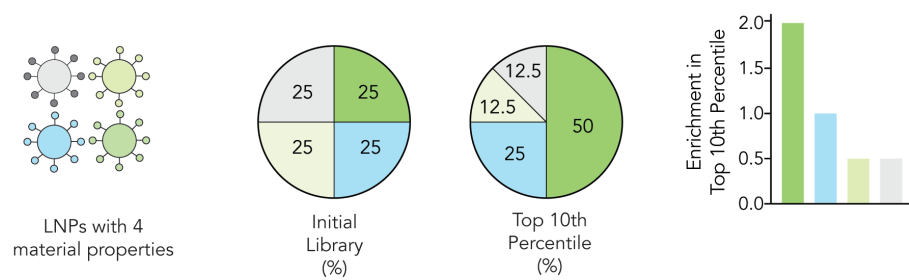
Figure 4.4. The efficiency with which >100 chemically distinct LNPs delivered siRNA to cells was tested simultaneously *in vivo*. (A) LNPs from library 1 were made with 7C1 lipomer and cholesterol. (B) 5 different PEG types were used in library 1; including PEGs with 14, 16, and 18 carbon alkyl tails and molecular weights of 2000 and 3000. (C) 24 different formulation ratios were used for each of the 5 PEG types in library 1. (D) Diameter of 115 LNPs from library 1 that were pooled and injected. The diameter of the pooled library was similar to the diameter of the individual LNPs. (E) Normalized DNA delivery in BMECs for 115 LNPs and the 2 negative controls, which were naked. (F) Correlation between LNP diameter (nm) and normalized DNA delivery in BMECs for all 115 LNPs in Library 1. (G) Correlation between LNP diameter (nm) and normalized DNA delivery in the top and bottom 10% LNPs based on performance from library 1. (H) Diameter (nm) of top and bottom 10% LNPs. Taken together, the data in (F-H) suggest the relationship between siRNA delivery and LNP size (between 20 and 200 nm) is non-existent.

A

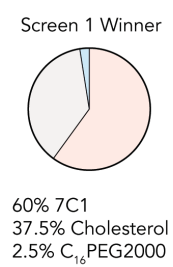
Library 1 Composition

LNP #	7C1 Mole %	Chol %	PEG %	DSPC %	PEG Type	LNP #	7C1 Mole %	Chol %	PEG %	DSPC %	PEG Type
1	60	37.5	2.5	0	C14PEG2000	61	45	42.5	12.5	0	C18PEG2000
2	60	35	5	0	C14PEG2000	62	45	40	15	0	C18PEG2000
3	60	32.5	7.5	0	C14PEG2000	63	45	37.5	17.5	0	C18PEG2000
4	60	30	10	0	C14PEG2000	64	45	35	20	0	C18PEG2000
5	60	27.5	12.5	0	C14PEG2000	65	45	32.5	22.5	0	C18PEG2000
6	60	25	15	0	C14PEG2000	66	45	30	25	0	C18PEG2000
7	60	22.5	17.5	0	C14PEG2000	67	85	12.5	2.5	0	C18PEG2000
8	60	20	20	0	C14PEG2000	68	85	10	5	0	C18PEG2000
9	45	52.5	2.5	0	C14PEG2000	69	85	7.5	7.5	0	C18PEG2000
10	45	50	5	0	C14PEG2000	70	85	5	10	0	C18PEG2000
11	45	47.5	7.5	0	C14PEG2000	71	85	2.5	12.5	0	C18PEG2000
12	45	45	10	0	C14PEG2000	72	85	0	15	0	C18PEG2000
13	45	42.5	12.5	0	C14PEG2000	73	60	37.5	2.5	0	C14PEG3000
14	45	40	15	0	C14PEG2000	74	60	35	5	0	C14PEG3000
15	45	37.5	17.5	0	C14PEG2000	75	60	32.5	7.5	0	C14PEG3000
16	45	35	20	0	C14PEG2000	76	60	30	10	0	C14PEG3000
17	45	32.5	22.5	0	C14PEG2000	77	60	27.5	12.5	0	C14PEG3000
18	45	30	25	0	C14PEG2000	78	60	25	15	0	C14PEG3000
19	85	12.5	2.5	0	C14PEG2000	79	60	22.5	17.5	0	C14PEG3000
20	85	10	5	0	C14PEG2000	80	60	20	20	0	C14PEG3000
21	85	7.5	7.5	0	C14PEG2000	81	45	52.5	2.5	0	C14PEG3000
22	85	5	10	0	C14PEG2000	82	45	50	5	0	C14PEG3000
23	85	2.5	12.5	0	C14PEG2000	83	45	47.5	7.5	0	C14PEG3000
24	85	0	15	0	C14PEG2000	84	45	45	10	0	C14PEG3000
25	60	37.5	2.5	0	C14PEG2000	85	45	42.5	12.5	0	C14PEG3000
26	60	35	5	0	C14PEG2000	86	45	40	15	0	C14PEG3000
27	60	32.5	7.5	0	C14PEG2000	87	45	37.5	17.5	0	C14PEG3000
28	60	30	10	0	C14PEG2000	88	45	35	20	0	C14PEG3000
29	60	27.5	12.5	0	C14PEG2000	89	45	32.5	22.5	0	C14PEG3000
30	60	25	15	0	C14PEG2000	90	45	30	25	0	C14PEG3000
31	60	22.5	17.5	0	C14PEG2000	91	85	12.5	2.5	0	C14PEG3000
32	60	20	20	0	C14PEG2000	92	85	10	5	0	C14PEG3000
33	45	52.5	2.5	0	C14PEG2000	93	85	7.5	7.5	0	C14PEG3000
34	45	50	5	0	C14PEG2000	94	85	5	10	0	C14PEG3000
35	45	47.5	7.5	0	C14PEG2000	95	85	2.5	12.5	0	C14PEG3000
36	45	45	10	0	C14PEG2000	96	85	0	15	0	C14PEG3000
37	45	42.5	12.5	0	C14PEG2000	97	60	37.5	2.5	0	C18PEG3000
38	45	40	15	0	C14PEG2000	98	60	35	5	0	C18PEG3000
39	45	37.5	17.5	0	C14PEG2000	99	60	32.5	7.5	0	C18PEG3000
40	45	35	20	0	C14PEG2000	100	60	30	10	0	C18PEG3000
41	45	32.5	22.5	0	C14PEG2000	101	60	27.5	12.5	0	C18PEG3000
42	45	30	25	0	C14PEG2000	102	60	25	15	0	C18PEG3000
43	85	12.5	2.5	0	C14PEG2000	103	60	22.5	17.5	0	C18PEG3000
44	85	10	5	0	C14PEG2000	104	60	20	20	0	C18PEG3000
45	85	7.5	7.5	0	C14PEG2000	105	45	52.5	2.5	0	C18PEG3000
46	85	5	10	0	C14PEG2000	106	45	50	5	0	C18PEG3000
47	85	2.5	12.5	0	C14PEG2000	107	45	47.5	7.5	0	C18PEG3000
48	85	0	15	0	C14PEG2000	108	45	45	10	0	C18PEG3000
49	60	37.5	2.5	0	C18PEG2000	109	45	42.5	12.5	0	C18PEG3000
50	60	35	5	0	C18PEG2000	110	45	40	15	0	C18PEG3000
51	60	32.5	7.5	0	C18PEG2000	111	45	37.5	17.5	0	C18PEG3000
52	60	30	10	0	C18PEG2000	112	45	35	20	0	C18PEG3000
53	60	27.5	12.5	0	C18PEG2000	113	45	32.5	22.5	0	C18PEG3000
54	60	25	15	0	C18PEG2000	114	45	30	25	0	C18PEG3000
55	60	22.5	17.5	0	C18PEG2000	115	85	12.5	2.5	0	C18PEG3000
56	60	20	20	0	C18PEG2000	116	85	10	5	0	C18PEG3000
57	45	52.5	2.5	0	C18PEG2000	117	85	7.5	7.5	0	C18PEG3000
58	45	50	5	0	C18PEG2000	118	85	5	10	0	C18PEG3000
59	45	47.5	7.5	0	C18PEG2000	119	85	2.5	12.5	0	C18PEG3000
60	45	45	10	0	C18PEG2000	120	85	0	15	0	C18PEG3000

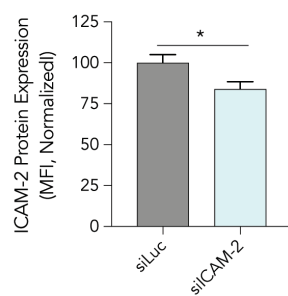
B



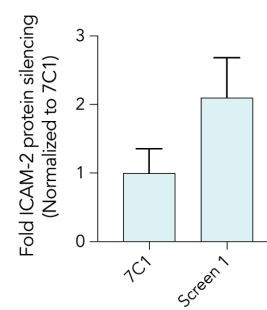
C



D



E

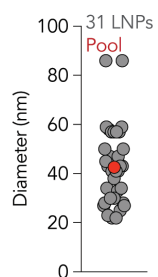


F

Library 2 Composition

LNP #	7C1 Mole %	Cholesterol Mole %	PEG Mole %	DSPC Mole %	
1	80	17.5	2.5	0	C16PEG2000
2	80	2.5	17.5	0	C16PEG2000
3	80	0	20	0	C16PEG2000
4	70	27.5	2.5	0	C16PEG2000
5	70	12.5	17.5	0	C16PEG2000
6	70	10	20	0	C16PEG2000
7	70	7.5	22.5	0	C16PEG2000
8	60	27.5	2.5	10	C16PEG2000
9	60	12.5	17.5	10	C16PEG2000
10	60	10	20	10	C16PEG2000
11	60	7.5	22.5	10	C16PEG2000
12	50	37.5	2.5	10	C16PEG2000
13	50	22.5	17.5	10	C16PEG2000
14	50	20	20	10	C16PEG2000
15	50	17.5	22.5	10	C16PEG2000
16	80	18.5	1.5	0	C16PEG2000
17	80	17.5	2.5	0	C18PEG2000
18	80	2.5	17.5	0	C18PEG2000
19	80	0	20	0	C18PEG2000
20	70	27.5	2.5	0	C18PEG2000
21	70	12.5	17.5	0	C18PEG2000
22	70	10	20	0	C18PEG2000
23	70	7.5	22.5	0	C18PEG2000
24	60	27.5	2.5	10	C18PEG2000
25	60	12.5	17.5	10	C18PEG2000
26	60	10	20	10	C18PEG2000
27	60	7.5	22.5	10	C18PEG2000
28	50	37.5	2.5	10	C18PEG2000
29	50	22.5	17.5	10	C18PEG2000
30	50	20	20	10	C18PEG2000
31	50	17.5	22.5	10	C18PEG2000
32	80	18.5	1.5	0	C18PEG2000
33	60	38.5	1.5	0	C16PEG2000
34	60	37.5	2.5	0	C16PEG2000
35	60	36.5	3.5	0	C16PEG2000
36	60	45	5	0	C16PEG2000
37	60	38.5	1.5	0	C18PEG2000
38	60	37.5	2.5	0	C18PEG2000
39	60	36.5	3.5	0	C18PEG2000
40	60	45	5	0	C18PEG2000

G



H

Experiment	Strain	Sex	Age	Weight (g)
Screen 1	C57BL/6J	F	7 weeks	19-21
Screen 2	C57BL/6J	F	5 weeks	15.2 - 18.3
Idv. LNP Testing	C57BL/6J	F	5 weeks	16.2 - 18.1
In Vivo Gene Editing	SpCas9 expressing on B6J background (Jax #026179)	F	5-7 weeks	17.0 - 18.4

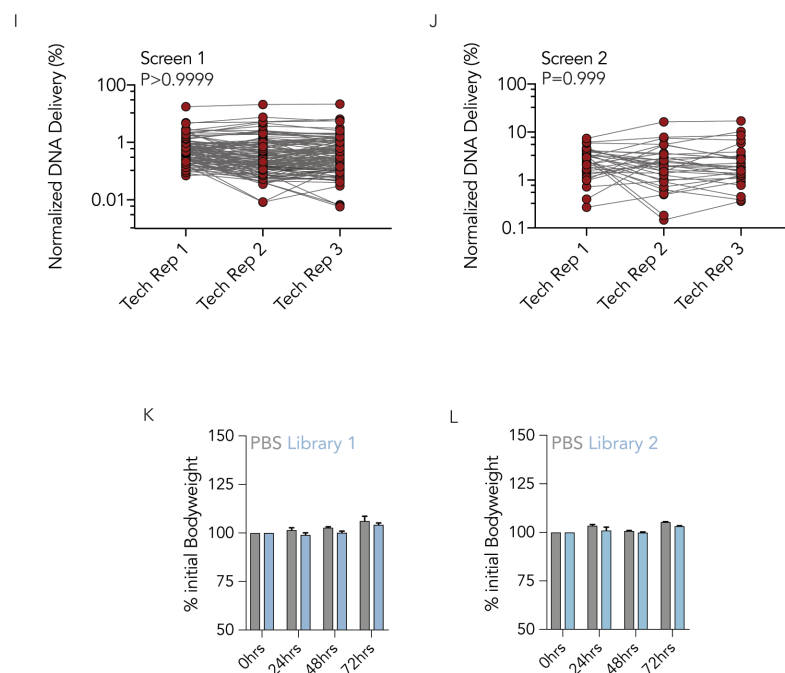


Figure 4.5. (A) The chemical composition of 120 LNPs formulated in library 1. (B) Representative example of enrichment calculation. (C) Molar and chemical composition of top performing LNP in BMECs from Library 1. (D) Normalized ICAM-2 protein expression in BMECs 3 days after administration of the top performing LNP from screen 1 carrying either siLuc or siICAM2 at a dose of 1.0 mg / kg. (E) Comparison of potency in BMECs of original 7C1 compared to the top performing LNP from library 1. The top performing LNP from library 1 was ~2.2x more potent than 7C1. (F) The chemical composition of 40 LNPs formulated in library 2. (G) Hydrodynamic diameter of all 40 LNPs, as well as the control (the pooled LNPs). (H) Mouse characteristics (age, sex, weight) for all experiments. (I) Comparison of normalized DNA delivery in each individual technical replicate in library 1 by Paired One-way ANOVA. (J) Comparison of normalized DNA delivery in each individual technical replicate in library 2 by Paired One-way ANOVA. (K,L) Mouse weight over time for PBS- and library-treated mice for both library 1 and 2.

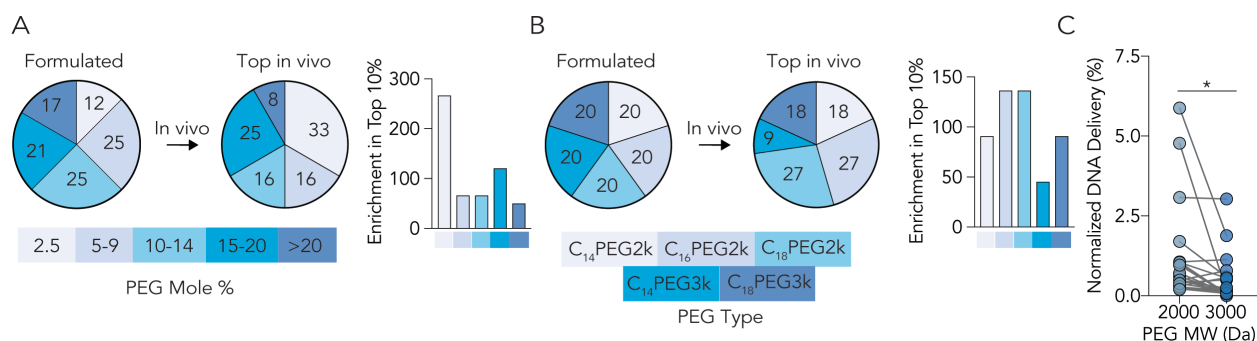


Figure 4.6. LNP delivery to BMEC changes with PEG structure. (A) Enrichment analysis suggests that (A) low and high PEG Mole% as well as (B) C₁₆PEG2000 and C₁₈PEG2000 can promote delivery to in BMECs *in vivo*. Enrichment is described in the Supplement. (C) Paired comparison of LNPs with identical formulation ratios suggest that C₁₈PEG₂₀₀₀ outperforms C₁₈PEG₃₀₀₀ promotes BMEC targeting *in vivo* (P<0.05, Paired 2-tail T-Test).

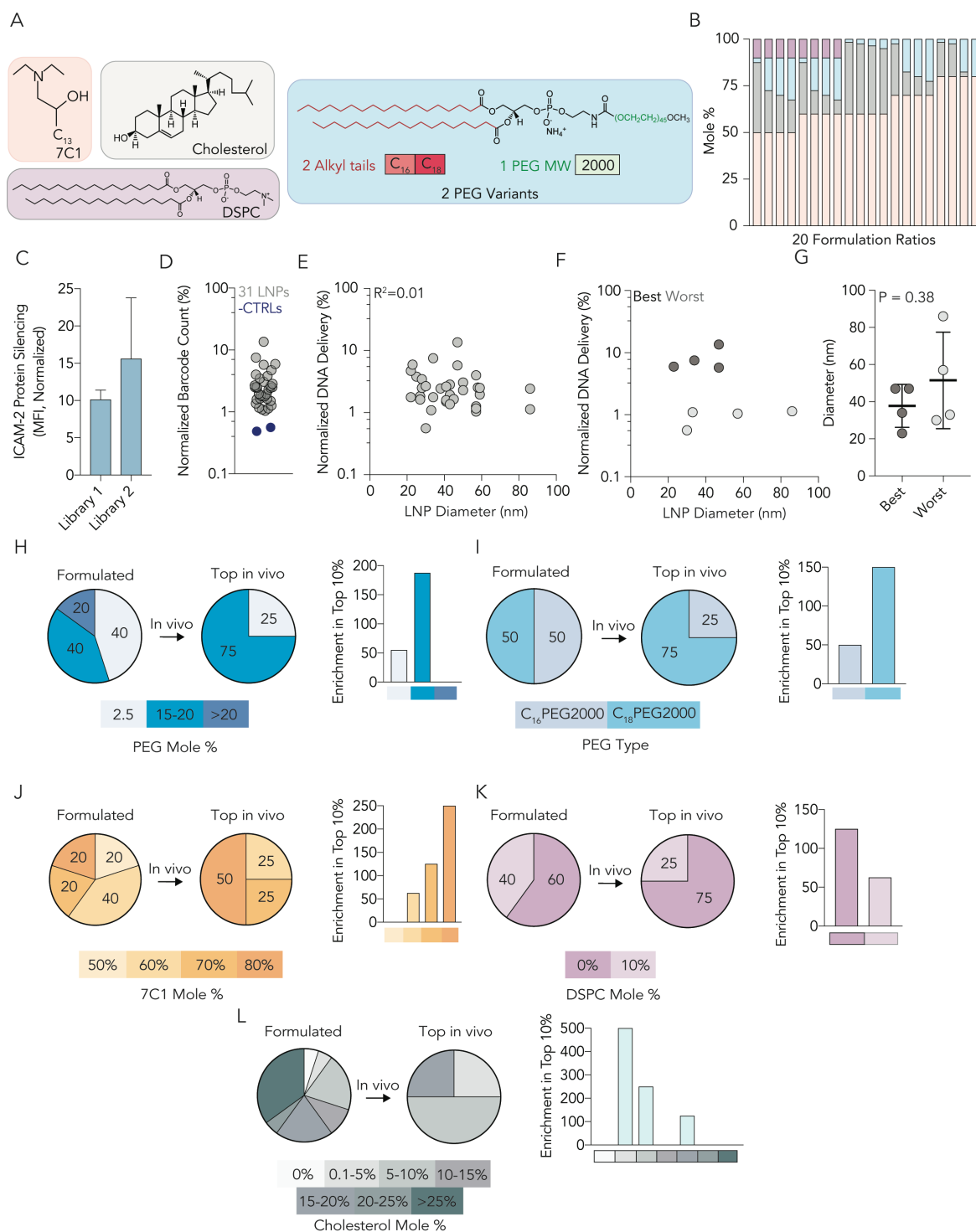
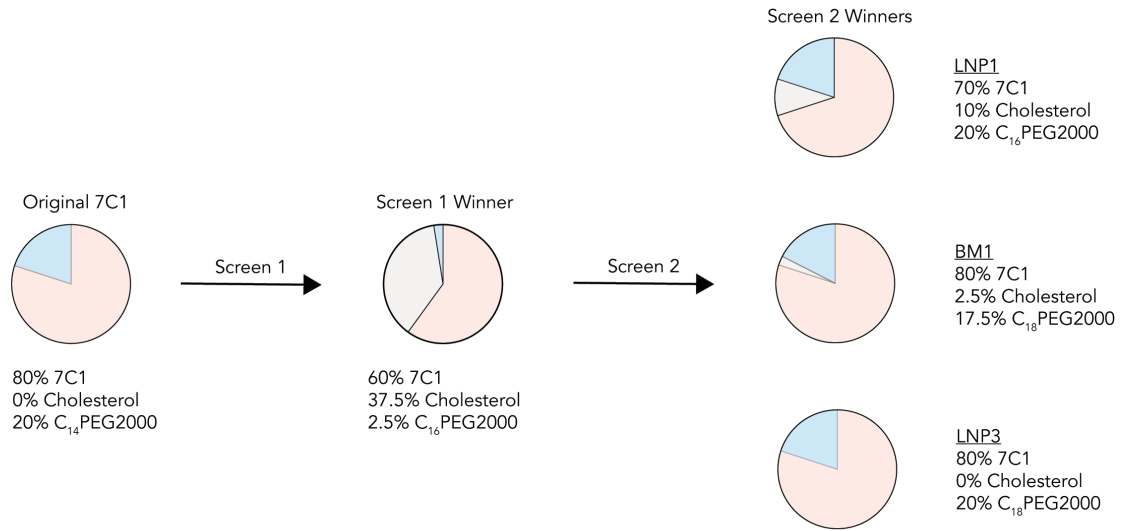


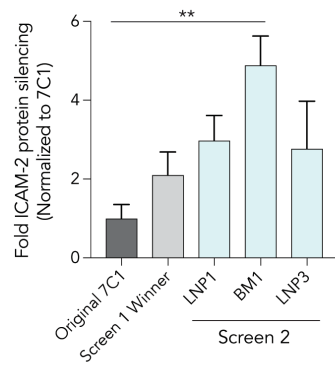
Figure 4.7. Analysis of LNP size and chemical traits from a second library further suggests BMEC targeting is influenced by LNP chemical composition. (A) LNPs from library 2 were made with 7C1 lipomer, cholesterol, and DSPC. (B) Two different PEG types were used in library 2 - C₁₆PEG₂₀₀₀ and C₁₈PEG₂₀₀₀. These structures were selected based on data from LNP library 1. (C) 20 different formulation ratios were used for each of the two PEG types in library 2. (D) ICAM-2 protein silencing in

BMECs 3 days after mice were injected with the library of LNPs at a total dose of 1.5 mg / kg. Notably, ICAM-2 silencing was more potent in BMECs than library 1. (D) Normalized DNA delivery in BMECs for 31 LNPs and 2 naked barcodes; as expected the naked barcodes performed poorly. (E) Correlation between LNP diameter (nm) and normalized DNA delivery in BMECs for all 31 LNPs in Library 2. (F) Correlation between LNP diameter (nm) and normalized DNA delivery in the top and bottom 10% LNPs based on performance from library 2. (G) Diameter (nm) of top and bottom 10% LNPs. Taken together, (E-G) further suggest BMEC targeting is not influenced by LNP size between 20 and 200 nm. (H) Enrichment of LNPs containing PEG Mole % between 15-20% in BMECs *in vivo*. (I) Enrichment of LNPs containing C₁₈PEG2000 in BMECs *in vivo*. (J) Enrichment of LNPs containing 80 mole % 7C1 in BMECs *in vivo*. (K) Enrichment of LNPs containing 0 mole % DSPC in BMECs *in vivo*. (L) Enrichment of LNPs containing 0.1 - 10 mole % cholesterol in BMECs *in vivo*.

A



B



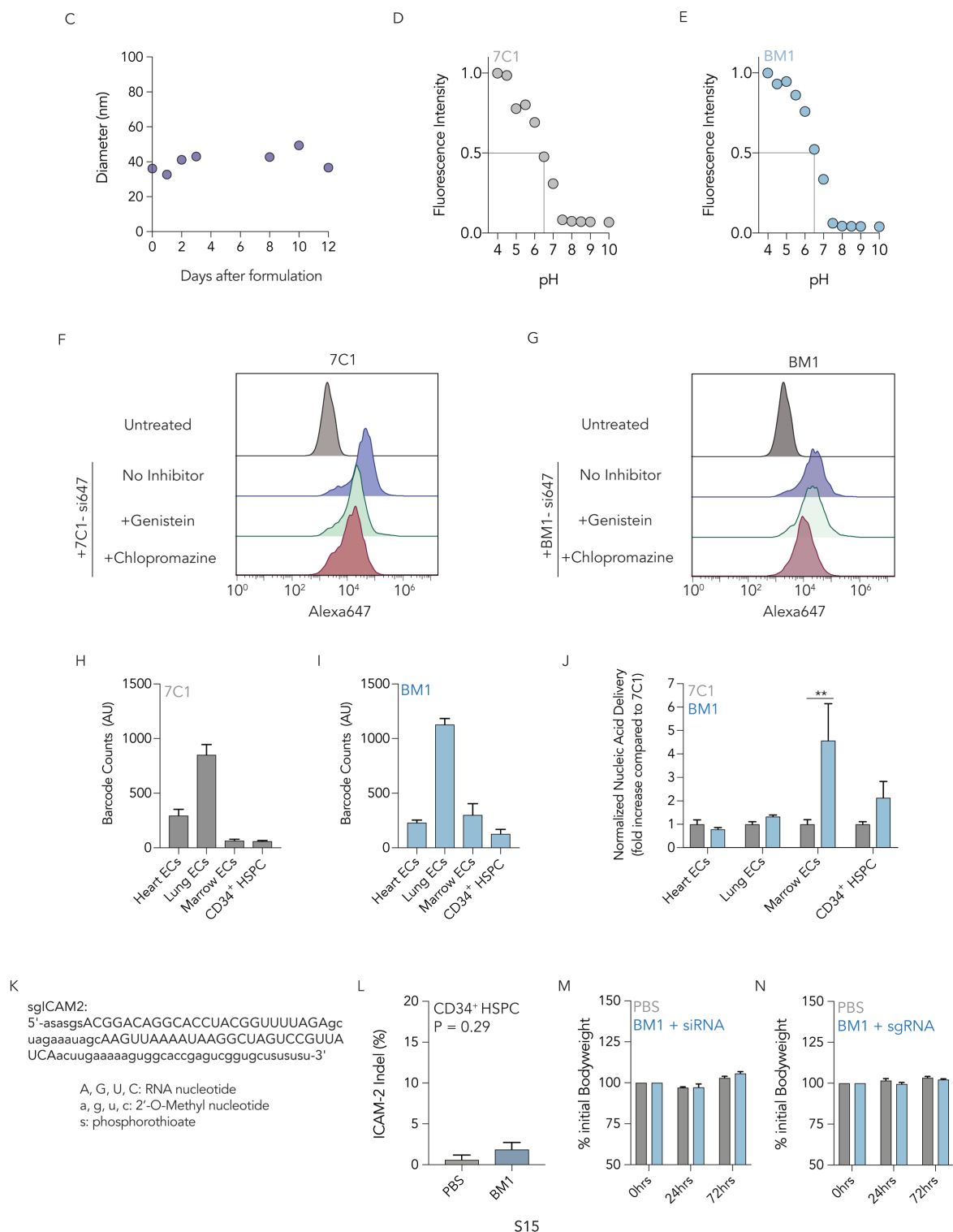


Figure 4.8. (A) Molar and chemical compositions of 7C1, the top performing LNP from library 1, and the top 3 performing LNPs from library 3. (B) Potency of ICAM-2 silencing of 7C1, the top performing LNP from library 1, and the top 3 performing LNPs from library 3 in BMECs 3 days after injecting mice with a dose of 1.0 mg / kg

siICAM-2. Notably, all top LNPs from library 2 were more potent than both 7C1 and the top performing LNP from library 1. (C) The top performing LNP from library 2 (BM1) is stable at 4°C for more than 10 days. (D) pKa of 7C1 LNP as measured by TNS assay. (E) pKa of BM1 LNP as measured by TNS assay. (F) Flow cytometry histogram of *in vitro* endocytosis of 7C1 carrying siRNA tagged with AlexaFluor647 in the presence of no endocytosis inhibitor, genistein (caveolin inhibitor), or chlorpromazine (clathrin inhibitor). (G) Flow cytometry histogram of *in vitro* endocytosis of BM1 carrying siRNA tagged with AlexaFluor647 in the presence of no endocytosis inhibitor, genistein (caveolin inhibitor), or chlorpromazine (clathrin inhibitor). (H) Biodistribution of 7C1 to endothelial cells in the heart, lung, and bone marrow, as well as CD34⁺ HSPCs. (I) Biodistribution of BM1 to endothelial cells in the heart, lung, and bone marrow, as well as CD34⁺ HSPCs. (J) Comparison of biodistribution between 7C1 and BM1. BM1 displays 4.6-fold higher biodistribution to BMECs than 7C1. Two-way ANOVA **P<0.01. (K) Sequence and chemical modification on sgICAM2. (L) Indels in CD34⁺ HSPCs mediated by a 1 mg / kg injection of BM1 carrying sgICAM2. (M) Normalized weight of mice injected with 1.0 mg / kg BM1-siRNA compared to mice injected with PBS. (N) Normalized weight of mice injected with 1.0 mg / kg BM1-sgRNA compared to mice injected with PBS.

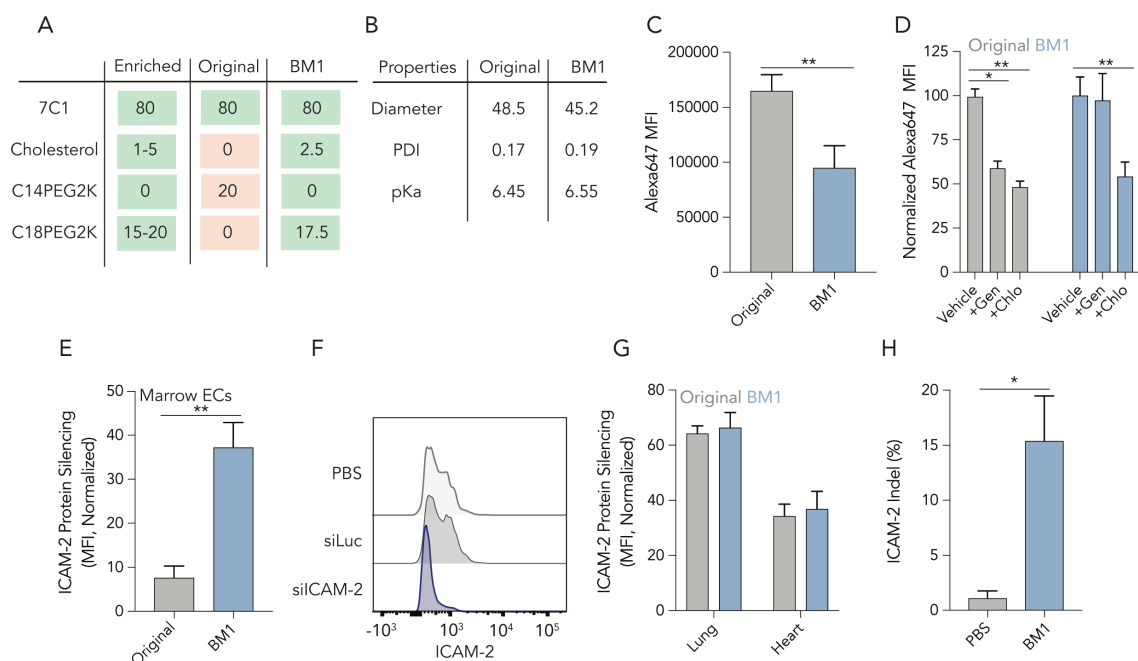


Figure 4.9. Comparing BM1 and the original 80: 20 7C1 formulation reveal differences in nanoparticle behavior. (A) A table of the chemical properties enriched by the *in vivo* screens, the original 7C1 formulation, and BM1. Notably, BM1 has all the properties that were enriched in BMECs selected from LNP library 2. **(B)** Diameter, polydispersity index, and pKa for original 7C1 and BM1. There are no significant differences between the formulations. **(C)** *In vitro* uptake of 7C1 and BM1 *in vitro* quantified as Alexa647 MFI 1 hour after immortalized aortic endothelial cells were treated with fluorescent LNPs. The original formulation is **(D)** is inhibited by the endocytosis inhibitors genistein (caveolin) and chlorpromazine (clathrin), whereas BM1 uptake is only inhibited by chlorpromazine. **(E)** ICAM-2 protein silencing in BMECs 3 days after mice were treated with siLuc carried by original 7C1 or BM1. BM1 delivered siICAM-2 to BMECs much more efficiently than 7C1 ($P < 0.01$, Unpaired 2-tail T-test) **(F)** Histogram of ICAM-2 protein expression in BMECs following the administration of PBS or BM1 carrying siLuc or siICAM-2 at 1 mg / kg. **(G)** ICAM-2 protein silencing mediated by a 1.0 mg / kg injection of 7C1 and BM1 in lung and heart endothelial cells. After evolving BM1 to target bone marrow, we did not observe any increased potency in lung or heart EC delivery. **(H)** The percentage of BMEC loci with targeted insertions or deletions (indels, i.e., mutations) after BM1 was formulated with another small RNA (sgICAM-2) and injected into Cas9 mice at a dose of 1 mg / kg.

4.4 Methods & Materials

Nanoparticle Formulation. Nanoparticles were formulated using a microfluidic device as previously described²⁶. Briefly, nucleic acids (siRNA and DNA barcodes) were diluted in citrate buffer while lipid-amine compounds, alkyl tailed PEG, cholesterol, and DSPC were diluted in ethanol. PEG, cholesterol, and DSPC was purchased from Avanti Lipids. Citrate and ethanol phases were combined in a microfluidic device by syringe pumps.

DNA Barcoding. Each chemically distinct LNP was formulated to carry its own unique DNA barcode and siRNA. For example, LNP1 carried DNA barcode 1 and siICAM2, while the chemically distinct LNP2 carried DNA barcode 2 and siICAM2. Single stranded DNA sequences were purchased from Integrated DNA Technologies (IDT). To ensure equal amplification of each sequence, we included universal forward and reverse primer regions. Each barcode was distinguished using a unique 8 nucleotide sequence. An 8 nucleotide sequence can generate 65,536 distinct barcodes. We used 156 distinct sequences designed to prevent sequence ‘bleaching’ on the Illumina MiniSeq sequencing machine.

Nanoparticle Characterization. LNP hydrodynamic diameter was measured using a plate reader formatted dynamic light scattering machine (Wyatt). LNPs were diluted in sterile 1X PBS to a concentration of ~0.06 µg/mL and analyzed. LNPs were only included if they formed monodisperse populations with diameter between 20 and 200nm. Particles that met these criteria were dialyzed with 1X phosphate buffered saline (PBS, Invitrogen), and were sterile filtered with a 0.22 µm filter.

Animal Experiments. All animal experiments were performed in accordance with the Georgia Institute of Technology's IACUC. C57BL/6J (#000664) and constitutive SpCas9 (#026179) mice were purchased from The Jackson Laboratory and used between 5-12 weeks of age. In all experiments, we used N=3-5 mice/group. Mice were injected intravenously via the lateral tail vein. The nanoparticle concentration was determined using NanoDrop (Thermo Scientific).

Cell Isolation & Staining. Cells were isolated 72 hours (for screens) or 120 hours (for *in vivo* gene editing) hours after injection with LNPs unless otherwise noted. Mice were perfused with 20 mL of 1X PBS through the right atrium. As we previously described^{4,33}, tissues were cut and placed in a digestive enzyme solution with Collagenase Type I (Sigma Aldrich), Collagenase XI (Sigma Aldrich) and Hyaluronidase (Sigma Aldrich) at 37 °C for 45 minutes. The digestive enzyme for heart included Collagenase IX. Cell suspension was filtered through 70µm mesh and red blood cells were lysed. Cells were stained to identify populations and sorted using the BD FACS Fusion in the Georgia Institute of Technology Cellular Analysis Core for *in vivo* experiments. The antibody clones used were: anti-CD31 (390, BioLegend), anti-CD102 (3C4, Biolegend), anti-CD45.2 (104, BioLegend), and anti-CD34 (SA376A4, Biolegend).

PCR Amplification for Illumina Sequencing. All samples were amplified and prepared for sequencing using nested PCR (**Supplementary Figure 1G**). 2 µL of primers were added to 5 µL of Kapa HiFi 2X master mix, and 3 µL template DNA/water. The second PCR, added Nextera XT chemistry, indices and i5/i7 adapter regions. Dual-indexed samples were run on a 2% agarose gel to ensure that PCR reaction occurred before being pooled and gel purified.

Deep Sequencing. Illumina sequencing was conducted in Georgia Institute of Technology's Molecular Evolution core. Runs were performed on an Illumina Miniseq. Primers were designed based on Nextera XT adapter sequences.

Barcode Sequencing Normalization. Counts for each particle, per cell type, were normalized to the barcoded LNP mixture applied to cells or injected into the mouse.

TNS Assay. The pKa of 7C1 and BM1 was measured as previously described⁴. Briefly, a stock solution of 10mM HEPES (Sigma), 10mM MES (Sigma), 10mM sodium acetate (Sigma), and 140mM sodium chloride (Sigma) was prepared and pH adjusted with hydrogen chloride and sodium hydroxide to a range of pH between 4 and 10. Using 4 replicates for each nanoparticle at each pH, 140 μ L pH-adjusted buffer was added to a 96-well plate, followed by the addition 5 μ L of 2-(p-toluidino)-6-naphthalene sulfonic acid (60 μ g / mL). 5 μ L of each nanoparticle was added to each well. After 5 minutes of incubation under gentle shaking, fluorescence absorbance was measured using excitation wavelengths of 325 nm and emission wavelength of 435nm.

***In vitro* Endocytosis.** Immortalized mouse aortic endothelial cells (IMAECs) were seeded in a 24 well plate at 40,000 cells per well and allowed to culture overnight. 7C1 and BM1 were formulated to carry Alexa647-tagged siRNA using microfluidics. After formulation, both LNPs were dialyzed for 2hrs in 1x PBS. 1 hour prior to incubation with each LNPs, inhibitors of clathrin-mediated endocytosis (chlorpromazine, 100mM, Alfa Aesar), caveolae-mediated endocytosis (genistein, 100mM, TCI America), and macropinocytosis (5-(N-Ethyl-N-isopropyl) Amiloride, EIPA, 50mM, Toronto Research Chemicals) were added to IMAECs at a dose of 20nM siRNA / well. LNPs were left on the cells for 1 hour

before the cells were washed 2x with PBS, trypsinized and prepared for flow cytometry using a BD Accuri C6.

RNA interference. siRNAs were chemically modified at the 2' position to increase stability and negate immunostimulation. 72 hours after injection, tissues were isolated and protein expression was determined via flow cytometry. ICAM2 mean fluorescent intensity in siLuc-treated mice was normalized to 100 percent.

QUANT Biodistribution. 7C1 and BM1 LNPs were formulated to carry the DNA barcodes utilized in this study. Mice were injected at a dose of 0.5 mg / kg. After 4 hours, tissues were isolated and endothelial cells from the lung, heart, and bone marrow, as well as CD34⁺ HSPCs were isolated by FACS. DNA barcodes were isolated using QuickExtract (Epicentre). Biodistribution was measured as previously described⁵⁰. Briefly, the QX200TM Droplet DigitalTM PCR System (Bio-Rad) was used to prep and analyze all ddPCR results. All PCR samples were prepared with 10 μ L ddPCR with ddPCRTM Supermix for Probes (Bio-Rad), 1 μ L of primer and probe mix (solution of 10 μ M of target probe and 20 μ M of Reverse/Forward Primers), 1 μ L of template, and 8 μ L water. 20 μ L of each reaction and 70 μ L of Droplet Generation Oil for Probes (Bio-Rad) were loaded into DG8TM Cartridges and covered with DG8TM Gaskets. Cartridges were placed in the QX200TM Droplet Generator to create water-oil emulsion droplets. Cycle conditions for PCR were as follows: 1 cycle of 95° for 10 minutes, followed by 40 cycles of 94°C for 30 seconds, 60°C for 1 minute, and 1 cycle of 95°C for 10 minutes. Plates were stored at 4°C until ran on the QX200TM Droplet DigitalTM PCR System. For each biological rep, 2 technical repetitions were completed. In all cases, technical reps were averaged.

***In vivo* Cas9 Editing.** Mice constitutively expressing SpCas9 were injected with BM1 carrying 1 mg / kg of sgICAM2. sgICAM2 was modified with 2' O-methyl ribose at select positions and 3 phosphorothioates at both the 5' and 3' termini. 5 days after injection, cells were isolated via FACS. Indels were measured by TIDES.

Data Analysis & Statistics. Sequencing results were processed using a custom R script to extract raw barcode counts for each tissue. These raw counts were then normalized with an R script prior for further analysis. Statistical analysis was done using GraphPad Prism 7; more specifically Paired 2-tail T-test or One-way ANOVAs were used where appropriate. Data is plotted as mean \pm standard error mean unless otherwise stated.

4.5 References

1. Semple, S. C.; Akinc, A.; Chen, J.; Sandhu, A. P.; Mui, B. L.; Cho, C. K.; Sah, D. W.; Stebbing, D.; Crosley, E. J.; Yaworski, E.; Hafez, I. M.; Dorkin, J. R.; Qin, J.; Lam, K.; Rajeev, K. G.; Wong, K. F.; Jeffs, L. B.; Nechev, L.; Eisenhardt, M. L.; Jayaraman, M.; Kazem, M.; Maier, M. A.; Srinivasulu, M.; Weinstein, M. J.; Chen, Q.; Alvarez, R.; Barros, S. A.; De, S.; Klimuk, S. K.; Borland, T.; Kosovrasti, V.; Cantley, W. L.; Tam, Y. K.; Manoharan, M.; Ciufolini, M. A.; Tracy, M. A.; de Fougères, A.; MacLachlan, I.; Cullis, P. R.; Madden, T. D.; Hope, M. J., Rational design of cationic lipids for siRNA delivery. *Nat Biotechnol* **2010**, *28* (2), 172-6.
2. Love, K. T.; Mahon, K. P.; Levins, C. G.; Whitehead, K. A.; Querbes, W.; Dorkin, J. R.; Qin, J.; Cantley, W.; Qin, L. L.; Racie, T.; Frank-Kamenetsky, M.; Yip, K. N.; Alvarez, R.; Sah, D. W.; de Fougères, A.; Fitzgerald, K.; Kotliansky, V.; Akinc, A.; Langer, R.; Anderson, D. G., Lipid-like materials for low-dose, in vivo gene silencing. *Proceedings of the National Academy of Sciences of the United States of America* **2010**, *107* (5), 1864-9.
3. Dong, Y.; Love, K. T.; Dorkin, J. R.; Sirirungruang, S.; Zhang, Y.; Chen, D.; Bogorad, R. L.; Yin, H.; Chen, Y.; Vegas, A. J.; Alabi, C. A.; Sahay, G.; Olejnik, K. T.; Wang, W.; Schroeder, A.; Lytton-Jean, A. K.; Siegwart, D. J.; Akinc, A.; Barnes, C.; Barros, S. A.; Carioto, M.; Fitzgerald, K.; Hettinger, J.; Kumar, V.; Novobrantseva, T. I.; Qin, J.; Querbes, W.; Kotliansky, V.; Langer, R.; Anderson, D. G., Lipopeptide nanoparticles for potent and selective siRNA delivery in rodents and nonhuman primates. *Proceedings of the National Academy of Sciences of the United States of America* **2014**, *111* (11), 3955-60.
4. Dahlman, J. E.; Barnes, C.; Khan, O. F.; Thiriot, A.; Jhunjunwala, S.; Shaw, T. E.; Xing, Y.; Sager, H. B.; Sahay, G.; Speciner, L.; Bader, A.; Bogorad, R. L.; Yin, H.; Racie, T.; Dong, Y.; Jiang, S.; Seedorf, D.; Dave, A.; Singh Sandhu, K.; Webber, M. J.; Novobrantseva, T.; Ruda, V. M.; Lytton-JeanAbigail, K. R.; Levins, C. G.; Kalish, B.; Mudge, D. K.; Perez, M.; Abezgauz, L.; Dutta, P.; Smith, L.; Charisse, K.; Kieran, M. W.; Fitzgerald, K.; Nahrendorf, M.; Danino, D.; Tuder, R. M.; von Andrian, U. H.; Akinc, A.; Panigrahy, D.; Schroeder, A.; Kotliansky, V.; Langer, R.; Anderson, D. G., In vivo endothelial siRNA delivery using polymeric nanoparticles with low molecular weight. *Nat Nano* **2014**, *9* (8), 648-655.
5. Novobrantseva, T. I.; Borodovsky, A.; Wong, J.; Klebanov, B.; Zafari, M.; Yucius, K.; Querbes, W.; Ge, P.; Ruda, V. M.; Milstein, S.; Speciner, L.; Duncan, R.; Barros, S.; Basha, G.; Cullis, P.; Akinc, A.; Donahoe, J. S.; Narayanannair Jayaprakash, K.; Jayaraman, M.; Bogorad, R. L.; Love, K.; Whitehead, K.; Levins, C.; Manoharan, M.; Swirski, F. K.; Weissleder, R.; Langer, R.; Anderson, D. G.; de Fougères, A.; Nahrendorf, M.; Kotliansky, V., Systemic RNAi-mediated Gene Silencing in Nonhuman Primate and Rodent Myeloid Cells. *Mol Ther Nucleic Acids* **2012**, *1*, e4.

6. Leuschner, F.; Dutta, P.; Gorbato, R.; Novobrantseva, T. I.; Donahoe, J. S.; Courties, G.; Lee, K. M.; Kim, J. I.; Markmann, J. F.; Marinelli, B.; Panizzi, P.; Lee, W. W.; Iwamoto, Y.; Milstein, S.; Epstein-Barash, H.; Cantley, W.; Wong, J.; Cortez-Retamozo, V.; Newton, A.; Love, K.; Libby, P.; Pittet, M. J.; Swirski, F. K.; Kotliansky, V.; Langer, R.; Weissleder, R.; Anderson, D. G.; Nahrendorf, M., Therapeutic siRNA silencing in inflammatory monocytes in mice. *Nat Biotechnol* **2011**, 29 (11), 1005-10.
7. Kedmi, R.; Veiga, N.; Ramishetti, S.; Goldsmith, M.; Rosenblum, D.; Dammes, N.; Hazan-Halevy, I.; Nahary, L.; Leviatan-Ben-Arye, S.; Harlev, M.; Behlke, M.; Benhar, I.; Lieberman, J.; Peer, D., A modular platform for targeted RNAi therapeutics. *Nat Nanotechnol* **2018**, 13 (3), 214-219.
8. Ramishetti, S.; Kedmi, R.; Goldsmith, M.; Leonard, F.; Sprague, A. G.; Godin, B.; Gozin, M.; Cullis, P. R.; Dykxhoorn, D. M.; Peer, D., Systemic Gene Silencing in Primary T Lymphocytes Using Targeted Lipid Nanoparticles. *ACS nano* **2015**, 9 (7), 6706-16.
9. Zeigerer, A.; Gilleron, J.; Bogorad, R. L.; Marsico, G.; Nonaka, H.; Seifert, S.; Epstein-Barash, H.; Kuchimanchi, S.; Peng, C. G.; Ruda, V. M.; Del Conte-Zerial, P.; Hengstler, J. G.; Kalaidzidis, Y.; Kotliansky, V.; Zerial, M., Rab5 is necessary for the biogenesis of the endolysosomal system in vivo. *Nature* **2012**, 485 (7399), 465-70.
10. White, K.; Lu, Y.; Annis, S.; Hale, A. E.; Chau, B. N.; Dahlman, J. E.; Hemann, C.; Oplotowsky, A. R.; Vargas, S. O.; Rosas, I.; Perrella, M. A.; Osorio, J. C.; Haley, K. J.; Graham, B. B.; Kumar, R.; Saggat, R.; Saggat, R.; Wallace, W. D.; Ross, D. J.; Khan, O. F.; Bader, A.; Gochuico, B. R.; Matar, M.; Polach, K.; Johannessen, N. M.; Prosser, H. M.; Anderson, D. G.; Langer, R.; Zweier, J. L.; Bindoff, L. A.; Systrom, D.; Waxman, A. B.; Jin, R. C.; Chan, S. Y., Genetic and hypoxic alterations of the microRNA-210-ISCU1/2 axis promote iron-sulfur deficiency and pulmonary hypertension. *EMBO Mol Med* **2015**, 7 (6), 695-713.
11. Sager, H. B.; Dutta, P.; Dahlman, J. E.; Hulsmans, M.; Courties, G.; Sun, Y.; Heidt, T.; Vinegoni, C.; Borodovsky, A.; Fitzgerald, K.; Wojtkiewicz, G. R.; Iwamoto, Y.; Tricot, B.; Khan, O. F.; Kauffman, K. J.; Xing, Y.; Shaw, T. E.; Libby, P.; Langer, R.; Weissleder, R.; Swirski, F. K.; Anderson, D. G.; Nahrendorf, M., RNAi targeting multiple cell adhesion molecules reduces immune cell recruitment and vascular inflammation after myocardial infarction. *Science translational medicine* **2016**, 8 (342), 342ra80-342ra80.
12. Sager, H. B.; Hulsmans, M.; Lavine, K. J.; Moreira, M. B.; Heidt, T.; Courties, G.; Sun, Y.; Iwamoto, Y.; Tricot, B.; Khan, O. F.; Dahlman, J. E.; Borodovsky, A.; Fitzgerald, K.; Anderson, D. G.; Weissleder, R.; Libby, P.; Swirski, F. K.; Nahrendorf, M., Proliferation and Recruitment Contribute to Myocardial Macrophage Expansion in Chronic Heart Failure. *Circ Res* **2016**, 119 (7), 853-64.
13. Budatha, M.; Zhang, J.; Zhuang, Z. W.; Yun, S.; Dahlman, J. E.; Anderson, D. G.; Schwartz, M. A., Inhibiting Integrin alpha5 Cytoplasmic Domain Signaling Reduces

Atherosclerosis and Promotes Arteriogenesis. *Journal of the American Heart Association* **2018**, 7 (3) DOI: 10.1161.

14. Yun, S.; Budatha, M.; Dahlman, J. E.; Coon, B. G.; Cameron, R. T.; Langer, R.; Anderson, D. G.; Baillie, G.; Schwartz, M. A., Interaction between integrin $\alpha 5$ and PDE4D regulates endothelial inflammatory signalling. *Nat Cell Biol* **2016**, 18 (10), 1043-53.
15. Yu, D.; Khan, O. F.; Suva, M. L.; Dong, B.; Panek, W. K.; Xiao, T.; Wu, M.; Han, Y.; Ahmed, A. U.; Balyasnikova, I. V.; Zhang, H. F.; Sun, C.; Langer, R.; Anderson, D. G.; Lesniak, M. S., Multiplexed RNAi therapy against brain tumor-initiating cells via lipopolymeric nanoparticle infusion delays glioblastoma progression. *Proceedings of the National Academy of Sciences of the United States of America* **2017**, 114 (30), E6147-e6156.
16. Xue, W.; Dahlman, J. E.; Tammela, T.; Khan, O. F.; Sood, S.; Dave, A.; Cai, W.; Chirino, L. M.; Yang, G. R.; Bronson, R.; Crowley, D. G.; Sahay, G.; Schroeder, A.; Langer, R.; Anderson, D. G.; Jacks, T., Small RNA combination therapy for lung cancer. *Proceedings of the National Academy of Sciences* **2014**, 111 (34), E3553-E3561.
17. Neumann, U. H.; Ho, J. S. S.; Chen, S.; Tam, Y. Y. C.; Cullis, P. R.; Kieffer, T. J., Lipid nanoparticle delivery of glucagon receptor siRNA improves glucose homeostasis in mouse models of diabetes. *Molecular metabolism* **2017**, 6 (10), 1161-1172.
18. Chen, P. Y.; Qin, L.; Barnes, C.; Charisse, K.; Yi, T.; Zhang, X.; Ali, R.; Medina, P. P.; Yu, J.; Slack, F. J.; Anderson, D. G.; Kotelianski, V.; Wang, F.; Tellides, G.; Simons, M., FGF regulates TGF-beta signaling and endothelial-to-mesenchymal transition via control of let-7 miRNA expression. *Cell Rep* **2012**, 2 (6), 1684-96.
19. Koga, J.; Nakano, T.; Dahlman, J. E.; Figueiredo, J. L.; Zhang, H.; Decano, J.; Khan, O. F.; Niida, T.; Iwata, H.; Aster, J. C.; Yagita, H.; Anderson, D. G.; Ozaki, C. K.; Aikawa, M., Macrophage Notch Ligand Delta-Like 4 Promotes Vein Graft Lesion Development: Implications for the Treatment of Vein Graft Failure. *Arteriosclerosis, thrombosis, and vascular biology* **2015**, 35 (11), 2343-53.
20. Adams, D.; Gonzalez-Duarte, A.; O'Riordan, W. D.; Yang, C. C.; Ueda, M.; Kristen, A. V.; Tournev, I.; Schmidt, H. H.; Coelho, T.; Berk, J. L.; Lin, K. P.; Vita, G.; Attarian, S.; Plante-Bordeneuve, V.; Mezei, M. M.; Campistol, J. M.; Buades, J.; Brannagan, T. H., 3rd; Kim, B. J.; Oh, J.; Parman, Y.; Sekijima, Y.; Hawkins, P. N.; Solomon, S. D.; Polydefkis, M.; Dyck, P. J.; Gandhi, P. J.; Goyal, S.; Chen, J.; Strahs, A. L.; Nochur, S. V.; Sweetser, M. T.; Garg, P. P.; Vaishnaw, A. K.; Gollob, J. A.; Suhr, O. B., Patisiran, an RNAi Therapeutic, for Hereditary Transthyretin Amyloidosis. *N Engl J Med* **2018**, 379 (1), 11-21.
21. Pasi, K. J.; Rangarajan, S.; Georgiev, P.; Mant, T.; Creagh, M. D.; Lissitchkov, T.; Bevan, D.; Austin, S.; Hay, C. R.; Hegemann, I.; Kazmi, R.; Chowdary, P.; Gercheva-

- Kyuchukova, L.; Mamonov, V.; Timofeeva, M.; Soh, C. H.; Garg, P.; Vaishnaw, A.; Akinc, A.; Sorensen, B.; Ragni, M. V., Targeting of Antithrombin in Hemophilia A or B with RNAi Therapy. *N Engl J Med* **2017**, *377* (9), 819-828.
22. Morrison, S. J.; Scadden, D. T., The bone marrow niche for haematopoietic stem cells. *Nature* **2014**, *505* (7483), 327-34.
23. Du, F.; Zhou, J.; Gong, R.; Huang, X.; Pansuria, M.; Virtue, A.; Li, X.; Wang, H.; Yang, X. F., Endothelial progenitor cells in atherosclerosis. *Frontiers in bioscience (Landmark edition)* **2012**, *17*, 2327-49.
24. Poulos, M. G.; Ramalingam, P.; Gutkin, M. C.; Llanos, P.; Gilleran, K.; Rabbany, S. Y.; Butler, J. M., Endothelial transplantation rejuvenates aged hematopoietic stem cell function. *J Clin Invest* **2017**, *127* (11), 4163-4178.
25. Augustin, H. G.; Koh, G. Y., Organotypic vasculature: From descriptive heterogeneity to functional pathophysiology. *Science* **2017**, *357* (6353).
26. Rafii, S.; Butler, J. M.; Ding, B. S., Angiocrine functions of organ-specific endothelial cells. *Nature* **2016**, *529* (7586), 316-25.
27. Tsoi, K. M.; MacParland, S. A.; Ma, X. Z.; Spetzler, V. N.; Echeverri, J.; Ouyang, B.; Fadel, S. M.; Sykes, E. A.; Goldaracena, N.; Kathis, J. M.; Conneely, J. B.; Alman, B. A.; Selzner, M.; Ostrowski, M. A.; Adeyi, O. A.; Zilman, A.; McGilvray, I. D.; Chan, W. C., Mechanism of hard-nanomaterial clearance by the liver. *Nat Mater* **2016**, *15* (11), 1212-1221.
28. Zhang, Y. N.; Poon, W.; Tavares, A. J.; McGilvray, I. D.; Chan, W. C. W., Nanoparticle-liver interactions: Cellular uptake and hepatobiliary elimination. *J Control Release* **2016**, *240*, 332-348.
29. Lorenzer, C.; Dirin, M.; Winkler, A. M.; Baumann, V.; Winkler, J., Going beyond the liver: progress and challenges of targeted delivery of siRNA therapeutics. *J Control Release* **2015**, *203*, 1-15.
30. Cheng, C. J.; Tietjen, G. T.; Saucier-Sawyer, J. K.; Saltzman, W. M., A holistic approach to targeting disease with polymeric nanoparticles. *Nat Rev Drug Discov* **2015**, *14* (4), 239-47.
31. Blanco, E.; Shen, H.; Ferrari, M., Principles of nanoparticle design for overcoming biological barriers to drug delivery. *Nat Biotechnol* **2015**, *33* (9), 941-51.
32. Zuckerman, J. E.; Choi, C. H. J.; Han, H.; Davis, M. E., Polycation-siRNA nanoparticles can disassemble at the kidney glomerular basement membrane. *Proceedings of the National Academy of Sciences of the United States of America* **2012**, *109* (8), 3137-3142.

33. Paunovska, K.; Sago, C. D.; Monaco, C. M.; Hudson, W. H.; Castro, M. G.; Rudoltz, T. G.; Kalathoor, S.; Vanover, D. A.; Santangelo, P. J.; Ahmed, R.; Bryksin, A. V.; Dahlman, J. E., A Direct Comparison of in Vitro and in Vivo Nucleic Acid Delivery Mediated by Hundreds of Nanoparticles Reveals a Weak Correlation. *Nano Lett* **2018**, *18* (3), 2148-2157.
34. Whitehead, K. A.; Dorkin, J. R.; Vegas, A. J.; Chang, P. H.; Veisheh, O.; Matthews, J.; Fenton, O. S.; Zhang, Y.; Olejnik, K. T.; Yesilyurt, V.; Chen, D.; Barros, S.; Klebanov, B.; Novobrantseva, T.; Langer, R.; Anderson, D. G., Degradable lipid nanoparticles with predictable in vivo siRNA delivery activity. *Nature communications* **2014**, *5*, 4277.
35. Dahlman, J. E.; Kauffman, K. J.; Xing, Y.; Shaw, T. E.; Mir, F. F.; Dlott, C. C.; Langer, R.; Anderson, D. G.; Wang, E. T., Barcoded nanoparticles for high throughput in vivo discovery of targeted therapeutics. *Proceedings of the National Academy of Sciences of the United States of America* **2017**, *114* (8), 2060-2065.
36. Paunovska, K.; Gil, C. J.; Lokugamage, M. P.; Sago, C. D.; Sato, M.; Lando, G. N.; Gamboa Castro, M.; Bryksin, A. V.; Dahlman, J. E., Analyzing 2000 in Vivo Drug Delivery Data Points Reveals Cholesterol Structure Impacts Nanoparticle Delivery. *ACS nano* **2018**. Doi: 10.1021/acsnano.8b03640
37. Yaari, Z.; da Silva, D.; Zinger, A.; Goldman, E.; Kajal, A.; Tshuva, R.; Barak, E.; Dahan, N.; HersHKovitz, D.; Goldfeder, M.; Roitman, J. S.; Schroeder, A., Theranostic barcoded nanoparticles for personalized cancer medicine. *Nature communications* **2016**, *7*, 13325.
38. Gilleron, J.; Querbes, W.; Zeigerer, A.; Borodovsky, A.; Marsico, G.; Schubert, U.; Manygoats, K.; Seifert, S.; Andree, C.; Stoter, M.; Epstein-Barash, H.; Zhang, L.; Koteliensky, V.; Fitzgerald, K.; Fava, E.; Bickle, M.; Kalaidzidis, Y.; Akinc, A.; Maier, M.; Zerial, M., Image-based analysis of lipid nanoparticle-mediated siRNA delivery, intracellular trafficking and endosomal escape. *Nat Biotechnol* **2013**, *31* (7), 638-46.
39. Wittrup, A.; Ai, A.; Liu, X.; Hamar, P.; Trifonova, R.; Charisse, K.; Manoharan, M.; Kirchhausen, T.; Lieberman, J., Visualizing lipid-formulated siRNA release from endosomes and target gene knockdown. *Nat Biotechnol* **2015**, *33* (8), 870-6.
40. Sigismund, S.; Confalonieri, S.; Ciliberto, A.; Polo, S.; Scita, G.; Di Fiore, P. P., Endocytosis and signaling: cell logistics shape the eukaryotic cell plan. *Physiological reviews* **2012**, *92* (1), 273-366.
41. Mui, B. L.; Tam, Y. K.; Jayaraman, M.; Ansell, S. M.; Du, X.; Tam, Y. Y.; Lin, P. J.; Chen, S.; Narayanannair, J. K.; Rajeev, K. G.; Manoharan, M.; Akinc, A.; Maier, M. A.; Cullis, P.; Madden, T. D.; Hope, M. J., Influence of Polyethylene Glycol Lipid Desorption Rates on Pharmacokinetics and Pharmacodynamics of siRNA Lipid Nanoparticles. *Mol Ther Nucleic Acids* **2013**, *2*, e139.

42. Deverman, B. E.; Pravdo, P. L.; Simpson, B. P.; Kumar, S. R.; Chan, K. Y.; Banerjee, A.; Wu, W. L.; Yang, B.; Huber, N.; Pasca, S. P.; Gradinaru, V., Cre-dependent selection yields AAV variants for widespread gene transfer to the adult brain. *Nat Biotechnol* **2016**, *34* (2), 204-9.

43. Dalkara, D.; Byrne, L. C.; Klimczak, R. R.; Visel, M.; Yin, L.; Merigan, W. H.; Flannery, J. G.; Schaffer, D. V., In vivo-directed evolution of a new adeno-associated virus for therapeutic outer retinal gene delivery from the vitreous. *Science translational medicine* **2013**, *5* (189), 189ra76.

44. Lisowski, L.; Dane, A. P.; Chu, K.; Zhang, Y.; Cunningham, S. C.; Wilson, E. M.; Nygaard, S.; Grompe, M.; Alexander, I. E.; Kay, M. A., Selection and evaluation of clinically relevant AAV variants in a xenograft liver model. *Nature* **2014**, *506* (7488), 382-6.

45. Chan, K. Y.; Jang, M. J.; Yoo, B. B.; Greenbaum, A.; Ravi, N.; Wu, W. L.; Sanchez-Guardado, L.; Lois, C.; Mazmanian, S. K.; Deverman, B. E.; Gradinaru, V., Engineered AAVs for efficient noninvasive gene delivery to the central and peripheral nervous systems. *Nat Neurosci* **2017**, *20* (8), 1172-1179.

46. LOKUGAMAGE, M. P.; SAGO, C. D.; DAHLMAN, J. E. TESTING THOUSANDS OF NANOPARTICLES *IN VIVO* USING DNA BARCODES. *CURRENT OPINION IN BIOMEDICAL ENGINEERING* **2018, *7*, 1-8.**

47. Perry, J. L.; Reuter, K. G.; Kai, M. P.; Herlihy, K. P.; Jones, S. W.; Luft, J. C.; Napier, M.; Bear, J. E.; DeSimone, J. M., PEGylated PRINT nanoparticles: the impact of PEG density on protein binding, macrophage association, biodistribution, and pharmacokinetics. *Nano Lett* **2012**, *12* (10), 5304-10.

48. Kulkarni, J. A.; Darjuan, M. M.; Mercer, J. E.; Chen, S.; van der Meel, R.; Thewalt, J. L.; Tam, Y. Y. C.; Cullis, P. R., On the Formation and Morphology of Lipid Nanoparticles Containing Ionizable Cationic Lipids and siRNA. *ACS nano* **2018**, *12* (5), 4787-4795.

49. Ni, C. W.; Kumar, S.; Ankeny, C. J.; Jo, H., Development of immortalized mouse aortic endothelial cell lines. *Vascular cell* **2014**, *6* (1), 7.

50. Sago, C. D.; Lokugamage, M. P.; Lando, G. N.; Djeddar, N.; Shah, N. N.; Syed, C.; Bryksin, A. V.; Dahlman, J. E. Modifying a Commonly Expressed Endocytic Receptor Retargets Nanoparticles in Vivo. *Nano Lett* **2018**.

51. Platt, R. J.; Chen, S.; Zhou, Y.; Yim, M. J.; Swiech, L.; Kempton, H. R.; Dahlman, J. E.; Parnas, O.; Eisenhaure, T. M.; Jovanovic, M.; Graham, D. B.; Jhunjhunwala, S.; Heidenreich, M.; Xavier, R. J.; Langer, R.; Anderson, D. G.; Hacohen, N.; Regev, A.; Feng, G.; Sharp, P. A.; Zhang, F., CRISPR-Cas9 knockin mice for genome editing and cancer modeling. *Cell* **2014**, *159* (2), 440-55.
52. Finn, J. D.; Smith, A. R.; Patel, M. C.; Shaw, L.; Youniss, M. R.; van Heteren, J.; Dirstine, T.; Ciullo, C.; Lescarbeau, R.; Seitzer, J.; Shah, R. R.; Shah, A.; Ling, D.; Growe, J.; Pink, M.; Rohde, E.; Wood, K. M.; Salomon, W. E.; Harrington, W. F.; Dombrowski, C.; Strapps, W. R.; Chang, Y.; Morrissey, D. V., A Single Administration of CRISPR/Cas9 Lipid Nanoparticles Achieves Robust and Persistent In Vivo Genome Editing. *Cell Rep* **2018**, *22* (9), 2227-2235.
53. Cheng, Z.; Al Zaki, A.; Hui, J. Z.; Muzykantov, V. R.; Tsourkas, A., Multifunctional nanoparticles: cost versus benefit of adding targeting and imaging capabilities. *Science* **2012**, *338* (6109), 903-10.
54. Kheirilomoom, A.; Kim, C. W.; Seo, J. W.; Kumar, S.; Son, D. J.; Gagnon, M. K.; Ingham, E. S.; Ferrara, K. W.; Jo, H., Multifunctional Nanoparticles Facilitate Molecular Targeting and miRNA Delivery to Inhibit Atherosclerosis in ApoE(-/-) Mice. *ACS nano* **2015**, *9* (9), 8885-97.
55. Muro, S.; Garnacho, C.; Champion, J. A.; Leferovich, J.; Gajewski, C.; Schuchman, E. H.; Mitragotri, S.; Muzykantov, V. R., Control of endothelial targeting and intracellular delivery of therapeutic enzymes by modulating the size and shape of ICAM-1-targeted carriers. *Mol Ther* **2008**, *16* (8), 1450-8.
56. Kauffman, K. J.; Dorkin, J. R.; Yang, J. H.; Heartlein, M. W.; DeRosa, F.; Mir, F. F.; Fenton, O. S.; Anderson, D. G., Optimization of Lipid Nanoparticle Formulations for mRNA Delivery in Vivo with Fractional Factorial and Definitive Screening Designs. *Nano Lett* **2015**, *15* (11), 7300-6.

CHAPTER 5. IDENTIFICATION OF LNPS WITH TROPISM TO T-CELLS

5.1 Background and Results

T lymphocytes help regulate immune responses, which makes them important drug targets. For example, antibodies that block T cell CTLA-4 or PD-1 signaling have driven anti-tumor responses^[1]. However, antibodies target druggable proteins, which constitute approximately 15% of total proteins. By contrast, siRNA can inhibit the translation of any gene; this approach may be useful, since many ‘undruggable’ proteins were recently implicated in T cell-mediated immunity^[2].

Clinically relevant RNA delivery to cells other than hepatocytes^[3] remains challenging^[4]. However, there have been advances in T cell siRNA delivery. For example, siRNA was delivered to T cells using a single chain antibody linked to a cationic peptide; this led to gene silencing at 5 mg / kg^[5]. In a second example, nanoparticles were coated with anti-CD4 antibodies, leading to 20% target gene silencing at 1 mg / kg doses^[6]. More recently, LNPs that target hepatocytes were re-targeted to T cells by coating them with CD4 antibodies, leading to 50% *in vivo* T cell gene silencing at 6 mg / kg doses^[7]. These papers (and others)^[8] achieve T cell delivery using peptide-, protein-, or aptamer-based targeting ligands; ligand-based targeting is used throughout nanomedicine. However, ligands can also make reproducible manufacturing at human scales more challenging^[9]. One alternative to active targeting is to exploit endogenous lipid trafficking; notably, the only FDA approved RNA nanoparticle therapy^[3] utilizes LNPs that are trafficked to hepatocytes without ligands via endogenous cholesterol transport pathways^[10]. Natural trafficking has not been exploited to promote nanoparticle delivery to T cells, yet these cells interact with

enveloped viruses, which are coated by lipids and have diameters similar to LNPs. For example, T cells uptake HTLV-1 virus^[11], which has a diameter of 105 nm. T cells also interact with lipoprotein particles, which can have structures similar to LNPs^[12]. We therefore hypothesized that LNPs could interact with T cells without targeting ligands.

To test this hypothesis, we quantified how well 168 LNPs delivered siRNA to 9 cell types *in vivo*. Using traditional 1-by-1 *in vivo* approaches, this would require FACS (fluorescent activated cell sorting) analysis of more than 800 mice. Thus, to generate large scale *in vivo* data, we developed a siGFP / DNA barcode-based screening system. This system quantifies how over 100 nanoparticles deliver siGFP to any desired combination of on- and off-target cell types *in vivo*. This *in vivo* approach contrasts with previous LNP research, which utilizes *in vitro* screening to select a small number of nanoparticles for *in vivo* evaluation. Our approach is supported by evidence that *in vitro* nanoparticle delivery can be a poor predictor of *in vivo* nanoparticle delivery^[13]. By combining high throughput *in vivo* analyses and bioinformatics, we found that a new class of materials, herein named conformationally constrained lipids, can form stable LNPs. We also found these ‘constrained LNPs’ (cLNPs) can deliver siRNA to T cells *in vivo*. These data demonstrate that the conformational state of lipids can alter LNP tropism and provide intriguing preliminary evidence that natural trafficking can promote T cell delivery, offering a potential alternative to active targeting.

We first synthesized 13 chemically diverse lipids containing amines or boronic acid. The library was constructed to investigate whether the structure of the (i) head groups and (ii) lipid tail affected delivery. We purified a ‘scaffold’ containing the unsaturated lipid linoleate and two ester bonds (**Figure 5.1A, Figure 5.2A, Supporting Information**). This

scaffold did not have any ionizable components; we attached head group variants to the reactive sites, in order to create chemical diversity. At reactive site 1, we added 11 head groups (labeled 1-11) via esterification, resulting in head groups linked by ester or carbonate linkages, respectively (**Figure 5.1B**). At reactive site 2, we added 3 lipid tails (labeled A-C) with diverse structures (**Figure 5.1C**) via esterification. Tail A contained adamantane, a constrained lipid with a defined ‘armchair’ structure. Tail B contained two lipid tails, bringing the total number of tails to 3. The control tail, C, was linoleate; this created a construct with two identical lipid tails. After synthesis, we confirmed the chemical structure of all 13 lipids using high resolution mass spectroscopy or ¹H-NMR (**Figure 5.2B-D, Supporting Information**). We named each lipid with the nomenclature ‘head group number – tail letter’ (e.g. 11-A).

We then investigated whether the 13 ionizable lipids formed stable LNPs. We measured the hydrodynamic diameter of LNPs carrying a siRNA targeting GFP^[12] (siGFP) as well as a DNA barcode^[14]; the LNPs were formulated using microfluidics^[15]. The siGFP was chemically modified to reduce immunostimulation and enhance on-target silencing via preferential antisense RISC loading (**Figure 5.3A, Supporting Information**). To minimize the chance our results were affected by other constituents added to the LNP, we added previously validated constituents: C₁₄PEG₂₀₀₀, unmodified cholesterol, and either 1-2-distearoyl-sn-glycero-3-phosphocholine (DSPC) or 1-2-dioleoyl-sn-glycero-3-phosphoethanolamine (DOPE) (**Figure 5.1D**). As a control to ensure our results were not affected by the molar ratio of the 4 components, we formulated each of the 13 lipids with 2 phospholipids and 4 molar ratios, producing a total of 104 chemically distinct LNPs (**Figure 5.1D**). Encouragingly, 100 of the 104 LNPs formed small, monodisperse

populations, as evidenced by hydrodynamic diameter and polydispersity index; these 100 LNPs were pooled together. The diameter for individual LNPs varied between 30 and 170 nm. As a control, we also measured the diameter and polydispersity of the pooled LNPs. We found them to be 76 nm (**Figure 5.1E**) and 0.23 (**Figure 5.1F**), respectively, which was within the range of the individuals comprising the pool. We then analyzed the hydrodynamic diameter as a function of ionizable lipid (**Figure 5.3B, Supporting Information**), molar ratio of the four constituents (**Figure 5.3C, Supporting Information**), and the type of phospholipid (DSPC / DOPE) added to the formulation (**Figure 5.3D, Supporting Information**). In all cases, the average diameter varied between 50 and 100 nm. These data led us to conclude these lipids could form LNPs with hydrodynamic diameters similar to lipoproteins and viruses.

We evaluated how each LNP delivered siRNA to target cells (in this case, T lymphocytes) as well as 8 off-target cell types *in vivo* (**Figure 5.4A,B, Supporting Information**). Our approach utilizes DNA barcodes and siGFP, to evaluate how many distinct LNPs functionally delivered siGFP, in any combination of target cells, in a single mouse. We formulated LNP-1, with chemical structure 1, to carry siGFP and DNA barcode 1; we separately formulated LNP-N, with chemical structure N, to carry siGFP and DNA barcode N (**Figure 5.5A**). We included naked barcodes as a negative control^[13], since DNA does not readily enter cells. We pooled the LNPs together, and intravenously injected them into mice that constitutively express GFP under a CAG promoter (**Figure 5.5B**). The GFP acted as the functional delivery readout; LNPs which functionally delivered siGFP into the cytoplasm would have lower GFP protein expression. Thus, 3 days after injecting mice, we isolated GFP^{Low} cells using fluorescence activated cell sorting (FACS), and deep

sequenced the DNA barcodes in GFP^{Low} cells. In this way, we isolated barcodes co-localized with cells in which GFP protein silencing occurred. After sequencing the barcodes, we calculated normalized delivery, i.e., the number of barcodes for each individual barcode, divided by the total number of barcodes within that sample. Normalized delivery is analogous to counts per million in RNAseq experiments^[16]. Since GFP is expressed in all cell types, this assay allows us to (i) compare GFP knockdown in any combination of on- / off-target cells and (ii) identify LNPs that co-localized in GFP^{Low} cells.

Three days after injecting a total dose of 1.5 mg / kg into mice (100 distinct LNPs, 0.015 mg / kg / particle on average), we quantified GFP silencing in 9 cell types. Compared to PBS treated mice, there was an increased number of GFP^{Low} splenic B cells and splenic T cells (**Figure 5.5C**). The average GFP protein silencing, quantified by mean fluorescent intensity, was highest in splenic T cells, followed by liver immune cells, splenic B cells, and lung endothelial cells (**Figure 5.5D**). Surprisingly, we found no evidence of silencing in hepatocytes (**Figure 5.5C,D**), which are preferentially targeted by most LNPs^[4]. We then monitored the controls included in our data; we sequenced the GFP^{Low} lung splenic T cells as well as lung endothelial cells, splenic B cells, and liver immune cells. In all 4 cell types, the normalized delivery of both negative controls (naked barcodes) was lower than barcodes delivered by LNPs, as expected (**Figure 5.5E**).

We then performed a large *in vivo* structure-function analysis, using the DNA sequencing data to evaluate whether any nanoparticle material properties promoted delivery to splenic T cells. First, we calculated the enrichment for different nanoparticle properties (**Figure 5.6, Supporting Information**). Briefly, we calculated the odds a nanoparticle with a

particular property would show up by chance in particles that (i) performed in the top 10%, and separately, (ii) particles that performed in the bottom 10%. Nanoparticles formulated with DSPC were enriched in effective particles (i.e., particles with high normalized delivery), whereas nanoparticles formulated with DOPE were enriched in particles that performed poorly (**Figure 5.5F**). To validate these results, we then compared the normalized delivery for all LNPs formulated with DSPC and DOPE, respectively, and found that DSPC-containing LNPs outperformed DOPE-containing LNPs (**Figure 5.7A, Supporting Information**). As an additional validation, we calculated the normalized delivery of ‘paired’ LNPs, i.e., LNPs that had the same molar ratios and ionizable lipids (but different phospholipids). We found that DSPC LNPs outperformed their paired DOPE containing LNP (**Figure 5.7B, Supporting Information**). Based on these data, we concluded that the phospholipid contained within the LNP affected splenic T cell delivery. We therefore limited future chemical analysis to DSPC containing formulations.

We then analyzed enrichment for the 13 ionizable lipids, in order to evaluate the effect of the lipid tail and head group, and found 3 ionizable lipids were enriched (**Figure 5.5G**). As a control, we plotted enrichment of each headgroup versus headgroup molecular weight, hydrophobicity (LogP), and polar surface area (**Figure 5.8A-D, Supporting Information**); we did not observe correlations between these traits and enrichment. The lipid that was most enriched, 11-A, contained a conformationally constrained adamantane tail. Notably, the enrichment (**Figure 5.5G**) and normalized DNA delivery (**Figure 5.5H**) of 11-A was higher than 11-B and 11-C, the two compounds with identical head groups, but unconstrained lipid tails. We then performed a paired analysis using compounds with the same molar ratio and found that adamantane containing tails outperformed other tail

structures (**Figure 5.8E, Supporting Information**). Finally, as a control, we analyzed how LNP size affected delivery. We plotted normalized T cell delivery against LNP size and found no relationship (**Figure 5.8F, Supporting Information**). Taken together, these data provided initial evidence that adamantane-containing LNPs could deliver nucleic acids to T cells *in vivo*, without the use of a targeting ligand.

To further investigate the relationship between adamantane and siRNA delivery, we performed a second *in vivo* screen with adamantane-containing LNPs. The second library was evolved based on the results of the first screen. To do this, we first synthesized new ionizable lipids, using the most enriched components from the first screen, head group 1 (**Figure 5.1B**) and adamantane tail (tail A, **Figure 5.1C**). More specifically, at reactive site 3, we added 15 lipids tails (labeled D-S) with diverse structures (**Figure 5.9A,B**) via esterification. We also included the top-ranked LNP from our first screen (**Figure 5.9C**). Thus, we synthesized 16 ionizable lipids in total. We named each lipid in the following manner: ‘head group number (R₁) – tail letter (R₂) – tail letter (R₃)’ (e.g. 11-A-M). We formulated each LNP with C₁₄PEG₂₀₀₀, cholesterol, and DSPC. Once again, to control against effects driven by the molar ratio of the components, we formulated all 16 ionizable lipids at 4 molar ratios, for a total of 64 LNPs (**Figure 5.9D**). Each LNP carried siGFP and a unique barcode. 55 of the LNPs formed small, monodisperse populations, based on the hydrodynamic diameter and polydispersity index, and were therefore pooled together. The diameter for individual LNPs varied between 20 and 200 nm, with an average of 92 nm (**Figure 5.9E**) and an average PDI of 0.20 (**Figure 5.9F**). We plotted hydrodynamic diameter for each ionizable lipid (**Figure 5.10A, Supporting Information**) and each molar

ratio (**Figure 5.10B, Supporting Information**), and found that all the compositions formed LNPs within the 20-200 nm range.

We then administered all 55 LNPs intravenously to mice at a total dose of 1.5 mg / kg. Three days later, we quantified GFP silencing in 9 cell types. Once again, we (i) found GFP^{Low} splenic T cells (**Figure 5.9G**), (ii) measured GFP protein silencing in splenic T cells (**Figure 5.9H**), (iii) found no evidence of silencing in hepatocytes (**Figure 5.9G,H**), and (iv) found no relationship between nanoparticle size and delivery (**Figure 5.10C, Supporting Information**). As a control, we quantified the normalized delivery of both negative controls (naked barcodes), and found they were lower than barcodes delivered by LNPs (**Figure 5.9I**). We then analyzed the data, to evaluate whether the molecule added to reactive site 3 (**Figure 5.9B**) altered delivery when adamantane was present. Using enrichment (**Figure 5.9J**), we found reactive group D, I, and M were enriched. We were unable to identify why these variants performed well. However, compared to the top performing cLNP from screen 1, we found delivery was not greatly improved with any alteration to the reactive site 3 molecule (**Figure 5.9K**). It is interesting to note that the top performing cLNP from screen 1 (11-A-M) was enriched more than any other cLNP (**Figure 5.9J**). These data provided additional evidence to support the hypothesis that LNPs can deliver siRNA to T cells without targeting ligands.

Like all high throughput screening systems, the value of this siGFP / DNA barcode assay is related to its ability to make predictions. We therefore evaluated whether the top-ranked LNPs from our first (11-A-M) and second (1-A-N) screens delivered siRNA *in vivo* (**Figure 5.11A**). We formulated each LNP with siGFP and analyzed physical traits; each LNP had similar hydrodynamic diameter, polydispersity and pKa (**Figure 5.11B**). We then

intravenously injected mice with 1.5 mg / kg; 3 days later, we isolated cells and measured GFP protein expression. When compared to mice treated with a non-targeting, chemically modified siRNA (siLuc), we found 11-A-M silenced GFP more than 1-A-N (**Figure 5.11C**). To validate the activity of 1-A-N, we formulated it with siCD45, and quantified CD45 silencing three days after injecting mice with 1.5 mg / kg; we found statistically significant silencing in T cells (**Figure 5.10D,E**). Based on these head-to-head data, we focused on compound 11-A-M for future subsequent analysis. We then performed a siRNA gene silencing dose response *in vivo*, and found that 11-A-M silenced GFP as doses as low as 0.5 mg / kg (**Figure 5.11D**). We quantified silencing in subsets of T cells, focusing on CD4⁺ and CD8⁺ cells, respectively, and observed more potent protein silencing in CD8⁺ T cells (**Figure 5.11E**). During this experiment, we also evaluated whether 11-A-M delivered siGFP to other common ‘off-target’ cell types by quantifying GFP silencing in cell subsets isolated from the liver and the spleen. Recapitulating observations made in both screens, we observed no significant silencing at doses as high as 1.5 mg / kg (**Figure 5.12A-F, Supporting Information**), suggesting that cLNPs may preferentially silence genes in splenic CD8⁺ T cells. Finally, we utilized 11-A-M to facilitate *in vivo* gene editing in T cells. We formulated it to carry a chemically modified sgRNA targeting GFP (**Figure 5.12G, Supporting Information**) into mice^[17] constitutively expressing Cas9 and GFP. Five days after administration, we quantified GFP expression in CD3⁺ T cells as well as in CD4⁺ and CD8⁺ T Cells. We observed a similar tropism; GFP protein was silenced more robustly in CD8⁺ than in CD4⁺ T cells (**Figure 5.11F**). Notably, cLNPs did not lead to weight loss 24 hours after administration in any experiment (**Figure 5.13 Supporting**

Information). Taken together, these data led us to conclude that cLNPs without targeting ligands can deliver siRNA and sgRNA to splenic T cells.

Nanoparticles that deliver RNA systemically to non-hepatocytes are difficult to design^[4], in large part because (i) there is no high throughput method to study nanoparticle siRNA delivery *in vivo* and (ii) natural trafficking mechanisms to non-liver cells remain elusive. This universal problem in nanomedicine slows the development of all RNA therapies; currently, scientists perform high throughput nanoparticle assays *in vitro*, even though cell culture does not^[13] recapitulate all the factors that affect delivery *in vivo*. Notably, the results from our first siGFP screen predicted that preferential T cell delivery would occur; these data were confirmed by the second siGFP screen, and by several *in vivo* experiments with cLNPs selected from the library. These data suggest that high throughput *in vivo* siRNA screens can identify nanoparticles with novel tropism.

It is important to acknowledge the limitations of our work. First, the siGFP system will not work with unstable nanoparticles. As a result, it is critical to (i) analyze the size and polydispersity of each individual nanoparticle before pooling, (ii) include the naked DNA barcode control, (iii) use untreated GFP mice to gate during FACS, and (iv) individually confirm any lead candidates identified by the screen. Second, although we observed protein silencing in T cells at 0.5 mg / kg doses, we will need to reduce this dose by at least 30-fold before it matches the potency of a FDA-approved siRNA delivery vehicle in mice^[18]. Lastly, we did not identify the natural trafficking pathways that promoted delivery to T cells. We believe that identifying the genes or pathways that promote LNP delivery to T cells without ligands constitutes an exciting scientific opportunity. Nonetheless, we believe these data, which provide the first < 1 mg / kg gene silencing in T cells *in vivo*, and do so

without targeting ligands. This provides an exciting starting point for further studies. We anticipate iterative *in vivo* approaches we recently reported^[19] may further improve T cell LNP potency. In this way, we hope that future work on cLNPs lead to more effective, scalable RNA immunotherapies, as well as fundamental advances in our understanding of T cell lipid trafficking. More generally, these data may inspire other efforts to identify natural mechanisms to target extra-hepatic cells which – to date – have only been targeted with active ligands.

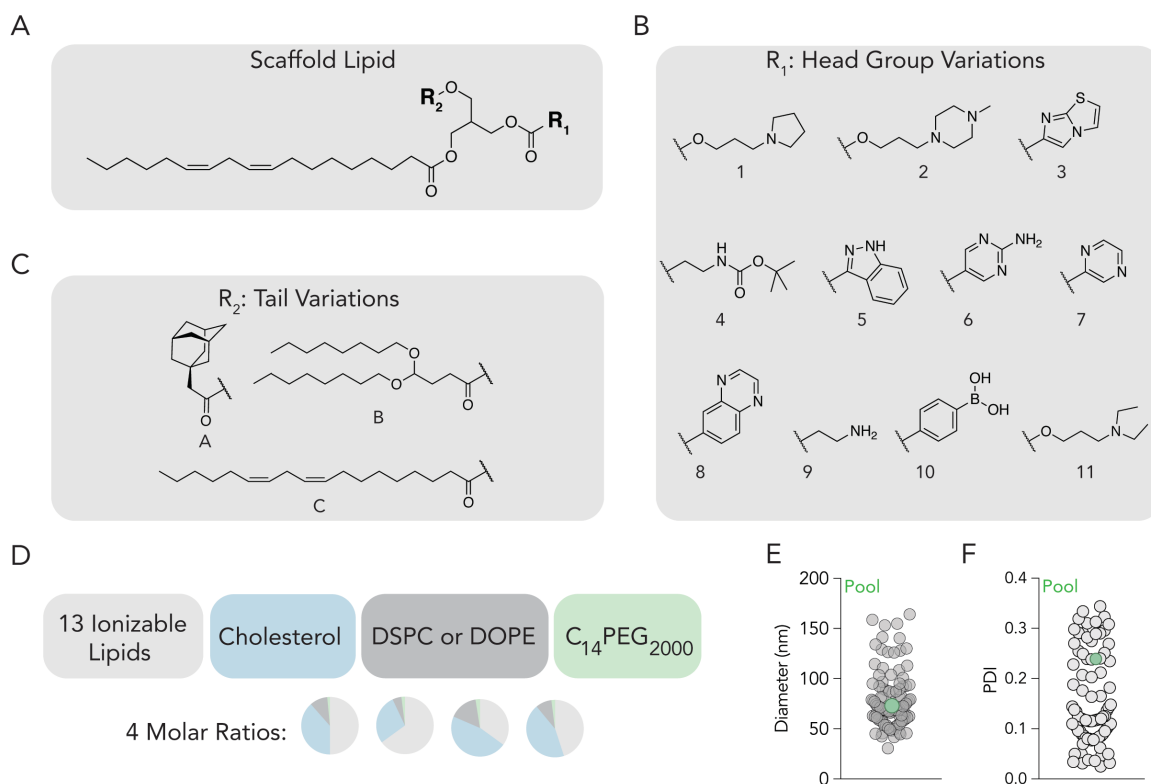
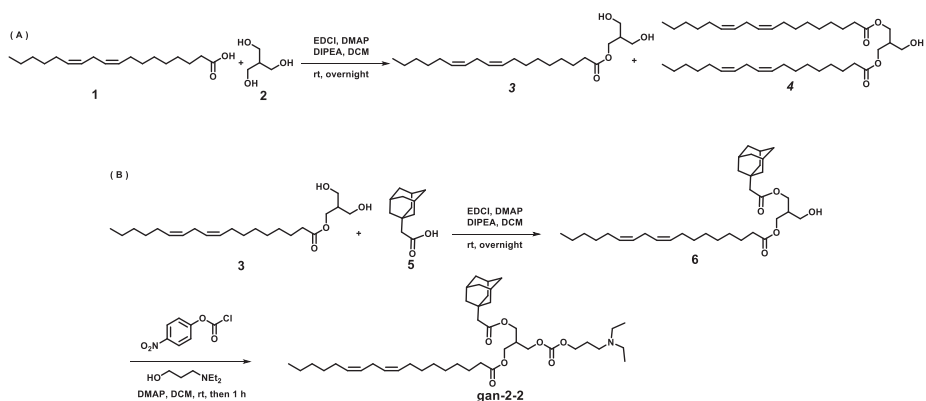


Figure 5.1. Lipid nanoparticles containing a constrained lipid can form stable LNPs. (A) Ionizable lipid scaffold to which (B) tail variants and (C) head group variants were added. (D) Using 4 molar ratios, each of the 13 ionizable lipids were formulated with cholesterol, lipid-PEG, and either DSPC or DOPE, to create 104 distinct LNPs. (E) Hydrodynamic diameter and (F) polydispersity index of all formulated LNPs, measured individually.

A



B

Lipid-1C: HRMS (ESI, m/z) calculated for $C_{48}H_{84}NO_7$ $[M + H]^+$: 786.6242, found 786.6227.

Lipid-2C: HRMS (ESI, m/z) calculated for $C_{49}H_{87}N_2O_7$ $[M + H]^+$: 815.6508, found 815.6494.

Lipid-3C: HRMS (ESI, m/z) calculated for $C_{46}H_{73}N_2O_6S$ $[M + H]^+$: 781.5187, found 781.5187.

Lipid-4C: HRMS (ESI, m/z) calculated for $C_{48}H_{84}NO_8$ $[M + H]^+$: 802.6191, found 802.6194.

Lipid-5C: HRMS (ESI, m/z) calculated for $C_{48}H_{75}N_2O_6$ $[M + H]^+$: 775.5620, found 775.5645.

Lipid-6C: HRMS (ESI, m/z) calculated for $C_{45}H_{74}N_3O_6$ $[M + H]^+$: 752.5572, found 752.5586.

Lipid-7C: HRMS (ESI, m/z) calculated for $C_{45}H_{73}N_2O_6$ $[M + H]^+$: 737.5463, found 737.5476.

Lipid-8C: HRMS (ESI, m/z) calculated for $C_{49}H_{75}N_2O_6$ $[M + H]^+$: 787.5620, found 787.5628.

Lipid-9C: HRMS (ESI, m/z) calculated for $C_{43}H_{76}NO_6$ $[M + H]^+$: 702.5667, found 702.5686.

Lipid-10C: HRMS (ESI, m/z) calculated for $C_{47}H_{76}BO_8$ $[M + H]^+$: 779.5628, found 779.5628.

Lipid-11C: HRMS (ESI, m/z) calculated for $C_{48}H_{86}NO_7$ $[M + H]^+$: 788.6399, found 788.6412.

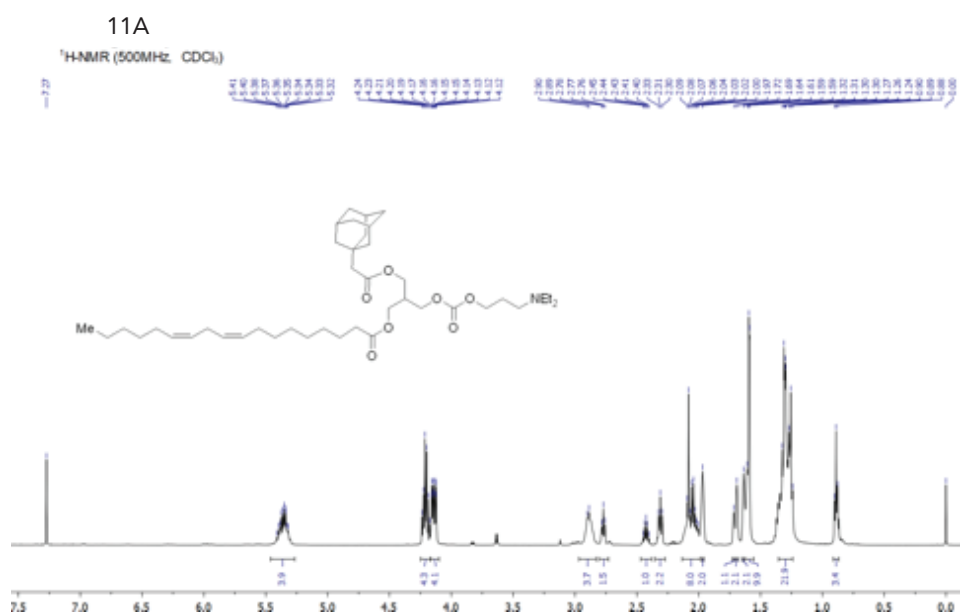
Lipid-11B: HRMS (ESI, m/z) calculated for $C_{50}H_{94}NO_9$ $[M + H]^+$: 852.6923, found 852.6903.

Lipid-11A: HRMS (ESI, m/z) calculated for $C_{42}H_{72}NO_7$ $[M + H]^+$: 702.5303, found 702.5277.

1H NMR (500 MHz, $CDCl_3$) δ 0.89 (t, $J = 7.0$ Hz, 3 H), 1.24-1.36 (m, 22 H), 1.57-1.62 (m, 10 H), 1.64 (s, 2 H), 1.69 (s, 2 H), 1.72 (s, 1 H), 1.97 (s, 2 H), 2.01-2.09 (m, 8 H), 2.31 (t, $J = 7.5$ Hz, 2 H), 2.43 (m, 1 H), 2.77 (t, $J = 6.5$, 2 H), 2.89 (m, 4 H), 4.15 (dd, $J_1 = 6.0$ Hz, $J_2 = 13.5$ Hz, 4 H), 4.21 (m, 4 H), 5.36 (m, 4 H); ^{13}C NMR (125 MHz, $CDCl_3$) δ 14.0, 14.2, 22.5, 24.8, 25.6, 27.2, 29.1, 29.3, 29.6, 29.7, 31.5, 31.9, 32.8, 34.1, 36.6, 37.4, 42.4, 46.7, 48.7, 49.1, 61.0, 61.1, 61.3, 61.4, 64.2, 65.1, 65.3, 65.8, 127.9, 128.0, 130.0, 130.2, 154.7, 171.4, 173.5;

!

C



D

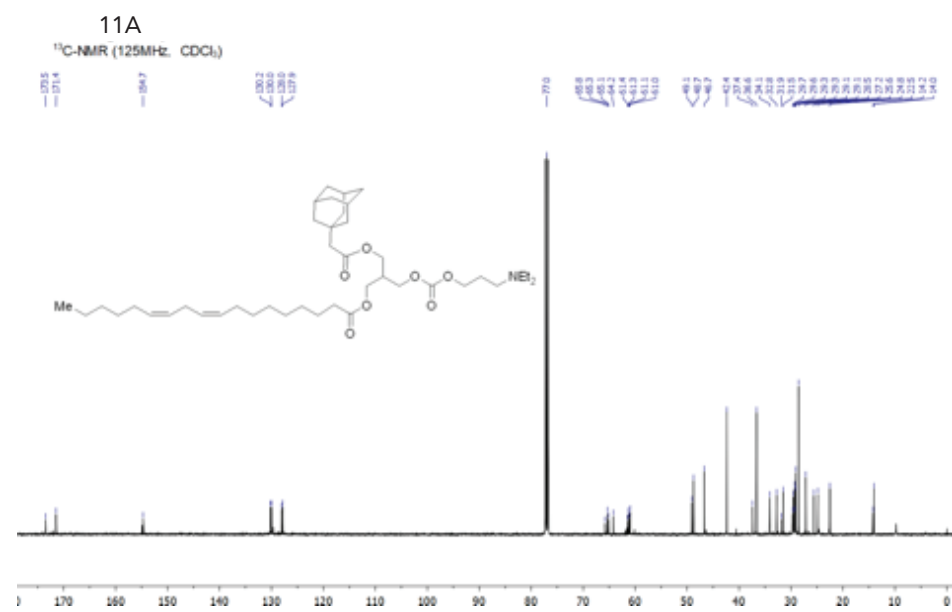


Figure 5.2. A) General synthesis flow for lipid 11A. B) Mass and NMR data for key ionizable lipids. C) ^1H NMR spectra for Lipid 11A. D) ^{13}C NMR spectra for Lipid 11A

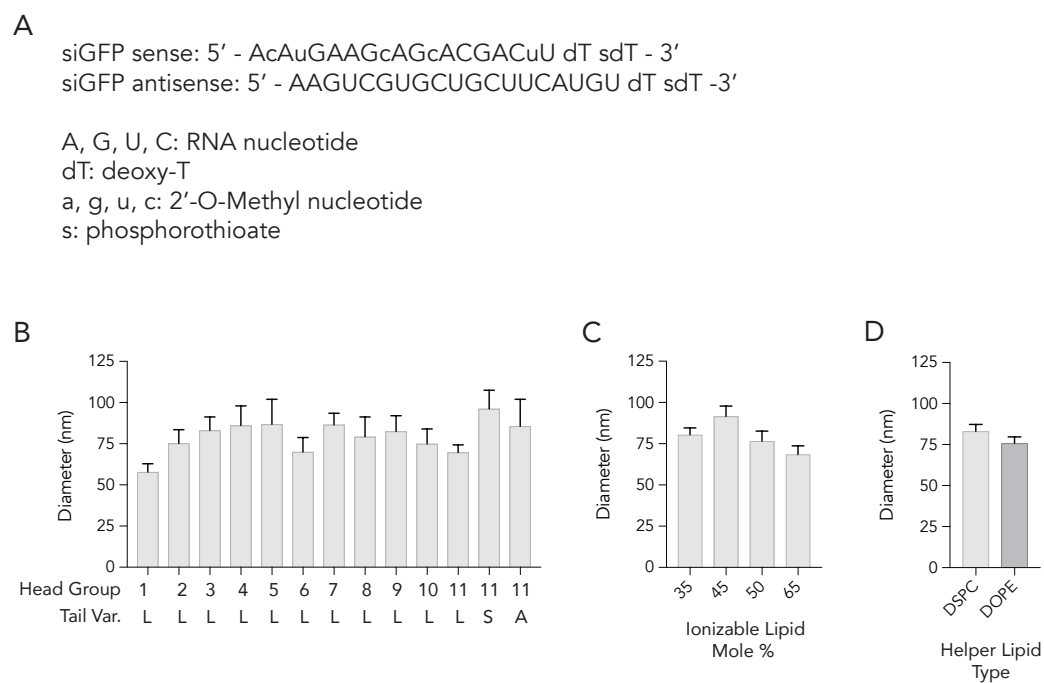


Figure 5.3. A) Sequence and chemical modifications of siGFP. Hydrodynamic diameter of LNPs plotted as a function of B) ionizable lipid type, C) molar percent of ionizable lipid, and D) phospholipid type.

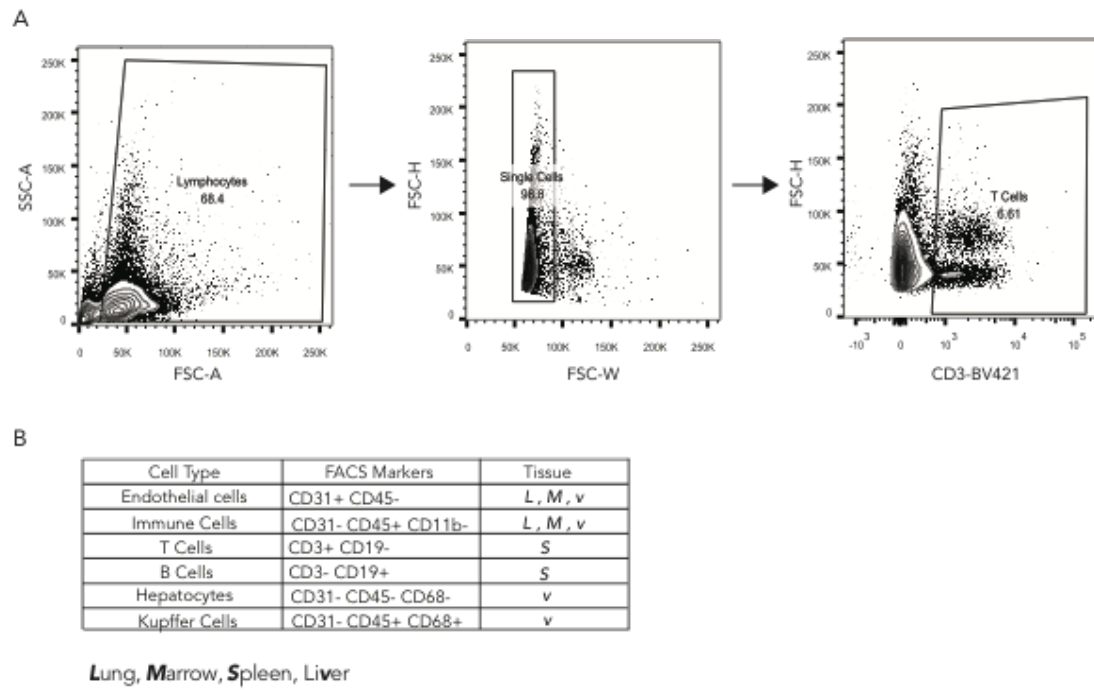


Figure 5.4. A) Representative FACS plots showing gating strategy for splenic CD3+ T cells. B) Cell-type specific markers.

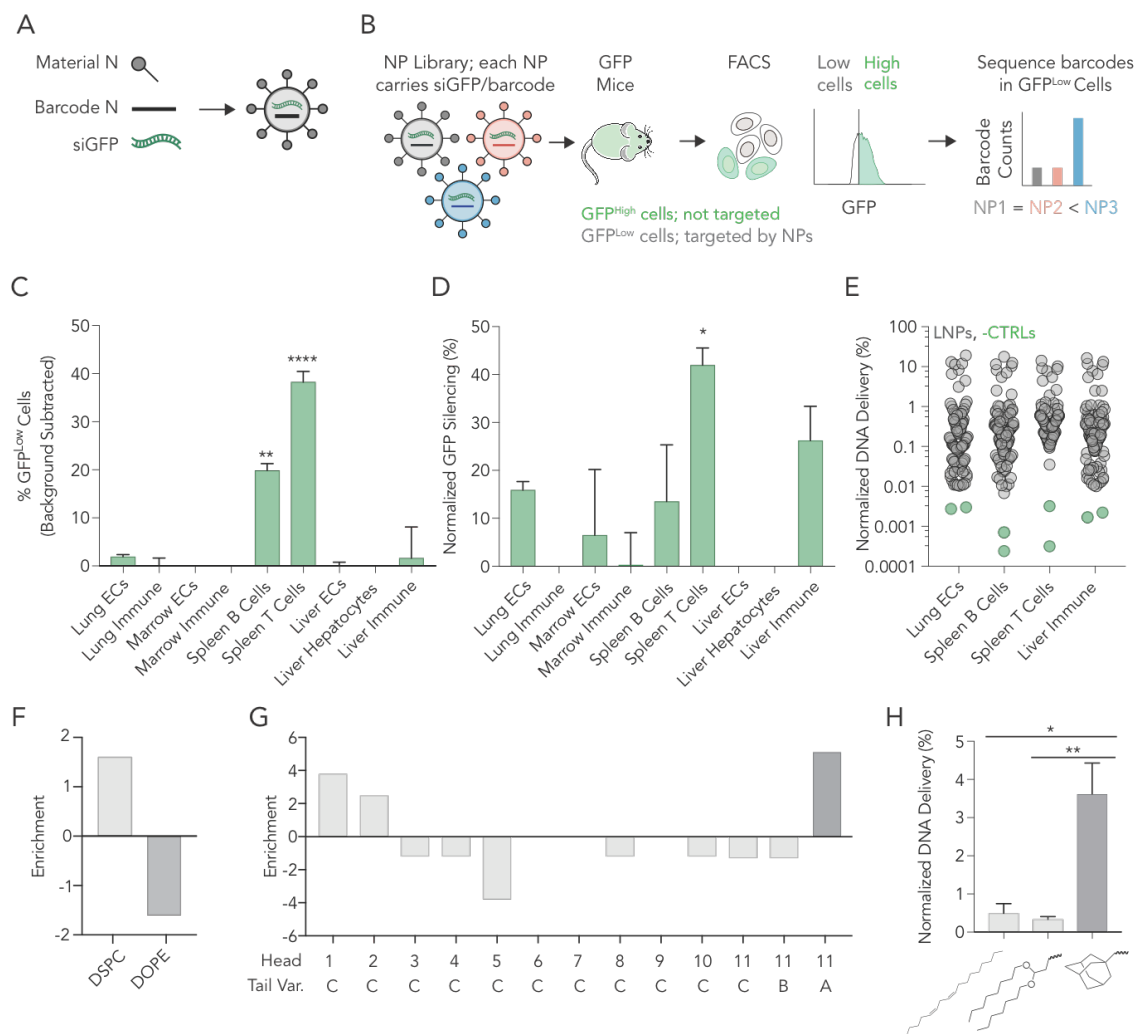


Figure 5.5. A high-throughput siRNA screen for in vivo activity reveals LNPs with constrained lipids have biological activity in T cells. (A) Nanoparticles were formulated to carry a distinct DNA barcode and siGFP. (B) Of the 104 LNPs formulated, we pooled 100 stable LNPs together, and administered them to mice expressing GFP. After 3 days, we isolated GFP^{Low} cells and sequenced the DNA barcodes within that population. (C) Percent GFP^{Low} cells in 9 cell types. Two-way ANOVA, **P<0.01, ****P<0.0001. (D) Normalized decrease in GFP MFI in 9 cell types. Two-way ANOVA, *P<0.05. (E) Normalized DNA delivery in lung endothelial cells, splenic B and T cells, as well as liver immune cells. (F) Enrichment of DSPC-containing LNPs in splenic T cells. (G) Enrichment for each of the 13 ionizable lipids. (H) Normalized DNA delivery of LNPs formulated with head group 11 and tail L, S, or A. One-way ANOVA, *P<0.05, **P<0.01.

A

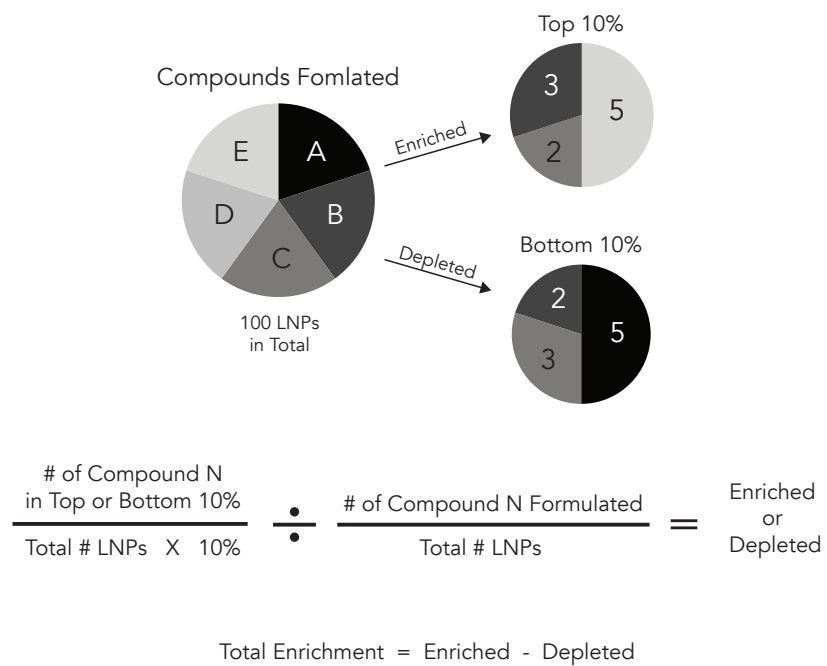


Figure 5.6. A) An example showing how enrichment is calculated.

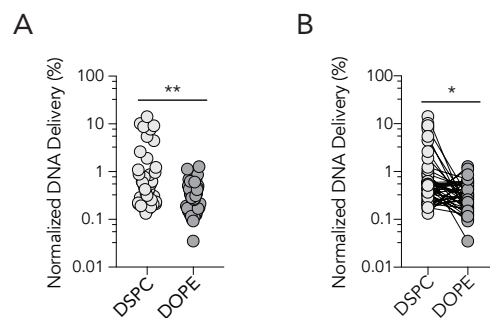


Figure 5.7. A) Normalized DNA delivery of LNPs plotted as a function of phospholipid. 2-way T test, $P < 0.01$. (B) Paired analysis of normalized DNA delivery of LNPs containing DSPC or DOPE. Paired 2-way T test, $*P < 0.05$.**

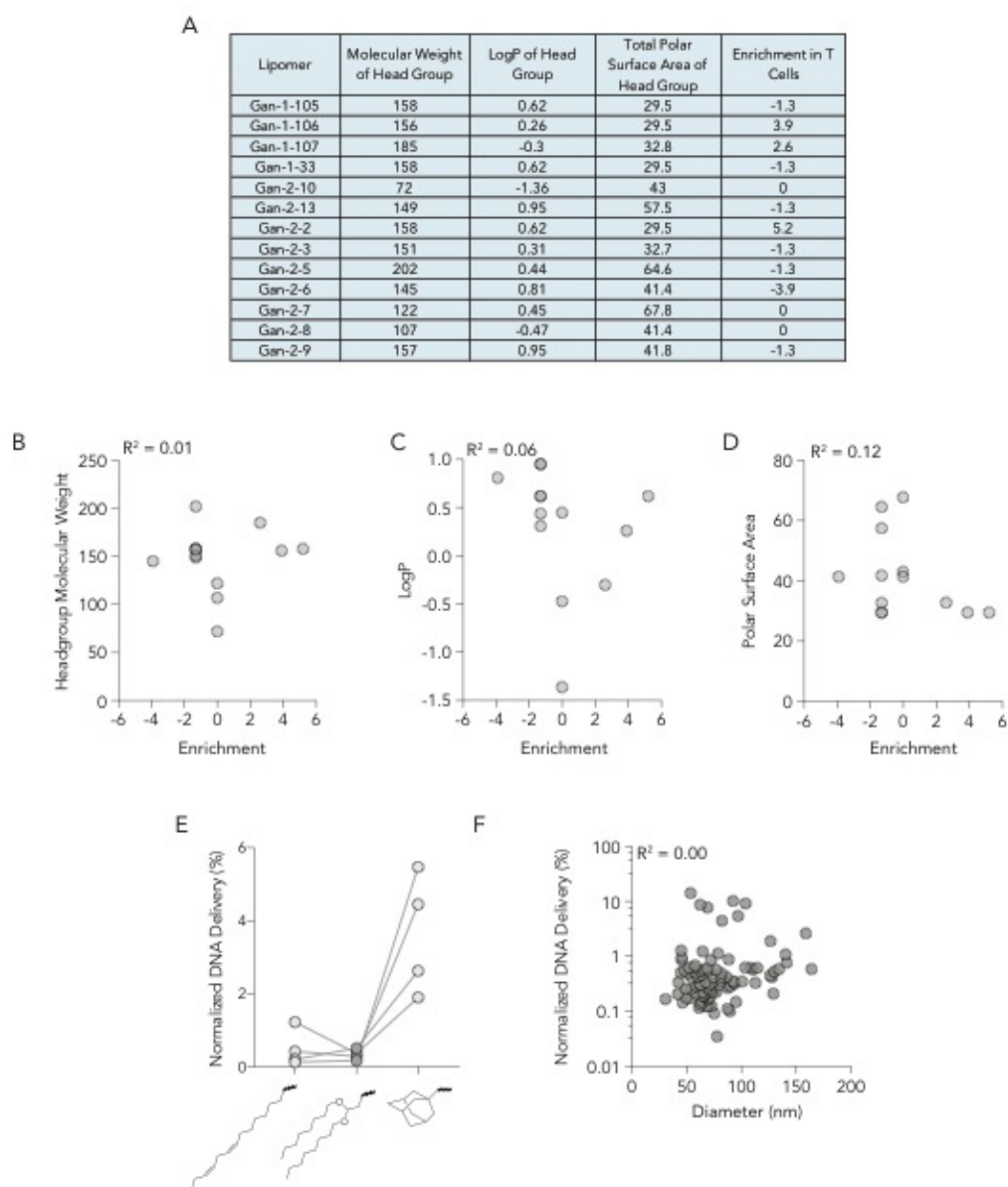


Figure 5.8. A) Physical and chemical analysis of headgroups. B) Correlation of headgroup molecular weight and enrichment. C) Correlation of headgroup LogP and enrichment. D) Correlation of headgroup polar surface area and enrichment. E) Normalized delivery of LNPs formulated with different ionizable lipids sharing headgroup 11, but with different tail structures. F) Correlation of LNP diameter and normalized DNA delivery.

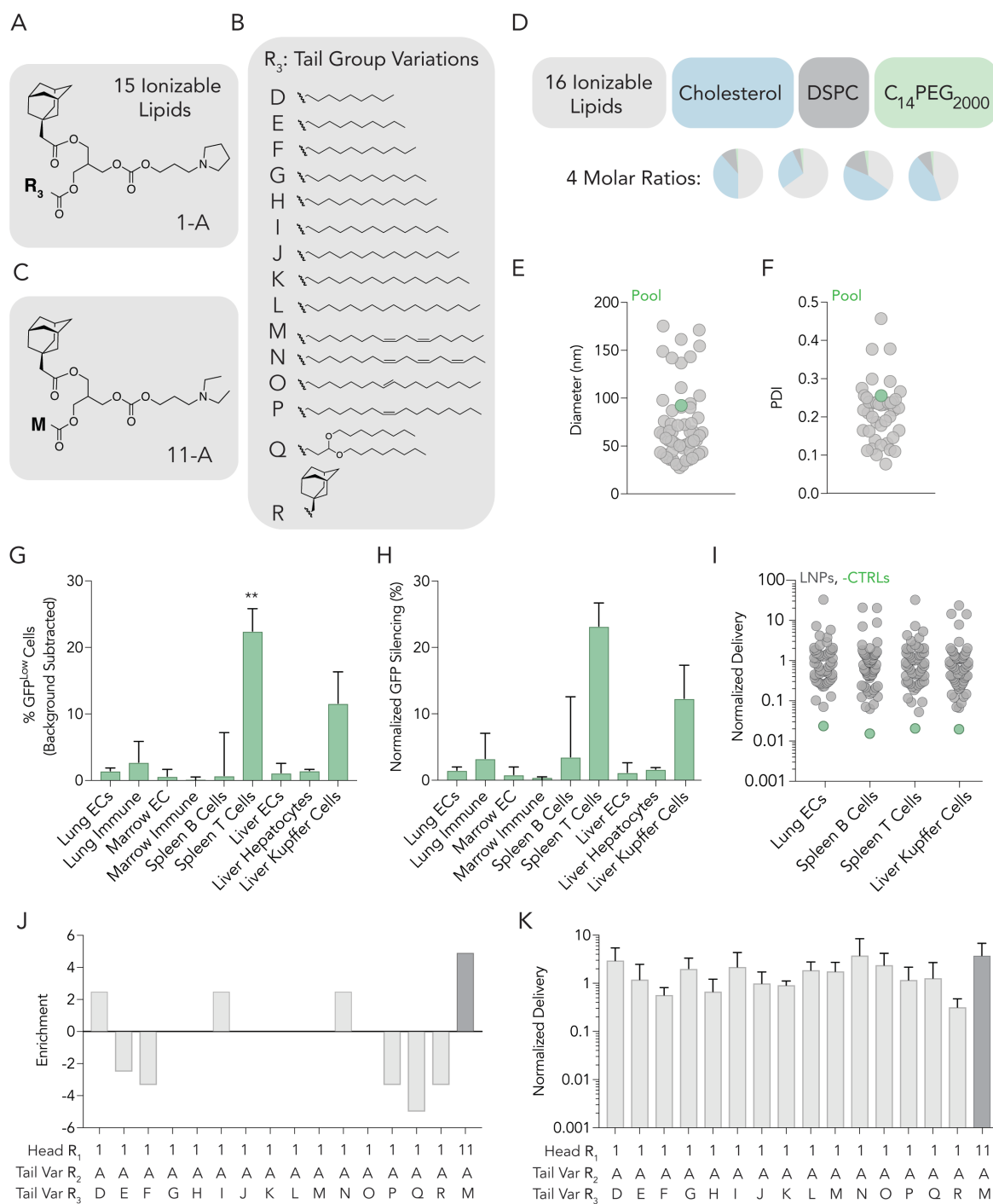


Figure 5.9. A second high-throughput siRNA screen suggests that the adamantane tail influences delivery. (A) 15 cLNPs can be formed with the top performing head group and (B) 15 tail variations. (C) The top performing constrained lipid from screen

1 was included. (D) Using 4 molar ratios, each of the 16 ionizable lipids were formulated with cholesterol, lipid-PEG, and DSPC to create 64 distinct LNPs. (E) Hydrodynamic diameter and (F) polydispersity index of all formulated LNPs, measured individually. (G) Percent GFP^{Low} cells in 9 cell types. Two-way ANOVA, *P<0.05. (I) Normalized decrease in GFP MFI in 9 cell types. (E) Normalized DNA delivery in lung endothelial cells, splenic B and T cells, as well as liver Kupffer cells. (J) Enrichment for each of the 16 ionizable lipids. (K) Normalized DNA delivery of each LNP formulated.

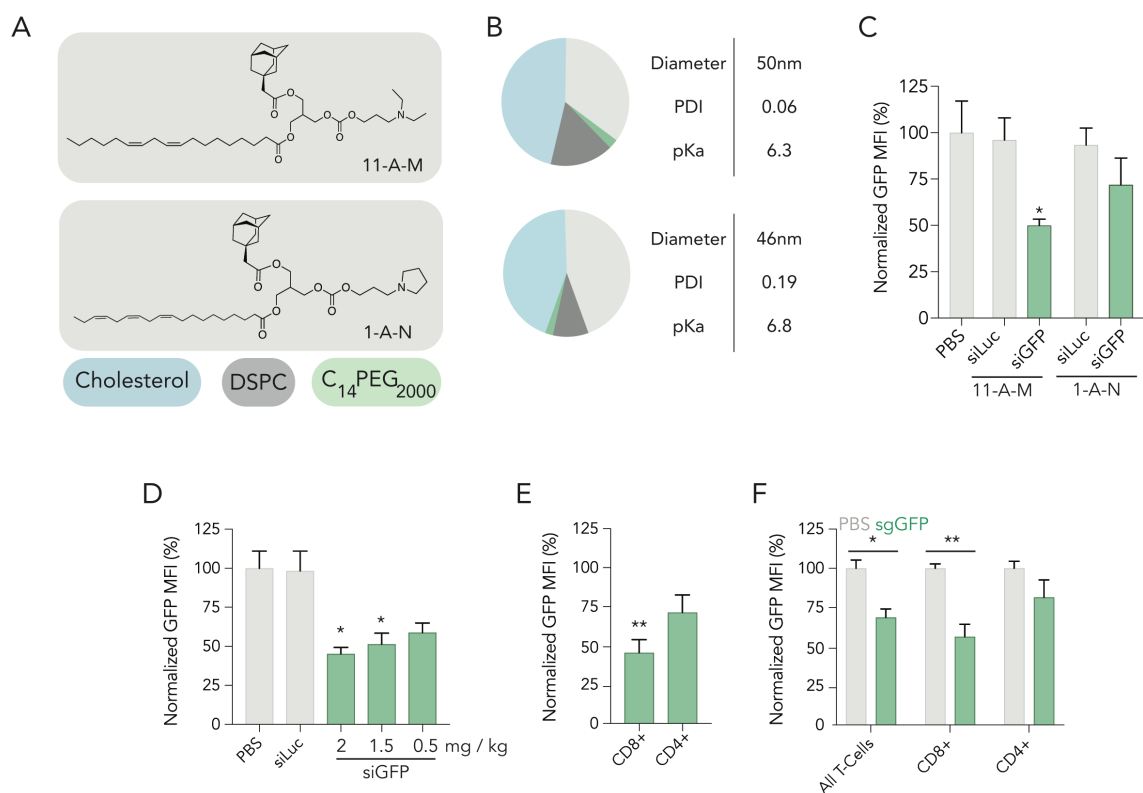


Figure 5.11. cLNPs deliver small RNAs that change gene expression in CD8⁺ T cells. (A) Structure of ionizable lipid 11-A-M and molar composition of top performing cLNP from screen 1. (B) Structure of ionizable lipid 1-A-N and molar composition of top performing cLNP from screen 2. (C) Normalized GFP expression in splenic CD3⁺ T cells 72 hours after treatment of 2 cLNP carrying siLuc at a dose of 1.5 mg / kg or siGFP at doses of 1.5 mg / kg. (D) Normalized GFP MFI in splenic CD3⁺ T cells 72 hours after treatment of cLNP carrying either siLuc or siGFP at various doses. One-way ANOVA, *P<0.05. (E) Normalized GFP MFI in splenic CD8⁺ and CD4⁺ T cells 72 hours after treatment of cLNP carrying siGFP at a dose of 2.0 mg / kg. unpaired 2-tail *t*-test, **P<0.01. (F) Normalized GFP MFI in splenic CD3⁺ T cells as well as CD8⁺ and CD4⁺ T cells after treatment of cLNPs carrying sgRNA at a dose of 2.0 mg / kg. Two-way ANOVA, *P<0.05, **P<0.01.

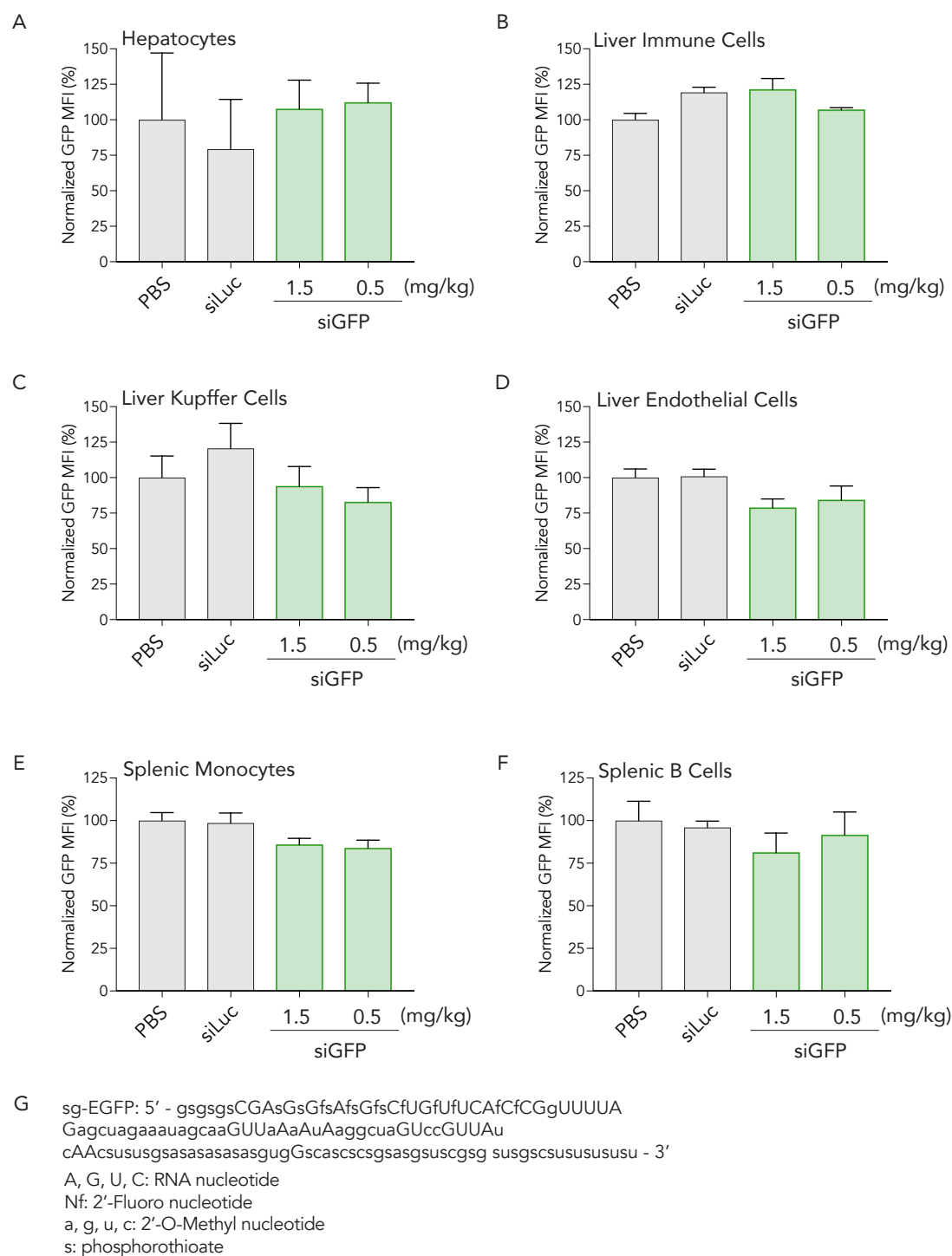


Figure 5.12. Normalized GFP MFI of mice treated with either PBS, cLNP carrying 1.5 mg / kg siLuc, or cLNP carrying siGFP at a dose of 0.5 or 1.5 mg / kg in A) hepatocytes, B) liver immune cells, C) liver kupffer cells, D) liver endothelial cells, E) splenic monocytes, F) splenic B cells.

splenic monocytes, and F) splenic B cells. G) Sequence and chemical modification for sgGFP.

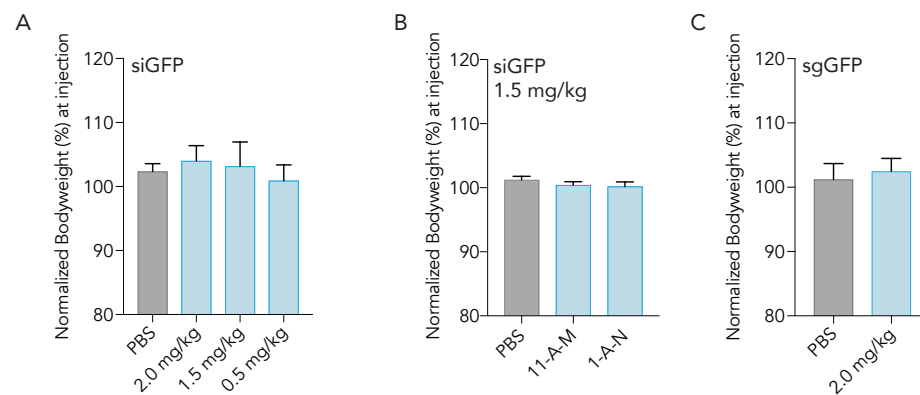


Figure 5.13. A) Mouse weights 24hrs after administration of PBS or cLNP at various doses of siRNA. B) Mouse weights 24hrs after administration of PBS or cLNP carrying siGFP. C) Mouse weights 24hrs after administration of PBS or cLNP carrying sgGFP.

5.2 Methods and Materials

Lipids were attached to the scaffold via esterification. Nucleic acids were diluted in citrate buffer; nanoparticle components were diluted in 100% ethanol. The phases were mixed together via microfluidics^[15]. LNP hydrodynamic diameter was measured using dynamic light scattering. pKa was calculated using the TNS assay, as we previously reported^[19]. Mice were purchased from Jackson Laboratory; all were 5-8 weeks old. N = 4-5 mice per group were injected intravenously via the lateral tail vein. All animal experiments were performed in accordance with the Georgia Tech IACUC. Sequencing was performed on MiniSeqTM using Illumina protocols.

5.3 References

- [1] D. N. Khalil, E. L. Smith, R. J. Brentjens, J. D. Wolchok, *Nat Rev Clin Oncol* 2016, 13, 273.
- [2] E. Shifrut, J. Carnevale, V. Tobin, T. L. Roth, J. M. Woo, C. T. Bui, P. J. Li, M. E. Diolaiti, A. Ashworth, A. Marson, *Cell* 2018, 175, 1958.
- [3] M. Rizk, S. Tuzmen, *Pharmacogenomics and personalized medicine* 2017, 10, 267.
- [4] C. Lorenzer, M. Dirin, A. M. Winkler, V. Baumann, J. Winkler, *J Control Release* 2015, 203, 1.
- [5] P. Kumar, H. S. Ban, S. S. Kim, H. Wu, T. Pearson, D. L. Greiner, A. Laouar, J. Yao, V. Haridas, K. Habiro, Y. G. Yang, J. H. Jeong, K. Y. Lee, Y. H. Kim, S. W. Kim, M. Peipp, G. H. Fey, N. Manjunath, L. D. Shultz, S. K. Lee, P. Shankar, *Cell* 2008, 134, 577.
- [6] S. Ramishetti, R. Kedmi, M. Goldsmith, F. Leonard, A. G. Sprague, B. Godin, M. Gozin, P. R. Cullis, D. M. Dykxhoorn, D. Peer, *ACS nano* 2015, 9, 6706.
- [7] R. Kedmi, N. Veiga, S. Ramishetti, M. Goldsmith, D. Rosenblum, N. Dammes, I. Hazan-Halevy, L. Nahary, S. Leviatan-Ben-Arye, M. Harlev, M. Behlke, I. Benhar, J. Lieberman, D. Peer, *Nat Nanotechnol* 2018, 13, 214.
- [8] T. T. Smith, S. B. Stephan, H. F. Moffett, L. E. McKnight, W. Ji, D. Reiman, E. Bonagofski, M. E. Wohlfahrt, S. P. S. Pillai, M. T. Stephan, *Nat Nanotechnol* 2017, 12, 813.
- [9] Z. Cheng, A. Al Zaki, J. Z. Hui, V. R. Muzykantov, A. Tsourkas, *Science* 2012, 338, 903.
- [10] A. Akinc, W. Querbes, S. De, J. Qin, M. Frank-Kamenetsky, K. N. Jayaprakash, M. Jayaraman, K. G. Rajeev, W. L. Cantley, J. R. Dorkin, J. S. Butler, L. Qin, T. Racie, A. Sprague, E. Fava, A. Zeigerer, M. J. Hope, M. Zerial, D. W. Sah, K. Fitzgerald, M. A. Tracy, M. Manoharan, V. Kotliansky, A. Fougerolles, M. A. Maier, *Mol Ther* 2010, 18, 1357.
- [11] E. Majorovits, M. Nejmeddine, Y. Tanaka, G. P. Taylor, S. D. Fuller, C. R. Bangham, *PLoS One* 2008, 3, e2251.
- [12] K. Paunovska, C. J. Gil, M. P. Lokugamage, C. D. Sago, M. Sato, G. N. Lando, M. Gamboa Castro, A. V. Bryksin, J. E. Dahlman, *ACS nano* 2018, 12, 8341.

- [13] K. Paunovska, C. D. Sago, C. M. Monaco, W. H. Hudson, M. G. Castro, T. G. Rudoltz, S. Kalathoor, D. A. Vanover, P. J. Santangelo, R. Ahmed, A. V. Bryksin, J. E. Dahlman, *Nano Lett* 2018, 18, 2148.
- [14] C. D. Sago, M. P. Lokugamage, G. N. Lando, N. Djeddar, N. N. Shah, C. Syed, A. V. Bryksin, J. E. Dahlman, *Nano Lett* 2018.
- [15] D. Chen, K. T. Love, Y. Chen, A. A. Eltoukhy, C. Kastrup, G. Sahay, A. Jeon, Y. Dong, K. A. Whitehead, D. G. Anderson, *J Am Chem Soc* 2012, 134, 6948.
- [16] M. P. Lokugamage, C. D. Sago, J. E. Dahlman, *Current Opinion in Biomedical Engineering* 2018, 7, 1.
- [17] R. J. Platt, S. Chen, Y. Zhou, M. J. Yim, L. Swiech, H. R. Kempton, J. E. Dahlman, O. Parnas, T. M. Eisenhaure, M. Jovanovic, D. B. Graham, S. Jhunhunwala, M. Heidenreich, R. J. Xavier, R. Langer, D. G. Anderson, N. Hacohen, A. Regev, G. Feng, P. A. Sharp, F. Zhang, *Cell* 2014, 159, 440.
- [18] S. C. Semple, A. Akinc, J. Chen, A. P. Sandhu, B. L. Mui, C. K. Cho, D. W. Sah, D. Stebbing, E. J. Crosley, E. Yaworski, I. M. Hafez, J. R. Dorkin, J. Qin, K. Lam, K. G. Rajeev, K. F. Wong, L. B. Jeffs, L. Nechev, M. L. Eisenhardt, M. Jayaraman, M. Kazem, M. A. Maier, M. Srinivasulu, M. J. Weinstein, Q. Chen, R. Alvarez, S. A. Barros, S. De, S. K. Klimuk, T. Borland, V. Kosovrasti, W. L. Cantley, Y. K. Tam, M. Manoharan, M. A. Ciufolini, M. A. Tracy, A. de Fougérolles, I. MacLachlan, P. R. Cullis, T. D. Madden, M. J. Hope, *Nat Biotechnol* 2010, 28, 172.
- [19] C. D. Sago, M. P. Lokugamage, F. Z. Islam, B. R. Krupczak, M. Sato, J. E. Dahlman, *Journal of the American Chemical Society* 2018.

CHAPTER 6. DEVELOPMENT OF IN VIVO OLIGONUCLEOTIDE ANTI-CRISPRS

6.1 Background & Results

CRISPR-based gene editing systems have therapeutic promise¹. However, their clinical utility is limited by ineffective drug delivery. Non-viral CRISPR therapies in adult animals have been limited to local delivery²⁻⁴, or if administered systemically, preferential editing in hepatocytes⁵⁻⁸. Unwanted hepatocyte delivery extends beyond CRISPR; many nanoparticles preferentially target the liver⁹. Thus, a pragmatic way to enable systemic, programmable, cell type-specific gene editing outside hepatocytes would constitute an important step for CRISPR therapeutics and nanomedicine.

To achieve non-hepatocyte drug delivery, scientists increase delivery to the ‘on-target’ cell type varying nanoparticle size, charge, chemical structure, or by adding targeting ligands that bind receptors on target cells¹⁰. Yet off-target hepatocyte delivery remains an unsolved problem, since the structure of hepatic sinusoids promotes unwanted nanoparticle accumulation¹¹. Thus, the current paradigm for systemic non-liver Cas9 therapies, which requires a nanoparticle to (i) efficiently target a new cell type and (ii) avoid hepatocytes, may be difficult to achieve in the short term. One alternative is to specifically block the activity of a drug in hepatocytes, thereby shifting the effective tropism of the nanoparticle away from the liver. We envision exploiting the relative ease with which nanoparticles are delivered to hepatocytes by delivering molecules that inactivate drugs. Here we use such an approach to control the cell type-specific activity of Cas9 drugs using synthetic anti-CRISPRs. By delivering a synthetic, chemically modified oligonucleotide anti-CRISPRs (termed inhibitory oligos, iOligos) to

hepatocytes, we markedly reduce hepatocyte gene editing, thereby achieving preferential gene editing outside the liver.

Recent descriptions of peptide- and protein-based anti-CRISPRs that reduce gene editing *in vitro*¹²⁻¹⁴ led us to hypothesize that chemically modified anti-CRISPR oligonucleotides could reduce Cas9 editing *in vivo*. Researchers have applied anti-CRISPRs to reduce the gene editing potency of pre-formed Cas ribonucleoprotein (RNP) complexes by blocking interactions between the pre-formed RNP and target DNA (**Figure 6.1a**). For example, the anti-CRISPR AcrE2 bound to NmeCas9/sgRNA complex *in vitro*; this resulted in decreased indel formation in HEK.293T cells¹². In another example, AcrIIA4, a naturally occurring peptide, reduced indel formation by >75%% in K562 cells¹³. These advances are important, yet oligonucleotide-based anti-CRISPRs targeting Cas9 derived from *Streptococcus Pyogenes* (*SpCas9*, hereafter referred to as Cas9) have not been reported. Moreover, anti-CRISPRs have not been successfully delivered in adult animals, limiting their ability to control nanoparticle tropism *in vivo*. To maximize the likelihood anti-CRISPRs could control systemically administered gene editing therapies *in vivo*, we focused on iOligos for several reasons. First, oligonucleotides are well tolerated in animals and humans¹⁵. Second, chemical modifications can increase oligonucleotide stability and potency¹⁶. Third, lipid nanoparticles (LNPs) that deliver oligonucleotides to hepatocytes are clinically approved¹⁵. Finally, we envisioned that iOligos could interact with the sgRNA and work independently of RNP complex formation (**Figure 6.1b**).

We first investigated whether small chemically modified oligonucleotides could act as a universal anti-CRISPR to Cas9. We tiled iOligo sequences across the conserved region of

sgRNA¹⁷ (**Figure 6.1c**). Each iOligo was chemically modified at every position with 2'-O-methyl ribose and phosphorothioate modifications (**Figure 6.2a**) to increase stability, reduce immunogenicity, and increase affinity between the iOligo and target RNA¹⁸. We performed initial experiments in immortalized aortic endothelial cells (iMAECs)¹⁹ which we transduced with lentivirus to stably express SpCas9 (hereafter termed Cas9-iMAECs). Using Lipofectamine 2000, we transfected iOligos into Cas9-iMAECs; 4 hours later, we transfected the same cells with 16nM sgRNA targeting ICAM-2 (sgICAM-2) (**Figure 6.2b**). Seventy-two hours later, we isolated genomic DNA from the cells and quantified insertions and deletions (indels) using Tracking of Indels by Decomposition (TIDE)²⁰. Compared to a scrambled oligonucleotide (same length, with the same chemical modifications), which acted as a control, all four iOligos reduced Cas9-mediated indels, suggesting the iOligos can block sgRNA activity in murine cells. iOligo-D, which was targeted to the 3' end of the sgRNA, reduced indels more than other iOligos (**Figure 6.1d**). All four iOligos reduced indel formation in a dose-dependent way in Cas9-iMAECs (**Figure 6.1e**) and exhibited ED₅₀ values between 53 and 91 nM (**Figure 6.1f**). We selected iOligo-D (hereafter termed iOligo) for further studies.

To probe the relationship between iOligo structure and anti-sgRNA activity, we first created iOligo mutants, truncating four nucleotides from the 5' and 3', respectively (**Figure 6.1g**). When we administered them to Cas9-iMAECs at a 50 nM dose, the 5' truncated mutant lost activity, as indicated by its inability to block gene editing. The 3' truncated mutant maintained as much activity as the non-mutant iOligo, suggesting that iOligo potency depends on the sgRNA region that was targeted, more than iOligo length (**Figure 6.1h**). To study the relationship between iOligo chemical modifications and anti-

sgRNA activity, we administered 50 nM iOligos with fewer modifications to Cas9-iMAECs. The original iOligo (i.e., fully modified) outperformed all iOligo variants with fewer modifications (**Figure 6.1i**, **Figure 6.2c**). These results also led us to conclude that iOligos are unlikely to act via RNase H-mediated degradation of sgRNA, since fully 2' O-methyl modifications prevent DNase H activity²¹. As further evidence for this RNase H-independent mechanism, 2' Methoxyethyl modifications did not increase the efficacy of iOligo compared to 2' O-methyl modifications (**Figure 6.1j**).

To confirm these results, which were all generated in Cas9-iMAECs, we investigated whether iOligos maintained functionality when Cas9 was delivered transiently via mRNA. We transfected iOligos at a dose of 16nM, then transfected wildtype iMAECs with 300ng Cas9 mRNA and 16 nM sgICAM-2. As expected, iOligos reduced indel formation. We then varied the time between iOligo administration and Cas9 administration, and found that iOligo efficacy was most effective 2 hours prior to the delivery of mRNA and sgRNA (**Figure 6.1k**). Taken together, these results led us to conclude that chemically modified, small oligonucleotides can block Cas9 activity *in vitro*.

Anti-CRISPR studies have been performed in biochemical assays and cell culture¹²⁻¹⁴. Thus, we investigated whether iOligo could control gene editing in adult mice using several models. First, we reduced gene editing in hepatocytes (**Figure 6.3a**). We formulated hepatocyte-targeting LNPs by mixing C₁₄PEG₂₀₀₀, cholesterol, 1,2-distearoyl-sn-glycero-3-phosphocholine (DSPC), and the ionizable lipid cKK-E12²² in a microfluidic device²³ (**Figure 6.2d**). This LNP delivers oligonucleotides to hepatocytes *in vivo*^{7, 22}. We formulated hepatocyte-targeting LNPs to carry iOligo, or as a control, the

scrambled sequence. We also formulated the hepatocyte-targeting LNPs to carry chemically modified sgGFP. In all three cases, small, stable LNPs with low polydispersity were formed (**Figure 6.2e**). We injected mice that express SpCas9-GFP under a ubiquitous CAG promoter²⁴ with either iOligo or the control oligo, and two hours later, injected the same mice with sgGFP (**Figure 6.3b**, **Figure 6.2f**). Five days later, we sacrificed the mice, isolated hepatocytes (CD31⁻CD45⁻) using fluorescence activated cell sorting (FACS), and quantified GFP protein expression as well as indels. Compared to control mice injected with PBS, GFP expression in mice injected with control oligo and sgGFP was reduced by 50% as measured by mean fluorescent intensity (MFI) (**Figure 6.3c**). GFP expression in mice treated with iOligo and sgGFP was statistically higher, suggesting that iOligo blocked sgGFP gene editing in Cas9 mice (**Figure 6.3c**). Indel percentages decreased by 58% in iOligo treated mice, relative to mice treated with the control oligo (**Figure 6.3d**), suggesting the effect was Cas9-mediated.

We then tested iOligos in wildtype C57BL/6 mice, a model that is more clinically relevant than transgenic mice expressing Cas9. We formulated the iOligo or scramble control into the hepatocyte-targeting LNP, then administered it intravenously to wildtype adult mice (**Figure 6.3e**). Two hours later, we injected the mice with LNPs carrying Cas9 mRNA and a chemically modified sgRNA targeting ICAM-2²⁴. Importantly, for the second injection, we utilized recently reported LNPs that deliver Cas9 mRNA and sgRNA to hepatocytes and splenic endothelial cells²⁵. After isolating hepatocytes and splenic endothelial cells (CD31⁺CD45⁻) using FACS, we found that pre-delivery of iOligos to hepatocytes resulted in a statistically significant reduction in hepatocyte indels

(**Figure 6.3f**), but not splenic endothelial cell indels (**Figure 6.3g**). In both *in vivo* experiments, iOligos were well tolerated by mice (**Figure 6.3a,b**). These data led us to conclude that iOligo delivery to hepatocytes can reduce hepatocyte editing without reducing editing in other cell types within the same animal.

Cas9 mRNA and sgRNA are often co-delivered in the same LNP^{5-8, 25}. Since iOligos target the sgRNA and do not affect the production of Cas9 protein, we reasoned that iOligos used in concert with siRNAs that degrade Cas9 mRNA could further reduce unwanted hepatocyte gene editing. To test this, we designed chemically modified Cas9 mRNA, such that it was particularly sensitive to a previously validated²⁶ siRNA targeting GFP (siGFP). Specifically, we *in vitro* transcribed a Cas9 mRNA with N1-methyl-pseudouridine to minimize immune stimulation and a 3' UTR containing five binding sites for siGFP (**Figure 6.5a**, **Figure 6.6a**). The five siGFP binding sites were placed throughout the 3' UTR, we term this engineered UTR 'siUTR'. Using Lipofectamine 2000, we transfected iMAECs with siGFP, or a control siRNA (**Figure 6.6b**). Ten hours later, a timepoint we selected based on previous work²⁷, we transfected the same cells with Cas9 mRNA and sgICAM-2. When compared to cells pre-treated with 20 nM siCtrl, cells pre-treated with 20 nM siGFP produced 65% less Cas9 protein, quantified by flow cytometry MFI (**Figure 6.5b**). We also observed a robust decrease in indel formation in cells treated with siGFP, compared to cells treated with siCtrl (**Figure 6.5c**). Similarly, we found that if we held the siRNA dose constant at 20 nM, the number of indels decreased with the amount of Cas9 mRNA we administered, as expected (**Figure 6.5d**). These data led us to conclude that a Cas9 mRNA rationally designed to be sensitive to siGFP could be efficiently degraded with siGFP.

After confirming siRNA could disrupt Cas9 mRNA translation and prevent downstream indel formation *in vitro*, we investigated whether we could achieve cell type-specific control of Cas9 gene editing *in vivo*. First, we intravenously injected mice with siCtrl or siGFP formulated into hepatocyte-targeting LNPs (**Figure 6.6c**). These previously validated LNPs formed small, stable nanoparticles (**Figure 6.6d**). Fourteen hours after injecting mice with siRNA, we injected the same mice with hepatocyte-targeting LNPs carrying Cas9 mRNA and sgICAM-2 (**Figure 6.6e,f**). Five days later, we isolated hepatocytes using FACS, and measured indels using TIDE (**Figure 6.5e**). Compared to mice treated with siCtrl, mice treated with siGFP had significantly fewer indels (**Figure 6.5f**), demonstrating that siGFP was capable of reducing gene editing in hepatocytes.

We then validated the siRNA / mRNA approach using an alternative mRNA. We *in vitro* transcribed chemically modified mRNA encoding Luciferase, such that it had five siGFP binding sites in the 3' UTR (**Figure 6.6g**). As an *in vitro* proof of concept, we pre-treated iMAECs with a control siRNA targeting ICAM-2 (siICAM-2) or siGFP, then administered Luciferase mRNA. In this case, we used siICAM-2 as a control, since siLuciferase (our previous siCtrl) was not a proper control for Luciferase mRNA. We found that, as expected, luminescence decreased by up to 79% in a dose-dependent manner in relation to amount of mRNA transfected in cells pre-treated with siGFP, relative to cells treated with siICAM-2 (**Figure 6.6**). To test whether we could reduce Luciferase *in vivo*, we pre-treated mice with LNPs containing siGFP or siICAM-2, waited fourteen hours, then treated mice with hepatocyte-targeting LNPs (**Figure 6.6i,j**) carrying Luciferase mRNA (**Figure 6.6k**). Six hours later, we administered luciferin to mice,

isolated the liver, and quantified luminescence. Compared to siICAM-2 treated mice, those treated with siGFP generated 74% less luminescence signal (**Figure 6.6l**). Taken together, these animal models convinced us that using siGFP to degrade mRNA that was rationally designed to be sensitive to siGFP was a feasible way to control gene editing *in vivo*.

We then tested the hypothesis that combining iOligo (which targets the sgRNA) and the siRNA approach (which targets Cas9 mRNA) would potentially reduce editing *in vivo* (**Figure 6.5g**). We intravenously injected mice with hepatocyte-targeting LNPs carrying siGFP, then 14 hours later, injected mice with hepatocyte-targeting LNPs containing iOligo. Two hours later, we intravenously injected mice with Cas9 mRNA and sgRNA in LNPs that edit splenic cells and hepatocytes. To compare the combination of iOligo and siUTR, we included the control groups of iOligo paired with control siRNA, as well as scramble iOligo paired with siGFP. Combining iOligo and siGFP potentially reduced editing in hepatocytes (**Figure 6.5h**); as expected, splenic editing was not reduced (**Figure 6.5i**). This led to preferential editing in the spleen (**Figure 6.5j**). The combinations of iOligo and siUTR were well tolerated in mice (**Figure 6.6m**).

These data are particularly exciting given that iOligo and siUTR combinations can be further optimized in future work. Specifically, we envision improving potency of iOligo by altering its chemical modifications and sequences. We also envision enhancing the potency of the siGFP (or another sequence), or alternatively, using naturally occurring hepatocyte-specific miRNA binding sites. Ideally, these improvements, along with an optimized dosing schedule (such that iOligo and siGFP are delivered in the same LNP) will reduce hepatocyte gene editing efficacy to undetectable levels.

This work will enable the development of systemic, non-hepatocyte Cas9 therapies by removing an important nanoparticle design criterion. Historically, a nanoparticle would need to deliver Cas9 mRNA + sgRNA exclusively to a new target cell; now a nanoparticle that delivers Cas9 mRNA + sgRNA to a desired target cell type and hepatocytes is sufficient. Excitingly, we note that we have changed the ‘functional tropism’ of a previously reported nanoparticle ²⁵ without changing the nanoparticle itself. Given the fact that many nanoparticles with activity in non-liver cell types still accumulate in the liver, this broad approach may accelerate the rate at which RNA therapies treat disease in new tissues.

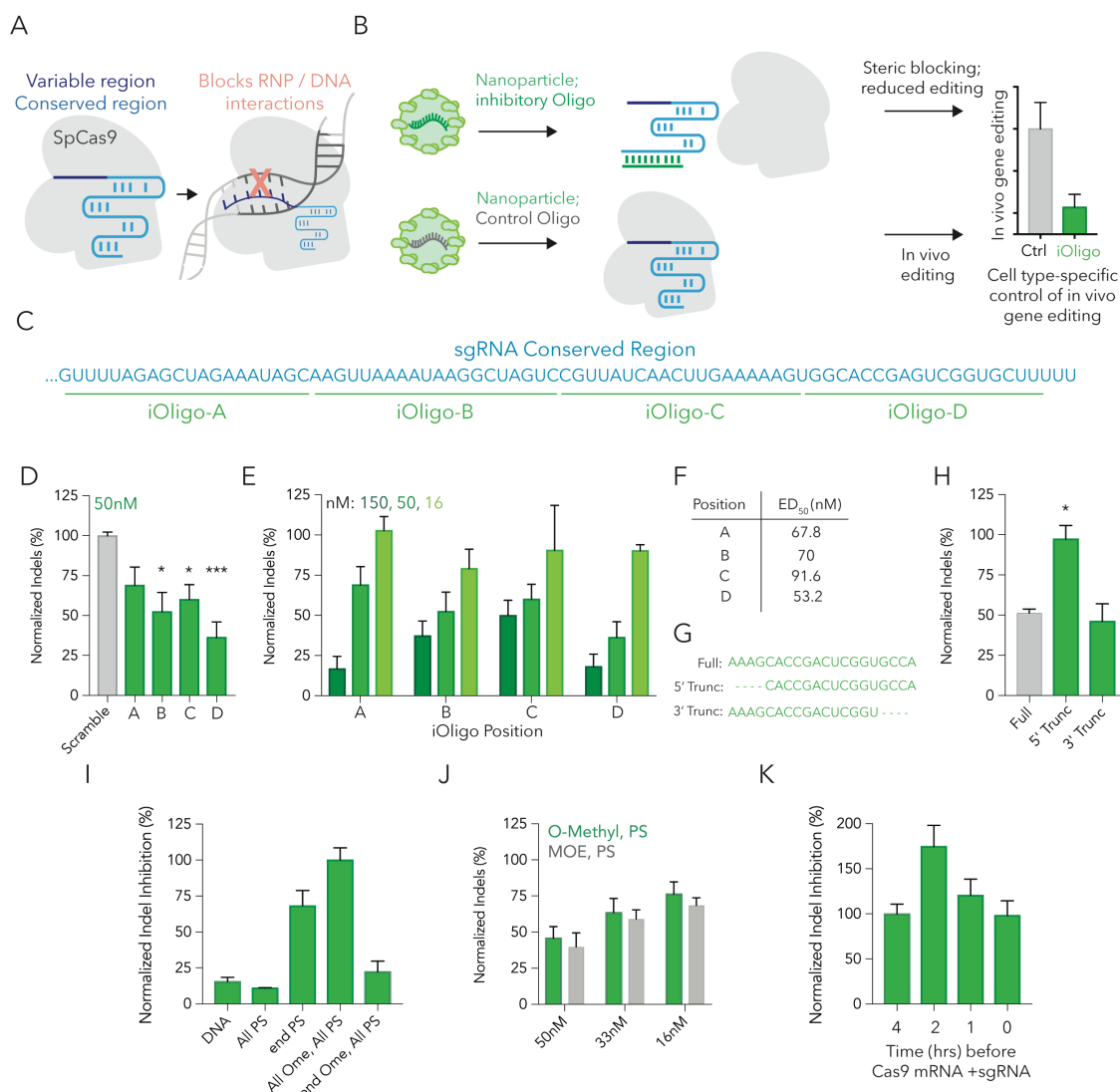


Figure 6.1. Small oligonucleotide anti-CRISPRs called inhibitory oligos (iOligos) inhibit Cas9 activity *in vitro*. (A) SpCas9 and sgRNA for a ribonucleoprotein (RNP) which then interacts with, and edits, DNA. Previously described anti-CRISPRs typically block RNA interactions with DNA. (B) Proposed mechanism by which iOligo functions. By interacting with the conserved region of the sgRNA, the iOligo prevents Cas9-mediated gene editing (C) iOligos were tiled in the conserved region of the sgRNA backbone. (D) Indel % in Cas9-expressing cells following treatment with iOligos or a control; iOligos prevent indel formation in cell culture when transfected 4 hours prior to sgRNA. * $p < 0.05$, *** $p < 0.001$, One-Way ANOVA. (E) Each of the 4 iOligos inhibit indel formation in a dose-dependent manner. (F) Calculated effective dose required to inhibit indel formation by 50%. (G) Sequence of full-length and truncated iOligo nucleotides. * $p < 0.05$, One-Way ANOVA. (H) Normalized indels in Cas9-expressing cells after treatment with full-length and truncated versions of iOligo. (I) Normalized indel inhibition of iOligos with ribose and linkage chemical modification patterns. (J) Normalized indels in cells treated with different doses of

iOligo chemically modified with phosphorothioate linkages and either O-Methyl and Methoxyethyl riboses. (K) Normalized indel inhibition in normal cells as a function of the time between iOligo treatment (first) and Cas9 mRNA + sgRNA (second) in normal cells.

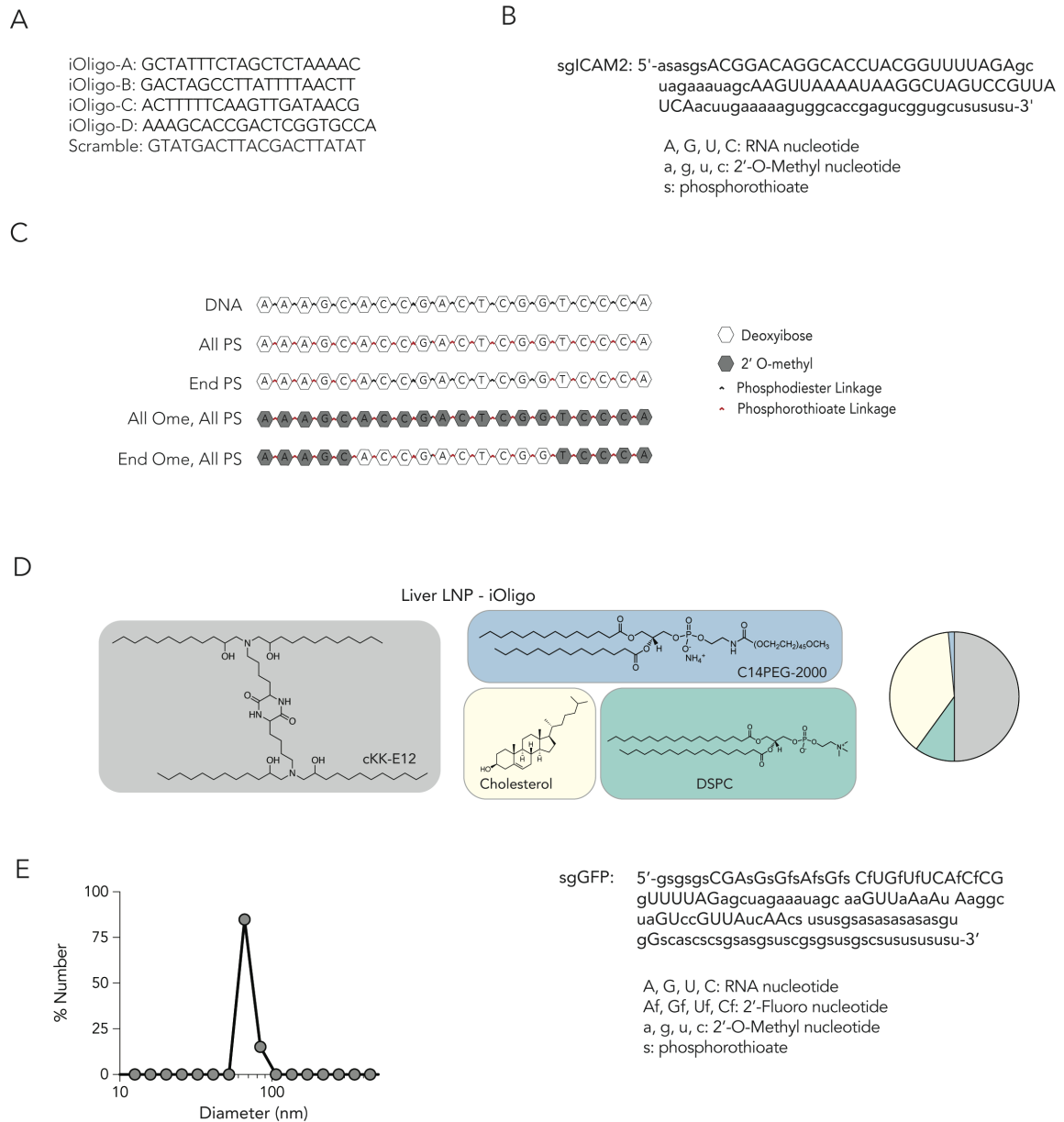


Figure 6.2. A) Sequences for iOligos. B) Sequence and chemical modifications for sgICAM2. C) LNP composition of hepatocyte trophic delivering siRNA. D) DLS spectrum of hepatocyte siRNA LNP. E) Sequence and chemical modifications for sgGFP.

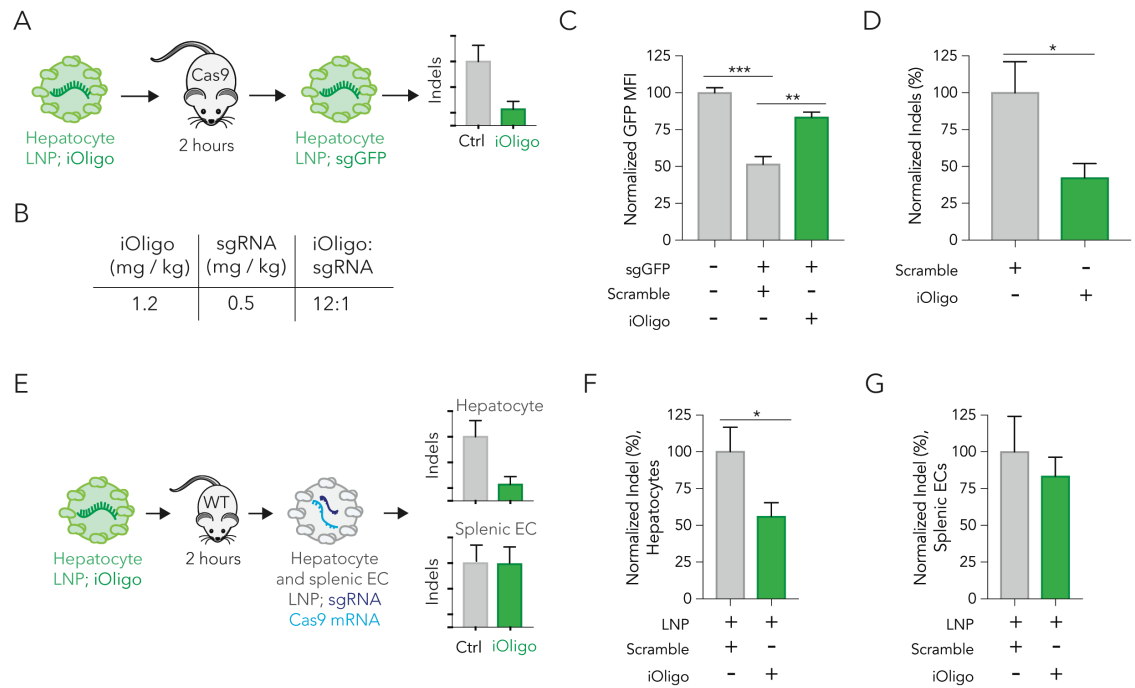
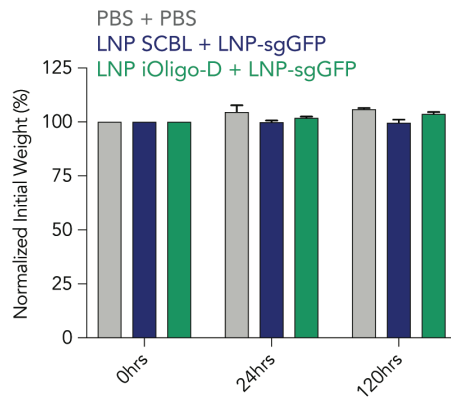


Figure 6.3. iOligos can control systemic gene editing therapies *in vivo*. (A) Mice that constitutively expression SpCas9 were pre-treated with iOligos delivered by a hepatocyte-trophic LNP; two hours later, the same LNP was used to deliver sgGFP. iOligos were expected to decrease indel formation in hepatocytes. (B) iOligos were administered at a total dose of 1.2 mg / kg before the administration of 0.5 mg / kg sgRNA, resulting in a 12:1 iOligo: sgRNA molar ratio. (C) Normalized GFP MFI in hepatocytes decreased in mice pre-treated with a control oligo, relative to mice treated with iOligo, as expected. **p<0.01, ***p<0.001, One-Way ANOVA. (D) Normalized indel percentage in hepatocytes also decreased in mice pre-treated with iOligo, relative to mice pre-treated with a control oligo. *p<0.05, 2-tail T-Test. (E) Wild-type mice were pre-treated with iOligos delivered by a hepatocyte-trophic LNP; two hours later, the same mice were treated with LNPs carrying Cas9 mRNA and sgICAM-2. iOligos were expected to decrease indel formation in hepatocytes, without impacting indels in splenic ECs. (F) Normalized indel percentage in hepatocytes in mice treated pre-treated with iOligo and control oligo. *p<0.05, Two-tail T-Test. (G) Normalized indel percentage in splenic ECs did not significantly change in mice pre-treated with iOligo, relative to control.

A



B

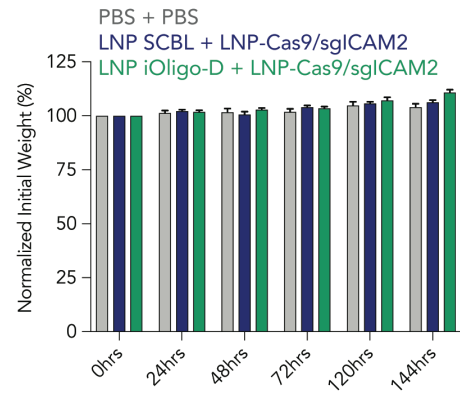


Figure 6.4. A) Normalized mouse weights for SpCas9-mice after administration of either PBS + PBS, Scramble iOligo + sgGFP, and iOligo-D + sgGFP. B) Normalized mouse weights for wild-type mice after administration of either PBS + PBS, Scramble iOligo + Cas9 mRNA / sgICAM2, and iOligo-D + Cas9 mRNA / sgICAM2.

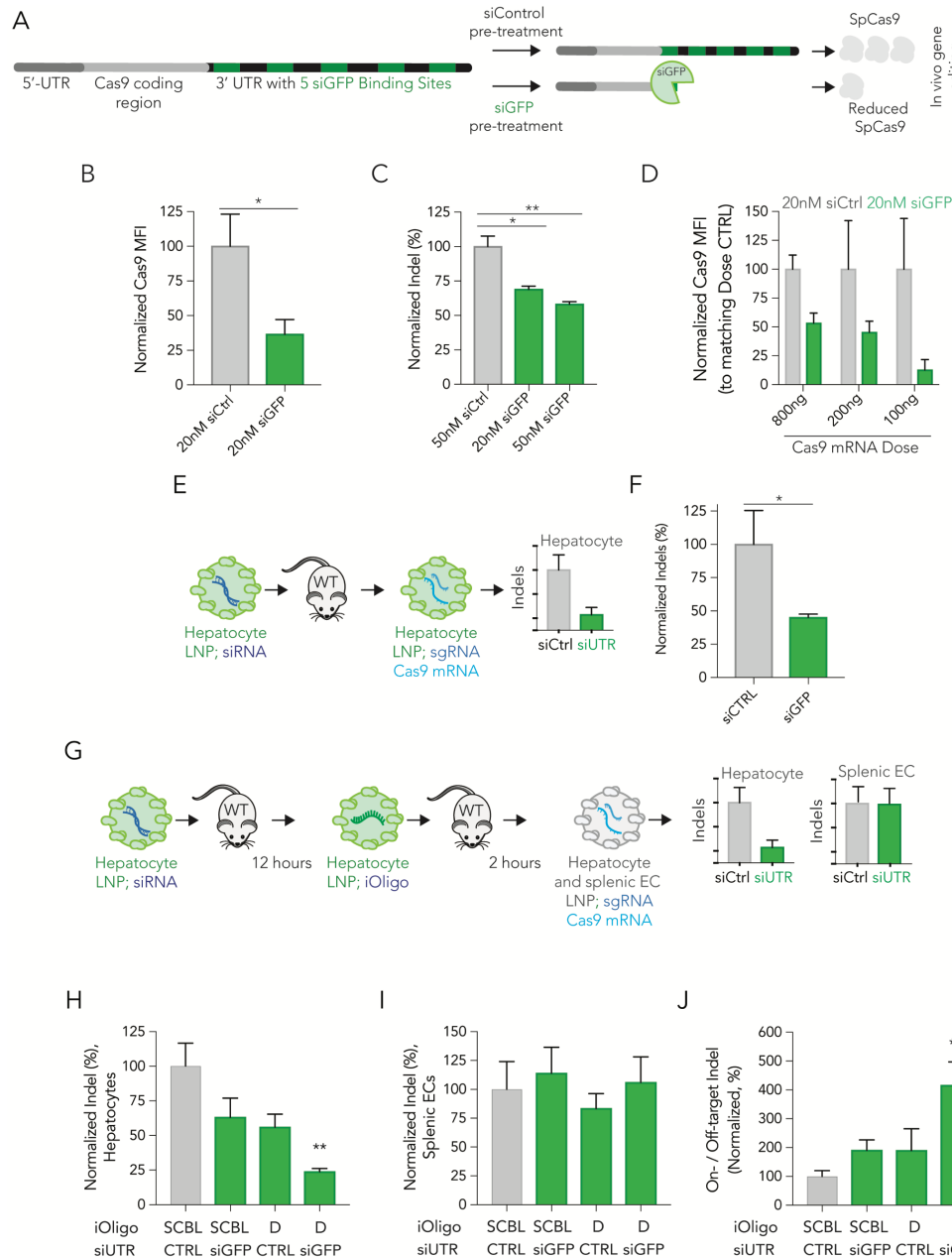


Figure 6.5. siRNA-mediated reduction of Cas9 expression can control editing *in vivo*, as can siRNA and iOligo combination treatments. (A) mRNA encoding for SpCas9 was rationally designed to be sensitive to siRNA degradation by including 5 siGFP binding sites in the 3' UTR. By reducing Cas9 protein expression, we expected reduced indel formation. **(B)** Pre-treating cells with siGFP decreases Cas9 protein translation, relative to cells treated with a control siRNA. *p<0.05, **p<0.01 One-Way ANOVA. **(D)** Pre-treating cells with siGFP decreases Cas9 protein translation in a dose-dependent manner. **(E)** Wild-type mice were pre-treated with either 1 mg / kg siCtrl or siGFP delivered by a hepatocyte-trophic LNP; 14 hours later, mice were injected with 3.0 mg / kg Cas9 mRNA (containing siGFP binding) and sgICAM-2

carried by the same LNP. siGFP was expected to decrease indel formation in hepatocytes. * $p < 0.05$, Two-tail T-Test. (F) Normalized indel percentage in hepatocytes was lower in mice pre-treated with siGFP, relative to siCtrl. (G) Wild-type mice were pre-treated with a combination of iOligo and siGFP. Mice received 1 mg / kg siCtrl or siGFP delivered by a hepatocyte-trophic LNP, then 1.2 mg / kg iOligos delivered by hepatocyte-trophic LNP. Two hours later, the same mice were treated with 3 mg / kg Cas9 mRNA and sgICAM-2 delivered by a hepatocyte- and splenic EC- trophic LNP. The combination of iOligo and siGFP were expected to decrease indel formation in hepatocytes, without reducing indels in splenic ECs. (H) Normalized indel percentage in hepatocytes for experimental groups pre-treated with combinations of control and active iOligos and siRNAs. The combination of iOligo and siGFP decreased indels in a synergistic manner. (I) Normalized indel percentage in hepatocytes for experimental groups pre-treated with combinations of control and active iOligos and siRNA. (J) Ratio of indels at on-target sites (splenic ECs) and off-target sites (hepatocytes), normalized to experimental group receiving control pre-treatment. ** $p < 0.01$ One-Way ANOVA.



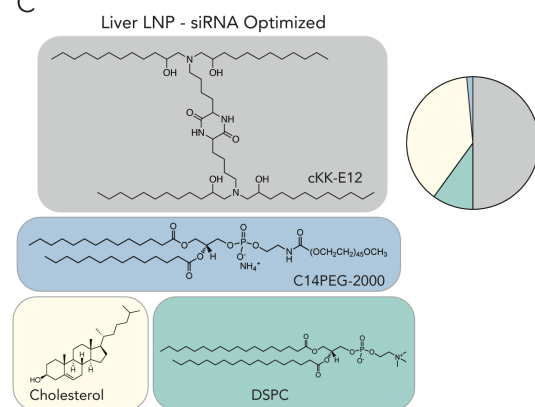
B

siLcAM-2 sense: 5' - AGGAcGGucAcAuuuuc dT sdT - 3'
 siLcAM-2 antisense: 5' - GAAAAGUuGAGACCGUCCU dT sdT -3'
 siLuciferase sense: 5' - cuuAcGcuGAGuAcuucGAdTsdT- 3'
 siLuciferase antisense: 5' - UCGAAGuACUcAGCGuAAGdTsdT -3'

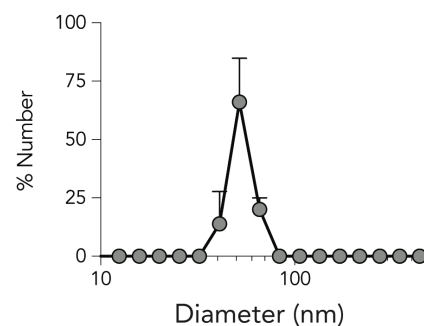
A, G, U, C: RNA nucleotide
 dT: deoxy-T
 a, g, u, c: 2'-O-Methyl nucleotide
 s: phosphorothioate

siGFP sense: 5' - AcAuGAAGcAGcACGACuU dT sdT - 3'
 siGFP antisense: 5' - AAGUCGUGCUGCUUCAUGU dT sdT -3'

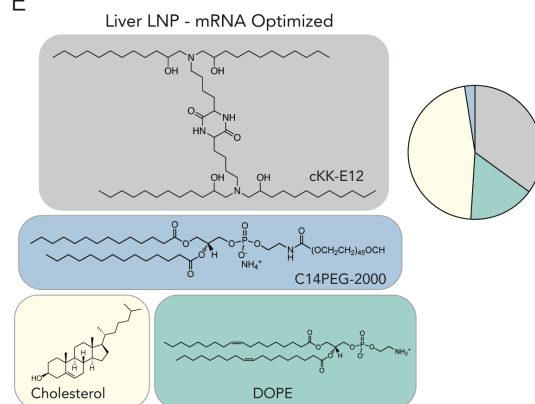
C



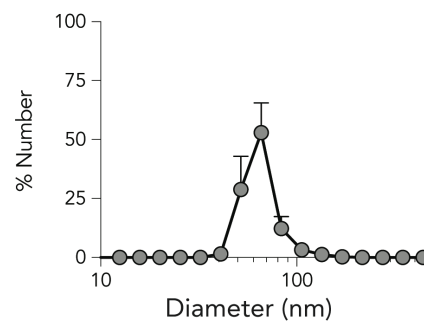
D



E



F



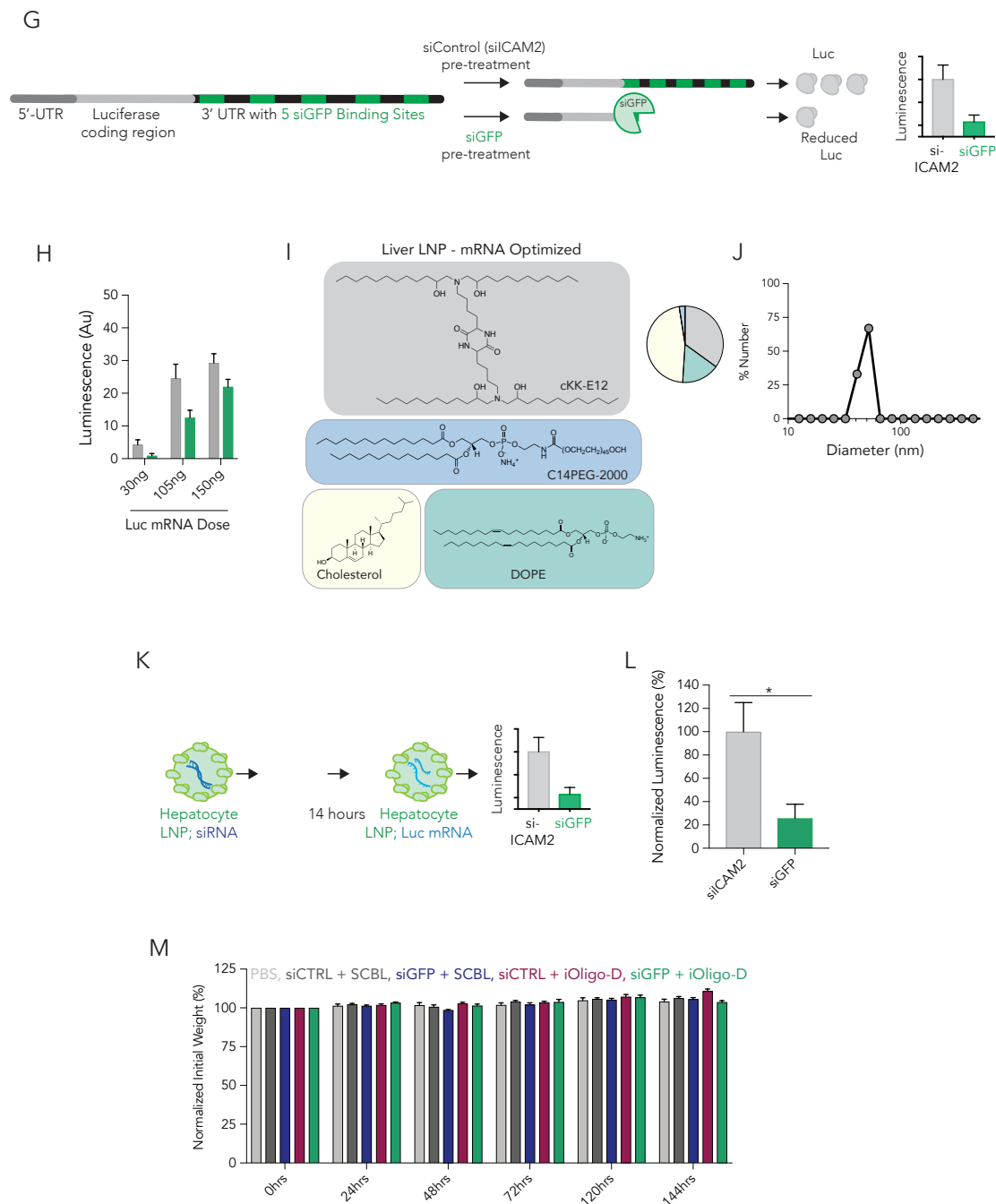


Figure 6.6. A) Engineered 3' UTR with 5 siGFP-binding sites. B) Sequence and chemical modifications of siRNAs used in this study. C) LNP composition of hepatocyte trophic delivering siRNA. D) DLS spectrum of hepatocyte siRNA LNP. E) LNP composition of hepatocyte trophic delivering mRNA. F) DLS spectrum of hepatocyte mRNA LNP. G) An engineered luciferase-encoding mRNA with the

custom 3' UTR will be degraded in the presence of siGFP, leading to decreased luciferase protein production as measured by luminescence. H) The engineered luciferase-encoding mRNA with the custom 3' UTR led to dose-dependent normalized expression in the presence of siGFP as compared to siCTRL. I) LNP composition of hepatocyte trophic delivering mRNA. F) DLS spectrum of hepatocyte mRNA LNP. K) Mice were pre-treated with either siGFP or siCTRL delivered by a hepatocyte-trophic LNP. 14 hours after pre-treatment, the engineered luciferase mRNA was delivered by a hepatocyte-trophic LNP. Liver luminescence is measured *ex vivo*. L) Normalized *ex vivo* luminescence the liver from mice pre-treated with either siCTRL (siICAM2) or siGFP. M) Normalized mouse weights for wild-type mice after administration of either PBS, siCTRL + Scramble iOligo, siGFP + Scramble iOligo, siCTRL + iOligo-D, and siGFP + iOligo-D.

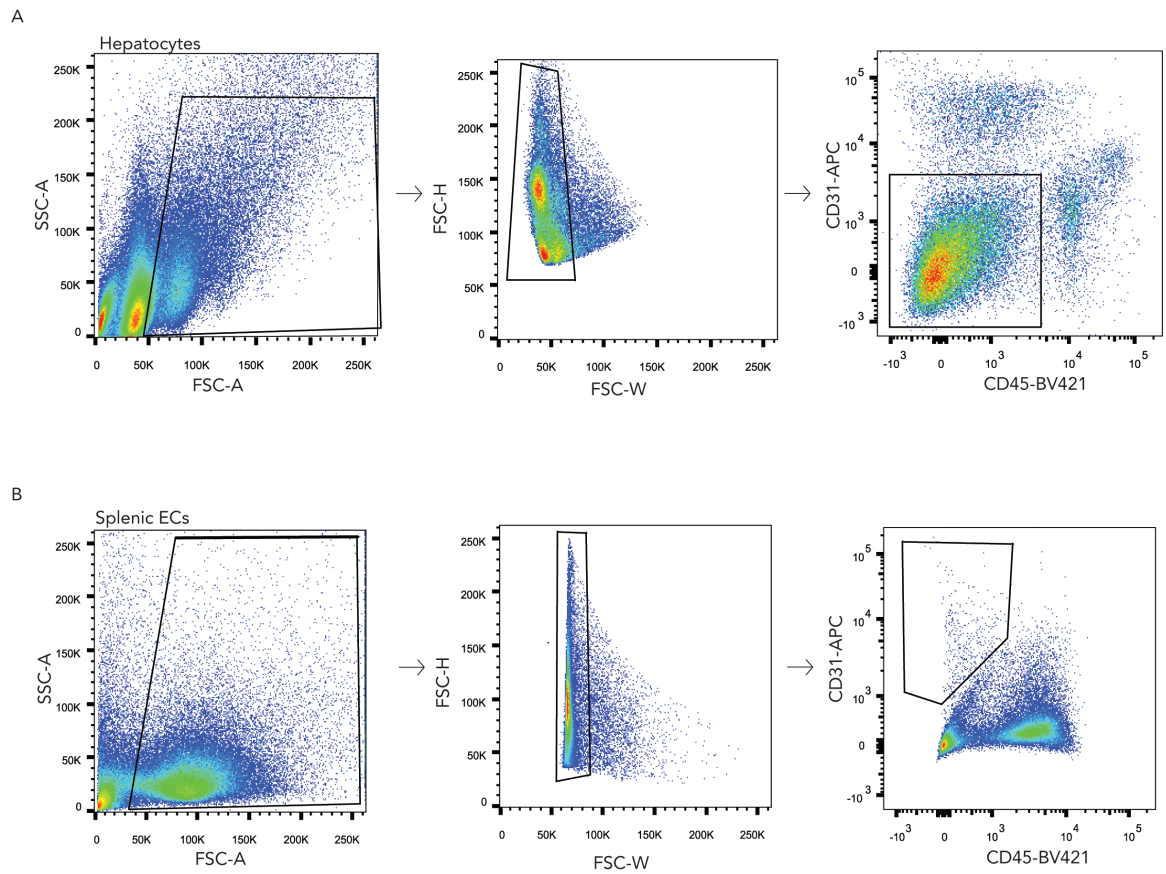


Figure 6.7. A) Representative FACS gating for liver hepatocytes. B) Representative FACS gating for splenic endothelial cells.

6.2 Methods & Materials

Oligonucleotide & siRNA Synthesis. iOligos were purchased from Integrated DNA Technologies (IDT). siRNAs (siLuc, siICAM2, siGFP) and sgRNAs (sgGFP, sgICAM2) were purchased from AxoLabs. Messenger mRNAs were either purchased from Trilink Biotechnologies (GFP) or synthesized as described below (Luciferase, SpCas9).

mRNA Synthesis. The Kozak consensus sequence and modified 3' UTR from murine α globin was modified with overlap extension PCR and was verified with Sanger sequencing (MWG Eurofins). The sequence of the 3' UTR is provided in the **Fig S3**. The DNA template was amplified using the Q5 high-fidelity DNA polymerase (New England Biolabs), purified using the QIAquick PCR purification kit (QIAGEN), digested with the restriction enzyme NOTI to create a 5' overhang, and then purified again. The T7 mScript Standard mRNA Production System was used to generate IVT mRNA (Cellscript), add a Cap-1 structure, and a poly(A) tail. Manufacturer's instructions were followed; the RNeasy mini kit (QIAGEN) was used to purify IVT mRNA when necessary. To incorporate modified bases, N1-methylpseudouridine- 5'-triphosphate (TriLink Biotechnologies and USB) were replaced in the 25 mM ribonucleotide cocktails. Cytosine triphosphate was purchased from Affymetrix. IVT mRNA was treated with Antarctic Phosphatase (New England Biolabs) for 30 min to remove residual 5'-triphosphates, and then purified with the RNeasy kit, quantified using the Nanodrop 2000 (Thermo Scientific), and then stored at -80°C .

Cell Culture. *In vitro* experiments were performed using Immortalized Aortic Endothelial Cells (iMAECs), or IMAECs stably transduced with CAG-SpCas9-EGFP. IMAECs were

cultured in EGM-2 Growth Media (Lonza). HEK293 cells were cultured in DMEM/F-12 50/50 media (Corning) supplemented by 10% (v/v) FBS (VWR) and 1% (v/v) penicillin-streptomycin (ThermoFisher Scientific). Cells were seeded in a 24-well plate at a density of 50k cells / well. DNA was isolated using 40 μ L of QuickExtract (EpiCentre).

TIDE. Indels were measured by Tracking Indels by Decomposition. Briefly, a ~600-800 nucleotide amplicon surrounding the sgRNA-binding sequence was amplified using PCR. This amplicon was then Sanger sequenced by Eton Biosciences.

Nanoparticle Formulation. Nanoparticles were formulated using a microfluidic device as previously described. Briefly, nucleic acids (siRNA and DNA barcodes) were diluted in citrate buffer while lipid-amine compounds (cKK-E12, 7C1), alkyl tailed PEG, cholesterol, and DSPC were diluted in ethanol. PEG, cholesterol, and DSPC was purchased from Avanti Lipids. Citrate and ethanol phases were combined in a microfluidic device by syringe pumps.

Animal Experiments. All animal experiments were performed in accordance with the Georgia Institute of Technology's Physiological Research Laboratory (PRL) animal care and services policy. C57BL/6J (#000664) and constitutive SpCas9 (#026179) mice were purchased from The Jackson Laboratory and used between 5-12 weeks of age. The nanoparticle concentration was determined using NanoDrop (Thermo Scientific).

Cell Isolation & Staining. Cells were isolated 72 hours after injection with LNPs unless otherwise noted. Mice were perfused with 20 mL of 1X PBS through the right atrium. Tissues were finely cut, and then placed in a digestive enzyme solution with Collagenase Type I (Sigma Aldrich), Collagenase XI (Sigma Aldrich) and Hyaluronidase (Sigma

Aldrich) at 37°C at 550rpm for 45 minutes. The digestive enzyme for spleen included Collagenase IV. Cell suspension was filtered through 70µm mesh and red blood cells were lysed. Cells were stained to identify specific cell populations and sorted using the BD FACS Fusion in the Georgia Institute of Technology Cellular Analysis Core. For *in vitro* experiments, a BD Accuri C6 was used. The antibody clones were used: anti-CD31 (BioLegend, 390), anti-CD45.2 (BioLegend, 104). We defined cell populations in the following manner: Splenic endothelial cells (CD31+CD45-), and hepatocytes (Liver, CD31-CD45-) as shown in **Figure 6.7**.

Cas9 Intracellular Staining. To determine Cas9 protein translation, the FoxP3 / Transcription Factor Staining Buffer kit (Tonbo Biosciences) was used to fix and permeabilize the cells. Anti-Cas9 primary antibody (Biolegend, 7A9) and AlexaFluor 647 anti-mouse IgG1 (Biolegend, RMG-1) was used to quantify Cas9 protein using a BD Accuri C6 flow cytometer.

In vitro luciferase. IMAECs were seeded at 10k cells per well in a 96 well plate. 16 hours after seeding, cells were transfected with either control (siICAM2) or active (siGFP) siRNA sequences with L2K. After 8 hours, engineered luciferase mRNA was transfected with L2K. 6 hours after the addition of the luciferase mRNA, luminescence was measured per manufactures recommendation using the Promega Bright-Glo Luciferase Assay System.

In vivo luciferase. C57BL/6J mice (Jackson Labs) were injected with the liver trophic LNP, cKK-E12, carrying either control (siICAM2) or active (siGFP) siRNA at a dose of

0.5 mg / kg. After 8 hours, mice were dosed with cKK-E12 carrying the engineered luciferase mRNA at a dose of 0.5 mg / kg. After 6 hours, mice underwent an intraperitoneal injection of CycLuc1. 15 minutes after IP administration, mice were sacrificed and livers isolated. Isolated livers were deposited in additional CycLuc1 solution and imaged by IVIS. Luminescence was normalized by mouse body weight.

6.3 References

1. Doudna, J.A. & Charpentier, E. Genome editing. The new frontier of genome engineering with CRISPR-Cas9. *Science* **346**, 1258096 (2014).
2. Lee, B. et al. Nanoparticle delivery of CRISPR into the brain rescues a mouse model of fragile X syndrome from exaggerated repetitive behaviours. *Nature biomedical engineering* (2018).
3. Lee, K. et al. Nanoparticle delivery of Cas9 ribonucleoprotein and donor DNA in vivo induces homology-directed DNA repair. *Nature biomedical engineering* **1**, 889-901 (2017).
4. Gao, X. et al. Treatment of autosomal dominant hearing loss by in vivo delivery of genome editing agents. *Nature* **553**, 217-221 (2018).
5. Miller, J.B. et al. Non-Viral CRISPR/Cas Gene Editing In Vitro and In Vivo Enabled by Synthetic Nanoparticle Co-Delivery of Cas9 mRNA and sgRNA. *Angew Chem Int Ed Engl* **56**, 1059-1063 (2017).
6. Jiang, C. et al. A non-viral CRISPR/Cas9 delivery system for therapeutically targeting HBV DNA and pcsk9 in vivo. *Cell research* **27**, 440-443 (2017).
7. Yin, H. et al. Structure-guided chemical modification of guide RNA enables potent non-viral in vivo genome editing. *Nat. Biotechnol.* (2017).
8. Finn, J.D. et al. A Single Administration of CRISPR/Cas9 Lipid Nanoparticles Achieves Robust and Persistent In Vivo Genome Editing. *Cell Rep* **22**, 2227-2235 (2018).
9. Lorenzer, C., Dirin, M., Winkler, A.M., Baumann, V. & Winkler, J. Going beyond the liver: progress and challenges of targeted delivery of siRNA therapeutics. *J Control Release* **203**, 1-15 (2015).
10. Blanco, E., Shen, H. & Ferrari, M. Principles of nanoparticle design for overcoming biological barriers to drug delivery. *Nat Biotechnol* **33**, 941-951 (2015).
11. Tsoi, K.M. et al. Mechanism of hard-nanomaterial clearance by the liver. *Nat Mater* **15**, 1212-1221 (2016).
12. Pawluk, A. et al. Naturally Occurring Off-Switches for CRISPR-Cas9. *Cell* **167**, 1829-1838.e1829 (2016).
13. Shin, J. et al. Disabling Cas9 by an anti-CRISPR DNA mimic. *Science advances* **3**, e1701620 (2017).

14. Zhu, Y., Zhang, F. & Huang, Z. Structural insights into the inactivation of CRISPR-Cas systems by diverse anti-CRISPR proteins. *BMC biology* **16**, 32 (2018).
15. Adams, D. et al. Patisiran, an RNAi Therapeutic, for Hereditary Transthyretin Amyloidosis. *N Engl J Med* **379**, 11-21 (2018).
16. Deleavey, G.F. & Damha, M.J. Designing chemically modified oligonucleotides for targeted gene silencing. *Chem Biol* **19**, 937-954 (2012).
17. Jinek, M. et al. A programmable dual-RNA-guided DNA endonuclease in adaptive bacterial immunity. *Science* **337**, 816-821 (2012).
18. Yildirim, I., Kierzek, E., Kierzek, R. & Schatz, G.C. Interplay of LNA and 2'-O-methyl RNA in the structure and thermodynamics of RNA hybrid systems: a molecular dynamics study using the revised AMBER force field and comparison with experimental results. *J Phys Chem B* **118**, 14177-14187 (2014).
19. Ni, C.W., Kumar, S., Ankeny, C.J. & Jo, H. Development of immortalized mouse aortic endothelial cell lines. *Vascular cell* **6**, 7 (2014).
20. Brinkman, E.K., Chen, T., Amendola, M. & van Steensel, B. Easy quantitative assessment of genome editing by sequence trace decomposition. *Nucleic Acids Res* **42**, e168 (2014).
21. Shen, X. & Corey, D.R. Chemistry, mechanism and clinical status of antisense oligonucleotides and duplex RNAs. *Nucleic Acids Res* **46**, 1584-1600 (2018).
22. Dong, Y. et al. Lipopeptide nanoparticles for potent and selective siRNA delivery in rodents and nonhuman primates. *Proceedings of the National Academy of Sciences of the United States of America* **111**, 3955-3960 (2014).
23. Chen, D. et al. Rapid discovery of potent siRNA-containing lipid nanoparticles enabled by controlled microfluidic formulation. *J Am Chem Soc* **134**, 6948-6951 (2012).
24. Platt, R.J. et al. CRISPR-Cas9 knockin mice for genome editing and cancer modeling. *Cell* **159**, 440-455 (2014).
25. Sago, C.D. et al. High-throughput in vivo screen of functional mRNA delivery identifies nanoparticles for endothelial cell gene editing. *Proceedings of the National Academy of Sciences* (2018).
26. Xue, W. et al. Small RNA combination therapy for lung cancer. *Proceedings of the National Academy of Sciences* **111**, E3553-E3561 (2014).

27. Pei, Y. et al. Quantitative evaluation of siRNA delivery in vivo. *Rna* **16**, 2553-2563 (2010).